

***D* REGION TOMOGRAPHY: A TECHNIQUE FOR IONOSPHERIC  
IMAGING USING LIGHTNING-GENERATED SFERICS AND INVERSE  
MODELING**

A Dissertation Presented to  
the Academic Faculty

by

Jackson C. McCormick

In Partial Fulfillment  
of the Requirements for the Degree of  
Doctor of Philosophy in the  
School of Electrical and Computer Engineering

Georgia Institute of Technology

December 2019

Copyright © Jackson C. McCormick 2019

***D* REGION TOMOGRAPHY: A TECHNIQUE FOR IONOSPHERIC  
IMAGING USING LIGHTNING-GENERATED SFERICS AND INVERSE  
MODELING**

Approved by:

Dr. Morris Cohen, Advisor  
School of Electrical and Computer  
Engineering  
*Georgia Institute of Technology*

Dr. Justin Romberg, Chair  
School of Electrical and Computer  
Engineering  
*Georgia Institute of Technology*

Dr. Sven Simon  
School of Earth and Atmospheric  
Sciences  
*Georgia Institute of Technology*

Dr. Malcolm Bibby  
School of Electrical and Computer  
Engineering  
*Georgia Institute of Technology*

Dr. Ryan Said  
*Vaisala Inc.*

Date Approved: September 25, 2019

*To the love of my life,  
my wife and best friend,*  
Holly

## ACKNOWLEDGEMENTS

I would like to begin with an effort to thank all those who have made my PhD journey possible, although it is impossible to state with such few words how grateful I am.

I am indebted to my advisor Morris Cohen who took a chance on me as his first graduate student. The impact of his mentorship and guidance to me has been immeasurable from the first research project assignment to my thesis work, a natural extension of this first project. It has been a truly fun and memorable experience to help establish and build the LF Lab from the ground floor into a flourishing and successful example of the academic research environment.

My early days in the LF Lab involved a lot of hardware design, development, and construction to which I am thankful to Jeff Chang for his assistance and many suggestions. In this regard, I am especially grateful to my friend and colleague Nick Gross, who helped to develop and deploy the next generation of the AWESOME receiver. I am also thankful to Nick for the many research discussions throughout the years. Thanks also to Amadeo Bellotti who volunteered his time to help in the early deployments despite having his own research and responsibilities in a different lab.

My work would not have been possible without the gracious hosts of the LF AWESOME receivers. The staff and volunteers at the Pisgah Astronomical Research Institute (PARI) deserve special thanks as the first site of the LF AWESOME receiver and hosts to the many visits while we debugged and tweaked the instrument.

My experience in the LF Lab was much more than research or a job, and for that I am thankful for the friendship of the LF Lab members: Nick Gross, Evan Worthington, Marc Higginson-Rollins, Nate Opalinski, Parker Singletary, Lee Thompson, Ted Slevin, and Nikhil Pailoor. Thanks for the great memories.

I am indebted to Vaisala Inc. for providing invaluable lightning location data to the LF Lab. Thanks especially to Ryan Said for his help to use and interpret the data. Ryan also made significant contributions to the data processing used in my work and co-authored my first journal paper. He served as the last member of my defense committee despite short notice and provided helpful comments on the manuscript.



Thanks to the rest of my thesis committee. First to Justin Romberg for chairing my committee and several helpful discussions on the DSP and imaging algorithms. Thanks to Sven Simon for his enthusiasm, encouragement, and helpful courses. Thanks also to Malcolm Bibby for the helpful discussions and suggestions.

I would not be who I am today without my parents Carol and Bill. My father is the most tenacious person I know, and this tenacity has inspired me to chase my dreams. My mother has remained a steadfast pillar of love and support. Last but certainly not least, finishing the long road to my PhD would not have been possible without my best friend and wife, Holly. She has always kept me on track and selflessly supported the pursuit of my dreams.

*This work was supported by the National Science Foundation under grants AGS 1451142 and 1653114 (CAREER) to Georgia Tech*

## TABLE OF CONTENTS

<b>Acknowledgments</b> . . . . .	vi
<b>List of Tables</b> . . . . .	ix
<b>List of Figures</b> . . . . .	x
<b>Summary</b> . . . . .	xiv
<b>Chapter 1: Introduction</b> . . . . .	1
1.1 Earth’s Ionosphere . . . . .	1
1.1.1 Formation and Structure of the Ionosphere . . . . .	3
1.1.2 Ionospheric Measurements and Perturbations . . . . .	7
1.1.3 Currents in the Ionosphere . . . . .	10
1.1.4 Review of Past <i>D</i> region Work . . . . .	12
1.2 Lightning . . . . .	19
1.2.1 The Lightning Flash . . . . .	19
1.2.2 Lightning-Driven Technology . . . . .	22
1.2.3 Sferic-Based <i>D</i> Region Remote Sensing . . . . .	24
1.3 Tomography . . . . .	27
1.3.1 Historical Development . . . . .	27
1.3.2 Mathematical Principles . . . . .	28
1.4 Contributions . . . . .	31
<b>Chapter 2: Sferic Propagation</b> . . . . .	34
2.1 Ray-Hop Analysis . . . . .	34

2.2	Finite-Difference Time-Domain . . . . .	36
2.3	Mode Theory and LWPC . . . . .	37
2.3.1	Wave Propagation in the Ionosphere . . . . .	37
2.3.2	Determining the Mode Solutions . . . . .	39
2.3.3	Excitation Factors and Height Gain Functions . . . . .	50
2.3.4	Mode Conversion and Sum . . . . .	51
2.3.5	LWPC Simplifications . . . . .	54
<b>Chapter 3: Experimental Setup and Data Processing . . . . .</b>		<b>56</b>
3.1	Lightning Variability . . . . .	56
3.2	Broadband Radio Receiver . . . . .	57
3.2.1	Receiver Data and Network . . . . .	59
3.2.2	Broadband Preprocessing . . . . .	62
3.3	Individual Sferic Processing . . . . .	67
3.3.1	Sferic Isolation and Deselection . . . . .	68
3.3.2	Representative Time-Domain Sferic . . . . .	71
3.3.3	Representative Frequency-Domain Sferic . . . . .	77
3.4	Sferic Processing Validation . . . . .	78
<b>Chapter 4: Ionospheric Electron Density Inferences from Sferics . . . . .</b>		<b>89</b>
4.1	Lightning Return Stroke Model . . . . .	89
4.2	Ionospheric Model . . . . .	92
4.2.1	Sensitivity to Electron Density . . . . .	94
4.2.2	The Split Model for Electron Density in the $D$ Region . . . . .	96
4.2.3	Evaluation of the Split Model . . . . .	98
4.3	Inverse Modeling Approach . . . . .	101
4.3.1	Matching Examples . . . . .	106
4.3.2	Discussion . . . . .	114
<b>Chapter 5: Tomographic <math>D</math> Region Imaging . . . . .</b>		<b>120</b>
5.1	Basic Principles . . . . .	120

5.2	<i>D</i> Region Tomography with Pixel Representation . . . . .	121
5.3	<i>D</i> Region Tomography Using a DCT Basis Representation . . . . .	129
5.4	<i>D</i> Region Image Results . . . . .	139
5.5	Discussion . . . . .	141
<b>Chapter 6: Conclusions and Suggestions for Future Work . . . . .</b>		<b>147</b>
6.1	Summary . . . . .	147
6.2	Suggestions for Future Work . . . . .	149
6.2.1	Refinement of the <i>D</i> Region Tomography Algorithms . . . . .	149
6.2.2	$B_r$ for <i>D</i> Region Studies . . . . .	149
6.2.3	Expanded Inverse Modeling for Nighttime and Local Perturbations .	150
6.2.4	A Modified Technique for Better Propagation Prediction . . . . .	150
6.2.5	An Iterative Technique for the Study of Lightning . . . . .	150
6.2.6	VLF Transmitters and Other Data Sources . . . . .	150
<b>Appendix A: Ionospheric Profiles . . . . .</b>		<b>153</b>
<b>Bibliography . . . . .</b>		<b>189</b>

## LIST OF TABLES

2.1	Important mode constant formulas . . . . .	50
2.2	Height gain functions and receiver excitation factors . . . . .	51
3.1	Receiver network details . . . . .	62
3.2	Transmitters subtracted from broadband data . . . . .	64
3.3	Information on lightning regions used in processing examples . . . . .	71
4.1	Current parameters for the lightning stroke model . . . . .	92
4.2	Parameter space used in split model comparison to FIRI . . . . .	99
4.3	Statistics of polynomial vs. split model fits . . . . .	99
4.4	Search space for split model parameters to use for ionospheric matching. . .	100
4.5	Survey of sferic-based Wait and Spies $N_e$ inferences . . . . .	101
4.6	Regions of study used for the ionospheric matching case studies. . . . .	110
4.7	Detailed information on sferic clusters used for matching examples . . . . .	111
4.8	Survey of relevant Wait and Spies $N_e$ inferences . . . . .	117
4.9	Electron density parameters for a solar flare example . . . . .	118
5.1	BPDN synthetic imaging analysis cases . . . . .	136
A.1	Split model parameters used in this work . . . . .	153

## LIST OF FIGURES

1.1	IRI example polar electron density curves . . . . .	4
1.2	IRI example polar ion density curves . . . . .	5
1.3	Diagram of the typical thundercloud charge structure . . . . .	21
1.4	Depiction of a projection measurement . . . . .	29
1.5	Backprojection imaging process . . . . .	30
1.6	Effect of undersampling on backprojection . . . . .	31
1.7	Filtered backprojection vs. backprojection . . . . .	32
1.8	Overall system block diagram . . . . .	33
2.1	Ray-hop method example diagram . . . . .	35
2.2	Comparison of narrow vs. bipolar pulse propagation . . . . .	35
2.3	Bipolar ray tracing results for different distances . . . . .	36
2.4	Diagram of self-consistent waves . . . . .	40
2.5	Illustration of TE modes . . . . .	41
2.6	Illustration of TM modes . . . . .	42
2.7	Diagram of the equivalent source model implicit in LWPC . . . . .	44
2.8	Portrayal of constant phase lines used by MODESRCH . . . . .	49
2.9	LWPC waveguide segmentation . . . . .	52
3.1	LF AWESOME block diagram . . . . .	58

3.2	LF AWESOME component pictures . . . . .	59
3.3	Example spectrogram and signal classes . . . . .	60
3.4	Comparison of quiet and noisy spectrograms . . . . .	61
3.5	Survey of broadband data availability for relevant receivers . . . . .	62
3.6	Receiver network map . . . . .	63
3.7	Comparison of MSK removal vs. notch filtering . . . . .	64
3.8	MSK removal performance . . . . .	66
3.9	Calibration curves . . . . .	67
3.10	Example of GLD360 data . . . . .	69
3.11	Map of measurement geometry for sferic processing examples . . . . .	71
3.12	Effect of time-alignment on processed time-domain sferics . . . . .	73
3.13	Block diagram of sferic processing steps . . . . .	73
3.14	Sferic rotation . . . . .	75
3.15	SNR calculation markup . . . . .	76
3.16	Removal of phase ramp to produce residual phase . . . . .	78
3.17	Initial vs. subsequent stroke processed sferic waveforms . . . . .	79
3.18	Positive vs. negative stroke processed sferic waveforms . . . . .	80
3.19	Error bars for processed sferics - near example . . . . .	82
3.20	Error bars for processed sferics - far example . . . . .	83
3.21	Example of individual sferics inside of a bin. . . . .	84
3.22	$B_\phi$ sferic ionosphere probe example . . . . .	87
3.23	$B_r$ sferic ionosphere probe example . . . . .	88
4.1	Sensitivity of simulated sferics to lightning base current parameters . . . . .	91
4.2	Positive and negative lightning models and associated current waveforms . . . . .	93

4.3	VLF sferic sensitivity to electron density for a daytime case . . . . .	95
4.4	VLF sferic sensitivity to electron density for a nighttime case . . . . .	96
4.5	Some example FIRI electron density curves . . . . .	97
4.6	FIRI diurnal electron density curves . . . . .	97
4.7	Markup of the split model for electron density . . . . .	98
4.8	Comparison of the split model to a polynomial model . . . . .	99
4.9	Comparison of simulated sferics produced with the Wait and Spies model vs. the split model for electron density . . . . .	102
4.10	Cartoon demonstrating the process used to simulate sferics with LWPC. . .	103
4.11	Map of measurement geometry for diurnal matching example . . . . .	104
4.12	Diurnal matching effects on the split model parameters . . . . .	105
4.13	Histograms of split model parameters for daytime matches . . . . .	107
4.14	Histograms of split model parameters for nighttime matches . . . . .	108
4.15	Map of measurement geometry for ionospheric probe matching examples . .	109
4.16	Diurnal matching example . . . . .	110
4.17	Solar eclipse matching example . . . . .	112
4.18	Solar flare matching example . . . . .	113
4.19	Solar flare effect on matched split model profiles . . . . .	115
4.20	Example of LEP effect on electron density curves . . . . .	116
4.21	Nighttime matching statistics . . . . .	119
5.1	Example great circle paths . . . . .	122
5.2	Pixel-based imaging approach markup . . . . .	122
5.3	Map of measurement geometry for expected error analysis . . . . .	124
5.4	Expected error analysis . . . . .	125



5.5	Noiseless pixel-based image performance . . . . .	126
5.6	Moderate noise pixel-based image performance . . . . .	127
5.7	Noiseless pixel-based image performance with Tikhonov regularization . . .	128
5.8	Moderate noise pixel-based image performance with Tikhonov regularization	129
5.9	Noiseless DCT-based image performance . . . . .	132
5.10	Moderate noise DCT-based image performance . . . . .	132
5.11	Noiseless DCT-based image performance with Tikhonov regularization . . .	133
5.12	Moderate noise DCT-based image performance with Tikhonov regularization	134
5.13	Cross-validation of the DCT-based approach with BPDN . . . . .	135
5.14	Map of measurement geometry for synthetic tuning . . . . .	136
5.15	Synthetic tuning analysis . . . . .	137
5.16	Performance of the DCT-based $D$ region imaging approach with BPDN for different error profiles . . . . .	138
5.17	Day/night electron density image examples . . . . .	140
5.18	Sunrise/sunset electron density image example . . . . .	142
5.19	Solar flare electron density image example . . . . .	143
5.20	Overall system block diagram . . . . .	144

## SUMMARY

The  $D$  region of the ionosphere (60–90 km altitude) is a plasma layer which is highly variable on timescales from fractions of a second to many hours and on spatial scales up to many hundreds of kilometers. VLF and LF (3–30 kHz, 30–300 kHz) radio waves are guided to global distances by reflections between the ground and the  $D$  region. Therefore, information about the current state of the ionosphere is encoded in received VLF/LF signals. VLF transmitters, for example, have a rich history in  $D$  region studies where received amplitude and phase are used to monitor and study the present state.

The return stroke of lightning is an impulsive VLF radiator, but, unlike VLF transmitters, lightning flashes are spread broadly in space allowing for much greater spatial coverage of the  $D$  region compared to VLF transmitters. Furthermore, sferics provide a broadband spectral advantage over the narrowband transmitters. The challenge is that individual lightning-generated waveforms, or ‘sferics’, vary due to uncertainty in the time/location information,  $D$  region ionospheric variability, and the uniqueness of each lightning flash.

In part, this thesis describes a technique to mitigate this variability to produce stable and high-SNR sferic measurements. Using a propagation model, sferics can be used to infer an ionospheric electron density profile that we interpret as an average along the path from lighting stroke to receiver. We develop a new model for the electron density vs. altitude, a natural extension of the Wait and Spies 2-parameter model. We call this new model the ‘split’ model after the fact that the  $D$  region seems to commonly split into two exponentially increasing electron density portions. The split model is described by four parameters:  $h'$ ,  $\beta$ ,  $s_\ell$ , and  $\Delta h$  indicating the height, slope, split location, and split magnitude respectively.

We introduce the  $D$  region tomography algorithm. The path-averaged electron density inferences are related to a 4D image specified by latitude, longitude, altitude, and time. For a given time window and altitude, we can produce a 2D image where the electron density is specified everywhere, even where there is not a transmitter-to-receiver path. Sparse and nonuniform spatial and temporal coverage of the ionosphere leads to artifacts and bias with the resulting images. We address these problems through sparse optimization techniques and a smoothness constraint using the discrete cosine transform (DCT).

# CHAPTER 1

## INTRODUCTION

Lightning flashes occur dozens of times per second across the Earth and emit a wide range of electromagnetic energy that spans from a few Hz to X-rays and even gamma rays. The return stroke of a lightning flash is a powerful event that generates a strong electromagnetic pulse known as a ‘radio atmospheric’ or ‘sferic’. Sferics are reflected by the Earth’s surface, a good conductor, as well as by the lower part of a plasma boundary known as the ionosphere ( $\sim 60\text{--}1000$  km), an electrically charged layer formed primarily by solar and background cosmic radiation. Together, the ground and lower ionosphere form what is known as the Earth-ionosphere waveguide (EIWG). It is possible to infer information about the lower ionosphere by combining remote sensing of very low frequency (3–30 kHz, VLF) waves with propagation modeling to solve for the modeled  $D$  region (60–90 km) ionospheric electron density vs. altitude profile. Sferics propagate with very low loss (a few dB per 1000 km attenuation) allowing for global reception with a sensitive radio receiver. This work is concerned with combining the broad spatial and temporal distribution of lightning with a network of receivers and the  $D$  region tomography method to study the spatial and temporal structure of the  $D$  region ionosphere.

### 1.1 Earth’s Ionosphere

Earth’s ionosphere is a plasma boundary from  $\sim 60\text{--}1000$  km, primarily created by solar and cosmic ionizing radiation. Plasma can be thought of as the fourth state of matter and occurs when a gas is ionized and the electrons are dissociated from the molecule, forming a mix of free electrons, ions, and any remaining neutrals. In 1839, Carl Friedrich Gauss posited the existence of a charged region in the atmosphere in order to explain variations in the magnetic field. 62 years later in 1901, Guglielmo Marconi received the first trans-Atlantic radio broadcast producing the first evidence of the ionosphere [*Marconi*, 1902], although he did not at the time realize that ionospheric reflection was the mechanism that allowed it.

Shortly after this work in 1902, Kennelly and Heaviside independently suggested that the existence of a conducting layer in the atmosphere would guide waves to global distances [Green, 1974], afterward dubbed the Kennelly-Heaviside layer, or the  $E$  region (90–150 km). Later, *Appleton and Barnett* [1925a] gave direct proof of its existence by radiating varying frequencies and noting the interference of the ground wave and a reflected sky wave. These experiments were soon verified by other workers as discussed later.

A steady period of progress followed for the young field of radio science. Using 750 kHz waves, *Appleton* [1927] observed clear reflections from the sky which became known as the Appleton-Barnett layer, or the  $F$  region (150–1000 km). In that work, he also suggested that varying wave frequency may allow for simultaneous measurements of both regions at any given time which he demonstrated [Appleton, 1931] along with an estimation of the peak electron density. Soon after, it was discovered that the  $F$  region occasionally split during the day into the  $F_1$  and  $F_2$  regions [Appleton, 1933; Schafer and Goodall, 1933]. Appleton’s name is ubiquitous with the development of radio and ionospheric theory (e.g. *Appleton and Ratcliffe* [1927a,b]; *Appleton* [1928, 1929]; *Appleton and Ratcliffe* [1930]; *Appleton and Builder* [1932]; *Appleton* [1932]), developing a nearly complete theory of radio propagation in the ionosphere. His work eventually led to a Nobel prize awarded in 1947.

Ionospheric reflections of short-wave radio, or HF ( $\sim 1.5$ –30 MHz), was extensively used for communication even in the infancy of ionospheric science [Marconi, 1922], and it is still employed by amateur radio operators (HAM), emergency services, and the military. Theory describing wave propagation in Earth’s ionosphere developed by Appleton and later *Hartree* [1929, 1931] spurred (for example) the development of over-the-horizon (OTH) radar. OTH radar reflects from the ionosphere, reflects off a target beyond line-of-sight sight, then makes a return traverse by another ionospheric reflection [Headrick and Skolnik, 1974]. With a sufficiently strong source, coherent source reflection, and a sensitive receiver, targets can be observed many hundreds even to thousands of km away.

OTH radar depends on the entire ionosphere. In the  $E$  and  $F$  regions refraction dominates as the density of the plasma increases with altitude, slowly bending an HF wave back towards the Earth. The path the ray will take limits the range and utility and depends on current ionospheric conditions. The lowest portion of the ionosphere, or the  $D$  region,

is a layer where the plasma density is still small, but neutral atmospheric particles are still dense enough to dominate. Hence, there is little to no refraction in the  $D$  region, but collisions between the electrons and the neutral gas species cause signal loss [*Headrick and Skolnik*, 1974]. Certain geophysical events can disturb the ionosphere, a solar flare for example, and these in turn cause blackouts to HF communication. This blackout is caused by enhancement of the  $D$  region electron density at lower altitudes which causes significantly higher absorption. At the time of OTH radar development, the  $D$  region was very poorly understood. In fact, Appleton himself, when announcing his discovery of the  $F$  region, noted that a lower more weakly ionized layer probably existed which caused extensive wave attenuation [*Appleton*, 1927]. Despite his suggestion of its impact on wave propagation in the ionosphere, a long running pattern has prevailed where the  $D$  region, due its difficulty in making measurements, is often ignored for convenience, hence its eventual nickname of the ‘ignorosphere’.

The regions of the ionosphere, although named for the historical reasons previously discussed, persist because of the different dynamics, effects, and scales that are important for their study and effect on radio wave propagation. Figure 1.1 shows the electron density of the regions of the ionosphere along for seasonal and diurnal variation in the polar regions as given by the 2016 International Reference Ionosphere (IRI) model described by *Bilitza et al.* [2017]. The IRI is an international collaborative research project to model the ionosphere from a large database of many different types of measurements. Some of these measurements will be discussed in the subsequent sections.

### 1.1.1 Formation and Structure of the Ionosphere

The primary driver of the daytime ionosphere is solar radiation. The ionosphere also connects to the plasmasphere, a shell of high-density plasma extending around the Earth. Plasma flows in and out of the ionosphere from the plasmasphere. Hence, even at nighttime, in the absence of direct solar radiation and secondary ionization processes, the  $F$  region ionosphere is maintained by a flow of plasma inward. In the  $D$  region however, because of collisions, the plasma degenerates chemically within 10s of seconds, so the lingering nighttime  $D$  region ionosphere is maintained by background cosmic radiation. Because the

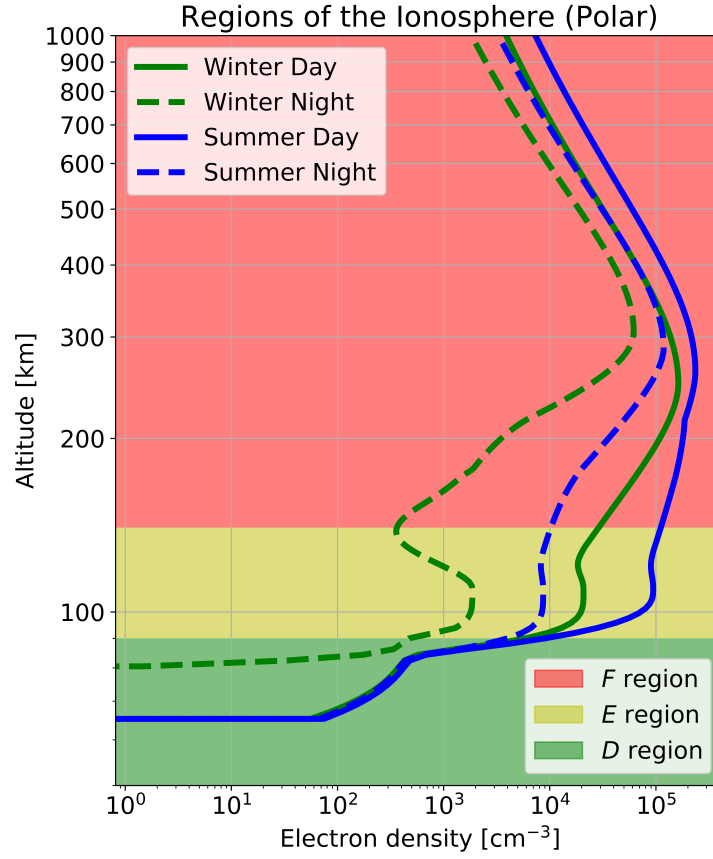


Figure 1.1: Example plot of the electron density,  $N_e$ , for the regions of the ionosphere with varied diurnal and seasonal effects. Modeled results from *Bilitza et al.* [2017]

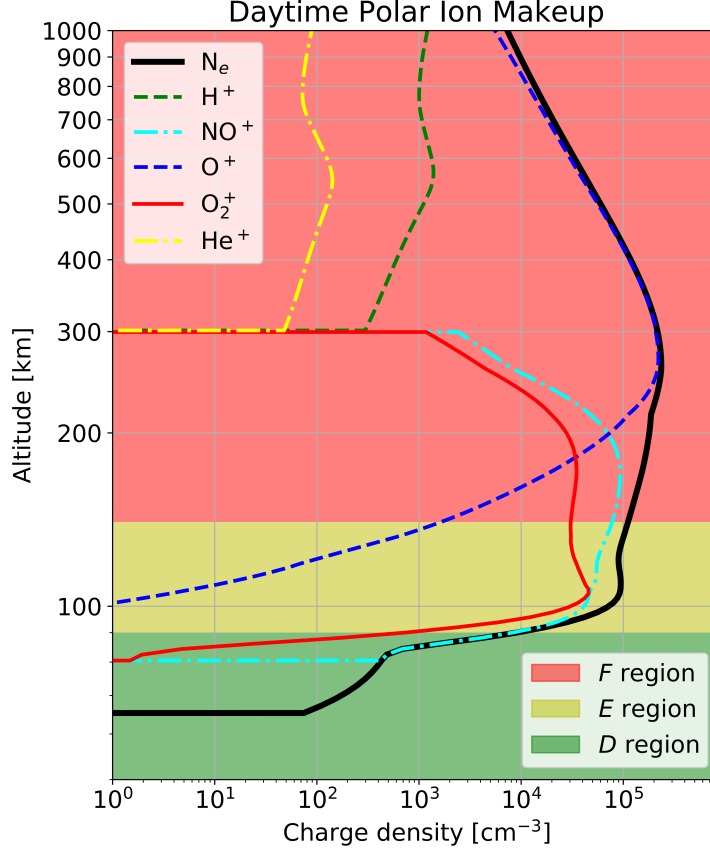


Figure 1.2: Dominant ion species for the ionosphere at high latitudes. Modeled results from *Bilitza et al.* [2017].

ionosphere spans a broad region of the near-Earth space environment, the relevant atmospheric chemistry, particle dynamics, currents, and transient modifiers are all functions of altitude, latitude/longitude, neutral dynamics, ionizing radiation, etc. [*Friedman*, 1974; *Hulburt*, 1974; *Massey*, 1974; *Ratcliffe*, 1974; *Rishbeth*, 1974]. To address the myriad of phenomena in our upper atmosphere, in parallel to radio science, the research field of aeronomy has developed with more interest in the physical phenomena over the application of radio wave systems and technology, although the two fields share many of the same interests and techniques [*Kockarts*, 2002].

The diurnal variation in long distance propagation due to ionospheric effects was an early discovery by *Marconi* [1902] shortly after his first trans-Atlantic transmissions. He discovered that he could receive daytime transmissions up to 700 miles ( $\sim 1026$  km), but could receive nighttime transmissions up to 2099 miles ( $\sim 3078$  km). He was unable to

explain this at the time, but it stood in contrast to his presumption that the long-range reception was due to refraction around the Earth’s curvature. Instead, the explanation of his long-distance transmission and detection as an ionospheric effect was left for others to discover. In an important early paper, *Eccles* [1912] considered wave action on a charged layer that varied with solar activity and guided propagation between the Earth and this charged layer. This effect was easily confirmed by the direct ionospheric measurement techniques of *Appleton and Barnett* [1925a], *Breit and Tuve* [1926], and *Hollingworth* [1926].

The various regions of the ionosphere are ionized by different portions of the solar and background radiation spectra. The dominant ion species for each region can be seen in Figure 1.2. In the upper portion of the *D* region of the ionosphere  $\text{NO}^+$  dominates [*Reid*, 1977], which is easily ionized by solar and cosmic Lyman- $\alpha$  radiation (where Lyman- $\alpha$  is the first hydrogen emission line at 121.6 nm, Lyman- $\beta$  is the second at 102.6 nm, etc.). In the lower portion of the *D* region, the ion structure changes quite drastically. Water cluster ions of the form  $\text{H}^+(\text{H}_2\text{O})_n$  start to become dominant [*Reid*, 1977]. In addition, due to electron attachment, the formation of a significant population of negative ions forms in the lowest portion of the *D* region [*Thomas et al.*, 1973].

The *E* region is made up of two important ion species:  $\text{NO}^+$  and  $\text{O}_2$ . They are primarily ionized in the daytime by extreme ultraviolet (EUV,  $\sim 2.81\text{--}3.48$  GHz) solar radiation and X-rays during a solar flare [*Robinson and Vondrak*, 1984; *Thome and Wagner*, 1971]. The *E* region is maintained during the nighttime by geocoronal backscattering of Lyman- $\beta$  and starlight EUV (911-1026 Å) [*Strobel et al.*, 1980]. The lower *F* region ions are also dominated by  $\text{NO}^+$  and  $\text{O}_2$  which gradually gives way to  $\text{O}^+$  which dominates for the rest of the *F* region. The nighttime *F* region is dominated by inward flow from the plasmasphere but is also maintained by Lyman- $\beta$  backscattering and starlight EUV, with secondary ionization in the lower *F* region caused by recombination of  $\text{O}^+$ . The most important ions in the topside ionosphere ( $>1000$  km) are  $\text{He}^+$  and  $\text{H}^+$ .

The *E* region is also home to occasionally forming thin layers of enhanced electron density of more than an order in magnitude [*Miller and Smith*, 1978] often collectively termed ‘sporadic *E*’ or  $E_s$ .  $E_s$  form as 1–3 km thick and hundreds of km in width layers which move with neutral winds and last minutes to hours [*Whitehead*, 1961, 1970, 1989;



*Smith and Mechtly*, 1972].  $E_s$  is better understood as two distinct phenomena tidal ion layers (TIL) and true  $E_s$  [Mathews, 1998] which are differentiated by different drivers and that TIL are somewhat predictable and therefore not ‘sporadic’. TIL are explained sufficiently by neutral wind shear that occurs in the  $E$  region, are connected to tides, and can be diurnal.  $E_s$  is more complicated as it requires a wind shear, but also electric fields and the presence of metal ions deposited by meteors is more accurately characterized by the term sporadic.

### 1.1.2 Ionospheric Measurements and Perturbations

Throughout the history of radio and ionospheric science, many tools and techniques have enabled the discovery of new phenomena. The earliest technique was established by *Appleton and Barnett* [1925a,b] known as the frequency change method. For a fixed receiver, the transmitter frequency is varied with time, and the corresponding changing wavelength creates an interference pattern between the ionospherically reflected wave and the ground wave. The number of interference variations, or ‘fringes’, is directly related to the reflection height of the transmitted wave. Shortly afterward, *Breit and Tuve* [1926] sent short radio pulses at vertical incidence and measured transit time to infer reflecting height. This technique is now known as the ‘ionosonde’ and it is still used extensively today. Another important early technique is known as the *Hollingworth* [1926] method which measures the interference of ground and sky waves for a set frequency. By varying distance (such as a receiver mounted on a plane flying away from a transmitter) and by noting the spatial frequency of the interference pattern, it is possible to infer an averaged reflection height.

One of the first applications of these radio technologies was direction-finding for storm tracking and navigation. These technologies assumed a linearly polarized wave and used multiple antennas, such as orthogonal loop antennas to receive the signal from an arbitrary angle. With a linearly polarized wave, it is possible to orient the antennas in such a way that all received signal is received on one channel and thereby estimate the arrival angle. For storm tracking, it is possible to use several receivers to locate a storm cell using a triangulation technique. For navigation, it is possible to use known transmitters to locate yourself. However, both applications depended on accurate angle of arrival estimation and

errors up to  $30^\circ$  in arrival angle were common and unexplained. Early experiments made observations that ionospheric reflections changed the polarization of the launched wave which explaining the cause of the angle of arrival errors [Eckersley, 1921; Green, 1974]. Ionospheric reflection can be modeled by a polarized incident wave multiplied by a reflection matrix which represents the of loss and polarization coupling. In other words, a linearly polarized wave becomes elliptically polarized wave after one or more ionospheric reflections. This formulation of the problem proved to be extremely important in modeling long distance propagation of waves with many reflections [Wait, 1970; Budden, 1961]. By combining an accurate model of ionospheric reflection, many researchers have inferred ionospheric structure by solving an inverse problem by varying the ionospheric conditions until the data is explained (e.g. Thomson [1993]; Cummer *et al.* [1998]). Other important ground-based measurements are used extensively such as partial reflection [Gardner and Pawsey, 1953], HF radar and absorption [Alfonsi *et al.*, 2008], VHF (30–300 MHz) radar [Farley *et al.*, 1970], and riometers [Hargreaves, 1969].

Soon after the cessation of the World War II, ionospheric scientists began to use surplus rockets from the war equipped with instruments to measure neutral and charged particles in ionosphere. An early achievement used mass spectrometers to determine the primary ion species for the various regions of the ionosphere [Narcisi and Bailey, 1965]. Some of the most important ionospheric instruments/techniques on board the sounding rockets are Langmuir probes [Cohen, 1963], Faraday rotation [Seddon, 1958], and differential absorption [Seddon, 1958]. Rocket measurements have been particularly helpful in characterizing the lower ionosphere, where the electron densities are too low for many other ionospheric techniques [Sechrist, 1974; Friedrich and Torkar, 2001].

Later, Gordon [1958] suggested a new type of measurement technique that would measure the incoherent volumetric backscatter of individual electrons known as incoherent scatter radar (ISR). The ISR is a very powerful tool that is capable of measuring electron and ion temperatures, velocities, and number density as a function of altitude. After the success of the ISR at the Arecibo Observatory, several other ISRs were constructed: Millstone Hill, EISCAT, ESR, Sondrestrom, Jicamarca, and AMISR (Poker Flat and Resolute Bay) [Gordon and LaLonde, 1961; Farley *et al.*, 1967; Wannberg *et al.*, 1997; Evans, 1965]. With

the advent and proliferation of satellites came a new generation of space-based and in-situ measurements as satellites can orbit in the  $F$  region of the ionosphere [Thomas, 1963]. Measurements of the topside ionosphere were also possible on global scales using on-board ionosondes [Thomas *et al.*, 1963]. Satellites have also been important in studying the magnetosphere [McDiarmid and Burrows, 1965], a region of plasma aligned with Earth’s magnetic field lines which couples with the ionosphere via particle precipitation and ion outflow [Yau *et al.*, 1985]. Using dual frequency transmissions from GPS satellites and the measured Faraday rotation, it is possible to derive a line-integral of electron density between the GPS satellite and receiver [Mannucci *et al.*, 1998]. Faraday rotation causes a delay of signals propagating through the ionosphere proportional to the total electron density along the path and the use of two signals allows for an unambiguous inference. It is known as the total electron content (TEC) and has been extensively used in ionospheric studies [Jakowski *et al.*, 1999; Reinisch and Huang, 2001; Tsugawa *et al.*, 2011].

The daytime ionosphere is relatively predictable due to the consistency and reliability of solar radiation [Thomson *et al.*, 2011]. However, many transient perturbations can cause disturbances from quiet daytime ionosphere. Solar flares cause an excess of ionization due to the burst in solar radiation lasting minutes to hours, affecting the entire dayside ionosphere [Mitra, 1964]. Solar eclipses can be thought of as causing a traveling shadow blocking some to all solar radiation. The totality occurs where sun’s radiation is totally blocked, but partial blockage occurs for a large geographical area reducing electron/ion populations [Cohen *et al.*, 2018a]. Geomagnetic storms, a temporary disturbance of Earth’s magnetosphere from impinging solar wind, cause an increase in particle precipitation onto and currents into the ionosphere [Belrose and Thomas, 1968]. This can last for days in the whole ionosphere, particularly at high latitudes. Ionospheric storms occur when large scale perturbations to the ionospheric electron density and currents are triggered by large energetic solar events such as solar flares or coronal mass ejections [Zhang *et al.*, 2001].

The nighttime ionosphere is relatively weakly ionized therefore it can be noticeably perturbed by smaller ionization changes. Lightning can couple with the lower ionosphere by multiple mechanisms, causing different classes of perturbations [Inan *et al.*, 2010], discussed in greater detail in later. Meteoric ablation in Earth’s atmosphere release easily ionized

metals, producing a short-lived, but highly dense plasma trail that can be used to enhance short-wave transmissions [Yavuz, 1990].

The polar regions of the ionosphere are dominated by precipitating particles that follow Earth’s magnetic field lines, causing excess ionization and the auroral electrojet [Arnoldy, 1974]. Substorms are a brief disturbance in Earth’s magnetosphere causing many highly energetic particles to be precipitated in the  $D$  region of the ionosphere lasting a few hours [McPherron, 1970]. Auroras are caused by significant particle precipitation, causes propagating plasma structures which can perturb the ionosphere. This effect is commonly observed by scattering of GPS navigation signals and is known as GPS scintillation [Smith *et al.*, 2008].

The neutral atmosphere is also a dynamic environment which in turn perturbs and modifies the ionosphere. Significant neutral winds persist in the  $D$  and  $E$  regions through diurnal tides propagating upwards and in the  $F$  region from solar heating [Titheridge, 1995]. Propagating neutral waves exist at ionospheric altitudes as diurnal tides, planetary waves, and acoustic gravity waves (AGW) [Yeh and Liu, 1974]. Diurnal tides are generated at ionospheric altitudes due to solar heating and are therefore somewhat predictable [Martyn, 1948]. Planetary waves, which occur over periods of 2-30 days, are often generated in the troposphere, which propagate upward to ionospheric altitudes [Liu *et al.*, 2010; Lastovicka, 2006]. AGWs are oscillations with periods from minutes to hours which can be thought of as transient since their excitation is driven by events such as: vertical forcing [Lastovicka, 2006], earthquakes, or a nuclear detonation [Row, 1967]. Many plasma irregularities and ‘bubbles’ have been widely observed from scales of meters to hundreds of km [McClure *et al.*, 1977]. In addition, turbulence in the ionosphere can cause local ionospheric disturbances [Farley *et al.*, 1981].

### 1.1.3 Currents in the Ionosphere

Because of Earth’s background magnetic field ( $\mathbf{B}_0$ ), the ionosphere is anisotropic, indicating that electric field wave action on the electron and ion population in the ionosphere is dependent on its orientation to  $\mathbf{B}_0$ . With an externally applied electric and magnetic field

$\mathbf{E}$  and  $\mathbf{B}_0$  each electron and ion will experience the Lorentz force

$$\mathbf{F} = q\mathbf{E} + q\mathbf{v} \times \mathbf{B}_0 \quad (1.1)$$

which states that the force on an individual particle will experience a force along  $\mathbf{E}$  as in an isotropic media, and along  $\mathbf{E} \times \mathbf{B}_0$ . If we assume  $\mathbf{B}_0$  is along the  $z$ -axis, without loss of generality the effects of anisotropy can be expressed as Ohm's law with a conductivity tensor for  $\bar{\sigma}$

$$\begin{bmatrix} J_x \\ J_y \\ J_z \end{bmatrix} = \begin{bmatrix} \sigma_P & -\sigma_H & 0 \\ \sigma_H & \sigma_P & 0 \\ 0 & 0 & \sigma_{\parallel} \end{bmatrix} \begin{bmatrix} E_x \\ E_y \\ E_z \end{bmatrix} \quad (1.2)$$

where  $\sigma_P$  and  $\sigma_H$  are known as the Pedersen and Hall conductivities causing currents parallel and perpendicular to the applied electric field respectively.  $\sigma_{\parallel}$  is the parallel conductivity which exists for the electric field along the magnetic field line. As the plasma parameters vary with altitude in the ionosphere, so do the various conductivities.  $\sigma_{\parallel}$  is stronger than the Hall and Pedersen contributions at all altitudes. At  $\sim 70$  km  $\sigma_H/\sigma_P$  is unity and it increases above and decreases below (See *Cohen* [2009, Section 2.2.2] for a more in-depth discussion).

The conductivity tensor gives rise to natural currents in the ionosphere in the polar regions as the auroral electrojet and at the equator as the equatorial electrojet. The equatorial electrojet is a current system at the geomagnetic equator marked by a strong enhancement of the magnitude of  $\mathbf{B}_0$  and therefore it is primarily driven by a Hall current [*Mayaud*, 1977]. The Auroral electrojet is caused by ionosphere-magnetosphere coupling which drives current systems in the polar ionosphere [*Kamide and Vickrey*, 1983]. Birkeland currents [*Arnoldy*, 1974], or magnetic field aligned currents, are driven by solar wind which then flow through the ionosphere as Pedersen currents. This in turn drives the electrojet in the form of circulating Hall currents.

#### 1.1.4 Review of Past *D* region Work

The *D* region of the ionosphere is a cold plasma with dynamics that are heavily controlled by collisions. The *D* region reflects extremely low frequency, very low frequency, and low frequency (ELF/VLF/LF 0.3–3/3–30/30–300 kHz) waves with low loss and some dispersion. It also causes significant losses to HF waves which slowly refracts through the upper ionosphere after passing through the *D* region. L-band and higher frequencies are only marginally impacted by the *D* region. The *D* region, like the rest of the ionosphere, is primarily driven by solar and cosmic radiation.

In the earliest days of long-range radio propagation studies, the most popular explanations for beyond line-of-sight propagation were diffraction of a wave on the Earth’s surface and guided propagation by a conducting layer in the atmosphere (an ionosphere). *Watson* [1918, 1919], in two groundbreaking papers, proved that wave diffraction by the Earth could not account for long range propagation of waves ( $> 2000$  km) and that an ionosphere could. He explained long distance propagation by assuming a homogeneous isotropic ‘ionosphere’ and developed a theory of self-reinforcing waves, or modes. This is now known as waveguide mode theory and is most applicable to ELF/VLF and the lower end of LF waves [*Ferguson*, 1995] for which reflection occurs entirely in the *D* region (with an exception of ELF waves propagating in QTEM mode).

##### *Direct Observations*

Due to the difficulty of generating efficient high power VLF waves and the common use of short-wave radio in communications in the early days of radio science, study of the *D* region developed slowly. Despite the lack of scientific attention, the *D* region critically impacted the operation of early communication systems. For instance, many of the first commercial transmitters were operating at frequencies that reflected from the *D* region, such as Marconi’s first trans-Atlantic communication ( $\sim 150$  kHz, [*Green*, 1974]). *Best et al.* [1936] used a VLF transmitter and nearly vertical transmission to observe the Hollingworth interference pattern from which they deduced diurnal effective reflection heights in the *D* region. Some considered ionosonde like observations of vertical pulsed VLF/LF waves

[*Brown and Watts*, 1950; *Helliwell et al.*, 1951]. *Bracewell et al.* [1951] summarized extensive work considering effective reflection height and the reflection coefficients from a single  $D$  region reflection. In an important study, *Deeks* [1966] unified many concepts of  $D$  region physics with a full wave model to infer  $D$  region electron density profiles with altitude. The general inversion technique used by Deeks became the gold standard of VLF/LF remote sensing of the  $D$  region, with many subsequent studies using similar techniques [*Shellman*, 1970; *Backus and Gilbert*, 1970; *Jones and Wand*, 1970].

Pioneering work and theoretical development by *Seddon* [1953] resulted in the first in-situ electron density and collision frequency profiles measured in the  $D$  region using two harmonically related CW frequencies. Further development by Seddon involved use of Faraday rotation and differential absorption techniques [*Seddon*, 1958]. Many early studies used transmitters on board rockets, but this eventually gave way to ground-based transmitters which provided more stable results and easier calibration [*Knoebel and Skaperdas*, 1966; *Mechtly et al.*, 1967; *Bennett et al.*, 1972; *Mechtly*, 1974; *Beynon and Williams*, 1976]. Many rocket flights are also equipped with a Langmuir probe (e.g. [*Bennett et al.*, 1972; *Beynon and Williams*, 1976] to complement RF techniques. Langmuir probes perform well, even with relatively low electron density, such as the lowest portion of the  $D$  region where wave techniques have greater uncertainty [*Sechrist*, 1974]. Other rocket-based techniques have been developed to measure electron density such as an LF absorption or VLF Doppler technique [*Hall and Fooks*, 1965, 1967; *Egeland et al.*, 1970]. Rocket measurements have also been useful in validating and advancing  $D$  region ionization and chemistry models [*Narcisi and Bailey*, 1965; *Zbinden et al.*, 1975].

More recently, rocket-based measurements have been combined with a simple ion chemistry model to create a semi-empirical model of the lower ionosphere called FIRI. The ‘F’ signifies the importance of Faraday rotation in the rocket measurements, and the IRI refers to the International Reference Ionosphere model which it augments [*Friedrich and Torkar*, 2001; *Friedrich et al.*, 2017]. However, rocket measurements are episodic, only measuring a single trace through the ionosphere at a single point in time and they cannot realistically be applied on a continuous and global basis.

## *Ionospheric Heating and Irregularities*

It has also been found that radio waves can alter the ionospheric conditions. *Tellegen* [1933] reported the reception of multiple radio stations on of different frequencies at a single location. This behavior was explained as the cross-modulation of another radio station (located under the propagation path) in the *D* region of the ionosphere [*Bailey and Martyn*, 1934]. Using this effect several workers devised an experiment using a pulse reflected from a higher altitude and a disturbing second pulse causing a systematic interaction [*Fejer*, 1955, 1970; *Thrane et al.*, 1968; *Ferraro and Lee*, 1968; *Ferraro et al.*, 1974; *Sulzer et al.*, 1982]. With some assumptions and an inversion method, it is possible to infer electron density profiles (e.g. *Coyne* [1973]).

Because of the difficulty of generating very long wavelength waves ( $< 10$  kHz), some workers have used HF wave absorption ‘heating’ of the *D* and *E* regions. The increase in electron temperature increases the collision frequency and thus the plasma conductivity so that modulation in the presence of any natural currents can act as a wireless antenna [*Getmantsev et al.*, 1974; *Ferraro et al.*, 1982; *Barr et al.*, 1986; *Moore et al.*, 2007; *Cohen et al.*, 2010; *Cohen and Golkowski*, 2013].

Although HF waves do not reflect from a smoothly varying *D* region, in reality many irregularities exist in the form of electron density enhancements [*Belrose et al.*, 1972] causing strong electron density gradients which cause a partial reflection by scattering of MF/HF frequencies. This ‘partial reflection’ technique was widely used in early studies of the *D* region [*Gardner and Pawsey*, 1953; *Belrose and Burke*, 1964; *Belrose*, 1970; *Flood*, 1968; *Hocking*, 1979; *Hocking and Vincent*, 1982]. The accuracy of the technique is limited to several factors such as pulse width, height of reflection, and current population of scatterers. In addition, some assumptions need to be made about the scattering mechanism, often that it is by the Fresnel scattering method. Despite these issues its use was widespread in early in *D* region studies and its use persists [*Singer et al.*, 2011].

While ISRs are optimized for *E* and *F* region measurements where the backscatter produces much higher SNR due to the much higher electron density, *D* region studies can be performed with careful attention and techniques optimized for the relatively low SNR.



Many workers used different ISRs to investigate the  $D$  region with good results in the upper  $D$  region ( $N_e \gtrsim 100 \text{ cm}^{-3}$ ) [Armistead *et al.*, 1972; Mathews, 1984; Turunen, 1996; Chau and Woodman, 2005; Friedrich *et al.*, 2006]. The most recent work at Arecibo [Raizada *et al.*, 2008] has shown promising results with electron densities as low as  $10 \text{ cm}^{-3}$ , which may allow for more promising studies in relation to VLF/LF frequencies as discussed later.

Terrestrial VLF [Thomson, 1993; Cummer *et al.*, 1998] and LF [Higginson-Rollins and Cohen, 2017] waves propagate to great distances ( $>2 \text{ Mm}$ ) guided by the Earth ground and the  $D$  region of the ionosphere, forming a waveguide commonly known as EIWG. Therefore, propagating VLF/LF signals carry with them information about the current state of the  $D$  region. Because of this global propagation and since waves can penetrate significantly into water via the skin effect, various navies have constructed and operated VLF transmitters for the purposes of submarine communications [Watt, 1967]. These transmitters operate almost continuously at constant power and frequency allowing an observer to employ them to monitor the current conditions of the ionosphere. Many used these VLF transmitters to infer the ionospheric conditions for VLF propagation [Thomson, 1993; McRae and Thomson, 2000; Thomson *et al.*, 2007; Thomson and McRae, 2009; Thomson, 2010]. In many VLF remote sensing studies, the  $D$  region is assumed to follow a 2-parameter electron density profile described by a height  $h'$  and a steepness  $\beta$ , as introduced by Wait and Spies [1964]. A propagation model such as the Long Wave Propagation Capability (LWPC) code [Ferguson, 1998] is then used to estimate ionospheric waveguide parameters that most closely match observations. Many have used VLF transmitters and LWPC to infer a simplified ionospheric parametrization of the electron density profile during solar flares [Thomson and Clilverd, 2001; McRae and Thomson, 2004; Thomson *et al.*, 2005; Grubor *et al.*, 2008; Dahlgren *et al.*, 2011; Singh *et al.*, 2013; Kolarski and Grubor, 2014; Šulić and Srećković, 2014]. Current VLF remote sensing techniques nearly always use this approach. A significant advantage of this type of study is the low cost of deploying a VLF receiver, which has enabled studies by many groups without the cost of other  $D$  region measurements [Scherrer *et al.*, 2008].

LWPC is a frequency-domain code that uses a mode solver of the EIWG to predict the amplitude and phase at up to  $20 \text{ Mm}$  from a simulated source. It divides the path into discrete slabs with constant parameters in each slab: an assumed ionosphere, magnetic

field parameters, and permittivity/conductivity of the ground (taken from a built-in lookup table). It has been well validated by the Space and Naval Warfare Systems Command (SPAWAR) [Ferguson, 1993, 1995], as well as the other studies mentioned here.

The techniques developed or tailored for  $D$  region studies have uncovered a myriad of complicated dynamics and perturbations varying on many spatial and temporal scales. A well-known ionosphere-wide phenomenon is the diurnal variation of the ionosphere due to varying solar flux and recombination during the nighttime [Reid, 1970]. The effect is particularly pronounced in the  $D$  region where recombination times are very short causing a significant reduction in electron density and leading many workers to say the  $D$  region disappears during the nighttime. However, the  $D$  region is still easily detectable at night when observed with VLF/LF reflection [Bracewell *et al.*, 1951]. Because the nighttime ionosphere is weakly ionized from extrasolar cosmic rays X-rays ( $<1\text{nm}$ ) and Lyman- $\alpha$  (121.6 nm) radiation [Thomas and Bowman, 1985], it should be no surprise that there are significant variations in the nighttime  $D$  region characteristics spatially and from night to night [Cheng *et al.*, 2006; Han and Cummer, 2010a].

The daytime ambient ionosphere ionization is dominated by Lyman- $\alpha$  radiation [Kockarts, 2002]. However, during an X-ray solar flare, the  $D$  region ionization is dominated by the photoionization of atmospheric gases [Grubor *et al.*, 2008]. It is more predictable and stable than the nighttime ionosphere with some important variations. The daytime ionosphere varies throughout the day as a function of the current solar zenith angle [Thomson, 1993; Han and Cummer, 2010b]. The daytime ionosphere also varies with the season and the 11-year solar cycle as demonstrated by the detectability of X-ray perturbations of the  $D$  region [Thomson and Clilverd, 2001]. Han and Cummer [2010b] noticed spatial variances in the daytime ionosphere which had significant variation during 15% of the days of observation. Furthermore, other studies have observed that the daytime ionosphere averaged over a period of days, approaches a repeatable daytime VLF pattern for a set transmitter-to-receiver path, while individual days can diverge from this curve [Clilverd *et al.*, 2001].

Despite the so-called ‘steady-state’ ionosphere and variations, there are many perturbations. Many of these perturbations have been commonly observed as amplitude and/or phase perturbations of ionospherically reflected VLF transmitters and subsequently have

been named based on the effect on those signals [*Inan et al.*, 2010]. The coupling between Earth’s magnetic field above the ionosphere and solar wind from the sun (quickly moving clouds of plasma from the sun) create a plasma region with many highly energetic particles known collectively as the ‘magnetosphere’. The magnetosphere also commonly couples to the ionosphere and is most often observed in the auroral regions through induced currents and enhanced electron density in the ionosphere as discussed in Section 1.1.2. Whistler mode waves are plasma waves which can propagate in a plasma below the plasma frequency as a right-hand circularly polarized wave. These signals had been commonly observed on long telegraph lines which were acting as an ELF/VLF antenna as a whistling like tone [*Barkhausen*, 1930]. *Storey* [1953] first suggested the mechanism of whistlers as terrestrial lightning generated waves which propagate through the ionosphere along the magnetic fields with frequency dispersion which increases with multiple traverses of the magnetic field. *Helliwell et al.* [1973] observed amplitude perturbations coincident with whistler waves and predicted a secondary ionization mechanism of precipitation electrons in the lower ionosphere due to cyclotron resonance interactions from whistler waves. *Voss et al.* [1984] first confirmed this with direct measurements of the so-called ‘loss-cone’ scattering due to incident whistlers in the magnetosphere and ground-based observations of whistlers and dubbed the term ‘lightning-induced electron precipitation’ (LEP) to describe the entire event. Subsequent studies investigated the interaction of whistlers and electrons, as well as the nature of the LEP perturbation discovering it typically lasts tens of seconds to minutes and hundreds to >1000 km in extent and is commonly observed at night [*Clilverd et al.*, 2002; *Dowden and Adams*, 1989, 1990; *Inan et al.*, 1988a,b,c].

Particularly strong lightning flashes are sometimes associated with perturbations of ionospherically reflected VLF waves known as ‘early/fast’ events [*Inan et al.*, 1988b], with rapid onset and direct coupling compared to the longer and indirect effects from LEP (First reported by *Armstrong* [1983]). The subsequent discovery of high altitude discharges along with the suggestion that sprites were related to early/fast events kicked off a scientific debate as to the nature of the subionospheric VLF perturbations [*Franz et al.*, 1990; *Inan et al.*, 1995; *Barr et al.*, 2000], although all involved agree that lightning is the source of the signal perturbations. For sprite-causative discharges it was suggested that the sprite columns as

ionized channels caused coherent scattering of the signals [Dowden *et al.*, 1994, 1996]. On the other side, it is possible that quasi-electrostatic (QE) [Inan, 1990; Pasko *et al.*, 1997, 1998] heating of the lower ionosphere due to charge imbalance or electromagnetic pulses (EMP) [Inan *et al.*, 1991; Adachi *et al.*, 2004; Marshall and Inan, 2010] could cause greater ionization. QE can be explained either by sustained lightning activity [Inan *et al.*, 1996] or strokes that lower much more charge by the continuing current mechanism [Cummer and Inan, 1997]. The debate has not been resolved and it may be possible that more than one of these mechanisms are involved in the VLF perturbations. More recently, quick onset but long recovery events (LORE) have been reported, which differ by the recovery of subionospheric signals taking up to 20 minutes instead of  $\lesssim 200$  seconds [Cotts and Inan, 2007]. Both early/fast and LORE events are smaller in spatial extent than LEPs. EMP from lightning has also been discovered to cause doughnut shape perturbations in the  $D$  region electron density that has been observed by subionospheric VLF signals [Dowden *et al.*, 1994; Mika *et al.*, 2006].

The most common perturbation to the daytime  $D$  region is X-ray solar flares. During an X-ray flare, ionization becomes dominated by the incident photons producing an excess of electron density. The suggestion of X-rays during a solar flare was considered much earlier (e.g. Müller [1935]), but it was not possible to verify this with direct measurements until the advent of ionospheric sounding rockets [Chubb *et al.*, 1957] and has been well verified since then [Nicolet and Aikin, 1960]. The geostationary operational environmental satellite (GOES) 13, 14, and 15 are equipped with dual band X-ray detectors (0.5–4, 1–8 Å) which are useful since the electron density responds differently to varying X-ray spectra [Han and Cummer, 2010b]. The effect on subionospheric VLF propagation of X-ray solar flares is now well understood [Nina and Čadež, 2014; Šulić *et al.*, 2016]. The occurrence and extent of solar eclipses is well known, but the effect on  $D$  region densities and wave propagation are not yet fully understood [Bracewell, 1952; Clilverd *et al.*, 2001; Maurya *et al.*, 2014; Cohen *et al.*, 2018a].

In addition to seasonal variation of the  $D$  region due to changing solar conditions, there is a persistent but anomalous effect known as the ‘winter anomaly’ causing an enhancement of  $D$  region electron density for days or weeks [Sechrist *et al.*, 1969]. Due to the impor-

tance of OTH radar for military applications, many sounding rockets have taken in-situ measurements [Sechrist *et al.*, 1969]. The  $D$  region also varies on a latitudinal basis. For example, the polar regions are dominated by particle precipitation and in strong events there is significant perturbation to the  $D$  region causing abnormal HF absorption known as Polar Cap Absorption (PCA) [Megill *et al.*, 1971].

Natural disasters may also couple into the  $D$  region by different mechanisms causing detectable perturbations in the dynamics and electron-ion populations. Gravity waves can be launched by mesoscale convective systems (MCS) and individual thunderstorm cells [Lay and Shao, 2011a,b; Yue *et al.*, 2009, 2013]. Earthquake precursor events may generate VLF emissions due to geophysical processes under certain conditions [Parrot and Mogilevsky, 1989]. Many workers have attempted to understand the nature of these potential precursor events in order to form early warning systems [Larkina *et al.*, 1989; Eftaxias *et al.*, 2001; Hayakawa *et al.*, 2010].

## 1.2 Lightning

Broadband emissions from lightning are ubiquitous in VLF remote sensing studies. To some workers, this is a noise source to be subtracted but others have used the emitted energy as a remote sensing tool itself. As that is the focus of this thesis, we now introduce the dynamics of how thunderclouds form, electrify, and generate VLF energy. Before the introduction of radio technology for communications, lightning was first studied for meteorological purposes with the world’s first radio receiver by Popoff of Cronstadt in 1895 [Cave and Watson Watt, 1922]. These observations were confirmed and advanced by several workers (for an extensive discussion of early radio telegraphic work for meteorological applications see [Cave and Watson Watt, 1922]). Early detection and many modern applications of lightning depend on the impulsive return stroke, only one component of a lightning flash.

### 1.2.1 The Lightning Flash

A lightning flash is a very complicated event with unique plasma dynamics such as the ‘lightning leader’ or nuclear particle interactions. Lightning tends to cluster around Earth’s

equator and on land because of the meteorological processes required to form a cumulonimbus or thunderstorm cloud. A thorough description of lightning processes and active research is given in [Dwyer and Uman, 2014] for the interested reader. When sufficiently strong convection (thermally driven updrafts) is present, water vapor is driven to higher altitudes. Water is then able to condense on existing atmospheric particles and pollutants forming a visible cloud. For thunderclouds, the convective forces are particularly strong and form very tall clouds. Because of the large variance in temperature throughout the cloud, water droplets form into water and ice. The varying buoyancy and varying size of these particles cause a gradient in vertical velocity leading to many collisions between small particles. In each collision, charge may be exchanged depending on the relative sizes of the ice particles [Macgorman and Rust, 1998]. These forces then lead to charge separation, which in the simplest picture yields positively charged ice particles near the cloud tops and negatively charged water droplets moving toward the bottom (other competing charging mechanism theories are discussed further in Saunders [1993]). These distinct charge regions, in addition to strong winds and turbulence, lead to highly fluctuating local electric fields. Each thundercloud is unique in the charge structure, varying in space/time and dynamics. A ‘typical’ thundercloud charge structure is depicted in Figure 1.3.

In addition to the main positive upper charge and main lower negative charge, a positive charge screening layer tends to form on the lowest region of the cloud and an upper negative screening charge can also form [Krehbiel *et al.*, 2008]. The lightning initiation mechanism is currently unknown, as in-situ measurements have never measured electric fields sufficient for traditional spark breakdown. Current theory suggests 3 possibilities: (1) lightning initiation may be due to enhanced local electric fields that haven’t been measured [Stolzenburg *et al.*, 2007]. (2) Lightning is created from streamers that form on charged ice or water droplets in the cloud (hydrometeors) [Liu *et al.*, 2012]. (3) Or that the breakdown is due to relativistic processes (i.e. runaway breakdown electrons) [Dwyer, 2003]. For a thorough discussion see [Dwyer and Uman, 2014, Chapter 3]. As the lightning flash begins, a ‘preliminary breakdown’ occurs and in turn develops into a lightning ‘leader’ characterized as a hot self-propagating plasma channel. The leader continues to propagate in pseudo-random steps until it ‘attaches’ in what is known as the ‘attachment process’. This typically occurs in the

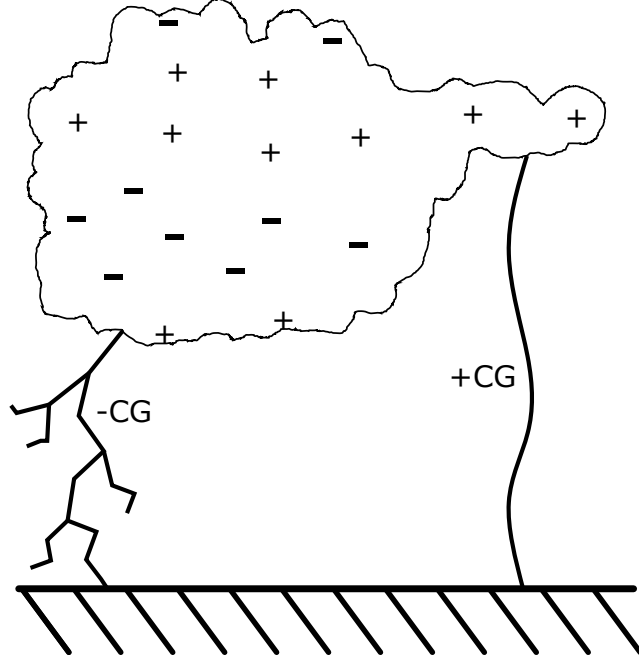


Figure 1.3: Example of the typical charge structure of a thundercloud with +/- CGs depicted propagating from the main positive and negative charge region respectively. Also pictured is the positive charge layer on the bottom of the cloud and a negative screening charge at the top.

opposite charge region of the same cloud or the Earth ground, inheriting names of intra-cloud or cloud-to-ground (IC or CG for short). The first leader of a lightning flash, known as the ‘initial leader’, differs from ‘subsequent leaders’ in the same lightning flash in that subsequent leaders do not appear to step and have different propagation velocities. Another important distinction is the propagation characteristics between positive and negative CG leaders. Negative leaders step as described above in discrete steps, whereas positive leaders do not appear to step but continuously propagate [Saba *et al.*, 2008].

The leader is an effective charge neutralization mechanism that typically lowering several coulombs to the ground and to the lightning branches [Proctor *et al.*, 1988]. When the leader attaches to ground, several coulombs are lowered to ground in the form of an unipolar current pulse 10s of  $\mu\text{s}$  wide at a velocity of  $1/2 - 2/3$  the speed of light [Brook *et al.*, 1962; Mallick *et al.*, 2014] and peak currents of 10s to 100s of kA. This event is known as a ‘return stroke’ and is the source of powerful ‘sferics’ detectable at global distances. After the initial return stroke of lightning, subsequent lightning strokes can occur on the same

established lightning channel, known as ‘initial strokes’ or ‘subsequent strokes’ differing in current pulse shape and propagation velocity.

In some cases, particularly after positive polarity strokes, 10s of amps of current continues to flow for up to 100 or more ms after the strokes has subsided [*Shindo and Uman*, 1989]. This event is known as ‘continuing current’ and is particularly dangerous in terms of human casualties and property damage. During the continuing current portion of a lightning flash, several pulses or perturbations to the relatively steady continuing current can occur and are known as M-components [*Thottappillil et al.*, 1995].

### 1.2.2 Lightning-Driven Technology

The ubiquity of lightning coupled with its destructive nature has always been an awesome sight for humanity. Early societies all had a deity who controlled lightning and we still refer to lightning damage as an ‘act of God’ in many contexts. Pioneering advances in our understanding of electricity were driven by lightning and it continues to motivate new technology. Here we discuss two major technologies developed to protect from and understand lightning.

#### *Lightning Protection*

The American inventor Benjamin Franklin is credited with proving that lightning is an electrical event. He determined charge convention and even invented the first lightning protection system: a lightning rod known as the ‘Franklin Rod’ in 1749. Lightning protection can be broken down into two basic types: diversion/shielding and the limiting of currents and voltages through the use of surge protection [*Rakov and Uman*, 2003, Section 18.3].

Diversion or shielding systems are passive systems that use one or more lightning rods or horizontal wires all held at the ground potential by a connection through one or more ‘down conductors’ which lower the current from the shielding to the ground. The down conductors are then connected to a grounding system. The entire system works by giving a lightning stroke a lower path of resistance to ground, thus diverting damaging currents away from sensitive electronics or equipment. Current US standards are described in the National Fire Protection Association standard NFPA-780 [*NFPA*, 2017].



Surge protection is a broad concept with many diverse devices suited for different applications. Surge protective devices (SPDs) have basically two types of devices: (i) Voltage crowbar devices (e.g. gas tube arresters, silicon-controlled rectifiers) which can handle higher power but act slower than voltage clamps. (ii) Voltage clamps which are semi-conductors that are highly non-linear devices where resistance tends to zero with higher voltages (e.g. metal oxide varistors, or Zener diodes). Other types of protection are circuit filters to remove unwanted voltages at unwanted frequencies or isolated circuits driven by devices such as optical isolators. The simple application of surge protection is a parallel connection of one or more of devices with sensitive circuit which limits transient damage. Many applications are also supplemented with fuses or series SPDs which open the circuit in the case of sustained damaging currents or voltages [NFPA, 2017].

### *Lightning Location Systems*

Modern ground-based lightning location systems (LLS) are conveniently divided into short-range systems, which use the ground wave of a lightning stroke, and long-range systems, that use ionospheric reflections and are capable of global detection. Short-range systems are typically located on land, therefore detection is restricted to over land and coastal waters. Long-range systems use ELF/VLF frequencies because of its efficient propagation in the EIWG, while short-range LLS tend to use higher frequencies (LF) for better arrival time accuracy. Short-range networks tend to be more accurate but typically require more receivers for a given geographical coverage area. Satellites are capable of detection from space by measuring optical signatures and multiple satellites have been launched with detectors for this purpose, including most recently the Global Lightning Mapper instrument aboard the GEOS-R satellite [Cecil *et al.*, 2014; Goodman *et al.*, 2013].

The most common techniques for LLS are magnetic direction finding (MDF) and time of arrival (TOA). MDF has the longest history with the first applications in storm tracking but with limited accuracy so that it was not possible to locate individual strokes [Cave and Watson Watt, 1922]. MDF is typically accomplished with the use of two magnetic field loop antennas placed orthogonal to each other, which operates on the assumption that most of the energy propagates in the azimuthal magnetic field or  $B_\phi$  component. TOA uses the

difference in time of arrival of multiple stations to determine the stroke location and time of occurrence.

The national lightning detection network (NLDN) is a short-range network that uses a combination of TOA and MDF to locate lightning strokes over the continental US operated by Vaisala Inc. [Cummins *et al.*, 1998]. Vaisala also operates the Canadian lightning detection network [Orville *et al.*, 2002] and the pacific lightning detection network amongst others (PacNet) [Pessi *et al.*, 2009]. They also operate the global long-range network called GLD360 [Said and Murphy, 2016]. GLD360 uses a combination of TOA, MDF, and a cross-correlation of expected lightning waveforms or ‘sferics’ with a global coverage [Said *et al.*, 2010, 2013]. GLD360 detects cloud-to-ground lightning with a global flash detection efficiency of greater than 70% and reports peak current estimates, polarity, location, and time of occurrence for each lightning event. The location accuracy is estimated to be 1–4 km. Another important long-range network is the worldwide lightning location network (WWLLN) which calculates a time of arrival based on the phase group delay at VLF frequencies [Dowden *et al.*, 2002]. The location accuracy of WWLLN has a detection efficiency of  $\sim 9.2\%$  and a location accuracy of 4–5 km [Rudlosky and Shea, 2013; Abarca *et al.*, 2010].

When the lightning leader propagates to form a lightning channel, each individual step produces strong emissions at VHF frequencies. Using the VHF emissions, with an array of receivers and interferometric techniques, Krehbiel *et al.* [Rison *et al.*, 1999] developed the lightning mapping array (LMA) which can map the full 3D structure of a lightning flash. Recently, VLF/LF interferometry has been developed contributing to the toolset for lightning studies [Lyu *et al.*, 2014, 2016; Füllekrug *et al.*, 2015a,b, 2016].

### 1.2.3 Sferic-Based $D$ Region Remote Sensing

Large current sources in lightning flashes, most notably the return stroke, generates powerful impulsive broadband radio wave packets in the VLF/LF bands known as ‘radio atmospherics’ or ‘sferics’. These sferics also propagate efficiently (few dB per Mm attenuation) to global distances guided by the EIWG. Sferics therefore provide a convenient signal of opportunity to monitor ionospheric conditions along the path from the lightning source to a VLF/LF receiver. Sferics have been used to study the  $D$  region alongside VLF transmitters,

but early studies had usually been limited by an unknown precise lightning stroke location. This is seen by the plethora of early propagation studies using VLF/LF frequencies [*Kitchen et al.*, 1953], whereas it was only shown much later that sferics reflect from the ionosphere [*Laby et al.*, 1938].

An early important study by *Burton and Boardman* [1933] considered sferics with highly dispersive frequency content near waveguide mode cutoffs and correctly explained these so-called ‘tweeks’ as due to many reflections from the lower ionosphere. Many other studies of sferics also suffered because of radio receiving instrumentation, namely because sferics were received on only one receiver. Although unreasonable assumptions were made about source spectral characteristics, many workers made important contributions [*Chapman and Macario*, 1956; *Chapman and Pierce*, 1957]. While many early studies focused on understanding the nature of sferic observations, others attempted to use sferics for radio propagation studies such as measuring attenuation rates and phase velocities [*Jean et al.*, 1960; *Croom*, 1964; *Chapman et al.*, 1966; *Taylor*, 1967; *Taylor and Sao*, 1970] which were useful in validating waveguide mode propagation theory [*Wait*, 1957, 1958].

After somewhat of a hiatus on sferic-based studies, some workers [*Cummer et al.*, 1998; *Cheng et al.*, 2006] developed a technique of monitoring the modal interference pattern in sferic amplitude spectrum to infer the Wait and Spies parameters. The observations were interpreted using the long wavelength propagation capability code (LWPC) leading to estimates of mid-latitude diurnal variations in the  $D$  region Wait and Spies parameters: height  $h'$  and sharpness  $\beta$ . Using a finite difference time-domain (FDTD) code [*Hu and Cummer*, 2006], some considered daytime and nighttime variations of Wait and Spies parameters for the  $D$  region ionosphere [*Han and Cummer*, 2010a,b; *Han et al.*, 2011]. For both VLF transmitter and sferic-based ionospheric remote sensing at large distances, the inferred  $D$  region waveguide parameters can be assumed to be a path averaged inference, being the summation of multiple waveguide modes, except in the presence of a sharp scattering feature such as an early/fast event [*Inan et al.*, 2010].

Using time-domain sferics, *Lay and Shao* [2011a,b] developed a technique to sense a small portion of the  $D$  region corresponding to the Fresnel refraction zone, or the region of the first ionospheric hop, and observed ionospheric disturbances in the effective reflection height

and reflection loss. Combining the experimental observations with the modeling technique developed by *Shao and Jacobson* [2009], *Shao et al.* [2013] and *Lay et al.* [2014] inferred the *Volland* [1995] electron density parameterization and  $h'$ ,  $\beta$  respectively. Both studies interpreted their results as a small spatial measurement covering the Fresnel refraction zone. Recently, *Carvalho et al.* [2017] looked at change in effective height using a cross-correlation technique for lightning sources characterized at the International Center for Lightning Research and Testing.

Waveguide mode theory predicts that as propagation frequencies near the cutoff of a particular mode, group velocity decreases dramatically, causing what is known as a ‘slow-tail sferic’ or tweek [*Burton and Boardman*, 1933]. The cutoff frequencies are sensitive to the properties of the  $D$  region of the ionosphere, therefore by monitoring the cutoff frequencies it is possible infer properties of the lower ionosphere [*Reeve and Rycroft*, 1972]. Many have monitored changing cutoff frequencies in order to deduce the changing effective reflection height in response to various geophysical drivers (e.g. *Kumar et al.* [1994]; *Ohya et al.* [2006]). Some have used tweek measurements to estimate the electron density profile along the source-to-receiver path [*Kumar et al.*, 2009; *Maurya et al.*, 2012].

The current literature using sferic-based ionospheric remote sensing techniques all use key features of sferics implying applicability in specific source-to-receiver geometries or times of the day. In contrast, the process technique described in this work relaxes this requirement and therefore allows for general applicability for sferic-based work. Furthermore, all prior sferic-based studies use only the azimuthal magnetic field ( $B_\phi$ ) or the vertical electric field ( $E_z$ ). In this paper we describe a generalized technique to recover stable sferics with both azimuthal and radial magnetic fields ( $B_\phi$  and  $B_r$ ) for any source-to-receiver geometry for both time-domain sferics and amplitude/phase frequency spectra. This technique extends the usable frequency range to higher frequencies (the examples in this work use up to 50 kHz but even higher frequencies may be useful in general), where VLF/LF propagation is even more sensitive to ionospheric changes. This allows sensitivity to higher altitudes since higher frequency waves can penetrate further into the  $D$  region.

With the more generalized sferic processing technique described here, as long as sferics are significantly higher than the background noise (Signal-to-Noise Ratio (SNR) of  $>5$  for

this work), the full availability of lightning data from one or more lightning location networks can be used with an arbitrary receiver network. Lightning flashes occur about 40–50 times per second throughout the Earth [Christian *et al.*, 2003]. An average of 600–700 lightning storms occur each day with a mean duration of  $\sim 15$  minutes [Hutchins *et al.*, 2014] creating a global time-varying distribution of lightning-generated VLF/LF sources with  $\sim 57\%$  of these sferics being measured at greater than our SNR threshold of 5. There is an opportunity to use this large dataset of natural lightning emissions and an arbitrary receiver network for regional to global ionospheric  $D$  region characterization. The extent of the ionospheric coverage is proportional to the number of lightning strokes and their locations as well as the placement of receivers.

### 1.3 Tomography

We now describe the field of tomography briefly, since these techniques will enable us to convert sferic observations over a large region into ionospheric  $D$  region maps. Since its debut in 1972, computed tomography (CT) has become one of the most important medical science breakthroughs of the 20<sup>th</sup> century leading to many other medical imaging technologies such as positron emission tomography (PET) or the well-known medical resonance imaging (MRI). Tomographic techniques have found their way into many non-medical fields as well even appearing in ionospheric 3D imaging studies of the  $E$  and  $F$  regions [Yao *et al.*, 2014].

#### 1.3.1 Historical Development

CT was first demonstrated by Godfrey Hounsfield in 1972 [Hounsfield, 1973] in order to make non-destructive internal images of the human body. However, extensive history and research was integrated into the first proof of concept. In 1895, Wilhelm Roentgen, a German professor of physics, discovered X-rays and was awarded a Nobel Prize in Physics in 1901 for his accomplishments.

In 1917, Johann Radon, an Austrian mathematician, published a paper on the mathematical transform to reconstruct an image from line-integral measurements or projections,

known as the *Radon* [1917] transform. Some of the first applications of this theory didn't appear until 1956, when Ronald Bracewell (the same Bracewell who made many early contributions to ionospheric physics) developed imaging applications in radioastronomy [Bracewell, 1956]. In 1963 A.M. Cormack demonstrated a method to calculate radiation absorption distributions in the human body [Cormack, 1963].

Synthesizing all the above work, Godfrey Hounsfield working at the British firm EMI Ltd., created the world's first CT scanner. In its first trial run, a cystic frontal lobe tumor was discovered in its first test subject leading to a 'media frenzy'. In the years that have followed, CT has made great advancements in medical science and public health. Accompanying research and more powerful computers have improved the capability and performance of CT, as well as our understanding of the underlying theory.

### 1.3.2 Mathematical Principles

Although there are many forms of tomography, we restrict discussion of the mathematical principles to CT since it is the easiest to understand. After a discussion of the principles, an analogy to the  $D$  region tomography technique developed in this work will be drawn. Further elaboration of  $D$  region tomography will be given in Chapter 5.

The essential intuition of tomography is that projections of an object onto a lower dimensional space contains information about the collapsed dimension. If a new projection is taken at a different angle, then it contains different information than the previous one. The Radon transform is a mapping from a uniformly sampled (varying angle) set of projections. Figure 1.4 demonstrates a single projection sample  $R_\theta(x')$ , where  $\theta$  is the example angle and  $x'$  is the  $x$ -axis rotated by  $\theta$ . Each projection can be described mathematically as

$$R_\theta(x') = \int_{-\infty}^{\infty} f(x \cos \theta - y \sin \theta, x \sin \theta + y \cos \theta) dy' \quad (1.3)$$

where

$$\begin{bmatrix} x' \\ y' \end{bmatrix} = \begin{bmatrix} \cos \theta & \sin \theta \\ -\sin \theta & \cos \theta \end{bmatrix} \begin{bmatrix} x \\ y \end{bmatrix} \quad (1.4)$$

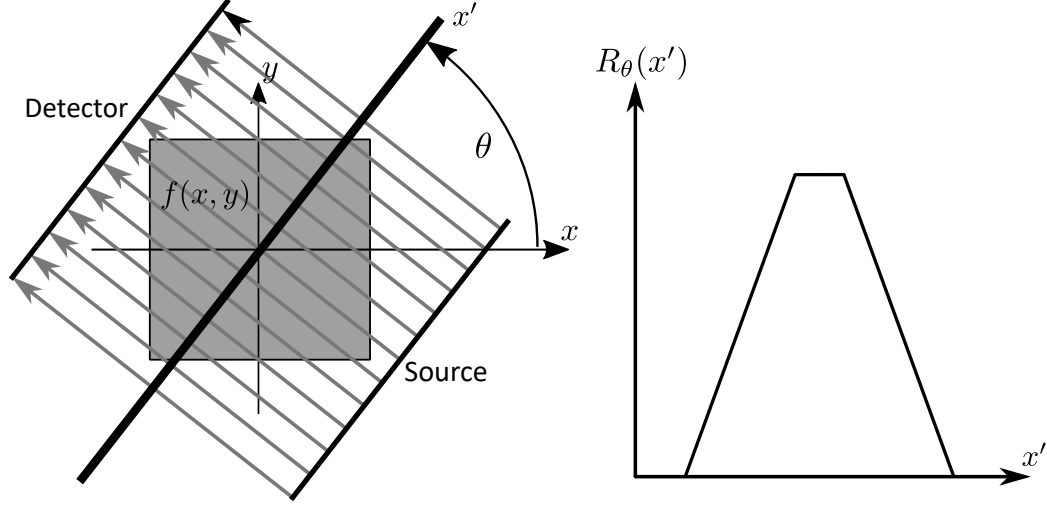


Figure 1.4: Example of a projection measurement of a square image, where the uniform color indicates that the underlying function is equal valued everywhere. The curve  $R_\theta(x')$  is the 2D projection for the given scan geometry along the rotated axis  $x'$ .

The Fourier transform of  $f(x', y')$  is given by

$$F(k_{x'}, k_{y'}) = \int_{-\infty}^{\infty} \int_{-\infty}^{\infty} f(x', y') e^{-2\pi j(x'k_{x'} + y'k_{y'})} dx' dy' \quad (1.5)$$

and the slice  $s(k_{x'})$  at  $k_{y'} = 0$  is

$$s(k_{x'}) = F(k_{x'}, 0) = \int_{-\infty}^{\infty} \int_{-\infty}^{\infty} f(x', y') e^{-2\pi jx'k_{x'}} dx' dy' \quad (1.6)$$

$$= \int_{-\infty}^{\infty} \left( \int_{-\infty}^{\infty} f(x', y') dy' \right) e^{-2\pi jx'k_{x'}} dx' \quad (1.7)$$

$$= \int_{-\infty}^{\infty} R_\theta(x') e^{-2\pi jx'k_{x'}} dx' \quad (1.8)$$

which is the same as the Fourier transform of  $R_\theta(x')$  and is known as the ‘Fourier slice theorem’. However, the straightforward application of the Fourier slice theorem to recover an image has two major shortcomings, namely that the measurements  $R_\theta(x')$  need to be transformed into Fourier space and that noise can perturb the straightforward reconstruction.

Another technique is known as backprojection in which each projection is assumed to be constant along the entire collapsed dimension. Figure 1.5 shows the process of reconstruction by backprojection. Figure 1.5a shows the original image. Figure 1.5b shows only the first

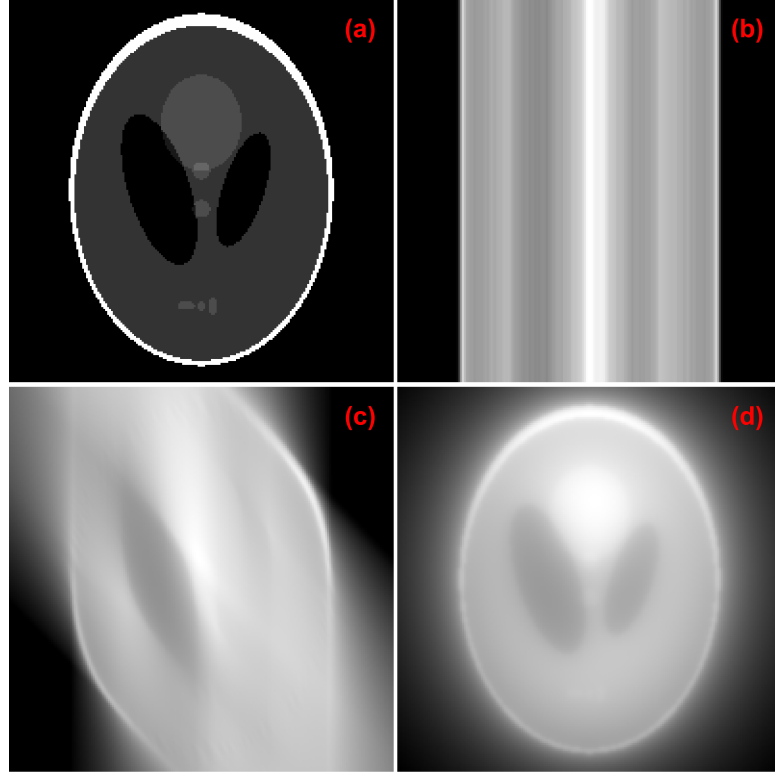


Figure 1.5: Demonstration of the image reconstruction using backprojection. The original image is sampled at  $1^\circ$  increments. (a) The original image of the Shepp-Logan phantom. (b) One projection at  $\theta = 0$  from the  $y$ -axis. (c) The backprojected image with the first 45 projections. (d) The full image reconstruction.

backprojection. Figure 1.5c shows the first 45 backprojections (scanned at uniform  $1^\circ$  increments). Lastly, Figure 1.5d shows the entire back projection. Some details of the image become clearer as backprojections are added in, however, the reconstruction suffers from blurring and therefore obscures important information in the reconstructed image.

In addition to the blurring problem, if the image is not sampled with high enough resolution (small enough  $\theta$ ) then other artifacts can start to dominate. This process is illustrated in Figure 1.6 and can be compared with Figure 1.5d where 180 scans are used.

In order to combat the blurring effect, projections are often filtered before being backprojected forming the filtered backprojection algorithm (FBP). The filter used can be arbitrarily chosen, but one popular filter is the Ram-Lak filter given as  $|f|$ . The results of applying this filter for FBP in contrast to simple backprojection can be seen in Figure 1.7. The Ram-Lak filter tends to amplify high frequencies which can often cause artifacts, especially



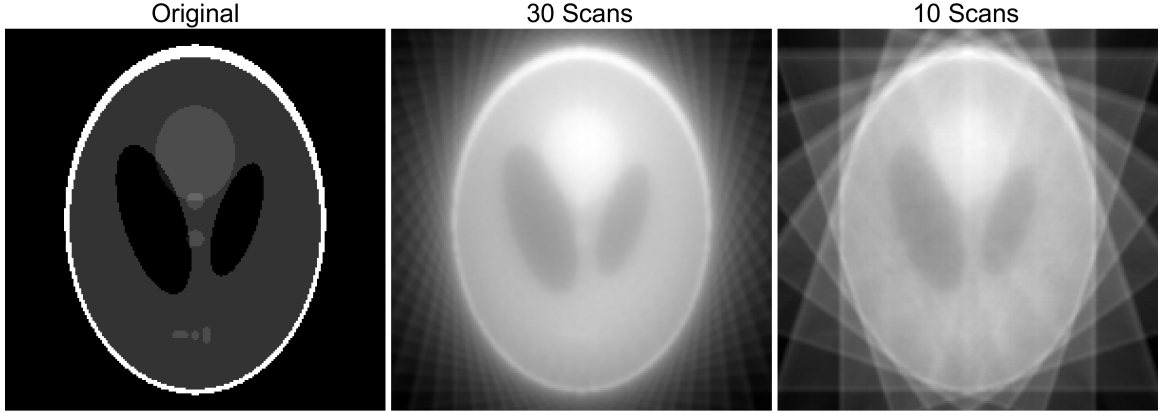


Figure 1.6: Demonstration undersampling effects when using backprojection. The original image is the Shepp-Logan phantom. Backprojection is performed using a uniform but sparsely sampled image. The middle and right-hand images are reconstructed with  $6^\circ$  and  $18^\circ$  sampling respectively.

in the presence of noise, therefore many other filters have been developed. FBP is very fast, but one major shortcoming of the technique is that it is very hard to know quantitatively the best possible performance of the algorithm and therefore it can be hard to choose the appropriate filter for the application where the underlying image is not generally known. Nonetheless, in this case, even for the standard filter, significant improvement is made by applying a filter before backprojection.

In the  $D$  region tomography problem, instead of uniform sampling, each ‘sample’ is a line-integral of inferred electron density model parameters from each source-to-receiver. The region of interest is the entire ionosphere and therefore the samples occur entirely inside of the object to be imaged. Because of these differences, traditional techniques like the Fourier slice theorem or FBP will not work. The relevant math and techniques chosen for the  $D$  region ionosphere tomography problem are discussed in Chapter 5.

#### 1.4 Contributions

The aim of this work is to develop a method to study the spatial structure of the  $D$  region of the ionosphere. Extensive work has been done to study the structure, composition, and dynamics of the  $D$  region, but most studies consider only temporal changes. In addition, most techniques are limited to measuring one altitude profile of the ionosphere or an aver-

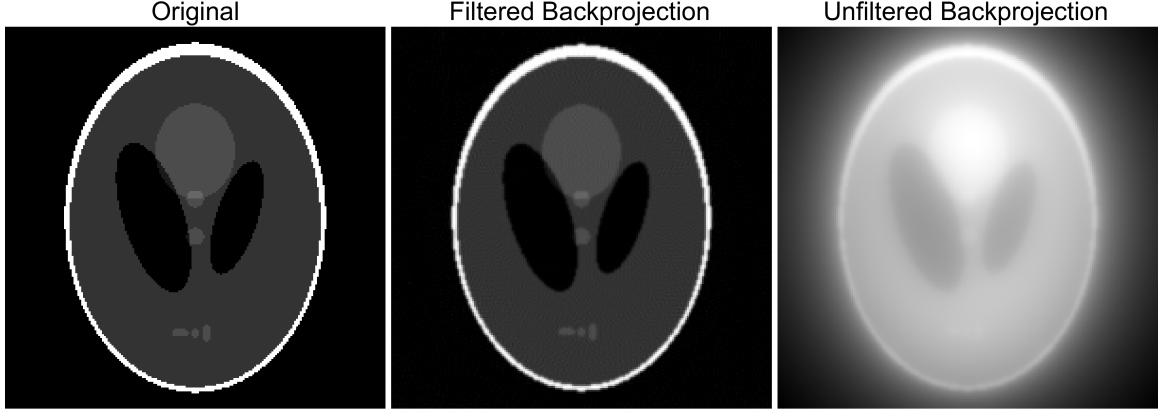


Figure 1.7: Performance comparison of filtered backprojection vs. backprojection. The original image is the Shepp-Logan phantom. The filtered backprojection result uses the Ram-Lak filter. Both reconstructions use projections sampled at  $1^\circ$  increments.

age along a path. This technique expands current VLF sensing capabilities with  $D$  region tomography applicable to large-scale spatial and temporal studies. This work can be summarized in a block diagram as in Figure 1.8 with references to the sections that describe them.

The main contributions of this thesis are:

- A generalized method to process sferics and produce stable representative measurements for  $D$  region remote sensing (Chapter 3).
- Demonstration of the ability to recover spectral phase information of sferics and the minor magnetic field component (Section 3.4).
- Introduction of the ‘split model’ for  $D$  region electron density vs. altitude profile that allows a ‘split’, a feature consistently measured by many techniques yet typically excluded from modeling (Section 4.2).
- A generalized  $D$  region ionospheric remote sensing method to infer path-averaged electron density from arbitrary source and receiver geometries (Section 4.3).
- Tomographic images of the  $D$  region tomography using the path averaged electron density inferences (Chapter 5).

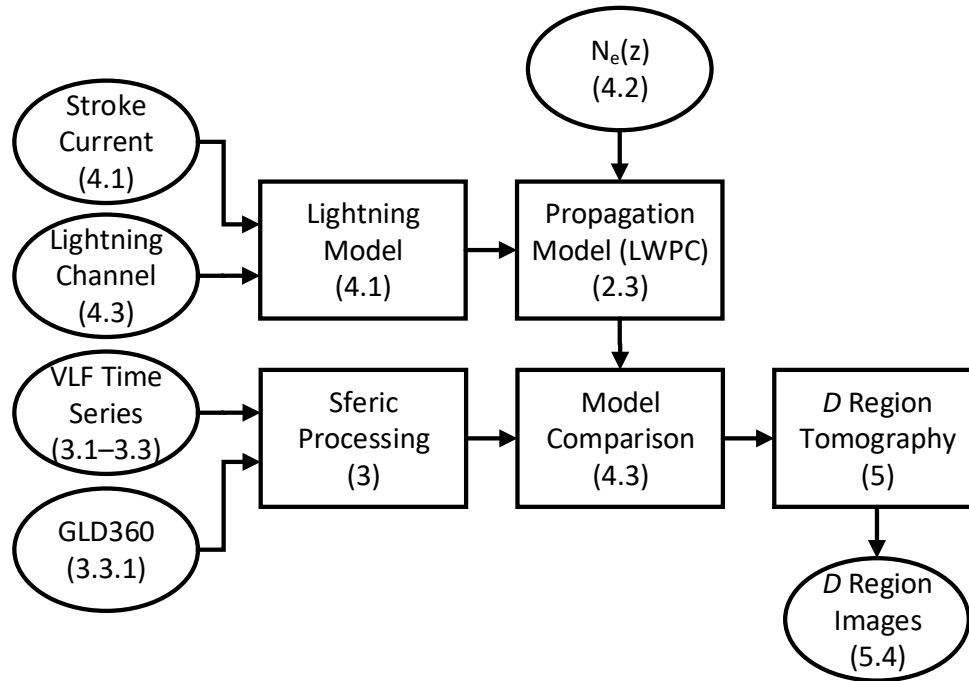


Figure 1.8: Overall block diagram of this work. Boxes indicate steps of the overall algorithm and ellipses represent the inputs/outputs. Chapter/section references to relevant sections are given in parentheses.

## CHAPTER 2

### SPHERIC PROPAGATION

VLF and LF frequencies can propagate to global distances because they are guided by the Earth and the  $D$  region of the ionosphere forming a spherical shell waveguide known as the Earth-ionosphere waveguide or EIWG. Along a given transmitter-to-receiver (Tx-Rx) path, Earth's electrical parameters (permittivity and conductivity) are nearly time-invariant at VLF/LF frequencies. However, the  $D$  region is decidedly unstable, where conditions at any given time are dominated by the real-time flux of ionizing energy from solar (dominant during daytime) and cosmic (dominant during nighttime) sources. An incident VLF/LF wave's action on the  $D$  region boundary is anisotropic because of Earth's magnetic field. Furthermore, the refractive index of the  $D$  region varies with height on length scales smaller than a wavelength, in contrast to many standard refractive materials considered in electromagnetic and optics studies. Because of these non-idealities, we must use a full-wave model which includes all important waveguide parameters with respect to VLF/LF propagation to produce accurate predictions, as opposed to a raytracing solution. In this chapter we introduce the intuition and theory behind EIWG propagation and the long wave propagation capability, or LWPC, a model implementing the theory of EIWG propagation with a long history of successful prediction of VLF/LF wave propagation.

#### 2.1 Ray-Hop Analysis

The simplest picture of wave propagation in the EIWG involves a sum of rays, similar to techniques commonly used in geometric optics. Figure 2.1 shows a simplified propagation picture, not to scale, with two perfectly conducting parallel plates and a perfect impulse source excitation (lightning) assumed to radiate uniformly in all directions. The individual rays are discretely divided into a ground wave, an ionospherically reflected wave once, twice, and three times. With these multiple rays or modes, an impulse propagating under these conditions is detected as a pulse train, as depicted in the upper panel of Figure 2.2, which

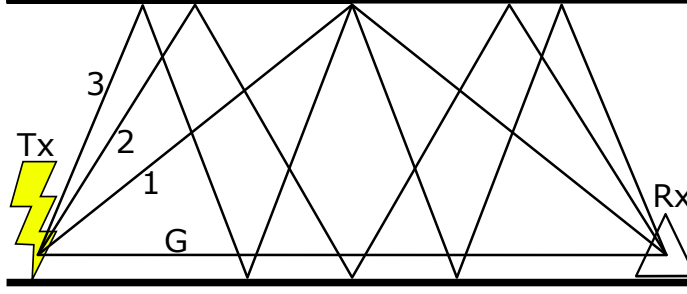


Figure 2.1: Example of the ray tracing approach for EIWG propagation with parallel perfectly electrical conducting (PEC) boundaries.

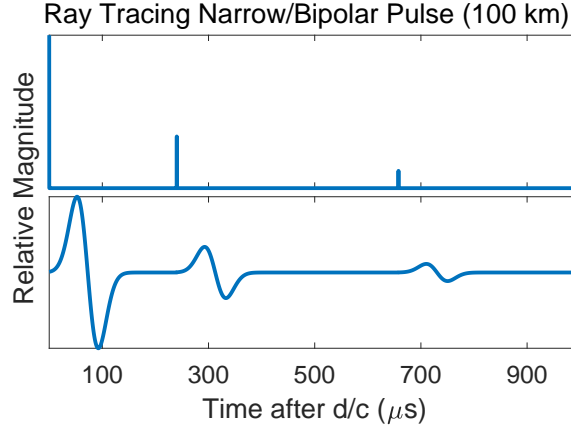


Figure 2.2: Example of received ‘sferic’ for a narrow pulse, and a bipolar pulse received at 100 km with a plate spacing of 70 km.

assumes a 70 km plate spacing and a distance from transmitter-to-receiver of 100 km. The geometric delay of each successive impulse is increasingly small, as the path difference between successive ray changes by a diminishing amount. We assume only spreading loss so that impulses decay due by  $1/r^2$ , where  $r$  refers to the total ray length from source-to-receiver. This ray picture is valid for short distances where the waves are not self-reinforcing (i.e. where the reflected wavefronts are consistent with the ones propagating without reflection in the waveguide).

A ray-hop model can be used to model VLF/LF wave propagation for short distances from source-to-receiver in the EIWG. However, for a finite width source excitation, the individual total electric field from waveguide reflections cannot be separated at greater distances. This is a direct result from the time delay between successive ray modes (ground, first sky, second sky, etc.) reducing as the distance from source-to-receiver increases until

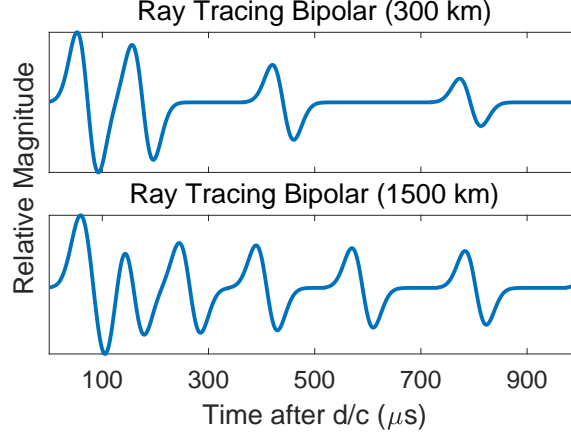


Figure 2.3: Example of received ‘sferic’ for a narrow pulse and a bipolar pulse received at 300 and 1500 km with a plate spacing of 70 km.

many ray-hop contributions are superposed. Figure 2.3 demonstrates with the source excitation as a finite width bipolar pulse. In contrast, for very short pulses (Figure 2.2a), or if the difference between ray lengths are large enough (Figure 2.2b), it is possible to clearly distinguish contributions from the different ray paths. In Figure 2.3a, as the difference between the ray lengths diminish, they start to interfere with each other making it difficult to distinguish individual contributions. In addition, if the distance to source increases further, multiple sources can interfere near the start of time of light arrival ( $d/c$ ). Even the short/moderate distances considered in this study (300/1500 km) can be problematic when considering the ray-tracing model, regardless of the many simplifying assumptions.

Because of the many shortcomings of the ray-tracing approach for sferic propagation where many lightning-generated electromagnetic pulse reflections combine into one waveform even for moderate distances, we must use a different approach for modeling sferic propagation.

## 2.2 Finite-Difference Time-Domain

Due to recent advantages in computing power and memory, it has become possible to numerically solve Maxwell’s equations in space and time for many systems. A commonly used technique is known as the Finite-Difference Time-Domain (FDTD) method (e.g. Yee’s method [Yee, 1966]). FDTD works by setting up a grid that is sufficiently small compared

to the wavelength of interest and then solving for the time-evolution of the electromagnetic solutions to Maxwell's equations in a leapfrog manner. This method has been recently used to solve VLF electromagnetic propagation in the EIWG [Cummer, 2000; Hu and Cummer, 2006; Marshall, 2012], with validations by comparison to other methods [Cummer, 2000]. The advantage to FDTD is that it is highly accurate when implemented properly and can simulate wave propagation with arbitrary geometries. It requires no analytical solution, just a slow evolution of the electromagnetic fields following direct solution of the Maxwell's differential equations.

However, because of the computational time required for long propagation paths considered here and the finer grid requirement due to the higher frequencies used in this work than past studies, we use the analytical waveguide mode method to predict VLF/LF propagation.

## 2.3 Mode Theory and LWPC

### 2.3.1 Wave Propagation in the Ionosphere

In addition to Appleton and Barnett's early important experimental confirmation of the ionosphere, Appleton produced the most important and first (nearly) complete description of cold plasma wave propagation. Soon after, *Hartree* [1929] produced a parallel formulation using a bottom up approach, giving rise to the name 'Appleton-Hartree' equation. However, due to the convenience of Appleton's formulation, his equations are usually preferred. Appleton's formulation has one major shortcoming, namely that the 'friction' term, or electron-neutral collisional frequency term  $\nu$ , is assumed to be independent of the electron velocity. This assumption has been shown to be invalid in general leading to the development of the 'generalized Appleton-Hartree' equation by *Sen and Wyller* [1960], given as

$$n^2 = 1 - \frac{X}{1 - jZ - \frac{Y^2 \sin^2 \theta}{2(1 - X - jZ)} \pm \left\{ \left[ \frac{Y^2 \sin^2 \theta}{2(1 - X - jZ)} \right]^2 + Y^2 \cos^2 \theta \right\}^{1/2}} \quad (2.1)$$

where  $n$  is the index of refraction and has two solutions that are in general complex numbers.  $X$ ,  $Y$ , and  $Z$  describe the normalized plasma frequency (squared), gyro frequency, and

collision frequency

$$X = \frac{\omega_p^2}{\omega^2}; \quad Y = \frac{\omega_H}{\omega}; \quad Z = \frac{\nu}{\omega} \quad (2.2)$$

which measures the relative importance of the electron density, magnetic field, and collisions, respectively. For a given ion species  $\alpha$ , the plasma frequency ( $\omega_p$ ) and ion gyrofrequency ( $\omega_H$ ) are

$$\omega_p = \sqrt{\frac{N_\alpha q_\alpha^2}{m_\alpha \epsilon_0}}; \quad \omega_{H\alpha} = \frac{B_0 |q_\alpha|}{m_\alpha} \quad (2.3)$$

where  $N_\alpha, q_\alpha, m_\alpha$  are the number density, charge, and mass of the species  $\alpha$  and  $B_0$  is the background (quasi-static) magnetic field. In most cases, the only relevant particle in plasma dynamics is an electron because the mass is much lower than a proton or the lightest ions. The two solutions for  $n$  in a plasma represent the ‘ordinary’ and ‘extraordinary’ wave respectively which have different attenuation rates and phase velocity and correspond to the two circular polarizations. The birefringence of the plasma respect to sense of rotation arises fundamentally from the electron gyration around the magnetic field, which imposes a preferred circular direction. This also creates an anisotropic material where the direction of propagation significantly changes the propagation conditions. The real part of  $n$  corresponds to diffraction, where the imaginary component describes the attenuation rate of each wave due to collisions.

The plasma frequency  $\omega_\alpha$  can be thought of as the ability of a plasma to block an incident wave. Higher plasma frequency implies that the plasma can do so on very short timescales, and thus can respond to higher wave frequencies. When an electromagnetic wave impinges on a plasma, the charges rearrange themselves in a way that effectively re-radiates the same signal back. The effect of magnetic fields ( $Y$ ) or collisions ( $Z$ ) is to reduce the ability of the charged particles to move freely in the medium, thereby affecting wave dynamics. When  $Z \gg Y$ , the plasma can be considered as non-magnetized and the effects of anisotropy can be neglected. On the other hand, if  $X \gg Z$  and  $Y \gg Z$ , then the effects of collisions can be neglected. However, for the  $D$  region ionosphere, none of these simplifications can be made in general, and therefore we turn to a full-wave solution in the form of mode theory.



### 2.3.2 Determining the Mode Solutions

When we consider medium to long-distance EIWG propagation a waveguide mode theory solution is elegant and computationally efficient. Mode theory can be summarized as a discrete series of ‘resonances’ which efficiently describe the wave solution in an arbitrary waveguide. The requirement of a mode is that it satisfies the conditions at the upper and lower boundaries of the waveguide. In order to solve for the general solution, we need to proceed through the following steps: **1. Mode Finding:** A way to determine the composition of modes propagating in an arbitrary waveguide. **2. Excitation Factors:** A method to understand how well an electromagnetic source (or receiver) can excite (or detect) each mode. **3. Height Gain Functions:** A function multiplied by the mode solution at the ground to allow for a general source and receiver position for a specified waveguide. **4. Mode Conversion:** A changing composition of modes at interfaces between two waveguides with different upper or lower boundaries. **5. Mode Sum:** Field calculation from a mode solution. Many workers have made important contributions to the general solution of wave propagation in the EIWG, most notably *Wait* [1970] and *Budden* [1961]. In this work we use LWPC to predict propagation in the EIWG which builds primarily on Budden’s formulation of the problem. LWPC’s included LWPM program automatically seeks a solution to the EIWG propagation problem by solving these given steps. Before proceeding to wave propagation in a complicated waveguide (such as the EIWG), we seek to develop waveguide propagation intuition by considering a simpler example.

#### *Waveguide Modes in a PEC Flat Earth*

We begin by considering perfectly conducting parallel plates of infinite length and width. Despite the relative simplicity of this this waveguide system, the basic theory has several important applications in real electromagnetic systems.

Waveguide modes, or resonances, can be thought of in analog to a Fourier series representation of a signal. Instead of tracking propagation as a number of discrete reflections as in ray-hop analysis or as a time solution of Maxwell’s equations as in FDTD, a propagating wave can be decomposed into a series of self-consistent waves called modes. An intuition

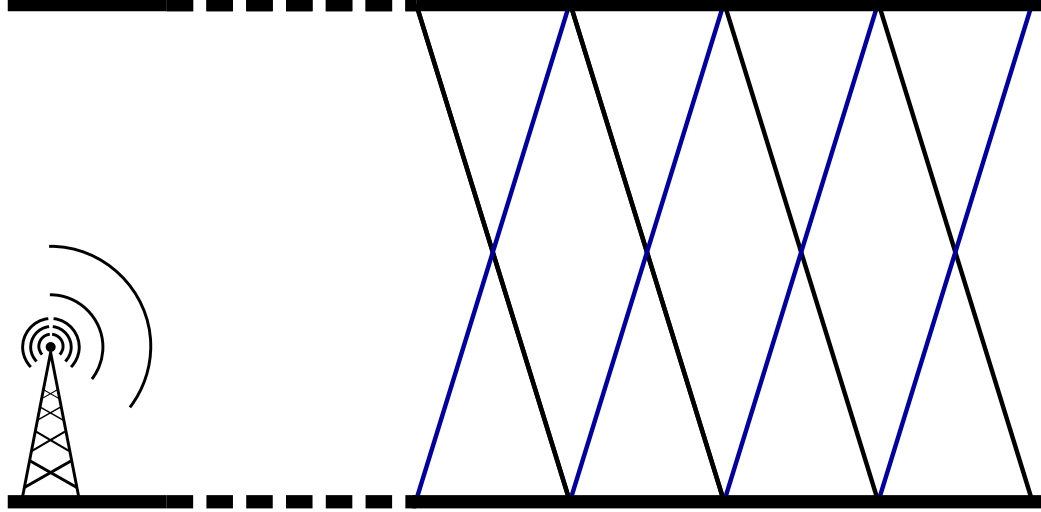


Figure 2.4: Example of self-consistent waves in a parallel plate PEC waveguide. Upgoing wavefronts are displayed as parallel black lines and downgoing wavefronts as blue lines. The broken black boundaries indicate that the source is far from the wavefronts in the right-hand side of the cartoon.

of a self-consistent wave can be gleaned from considering an incident oblique plane wave that is launched between two perfectly electrically conducting (PEC) parallel plates. The incident wave will reflect with no loss from the upper boundary and then from the bottom boundary. If the twice reflected wavefronts are exactly in line, or at the same phase as the initially propagated wave, then the wave is self-consistent. This condition is pictured in Figure 2.4 with parallel lines representing the wavefronts of the upward and downward propagating waves. The plane-wave assumption, in which wavefronts are assumed to be parallel, is reasonable for long distances.

The main boundary conditions of this waveguide are that the electric field cannot have a component along the conducting boundary (at the boundary), nor can the magnetic field have a component perpendicular to the conducting boundary. In a typical waveguide, the mode solutions are further subdivided into transverse electric (TE) or transverse magnetic (TM) modes indicating that its respective field is linearly polarized and transverse (perpendicular) to the wave normal. The other component, however, can exist in either transverse or parallel directions (except at the boundary where only one is allowed). This is equivalent to an ordinary plane wave except propagating not directly down the waveguide but at some angle  $\theta$ , effectively zigzagging between the two boundaries. For the following examples, we

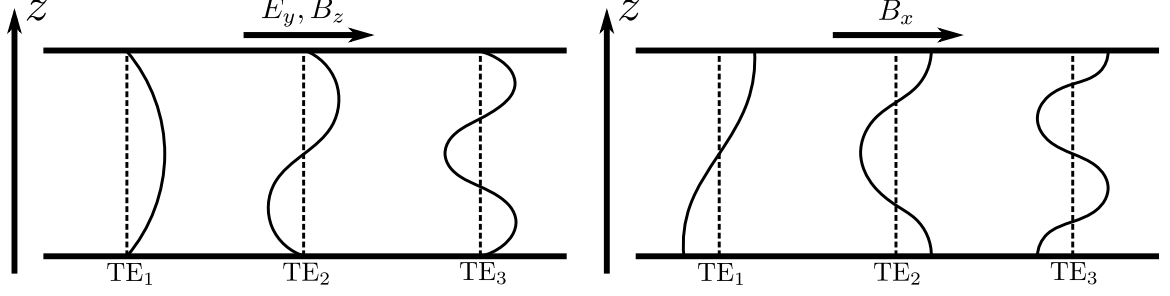


Figure 2.5: Illustration of the height variation of the TE modes with  $z$  in an invariant  $y$  waveguide system.

assume a PEC plate at  $z = 0$  with a linearly polarized time-harmonic electric field propagating along the  $x$ - $z$  plane with some angle  $\theta$  from the  $x$ -axis in free space and linearly polarized in the  $y$  direction, or transverse to the propagation plane. Therefore, the electric field incident on the boundary is:  $E_y = E_0 \exp\{-jk(x \cos \theta - z \sin \theta)\} \exp\{j\omega t\}$ . After reflection, the upward wave is:  $E_y = E_0 \exp\{-jk(x \cos \theta + z \sin \theta)\} \exp\{j\omega t\}$ . Therefore, the total fields calculated from the sum and Faraday's law are

$$\begin{aligned} E_y &= 2jE_0 \sin\{kz \sin \theta\} \exp\{-jkx \cos \theta\} \exp\{j\omega t\} \\ B_x &= (2/c)E_0 \sin \theta \cos\{kz \sin \theta\} \exp\{-jkx \cos \theta\} \exp\{j\omega t\} \\ B_z &= (2j/c)E_0 \cos \theta \sin\{kz \sin \theta\} \exp\{-jkx \cos \theta\} \exp\{j\omega t\} \end{aligned} \quad (2.4)$$

next, we introduce a PEC at  $z = h$  with

$$kh \sin \theta = n\pi \quad (2.5)$$

where  $n = 0, 1, 2, 3 \dots$  this satisfies the boundary conditions, namely that  $\bar{B}_\perp = 0$  and  $\bar{E}_\parallel = 0$  are therefore a valid solution to Maxwell's equations. The solutions represented by each value of  $n$  are the  $TE_n$  mode solutions of the PEC waveguide system. Modes of constant phase are at  $\omega t - kx \cos \theta = \text{constant}$ , with a phase velocity of  $c/\cos \theta$ . From Equation 2.5, we can define a cutoff frequency

$$f_n = \frac{nc}{2h} \quad (2.6)$$

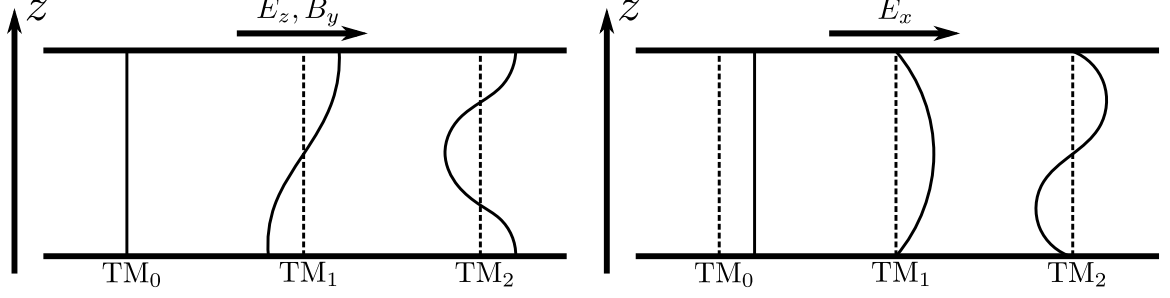


Figure 2.6: Illustration of the height variation of TM modes with  $z$  in an invariant  $y$  waveguide system.

for frequencies below the cutoff frequency, the mode does not propagate and is known as an ‘evanescent’ mode.

A similar procedure can be used to solve for TM modes in the system. We start by assuming a linearly polarized magnetic field in the transverse or  $y$  direction. The field is propagating at an angle  $\theta$  from the  $x$ -axis is then  $B_y = -B_0 \exp\{-jk(x \cos \theta - z \sin \theta)\} \exp\{j\omega t\}$ . The reflected wave from the boundary at  $z = 0$  is:  $B_y = -B_0 \exp\{-jk(x \cos \theta + z \sin \theta)\} \exp\{j\omega t\}$ . From the wave sum and from Ampere’s law we get the total fields

$$\begin{aligned} B_y &= -2B_0 \cos\{kz \sin \theta\} \exp\{-jkx \cos \theta\} \exp\{j\omega t\} \\ E_x &= 2jcB_0 \sin \theta \sin\{kz \sin \theta\} \exp\{-jkx \cos \theta\} \exp\{j\omega t\} \\ E_z &= 2cB_0 \cos \theta \cos\{kz \sin \theta\} \exp\{-jkx \cos \theta\} \exp\{j\omega t\} \end{aligned} \quad (2.7)$$

With the condition from Equation 2.5, we get another valid solution to Maxwell’s equations. For  $TE_n$  modes we get non-trivial solutions for  $n = 1, 2, 3 \dots$ , but for  $TM_n$  modes, we get solutions a special solution at  $n = 0$ , the  $TM_0$  or more commonly the TEM mode since both the electric and magnetic fields are transverse to the propagation plane. The first few TE and TM mode solutions for the parallel plate PEC waveguide are shown in Figures 2.5 and 2.6 respectively.

### *Overview of Budden’s Theory*

The Hertz vector  $\mathbf{U}$  is a convenient tool in electromagnetics since it is specified as an electric source and from which electric and magnetic radiating fields can be easily determined. It

is a solution to the wave equation

$$\nabla^2 \mathbf{U} = \frac{1}{c^2} \frac{\partial^2 \mathbf{U}}{\partial t^2} \quad (2.8)$$

where we define  $\mathbf{U}$  to satisfy the following relationships with  $\mathbf{A}$  (The magnetic vector potential) and  $\Phi$  (The electric scalar potential)

$$\Phi = -\frac{1}{\epsilon} \nabla \cdot \mathbf{U} \quad (2.9)$$

$$\mathbf{A} = \mu \frac{\partial \mathbf{U}}{\partial t} \quad (2.10)$$

$$\mathbf{B} = \nabla \times \mathbf{A} \quad (2.11)$$

$$\mathbf{E} = -\mu \frac{\partial \mathbf{A}}{\partial t} - \nabla \Phi \quad (2.12)$$

from which the electric and magnetic fields can be recovered in terms of  $\mathbf{U}$  by combining Equations 2.9–2.12

$$\mathbf{E} = -\mu \frac{\partial^2 \mathbf{U}}{\partial t^2} + \frac{1}{\epsilon} \nabla (\nabla \cdot \mathbf{U}) \quad (2.13)$$

$$\mathbf{B} = \mu \frac{\partial}{\partial t} (\nabla \times \mathbf{U}) \quad (2.14)$$

We introduce a Hertzian dipole at the origin aligned with the  $z$ -axis (vertical) with an electric dipole moment  $M = ql$  in free space. Then, at a distant point  $r$  and time  $t$ ,  $\mathbf{U}$  becomes

$$U_x = U_y = 0; \quad U_z = \frac{M}{4\pi r} \quad (2.15)$$

when the current is harmonically time varying with frequency  $\omega$ ,  $U_z$  becomes

$$U_z = \frac{M_0 \exp(j\omega t) \exp(-jkr)}{4\pi r} \quad (2.16)$$

which is compact, but unfortunately not conducive for direct calculation of how fields traverse a waveguide. Instead, Budden takes a different approach as he first shows that the Hertzian dipole is equivalent to an infinite set of line quadrapole sources parallel to the  $y$ -axis. The fields radiated from a single quadrapole line source elevated at  $z = z_1$  is given

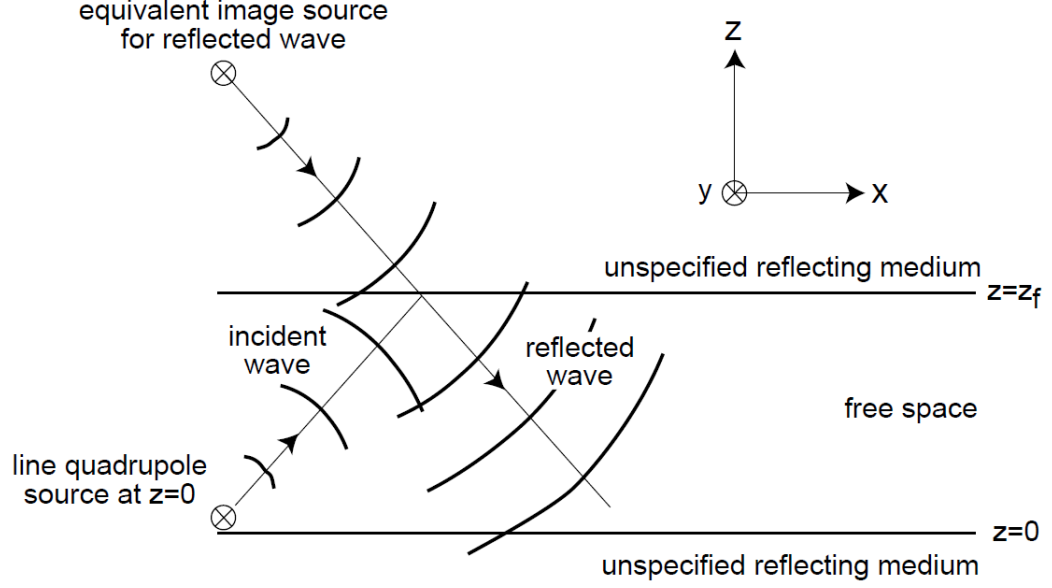


Figure 2.7: Illustration of the equivalent source model used by Budden's formulation, fully described in *Budden* [1962]. Figure adapted from *Cummer* [1997].

with strength  $Q_1$  is given by

$$U = \left( \frac{kQ_1}{4\pi} \right) \int_C \exp \{ -jk(x \cos \theta + |z - z_1| \sin \theta) \} \cos \theta d\theta \quad (2.17)$$

When we then take the location of the bottom reflector to be  $z = 0$  and the top reflector to be at  $z = z_f$ , the equivalent system can be described as line quadrupole image sources placed at  $z = 2Kz_f$ , where  $K = -\infty, \dots, \infty$ . Graphically, this situation is shown a source at the origin, and at  $2z_f$  in Figure 2.7. For Budden's derivation, we assume that the bottom reflector is located at  $z = \alpha$  and the top reflector is located at  $z = \beta$ .

The infinite series can be summed to

$$\begin{bmatrix} U_z \\ \sim \end{bmatrix} = \left( \frac{Q_1 k}{4\pi} \right) \int_C \exp(-jkx \cos \theta) \exp \{ -jk(z - z_1) \sin \theta \} (\mathbf{I} + \mathbf{R}_u) \mathbf{W} (\mathbf{I} + \bar{\mathbf{R}}_l) d\theta \quad (2.18)$$

where  $\sim$  indicates it is not used here and

$$\bar{\mathbf{R}}_l = \bar{\mathbf{R}}_\alpha \exp\{2jk(\alpha - z_1) \sin \theta\} \quad (2.19)$$

$$\mathbf{R}_u = \mathbf{R}_\beta \exp\{-2jk(\beta - z_1) \sin \theta\} \quad (2.20)$$

$$\mathbf{W} = [\mathbf{I} - \bar{\mathbf{R}}_l \mathbf{R}_u \exp\{2jk(z - z_1) \sin \theta\}]^{-1} \quad (2.21)$$

the integral in Equation 2.18 can be solved by extending the integration to the complex plane, where the most important singularities are located within  $\mathbf{W}$  at

$$\det[\mathbf{I} - \bar{\mathbf{R}}_l \mathbf{R}_u \exp\{-2jk(z - z_1) \sin \theta\}] = 0 \quad (2.22)$$

which is the mode condition. For now, we assume the transmitter and receiver are at the same altitude ( $z - z_1 = 0$ ) causing the exponential term to become unity (the effect of different altitude receiver and transmitters will be taken care of with height gain functions included in a correction factor to the excitation factors discussed in a subsequent section). In addition, the mode condition is true regardless of the thickness of the waveguide, so we allow  $\beta - \alpha$  to tend to zero, reducing the mode condition to

$$\det[\mathbf{I} - \bar{\mathbf{R}}_l \mathbf{R}_u] = 0 \quad (2.23)$$

the contribution of each mode to the total field in Equation 2.18 can be found by evaluating

$$\begin{bmatrix} \Lambda_n \\ \sim \end{bmatrix} = \frac{\frac{1}{2}jkQ_1 \exp(-jkx \cos \theta_n)(\mathbf{I} + \mathbf{R}_{un})\mathbf{Y}_n(\mathbf{I} + \bar{\mathbf{R}}_{ln})}{\left. \frac{\partial \Delta}{\partial(\sin \theta)} \right|_{\theta=\theta_n}} \quad (2.24)$$

where  $\Delta = \det[\mathbf{W}^{-1}]$  and  $\mathbf{Y} = \lim_{\theta \rightarrow \theta_n} \mathbf{W}\Delta$ .  $\Lambda_n$  is known as an ‘excitation factor’ for a given mode.

It should be noted that this derivation is complete for a vertical dipole source and receiver located at the same altitude in a horizontally homogeneous waveguide. The generalization of the source, receiver, and horizontally varying ionosphere is accomplished in steps by LWPC and is elaborated on in the following sections.

### *Reflection Coefficients of the EIWG*

In the EIWG, the real upper and lower boundaries are not perfect conductors. The Earth ground has a finite conductivity  $\sigma$  and permittivity  $\epsilon$  which varies depending on soil composition [Morgan, 1968a,b]. Furthermore, the upper boundary of the  $D$  region of the ionosphere is an anisotropic and inhomogeneous plasma with complex permittivity whose properties in general are a function of altitude and location. Because of the anisotropic nature of the lower ionosphere caused by the Earth's background magnetic field, the modes propagating in the EIWG couple together at the boundary, so they are often referred to as quasi modes or QTE, QTM, and QTEM modes. A convenient formulation to characterize the effects of such a system on an incident wave are the so-called reflection matrices

$$\mathbf{R}_u(\theta) = \begin{bmatrix} {}_{\parallel}R_{\parallel}(\theta) & {}_{\parallel}R_{\perp}(\theta) \\ {}_{\perp}R_{\parallel}(\theta) & {}_{\perp}R_{\perp}(\theta) \end{bmatrix} \quad \bar{\mathbf{R}}_l(\theta) = \begin{bmatrix} {}_{\parallel}\bar{R}_{\parallel}(\theta) & 0 \\ 0 & {}_{\perp}\bar{R}_{\perp}(\theta) \end{bmatrix} \quad (2.25)$$

where  $u$  and  $l$  represent the upper and lower reflection matrices corresponding to the lower ionosphere and the Earth ground. The subscript before each coefficient corresponds to the polarization before reflection, and the subscript afterwards is the new polarization. The anisotropic coupling modes is the result of the non-diagonal coefficients of  $\mathbf{R}_u(\theta)$ . The reflection coefficients can be used for a traditional ray-hop analysis of propagation or for modal propagation where  $\theta$  is replaced by  $\theta_m$  where  $m$  refers to the generally complex eigenangle corresponding to the mode solution [Budden, 1955a,b].

### *Solution for Waveguide Modes in the EIWG*

Before solving for the waveguide modes, the user must specify the waveguide parameters for a transmitter-to-receiver path. First, the path is divided into segments where the waveguide parameters are then held piecewise constant to account for shifting conditions such as the day to night transition. The ground parameters are specified as a complex permittivity  $\epsilon' = \epsilon_0\epsilon_r - j\frac{\sigma}{\omega}$ . The user can specify arbitrary ionosphere parameter profiles vs. altitude, namely: the electron density ( $N_e$ ), ion density (positive and negative,  $N_i$ ), electron-neutral collision frequency, electron-ion collision frequency. In addition, the user can specify the



charge and mass of the positive and negative ions. The user can also specify the magnetic field background strength, dip angle, and azimuthal bearing to the propagated field.

Earth's curvature is considered by a modified index of refraction

$$n^2 = 1 - \frac{2}{r_e}(H - z) \quad (2.26)$$

where  $n$  is the refractive index,  $r_e$  is the radius of the Earth, and  $H$  is a reference altitude, just below the base of the ionosphere. We can rewrite the mode condition of Equation 2.23 in terms of the reflection coefficients as

$$F_1(\theta) = \det[1 - \bar{\mathbf{R}}_l(\theta)\mathbf{R}_u(\theta)] = 0 \quad (2.27)$$

where  $\theta$  is in general complex. LWPC assumes a discrete number of modes can represent the bulk of the propagating wave and solves for each mode solution in each slab. To perform this, LWPC includes a built-in mode finding routine in the LWPM program whose functional description is essentially that of MODESRCH described in *Morfitt and Shellman* [1976]. However, MODESRCH solves a related problem

$$F(\theta) = (\|n_{\parallel} -_{\parallel} \bar{X}_{\parallel} \|d_{\parallel})(_{\perp} n_{\perp} -_{\perp} \bar{X}_{\perp} _{\perp} d_{\perp}) -_{\parallel} \bar{X}_{\perp} _{\perp} \bar{X}_{\parallel} \|d_{\parallel} \|d_{\perp} \quad (2.28)$$

where,

$$\bar{\mathbf{X}} = (\mathbf{R} + \mathbf{I})/C \quad (2.29)$$

$$C = \cos(\theta) \quad (2.30)$$

$$\mathbf{n} \mathbf{d}^{-1} = (\bar{\mathbf{R}}^{-1} + \mathbf{I})/C \quad (2.31)$$

and  $\mathbf{I}$  is the identity matrix. The problem substitution is important since the zeros are still the same, but no poles exist, simplifying the solution procedure. Next, we need to solve for the modified reflection coefficients for both boundaries for arbitrary  $\theta$ . The reflection coefficient of the Earth-ground is relatively straightforward and are given by the solutions

to Stokes' equation, where  $h_1$ ,  $h_2$  and are modified Hankel functions of order  $\frac{1}{3}$  [*of the Computation Laboratory at Cambridge, Mass, 1945*] with the full solutions given by *Pappert et al.* [1967].

$$\frac{d^2 h_{1,2}}{dz^2} + zh_{1,2} = 0 \quad (2.32)$$

Unfortunately for an anisotropic, inhomogeneous ionosphere, no analytical solution generally exists for the reflection coefficients and the problem becomes a fourth order differential equation known as the 'Booker Quartic' [Unz, 1966]. LWPC solves the reflection matrix using a Range-Kutta technique fully described in [Budden, 1955a]. The initial guess is determined by assuming a sharply bounded homogeneous ionosphere with constant electron density, then determining the reflection coefficient at the top [Sheddy, 1968]. The solution is then integrated to a sufficiently low height, such that the ionospheric effects are negligible, i.e. propagation is the same as free space. We are now prepared to find the mode solutions.  $F$  can be written as

$$F(\theta) = F_R(\theta_r, \theta_i) + jF_I(\theta_r, \theta_i) \quad (2.33)$$

where,

$$\theta = \theta_r + j\theta_i \quad (2.34)$$

also,

$$F(\theta) = [F_R(\theta_r, \theta_i)^2 + jF_I(\theta_r, \theta_i)^2]^{1/2} e^{j\phi} \quad (2.35)$$

where,

$$\phi = \tan^{-1} \left( \frac{F_I(\theta_r, \theta_i)}{F_R(\theta_r, \theta_i)} \right) \quad (2.36)$$

Since  $F(\theta)$  has no poles, lines of constant phase  $\phi = \phi_{cn}$  radiating from a zero of  $F(\theta)$  must cross a closed contour at least once. In addition, the phase line will not intersect any other zero. This is demonstrated in Figure 2.8.

These facts are the key which allow an iterative procedure to locate the zeros of  $F(\theta)$  numerically by tracing the lines of constant phase back to the contour or to a zero. Specifically, at values of  $\phi_c = 0^\circ, 180^\circ$  then  $F_I(\theta_r, \theta_i) = 0$  and when  $\phi_c = 90^\circ, 270^\circ$  then  $F_R(\theta_r, \theta_i) = 0$ .

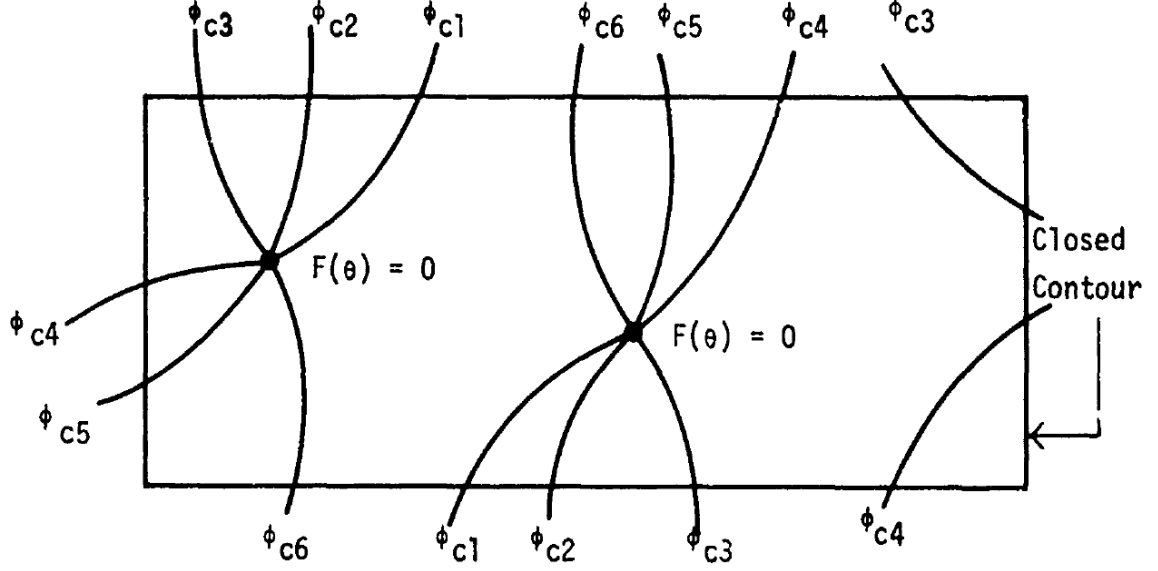


Figure 2.8: Illustration of constant phase lines from zeros of  $F(\theta)$ . Adapted from *Morfitt and Shellman* [1976].

Therefore, by systematically looking for numerical sign changes, it may be possible to locate convenient lines of constant phase. MODESRCH then performs the following procedure:

1. A mesh grid is established by an expected zero spacing.
2. Progressing in a counterclockwise manner, the convenient lines of phase are located by a sign change in the real component  $F(\theta)$ .
3. The line of constant phase is then traced until it exits the closed contour.
4. For each mesh along the phase line, a check for a zero of  $F(\theta)$  occurs and its location is approximately determined by a hyperbolic assumption.
5. These steps are repeated for the entire mesh grid bounded by the contour.
6. More exact solutions are determined by using a preset adjustment  $\Delta\theta$  to the zeros  $\theta_0$  Newton-Raphson iteration method in Equation 2.37.

$$\Delta\theta = -\frac{F(\theta_0) \delta\theta}{F(\theta_0 + \delta\theta) - F(\theta_0)} \quad (2.37)$$

With the eigenangles of the mode solutions determined, it is now simple to determine some important mode constants, namely the attenuation rate and phase velocity described

in Table 2.1

Table 2.1: Important mode constant formulas	
Mode Constant	Equation
Attenuation Rate, $\alpha$ (dB/Mm)	$-8686 k \text{Im}(\sin \theta')$
Phase Velocity $v/c$	$1/\text{Re}(\sin(\theta'))$

where  $k$  is the wavenumber  $c$  is the speed of light, and  $\theta'$  is the eigenangle of a given mode referenced to ground. Now that mode solutions are determined in each slab, LWPC calculates the excitation factors and height gain functions to be able to solve for arbitrary propagation schemes.

### 2.3.3 Excitation Factors and Height Gain Functions

The mode-finding algorithm implemented by MODESRCH finds the complex eigenangles for arbitrary EIWG specifications but says nothing about how well an arbitrary source can launch waves into the system. This functionality is implemented by the calculation of excitation factors [Pappert and Bickel, 1970] representing the efficiency of wave energy coupling into the waveguide in a particular mode and height gain functions [Pappert, 1970], describing the effect of altitude of a transmitter or receiver on observed waves.  $B_\phi$  can be simulated by normal LWPC process; however, as of LWPC 2.0, native calculation of  $B_r$  is not available. The calculation of the new parameter is assisted by the derivation of the receiver excitation factor  $\Lambda_R$  for the  $B_r$  component by Maxwell's (with invariant  $y$ )  $f_{bx} = \frac{1}{j\omega} \frac{\partial E_y}{\partial z}$ , where everything is a constant with respect to  $z$  except for the height gain function  $f_{ey}$ , therefore we get

$$f_{bx} = \frac{1}{j\omega} \frac{\partial f_{ey}}{\partial z} \quad (2.38)$$

where  $z_r$  is the altitude of the receiver,  $r_e$  is the radius of the Earth,  $k$  is the wavenumber,  $d$  is the integration reference point.

The height gain functions given in Table 2.2 are consistent with Pappert and Ferguson [1986] without the normalization constants since LWPC does not use them. In addition,  $F_m, 1...4$ ,  $h_p, 1...2$ , and  $q$  are also as defined by Pappert and Ferguson [1986]. In this work,

Table 2.2: Height gain functions and receiver excitation factors for five output field components

Component	Height Gain Functions ( $g$ )	Receiver Excitation Factors ( $\Lambda_r$ )
$B_\phi$	$g_{b\phi} = e^{z/r_e} (F_1 h_1(q) + F_2 h_2(q))$	$g_{b\phi}(z_r)$
$B_r$	$g_{br} = \frac{2f}{r_e} (F_3 h_1'(q) + F_4 h_2'(q))$	$f\left(\frac{g_{b\phi}(d)}{g_{e\phi}(d)}\right) g_{br}(z_r)$
$E_\phi$	$g_{e\phi} = f(F_3 h_1(q) + F_4 h_2(q))$	$f\left(\frac{g_{b\phi}(d)}{g_{e\phi}(d)}\right) g_{e\phi}(z_r)$
$E_r$	$g_{er} = -\frac{1}{jk} \frac{\partial g_{b\phi}}{\partial z}$	$-g_{er}(z_r)$
$E_z$	$g_{ez} = -\sin(\theta_n) g_{b\phi}$	$g_{ez}(z_r)$

we use an electric dipole as a source at an angle  $\psi$  to the  $x$ -axis (propagation direction), and an angle  $\gamma$  to the  $z$ -axis (vertical direction). A convenient formulation is given by *Cummer* [1997, Section 2.4.3] (See also *Pappert and Bickel* [1970])

$$\Lambda_{tn} = -A \sin(\theta_n) \cos(\gamma) g_{b\phi}(z_t) + B \sin(\gamma) \cos(\psi) g_{e\phi}(z_t) + A \sin(\gamma) \sin(\psi) g_{er}(z_t) \quad (2.39)$$

with

$$A = \frac{\sin^{1/2}(\theta_n) (1 + \|\bar{R}_\parallel\|)^2 (1 - \|\bar{R}_\perp\| \|\bar{R}_\perp\|)}{\|\bar{R}_\parallel\| \frac{\partial \Delta}{\partial (\sin \theta)} \Big|_{\theta=\theta_n} g_{b\phi}^2(d)} \quad (2.40)$$

$$B = \frac{\sin^{1/2}(\theta_n) (1 + \|\bar{R}_\parallel\|) (1 + \|\bar{R}_\perp\| \|\bar{R}_\perp\|)}{\frac{\partial \Delta}{\partial (\sin \theta)} \Big|_{\theta=\theta_n} g_{b\phi}(d) g_{e\phi}(d)} \quad (2.41)$$

#### 2.3.4 Mode Conversion and Sum

With determined mode solutions for a specified ionosphere, it is now possible to calculate the fields for an arbitrary source-to-receiver geometry within a horizontally homogenous waveguide section given as a convenient expression by *Cummer* [1997, Section 2.4.3]:

$$\Gamma = P(\Gamma) \frac{jk^{(3/2)} Il}{\sqrt{8\pi r}} \exp\left(\frac{j\pi}{4}\right) \sum_n \Lambda_{tn} \Lambda_{rn} \exp(-jkx \sin \theta_n) \quad (2.42)$$

where  $P(\Gamma) = \mu_0$  for components of  $\mathbf{B}$ , and  $P(\Gamma) = \sqrt{\mu_0/\epsilon_0}$  for components of  $\mathbf{E}$ .

We have discussed how LWPC calculates the mode solution for arbitrarily specified horizontally homogeneous waveguides, but, the real EIWG system commonly varies over

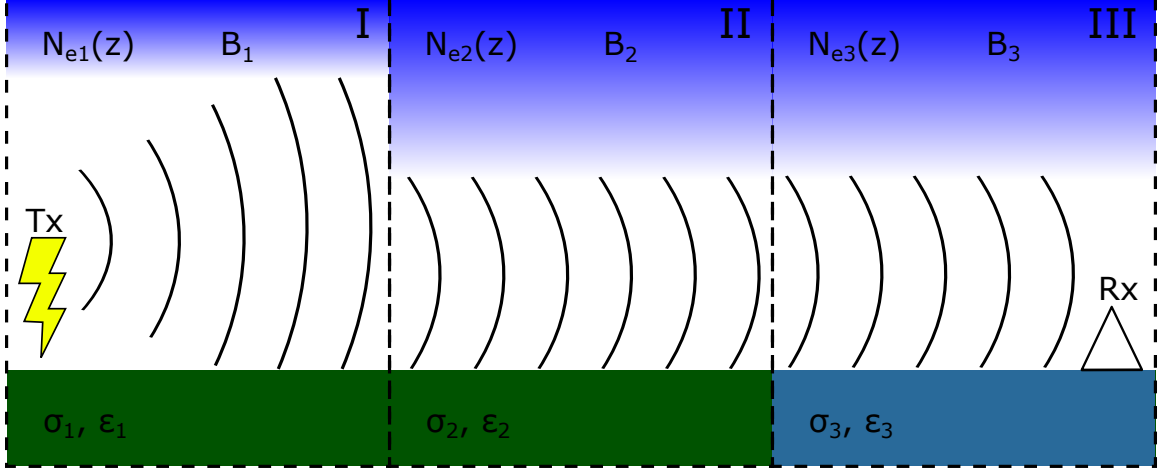


Figure 2.9: An illustration of the slab model of the EIWG with horizontally homogeneous slabs.

a path. *Crombie* [1964] suggested that this horizontal inhomogeneity would lead to mode conversion at the boundary and suggested that phase variations on a path from nighttime to daytime could be explained by two dominant modes converting into a single mode on the daytime side. Other types of discontinuities can exist due to terrain differences such as a land/ocean boundary or an elevated bottom boundary in the case of a mountain range for instance.

In general, incident waves at a waveguide discontinuity will cause waves to couple into the next waveguide slab also known as ‘forward scattering,’ it will also cause some backward reflection known as backscattering. For example, as in Figure 2.9, waves are transmitted in slab I and are incident at a boundary between I/II. Therefore, at the boundary the total fields exist as a summation of forward and back scattered waves:

$$\vec{\mathbf{e}}_j^{\text{I}}(z) + \sum_m \mathcal{A}_{mj} \overleftarrow{\mathbf{e}}_m^{\text{I}}(z) = \sum_n \mathcal{B}_{nj} \vec{\mathbf{e}}_n^{\text{II}}(z) + \sum_l \mathcal{C}_{lj} \overleftarrow{\mathbf{e}}_l^{\text{II}}(z) \quad (2.43)$$

where  $\mathbf{e}$  is a vector containing the fields, a forward arrow indicates the wave is a forward propagating wave, and a backwards arrow indicates a backscattered wave. Importantly, LWPC assumes only forward scattering which is termed ‘mode conversion’. This assumption is not in generally true (e.g. *Dowden et al.* [1996]) in the EIWG at VLF/LF frequencies

but is justified in certain cases (e.g. *Pappert et al.* [1971]). This can be represented as:

$$\vec{\mathbf{e}}_j^{\text{I}}(z) = \sum_n \mathcal{B}_{nj} \vec{\mathbf{e}}_n^{\text{II}}(z) \quad (2.44)$$

where  $\mathcal{A}$ ,  $\mathcal{B}$ , and  $\mathcal{C}$  are the mode conversion coefficients for the respective fields for all considered modes and where the solution is independent of position in the slab I or II. At an arbitrary waveguide boundary  $y$ - $z$  plane, it is possible to define two sets of orthogonal height gain functions related to the height gain functions given in Equation 2.2 as

$$\mathbf{F}_i^p(z) = \begin{bmatrix} f_{ey,i}^p(z) \\ f_{ez,i}^p(z) \\ f_{by,i}^p(z) \\ f_{bz,i}^p(z) \end{bmatrix} \quad \mathbf{G}_i^p(z) = \begin{bmatrix} g_{ey,i}^p(z) \\ g_{ez,i}^p(z) \\ g_{by,i}^p(z) \\ g_{bz,i}^p(z) \end{bmatrix} \quad (2.45)$$

so that the inner product,

$$\langle \mathbf{F}_i^p, \mathbf{G}_m^p \rangle = \int_{-\infty}^{+\infty} (\mathbf{F}_i^p)^H \mathbf{G}_m^p dz = \delta_{im}, \quad \delta_{im} \begin{cases} 1, & \text{if } i = m \\ 0, & \text{otherwise} \end{cases} \quad (2.46)$$

where  $H$  is the conjugate transpose operator. Because of the orthogonality condition, it is possible to determine the mode conversion coefficients  $a_{im}^p$  for the  $p$ th slab in terms of the  $(p-1)$ th slab.

$$\begin{aligned} a_{im}^p &= I_{i,m}^{p,p-1} \\ &= \sum_l a_{lm}^{p-1} \exp[-jk \sin \theta_l^{p-1} (x_p - x_{p-1})] I_{l,m}^{p,p-1} \end{aligned} \quad (2.47)$$

where  $a_{ik}^p$  describes the conversion of mode  $m$  to  $i$  and the mode coupling integral

$$I_{l,m}^{p,p-1} = \int_{-\infty}^{+\infty} (\mathbf{F}_l^p)^H \mathbf{G}_m^{p-1} dz \quad (2.48)$$

where  $\mathbf{F}$  and  $\mathbf{G}$  are solved by full wave methods in the case of FULLMC [*Pappert and Snyder*, 1972]. An alternative program has been developed, known as FASTMC [*Pappert and*

*Morfitt, 1975; Ferguson and Snyder, 1980*] which does not use orthogonality but instead approximates the solution by only integrating from the ground to the bottom of the ionosphere and replaces the functions  $\mathbf{F}$  and  $\mathbf{G}$  with Airy functions. These functions have the advantage of being easily solved analytically and an extensive validation has shown good agreement between the two models [*Pappert and Ferguson, 1986*].

LWPC implements both solutions, defaulting to FASTMC. The documentation of LWPC 2.0 suggests that FASTMC may not always be a stable solution [*Ferguson, 1998*], and that inspection of the solution is the best way to determine if the output is reasonable. With the massive set of simulations performed in this work, we use FASTMC and accept possible perturbations in solutions to add to the noise, although we do not expect it be a significant factor.

### 2.3.5 LWPC Simplifications

LWPC takes many real effects into account in order to model VLF propagation in the EIWG, nonetheless it does not natively consider every possible effect. Therefore, for the sake of completeness we will reiterate some limitations already covered and note a few more.

First, LWPC is modeled by a series of slabs where waveguide parameters are horizontally homogeneous. However, the slab size is discrete and necessarily an approximation to a real situation where the parameters are changing in a continuous manner. This is potentially more serious if either surface is ‘rough’ and acts more like a diffuse reflector than a specular one. This potential impact is being investigated at higher frequencies and may not have a serious impact at VLF [*Higginson-Rollins and Cohen, 2017*].

LWPC uses a mode conversion technique to calculate how wave energy from a mode structure in one slab couples into the next. LWPC neglects possible modes resulting from backscatter at a discontinuity, which may perturb the forward solution if the backscatter is significant enough. Furthermore, while LWPC uses the mode conversion techniques discussed in Section 2.3.4, it uses a higher-level wrapper procedure. It groups similar slabs and extrapolates an initial guess for the mode solutions using up to three slab solutions and iterates to a solution using a Newton-Raphson technique to adjust for varying geomagnetic field effects. If the integration is too large, or it results in invalid modes, then a solution is



found by starting back at the FULLMC or FASTMC choice. Furthermore, the stratification within waveguide segments is necessarily discretized as an approximation to the real continuous condition.

Although not a limitation of LWPC, an inverse modeling approach is typically limited by the non-uniqueness of a solution in addition to the number of free parameters. We use built-in values for many free parameters such as the collision frequency profile, ion species, and ground conductivity parameters. While the choice of these parameters in the design of LWPC was validated for many cases, they may not be exhaustively correct and therefore they must approximate the real case.

Despite the approximations used in LWPC, it has been well validated, and is capable of matching diverse measurements [Cummer *et al.*, 1998; Thomson and Clilverd, 2001; Lay *et al.*, 2015], therefore we accept the approximations made here. Importantly, we seek to extend the standard Wait and Spies ionospheric model to achieve a solution motivated by rocket-based ionospheric modeled profiles (See the discussion in Section 4.2).

For close ranges ( $< 50$  km) and lower frequencies ( $< 500$  Hz), FDTD will outperform mode theory because of the evanescent fields and post-discharge ionospheric currents which are not possible to model natively in LWPC. To achieve accurate numerical results with FDTD, the grid spacing must be small. The source-to-receiver paths used in this work are as long as 10.1 Mm, and we use higher frequencies than considered in the stability and timing analysis of Cummer [2000], increasing computational demand in squared sense. Therefore, we use mode theory through LWPC to simulate spheric propagation. We restrict source-to-receiver analysis to  $> 100$  km to avoid near-field and post-discharge effects. We also restrict frequencies to  $> 4$  kHz to avoid the aforementioned problems, as well as the high attenuation from  $\sim 1$ -4 kHz resulting from EIWG propagation [Barr, 1970a,b, 1971a,b]. Furthermore, most of the ELF energy is generated by continuing current which is much more unpredictable than the main portion of the return stroke which predominantly radiates VLF/LF energy.

## CHAPTER 3

### EXPERIMENTAL SETUP AND DATA PROCESSING

#### 3.1 Lightning Variability

Each lightning flash is a unique event generating highly variable and broad spectral radio frequency (RF) emissions. This is in direct contrast to narrowband VLF communications which strive for stable communication channels and constant power making them useful for ionospheric remote sensing. Since we seek to use lightning sferics to probe the  $D$  region, we must find some way to normalize the variations in lightning. Two aspects of the lightning flash dominate the uncertainty that affects this work: (1) the lightning channel properties and (2) the return stroke current.

The uniqueness of each lightning flash starts from the fact that the lightning leader may originate from many possible heights in the cloud. Negative and positive lightning flashes start from different parts of the cloud because of the charge separation which creates distinct charge regions [Macgorman and Rust, 1998]. The exact structure of the cloud varies and is influenced by geographical and seasonal effects. For example, the base of thunderclouds in Japan during the winter are much closer to the ground at  $\sim 2$  km, whereas the typical cloud base of summertime thunderclouds in Florida, USA are between 6 and 8 km.

The lightning leader develops in pseudo-random branches and terminates in various locations. Most lightning flashes take place entirely inside the cloud and are known as intra-cloud or IC flashes [Rakov and Uman, 2003]. However, many flashes terminate into the neutral air, in another thundercloud, or even upward in the  $D$  region (a phenomenon known as a gigantic jets). The lightning flashes used in this work are cloud-to-ground or CG flashes and they typically make up around 10% of lightning flashes. The pseudo-random steps taken by a negative CG lightning leader create a jagged pattern generally trending toward the ground. The variation of the lightning channel from a vertical is known as tortuosity and impacts radiated fields [Carvalho *et al.*, 2017]. A cartoon depicting a negative branch CG leader and a positive is shown in Figure 1.3.

Each lightning channel varies significantly in height and shape due to the cloud structure and tortuosity as mentioned, but also due to whether the CG stroke lowers positive or negative charge (+/- CG stroke). Positive and negative leaders develop significantly differently, and the dominant effect is that positive lightning channels tend to have much lower tortuosity, appearing to propagate without stepping, and are nearly vertical.

Once a lightning channel to ground is established the initial return stroke occurs, partially neutralizing the cloud. However, in  $\sim 80\%$  of CG lightning flashes, particularly negative flashes, one or more subsequent strokes occur with a mean occurrence of 3–5 strokes per flash with some geographical dependence [Rakov and Uman, 2003, Table 1.1] [Cooray and Jayaratne, 1994; Cooray and Pérez, 1994; Rakov and Uman, 1990]. The subsequent strokes mostly follow the original channel and start off with a dart leader instead of a stepped leader. The speed of stepped leaders is much slower than dart leaders, both of which are substantially slower than the speed of light. However, the return stroke is much closer to the speed of light.

The natural variations of lightning, while significant on an individual sferic basis and important for study of lightning features, are a source of considerable uncertainty in this work. To address this, we will implement a sferic stochastic normalization technique to produce a more stable sferic, via proper averaging and processing. In subsequent sections in this chapter, we describe a technique to remove the variations in lightning characteristics and arrive at a sferic independent of source characteristics (See also *McCormick et al.* [2018]).

### 3.2 Broadband Radio Receiver

The data used in this work is VLF/LF ( $\sim 0.5\text{--}470$  kHz) magnetic field data sampled by AWESOME LF receivers [Cohen et al., 2018b]. A diagram and corresponding pictures are shown in Figures 3.1 and 3.2. Two wire loops are mounted in the North/South and East/West directions to capture both horizontal magnetic field components (1). The raw signal is fed into the preamplifier box (2) which is then amplified by a matched differential VLF/LF amplifier. The preamplifier box and antenna are physically isolated from the rest

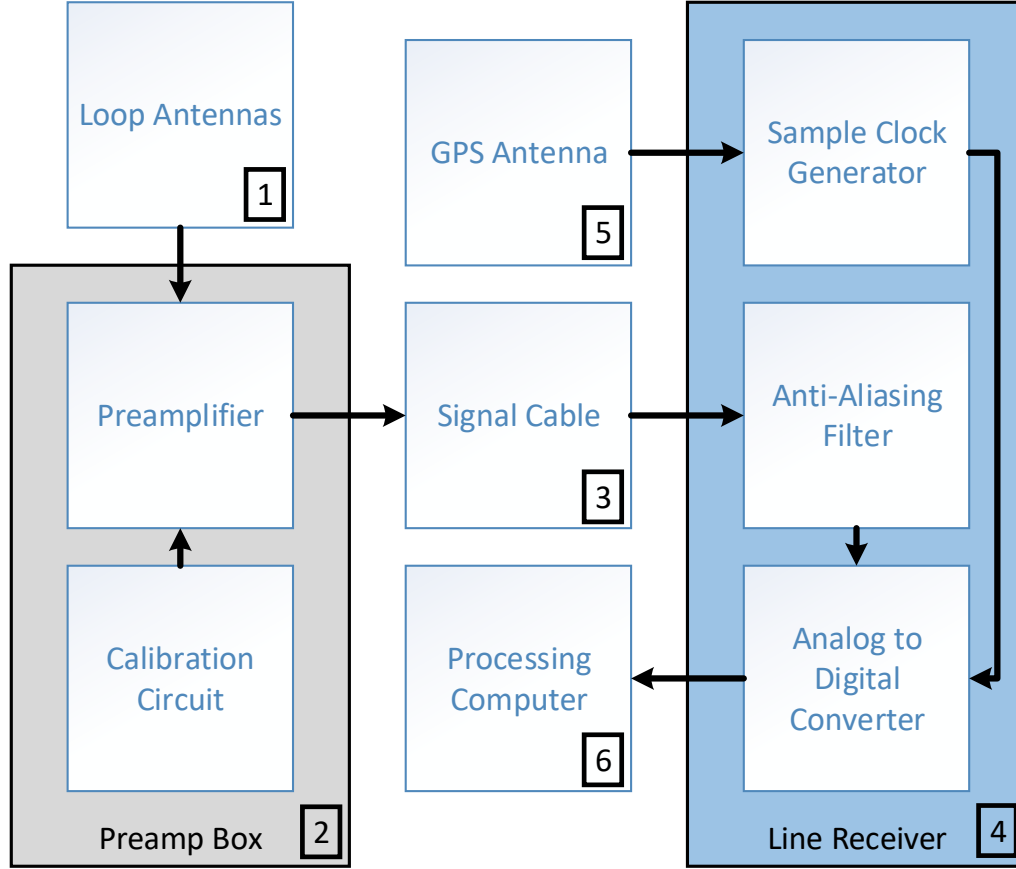


Figure 3.1: Block diagram of the LF AWESOME receiver. The numbers correspond to the numbers in the pictures (Figure 3.2).

of the system by a low noise signal cable (3) up to 2000 ft away. The signal cable connects to the line receiver (4) which is first low pass filtered by an anti-aliasing filter with 470 kHz cutoff frequency to prevent aliasing. A sampling signal is generated at 1 MHz using a control loop and a 1 pulse per second GPS reference obtained by an external GPS antenna (5) for an absolute accuracy of less than 20 ns for each sample. The 1 MHz signal is then downsampled to 100 kHz, as we are interested in this work only in the spectral band from 1-45 kHz. The sampling signal is used by a NI-DAQ USB-6356 to digitize the data with 16-bit resolution and sensitivity of 0.03–0.1 fT/rt-Hz, depending on the size of the antenna. Lastly, the data is stored on a local PC (6) and transferred to a central database.

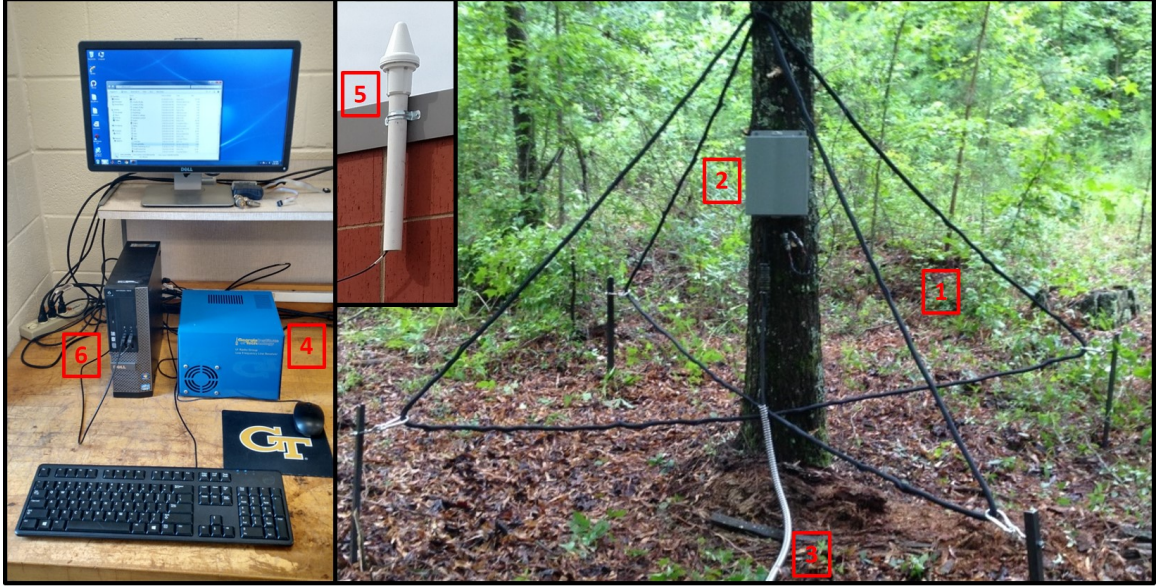


Figure 3.2: Components of receiver in pictures. The numbers correspond to the numbers in the block diagram (Figure 3.1).

### 3.2.1 Receiver Data and Network

The broadband data record contains some features we will aim to remove. A portion of example data highlighting some of the common signals at the Burden receiver is shown in Figure 3.3. Naval transmitters are observed as narrowband minimum shift keyed (MSK) communication signals. Russia also operates three keyed transmitters known as Alpha transmitters, though they are usually received in the eastern US with low SNR, if at all. The information of the relevant narrowband signals to this work are given in Table 3.2. Figure 3.3a shows two VLF transmitters NAA and NLK and the MSK communication bit encoding can be easily observed in the data. Figure 3.3b shows the effects of non-ideal power generation in the form of many harmonics of the fundamental power line frequency. Typically, the lowest frequency portion of the spectrum is dominated by power line noise (50 or 60 Hz) and their harmonics visible up to 10 kHz or greater depending on the noise environment at a given site for a given time period.

These signals can be viewed as noise for the signals of interest in this work, lightning sferics. These are dominant in most of the data records and can be easily observed in the example data of Figure 3.4b as vertical streaks (narrow in time, broad in frequency). In

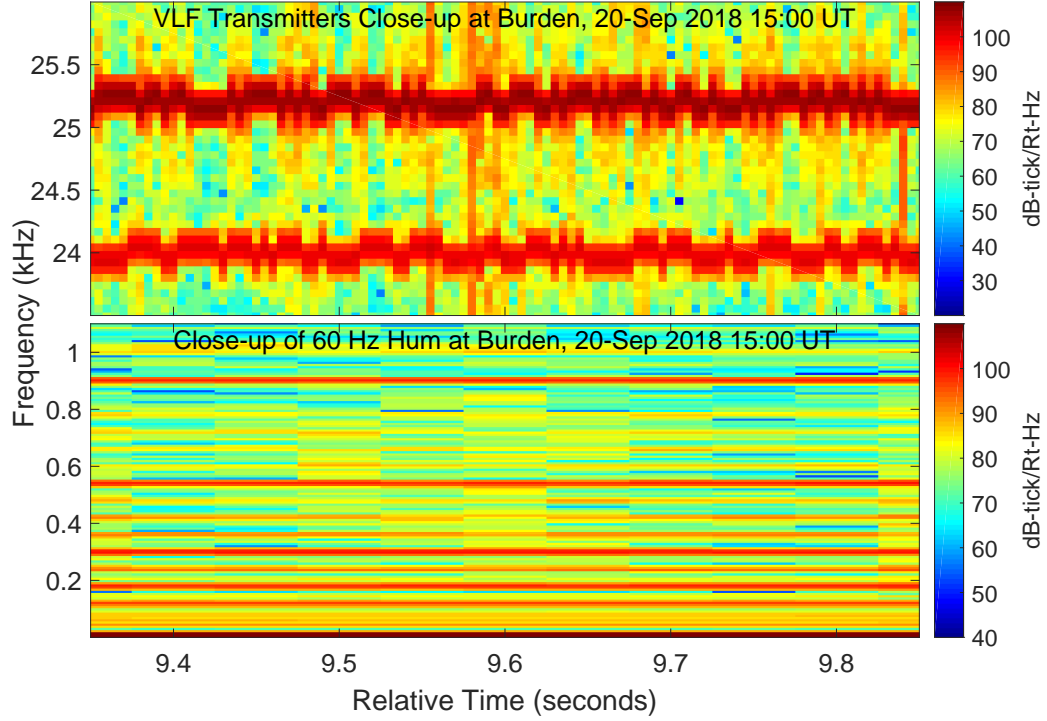


Figure 3.3: Example spectrogram from data sampled from the receiver at Burden, KS, USA (described in Table 3.1). The spectrogram is sampled with 10 ms windows and 5 ms overlap. The data is a 10 second snippet sampled at 1 MHz starting at 20-Sep-2018, 20:15:00 UT.

addition to these common features are a myriad of effects, both manmade and natural. A given set of features observed are highly dependent on the given receiver location and make up the noise environment. The receivers in this work were strategically located to minimize the total noise in the VLF/LF RF spectral band as much as possible.

The importance of site selection and its associated noise environment can be highlighted by a simple example. Figure 3.4a shows a spectrogram on the roof of the Van-Leer building at Georgia Tech, Atlanta. In contrast, Burden, a very quiet site in Burden, Kansas is shown in Figure 3.4b. Both sites have the same size antenna and system settings, so the difference in noise is due to the differences between the natural and manmade electromagnetic noise in the city of Atlanta, vs. Burden and the different propagation conditions for the received coherent signals.

All the data in this work was recorded during July and August of 2017. Not all the receivers were continuously operating during the entire date range with some being installed during these months. The general availability of broadband during the data range is shown



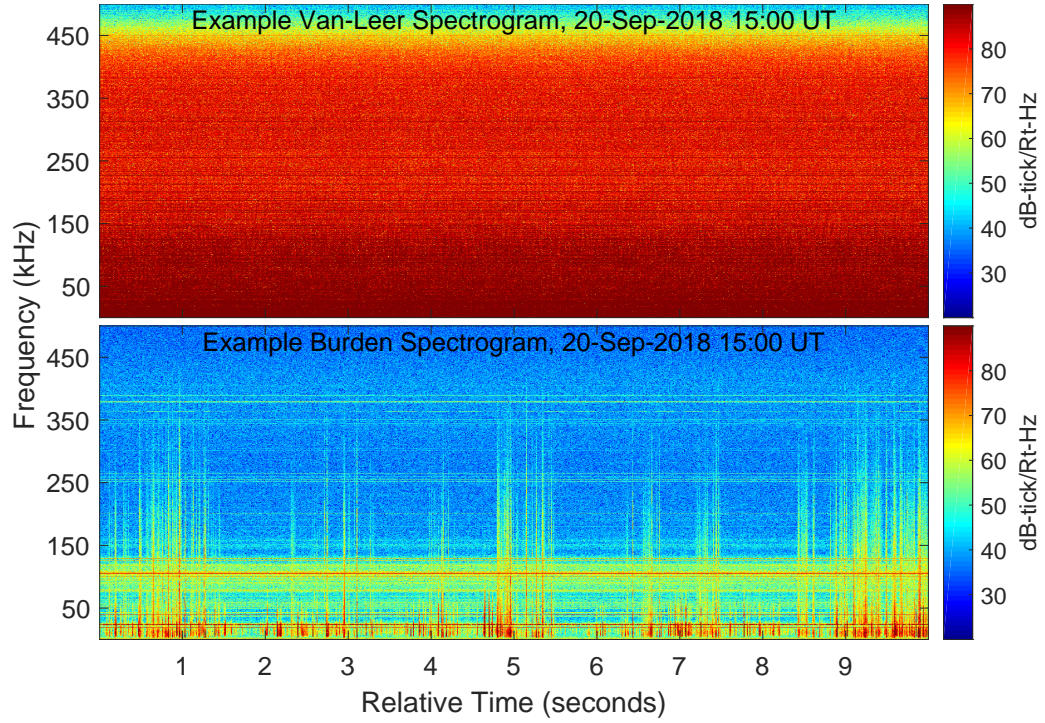


Figure 3.4: Example spectrograms from data sampled simultaneously from the receiver on the roof of Van-Leer building, Georgia Tech, Atlanta, USA and from the receiver at Burden, KS, USA (described in Table 3.1). The spectrogram is sampled with 10 ms windows and 5 ms overlap. The data is a 10 second snippet sampled at 1 MHz starting at 20-Sep-2018 20:15:00 UT.

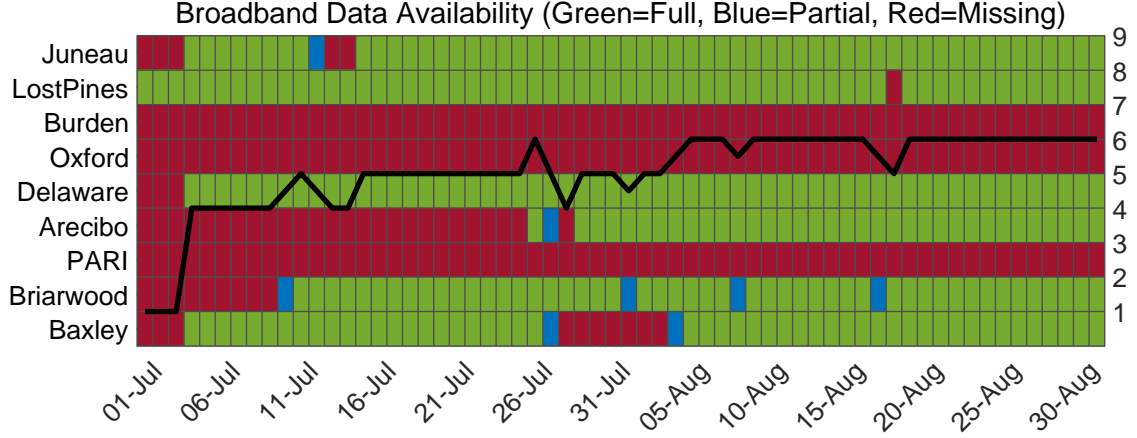











Figure 3.5: Broadband data available for each receiver during July and August of 2017. Full/partial/missing data is defined for a receiver recording at least 90/33/10% respectively. The sum of availability for each day is overlaid as a black curve.

Table 3.1: Receiver network details

Color	Receiver Name	Short Name	Latitude	Longitude	Established
	PARI	PA	35.20°N	-82.87°E	26-Sep-2014
	Briarwood	BW	33.43°N	-82.58°E	10-Jun-2015
	Baxley	BX	31.88°N	-82.36°E	16-Jan-2016
	Delaware	DA	39.28°N	-75.58°E	24-Mar-2016
	Burden	BD	37.32°N	-96.75°E	26-Mar-2016
	Juneau	JU	58.59°N	-134.90°E	30-Jul-2015
	Lost Pines	LP	30.09°N	-97.17°E	15-Jun-2016
	Oxford	OX	33.17°N	-91.23°E	01-Aug-2017
	Arecibo	AO	18.35°N	-66.75°E	28-Jul-2017

in Figure 3.5. The constellation of receivers used in this work is shown on a map in Figure 3.6, with more detailed information shown in Table 3.1.

### 3.2.2 Broadband Preprocessing

Before processing individual sferic waveforms, the entire continuous time series data is preprocessed for efficiency and to produce the maximum signal to noise ratio for individual and representative sferics.



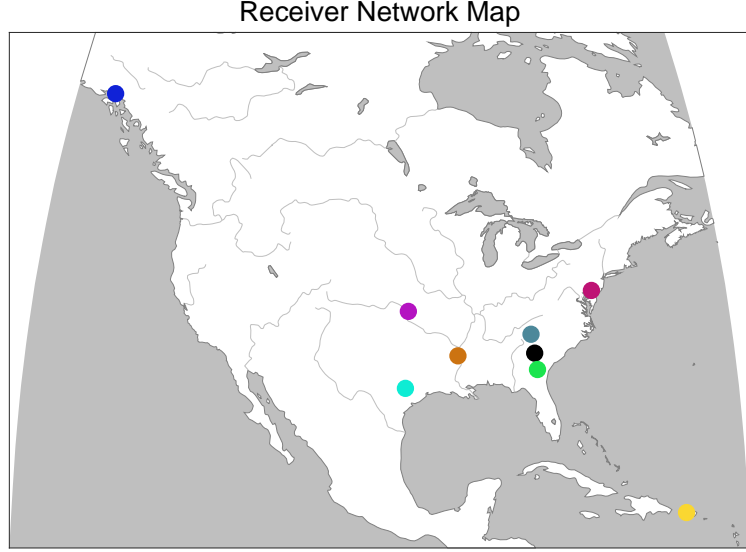


Figure 3.6: Locations of all receivers to be used in this work. Colors correspond to more detailed information in Table 3.1.

#### *Narrowband Transmitter Removal*

The two dominant sources of energy in the VLF/LF frequency band are lightning generated sferics and communications transmitters [Chrissan and Fraser-Smith, 1996]. These transmitters are used, for instance, by the US Navy at high power with a very narrow bandwidth for submarine communications. To mitigate this ‘interference’ source and improve the underlying sferic waveforms, we estimate and subtract the transmitters recorded by our receivers.

We first demodulate each VLF MSK signal as described in Gross *et al.* [2018]. Next, we reconstruct each transmitter signal and subtract from the time series data. We observe a significant improvement in sferic quality over the frequency spectrum usually dominated by these transmitters, allowing recovery of underlying sferic information. The transmitters removed from the broadband data are detailed in Table 3.2. We demonstrate typical results by showing a the MSK subtraction effects on an example time-domain sferic and the spectral amplitude of a time series snippet before and after narrowband removal in Figure 3.7.

The transmitters can be clearly seen in Figure 3.7d as very strong, but narrow frequency-band signals. The results showing the same spectrum after notch filtering and subtraction are displayed in Figures 3.7e and 3.7f. After removal of the transmitters, sferic information

Table 3.2: Transmitters subtracted from broadband data

Location of Transmitter	Call Sign	Frequency (kHz)
Rosnay, France	HWU	18.3
Anthorn, UK	GBZ	19.6
Exmouth, Australia	NWC	19.8
Tavolara, Italy	ICV	20.27
Lualuahei, HI	NPM	21.4
Shelton, UK	GQD	22.1
Rhauderfehn, Germany	DHO	23.4
Cutler, ME	NAA	24.0
Jim Creek, WA	NLK	24.8
La Moure, ND	NML	25.2
Aguada, Puerto Rico	NAU	40.75

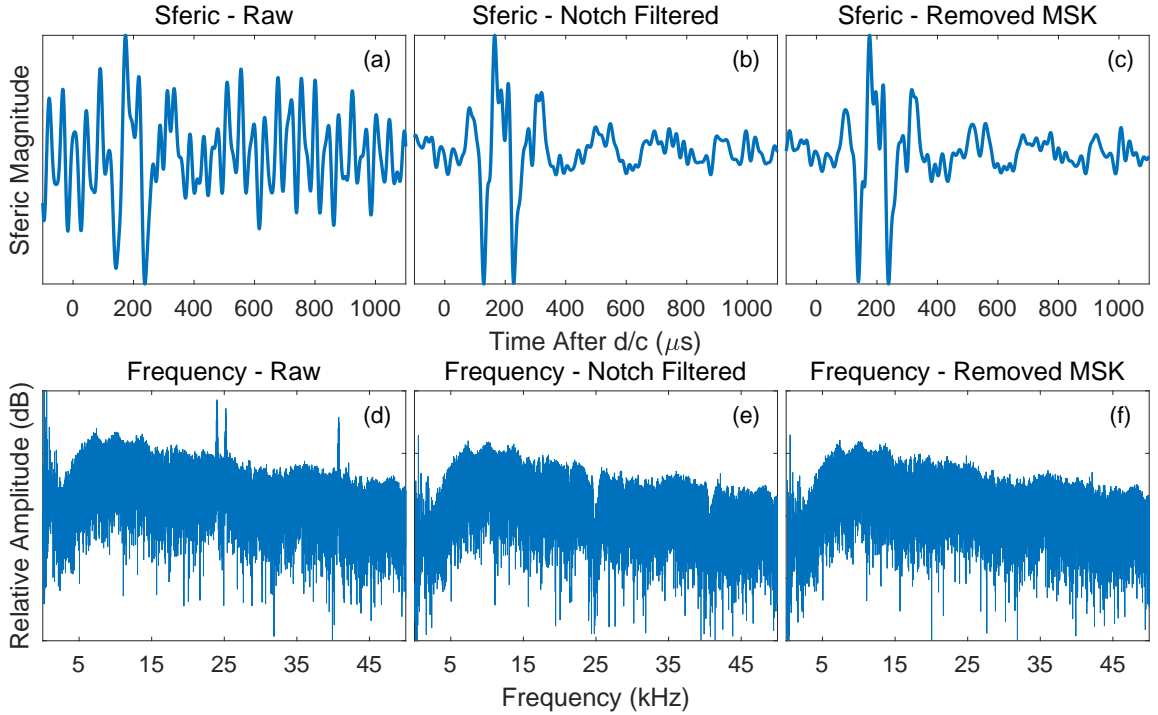


Figure 3.7: An example of coherent MSK signal subtraction. (a,d) A time-domain sferic and broadband amplitude spectrum data, (b,e) notch filtered data, (c,f) and the MSK subtracted data.

in the same frequency range as the transmitters can now be used in ionospheric remote sensing studies. This result contrast with the notch filtering results which subtracts more than the transmitter energy, thus removing portions of the spectrum from usability. A raw time-domain sferic example is shown in Figure 3.7a with the same sferic after notch filtering/MSK subtraction in Figures 3.7b and 3.7c. The example sferic SNR as described in Figure 3.15 and accompanying text improves from 2.4 to 6.4 with this technique while also recovering the underlying sferic spectrum.

We now evaluate the performance of the coherent MSK removal algorithm compared to applying a simple notch filter. In the following analysis, the interference signal is a 1-second recording of an MSK transmitter with a high SNR filtered over a 400 Hz bandwidth. The signal of interest is an impulse with a 2 kHz bandwidth centered on the transmitter. The results below indicate an upper bound on the performance difference between the coherent and notch filtering approaches because in practice the impulsive signals will have a much larger bandwidth.

The performance of the coherent MSK subtraction technique can be quantified by the mean-squared-error (MSE) between the recovered impulse  $\hat{x}_s(t)$  and the original impulse  $x_s(t)$ . Using a 200  $\mu\text{s}$  integration window centered on the impulse time  $t_0$  gives

$$\text{MSE} = \frac{1}{200 \mu\text{s}} \int_{t_0-100\mu\text{s}}^{t_0+100\mu\text{s}} [\hat{x}_s(t) - x_s(t)]^2 dt \equiv \|\hat{x}_s - x_s\|^2 \quad (3.1)$$

If we write the original narrowband transmitter signal as  $x_{\text{nb}}$  and the recovered transmitter signal as  $\hat{x}_{\text{nb}}$ , then  $\hat{x}_s = (x_s + x_{\text{nb}}) - \hat{x}_{\text{nb}}$  and so the MSE can also be written as  $\|x_{\text{nb}} - \hat{x}_{\text{nb}}\|^2$ . That is, the MSE of the signal of interest is equivalent to the MSE of the reconstructed MSK signal compared to the original MSK signal.

Figure 3.8 plots the MSE of the recovered impulse using the coherent removal technique. For reference, the figure also shows the MSE with no filtering and using a notch filter with 600 Hz bandwidth. The notch filter effectively removes both the narrowband transmitter and the in-band energy of the impulse. Thus, the MSE using a notch filter is relatively insensitive to the narrowband amplitude for modest narrowband amplitudes. For large amplitudes, evidently the notch filter attenuation outside the pass band is insufficient and

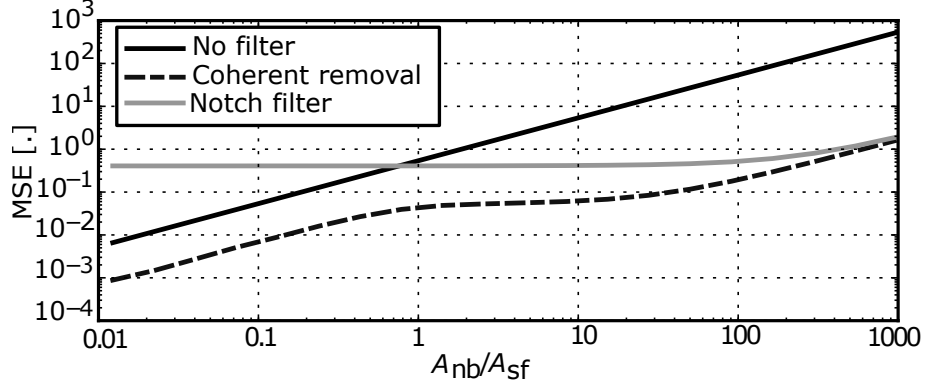


Figure 3.8: MSE of the recovered impulse as a function of narrowband amplitude normalized to the peak amplitude of the original impulse  $A_{sf}$ . The MSE is evaluated for three narrowband removal techniques: no filter (solid black line), 600 Hz notch filter (grey line), and coherent MSK removal (dashed line).

the performance degrades slightly.

Across all narrowband magnitudes, the coherent removal technique outperforms the notch filtering. For weak narrowband signals, where  $A_{nb} \lesssim A_{sf}$ , the notch filter performs worse than applying no filter, since it removes both the (weak) narrowband signal and the energy of the impulse in that band. In contrast, for weak narrowband amplitudes the coherent removal approach reduces the MSE over the unfiltered case by nearly a factor of 10. For larger narrowband amplitudes, using a notch filter improves the MSE compared to the unfiltered case. However, coherently demodulating and removing the narrowband signal still outperforms notch filtering in this regime, since less energy in the impulse is removed. As the narrowband signal strength increases, the relative improvement of the coherent subtraction technique compared to notch filtering decreases due to limits from the various filtering operations involved in the coherent subtraction technique.

### *Broadband Calibration*

In order to calibrate the received data for variations in the system, a pseudo-random 1023-bit sequence is injected into the preamplifier front-end. Each frequency component is uniformly spaced with  $\sim 2.5$  kHz spacing and a known voltage of 1 mV RMS. Faraday's law is used to connect this voltage to magnetic field given the area and number of turns of the antenna loop. This calibration measurement is used at the beginning of processing to calibrate to

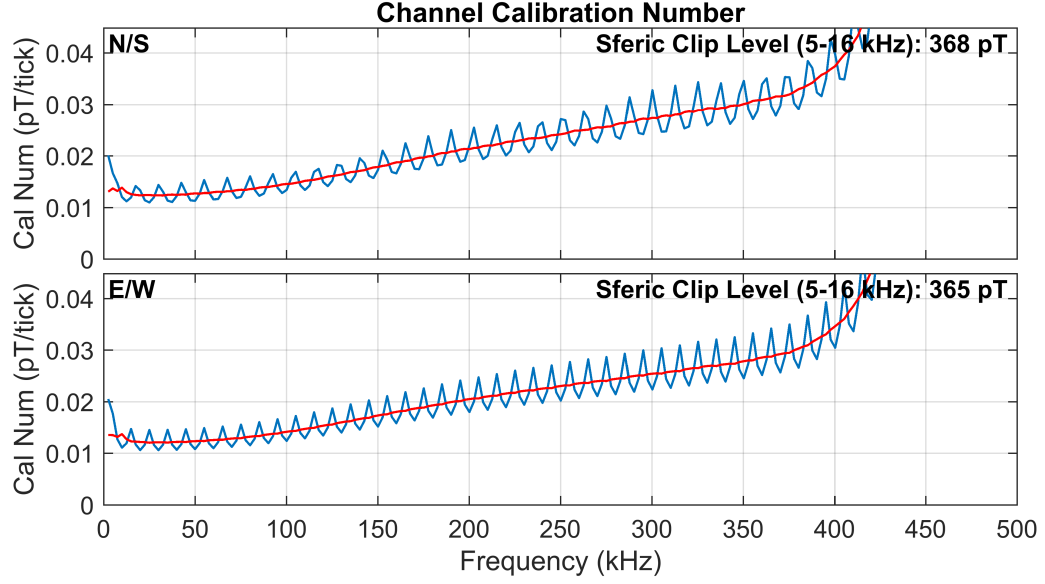


Figure 3.9: Example calibration number curves for Juneau. The blue curves are the raw calibration values recorded in the instrument and the red is the smoothed curve. The sferic clip level refers to the maximum level of magnetic field intensity received before saturation on the receiver.

real magnetic field strength.

Since the analog-to-digital converter (ADC) samples the signal at 16 bits each sample takes an integer value noted as a ‘tick’. By taking the Fourier transform of the time series and multiplying the frequency components by the appropriate calibration number we have calibrated data in Fourier space. After calibration, we take the inverse Fourier transform and time series data is now referenced in pT. An example calibration curve from Juneau, AK is shown in Figure 3.9. The blue curve is the raw values of the calibration curve which is an artifact of the calibration circuit. Therefore, we use the smoothed calibration numbers in red.

### 3.3 Individual Sferic Processing

After the entire data record is preprocessed, we turn our attention to individual sferics. In order to locate the individual sferic waveforms in the time series data, we use lightning location data, an assumed speed of light propagation, and the absolute time reference of both the lightning data and the receiver time stamps.

### 3.3.1 Sferic Isolation and Deselection

Lightning data used is from the GLD360 network operated by Vaisala Inc. GLD360, whose basic operating principles are described by *Said et al.* [2010, 2013], uses a combination of time of arrival, sferic shape, and a network of AWESOME VLF receivers (as described in *Cohen et al.* [2018b]) to geolocate lightning. GLD360 detects cloud-to-ground lightning with a global flash detection efficiency of greater than 70% and reports peak current estimates, polarity, location, and time of occurrence for each lightning event. The location accuracy is estimated to be 1–4 km [*Said and Murphy*, 2016].

An example of GLD360 data is shown in Figure 3.10. The data range is during late afternoon summer in the northern hemisphere, so the distribution of lightning data is reflected accordingly, namely the lightning is most densely distributed in and around Caribbean and Gulf of Mexico land masses, with many broadly distributed storms seen at high latitudes. Two example storm systems are shown with more detail indicating the variance in storm system structure. Close-up 1 shows a very large and coherent storm system in the Midwest and its clear time-evolution can be observed as the system moved eastward. In contrast, close-up 2 is a much smaller system with more relatively incoherent storm clouds developing and ceasing at different times. Before discussing the sferic processing performed on individual sferics, we consider the effects of different types of lightning data on the overall processing algorithm outputs, then proceed with the functional description.

GLD360 does not distinguish between intra-cloud (IC) and cloud-to-ground (CG) strokes whose current sources differ significantly. Therefore, to further increase the integrity of processed sferics, only sferics greater than 10 kA in magnitude are included. This cutoff works to deselect IC strokes since they tend to be reported as low peak current events by the network [*R. K. Said, private communication*].

All lightning detection networks do not distinguish between initial and subsequent strokes, although it can be generally inferred from the time and distance separation between any two strokes, thus grouping strokes into flashes. However, it is known that first and subsequent strokes have different source characteristics [*Rakov and Uman*, 2003, Section 4.6]. We assume that the differences will be small enough to not significantly perturb

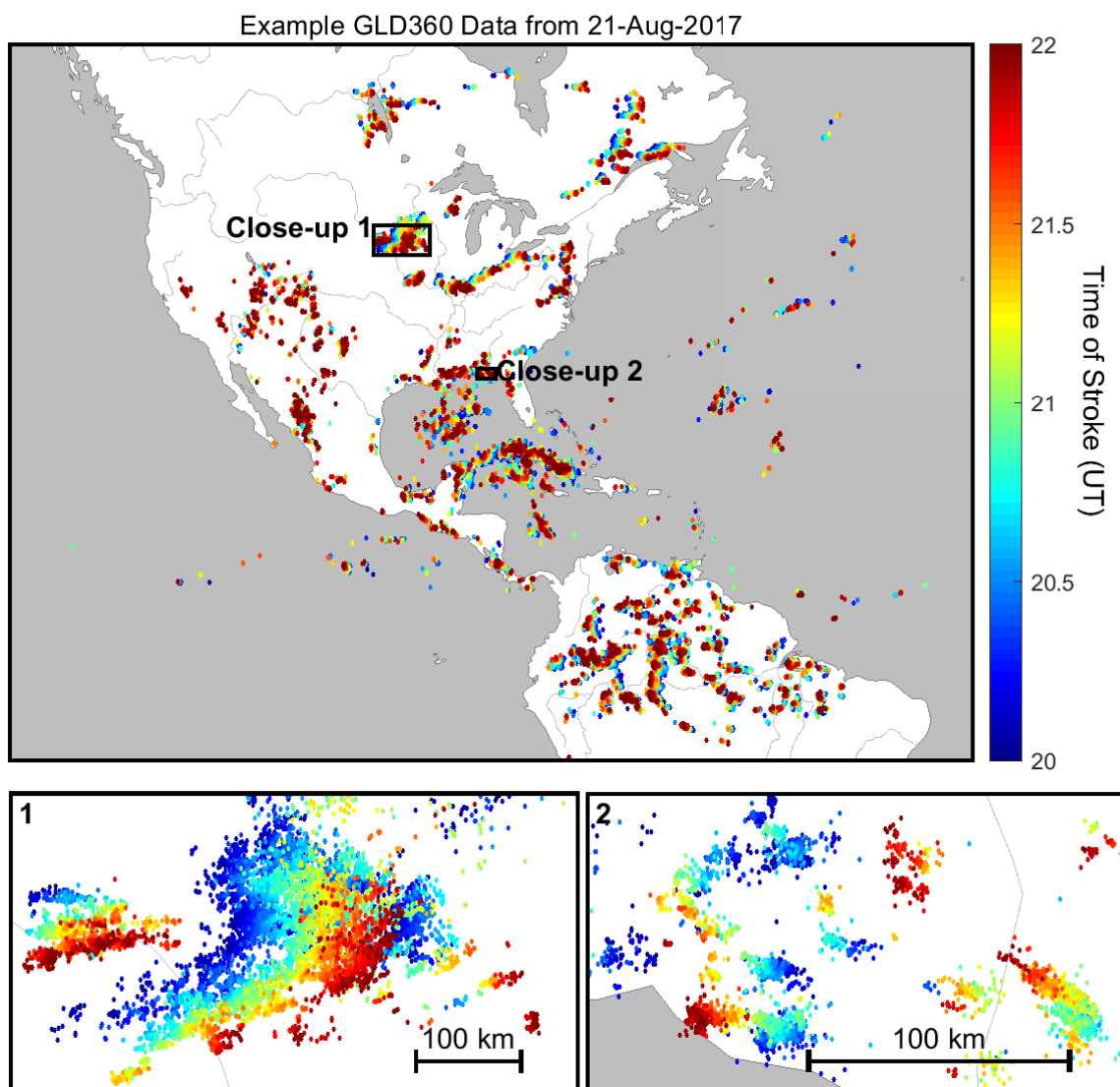


Figure 3.10: Example of GLD360 lighting location data. Strokes from 20:00:00–22:00:00 UT on 21-Aug-2017 with colors corresponding to the time location of the stroke. Two storm regions are shown as close-ups.

the processing results by not sorting them separately.

Positive and negative lightning have different characteristics from each other [Rakov and Uman, 2003, Chapters 4–5]. The most important differences in terms of radiated sferics are the channel geometry and the return stroke current characteristics. Since these are not known in general and since they are different than each other we process positive and negative strokes separately to select out any systematic problems they might cause.

In addition to CG/IC events lightning detection networks occasionally observe highly energetic and short pulses known as narrow bipolar events (NBE) [Le Vine, 1980] or newly discovered energetic in-cloud pulses (EIP) [Lyu et al., 2015] and label them as very high peak current IC strokes. Using 5 receivers Lyu et al. [2015] found and classified merely 139 NBE/EIPs over a period of 44 days. Therefore, we do not screen out these events from our dataset.

The technique that follows to adjust for individual sferic variation can be thought of as a ‘normalization’ technique, a type of superposed epoch analysis where we seek a stochastic normal sferic waveform in both time- and frequency-domains. In order to minimize distortion, we seek to use sferics that are closely spaced in distance since sferic waveforms are a strong function of distance. Therefore, we use a modified version of k-means clustering, an unsupervised machine learning technique which seeks to identify clusters on unlabeled data. In our case, we don’t seek to ‘correctly’ classify clusters, but merely to output clusters which are tightly grouped to minimize spatial and temporal distortion.

The k-means algorithm works by determining cluster centers or ‘centroids’, and then each stroke is grouped with the closest centroid. We start with the k-means++ algorithm [Gabow, 2007], which uses a heuristic in order to find the centroid initial location. Each stroke is then grouped with the closest centroid. After all strokes are assigned, new centroids are calculated as the mean of the clusters. Next, the strokes are reassigned to the new centroid locations. This process is repeated until convergence occurs at a minimum.

In this application of k-means++ we have labeled lightning stroke locations and times. We use all three of these parameters by normalizing the time of the lighting stroke in seconds by 150 and taking the latitude and longitude as reported values. We empirically chose the number of clusters  $k = N/21$  where  $N$  is the number of strokes to cluster in order to reduce



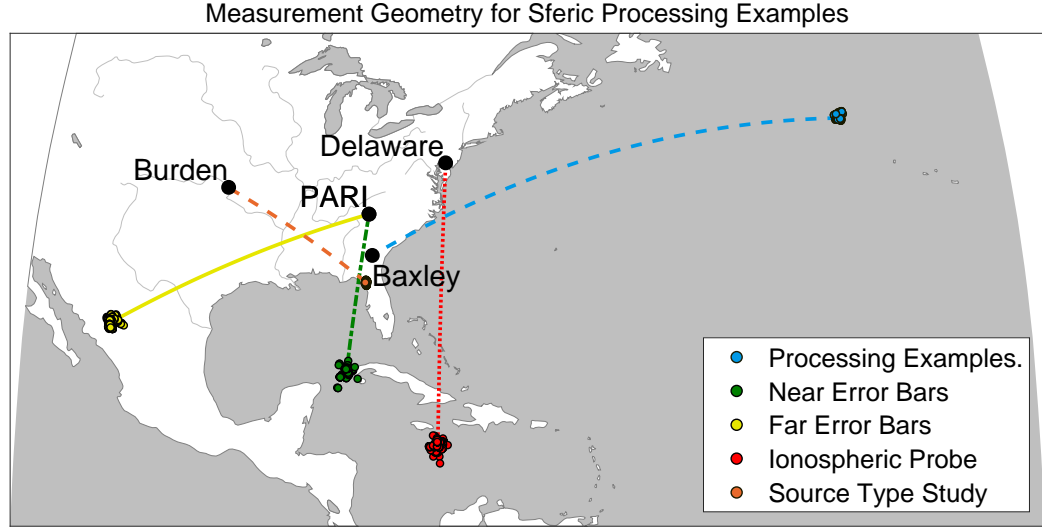


Figure 3.11: Example sferic groups used in processing examples and technique validation.

Table 3.3: Information on lightning regions used in this study. Some figures use multiple dates and/or bins, for those studies the range information is given.

Lightning Region	Date	Center Time	Strokes	Size (km)	Receiver
Processing Examples	08-Aug-2017	04:16 UT	846	105	Baxley
Near Error Bars	30-Jul-2017 to 13-Aug-2017	20:52 UT	2–39	37–222	PARI
Far Error Bars	30-Jul-2017 to 13-Aug-2017	21:22 UT	23–38	16–150	PARI
Ionospheric Probe	20-Aug-2017	Figure 3.22	68–1193	129–426	Delaware
Source Type Study	11-Aug-2017	22:28 UT	573	52	Burden

spatial distortion, while ensuring enough strokes are present in each cluster to improve SNR and mitigate variations in individual lightning strokes. For clusters containing more than 40 strokes, they are subdivided sequentially into clusters of at least 20. Positive and negative strokes are clustered, processed, and compared to a propagation model separately.

### 3.3.2 Representative Time-Domain Sferic

The sferic waveform changes as a function of return stroke current parameters, but more dominantly as a function of distance and propagation conditions, namely the ionospheric conditions along the path, as shown by *Said et al.* [2010].

In principle, one could do ionospheric remote sensing with an individual sferic, but this has shortcomings. First, the single sferic must have high SNR, which is often not the case

for sferics from distant thunderstorms. Secondly, source variability will have a significant impact on the shape of an individual sferic. For these reasons, it is advantageous to take many sferics with the same propagation path and sum them up, both to increase the SNR and to mitigate varying source current and geometry.

Unfortunately, the uncertainty of propagation conditions by time and location contribute significantly to errors in lightning location estimates by networks such as GLD360. In turn, this error makes a straightforward time-alignment of many sferics difficult since error in timing and location translate into timing uncertainty of the sferic waveforms that we call ‘jitter’, even when the sferics have nearly the same propagation path. For example, assuming the speed of light propagation,  $1\ \mu\text{s}$  of jitter could be simply  $1\ \mu\text{s}$  in timing error, 300 m of location error, or likely an unknown combination of both. We demonstrate the effects of inherent jitter in Figure 3.12. We show a superposition of 846 sferics in gray over a period of 30 minutes, all originating from the cluster of blue dots in Figure 3.11 (each dot indicates a lightning stroke). For each stroke, its precise time and location as estimated by GLD360 is used to infer the arrival time of the sferic, which, assuming speed of light propagation, corresponds to  $t = 0$ . We also refer to this time as  $d/c$ , where  $d$  is the source-to-receiver distance and  $c$  is the speed of light. In Figure 3.12a, it is evident that there is significant jitter and waveform variation. In this example, the time-alignment standard deviation is  $22.6\ \mu\text{s}$ . The black curve represents the mean of all the sferics which does not accurately capture the average shape due to the degraded time alignment and variation in sferic magnitude. Figures 3.12b and 3.12c show the same set of sferics after two critical steps in the sferic processing and time-alignment technique described in Section 3.3.2. Following processing, we observe a significant improvement in the quality of the averaged sferic. In the remainder of this section, we detail how this is achieved.

Our goal is to time-align sferics in order to mitigate the effects of arrival time jitter as previously discussed thus we begin with time-domain processing. Later, we will describe frequency-domain techniques. The block diagram depicting our approach is given in Figure 3.13.

We begin sferic processing by taking the GLD360 location and timing estimate. Assuming the speed of light propagation delay, the propagation time from source-to-receiver

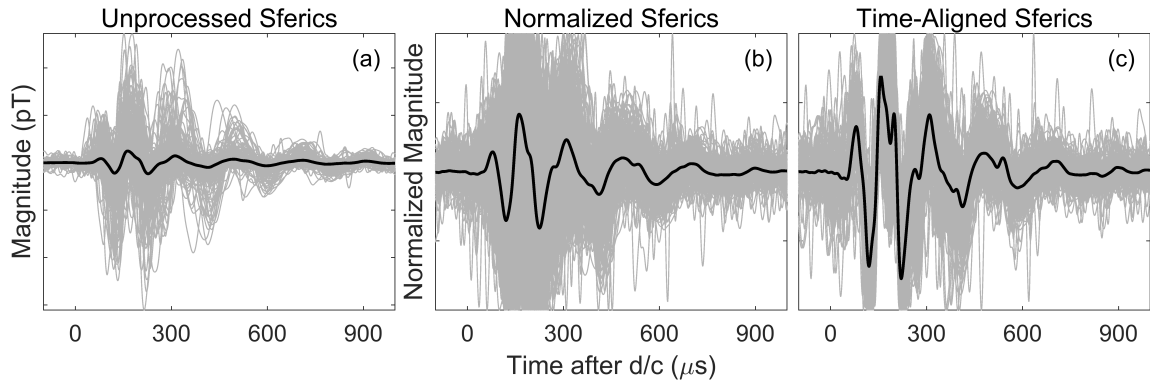


Figure 3.12: Example of the timing and location-induced timing jitter and its effect on sferic processing. 846 sferics from lightning events plotted as blue dots in Figure 1 are plotted as gray curves representing individual lightning strokes for (a) unprocessed raw sferics, (b) normalized sferics, (c) and time-aligned sferics. The black curves represent the respective arithmetic mean.

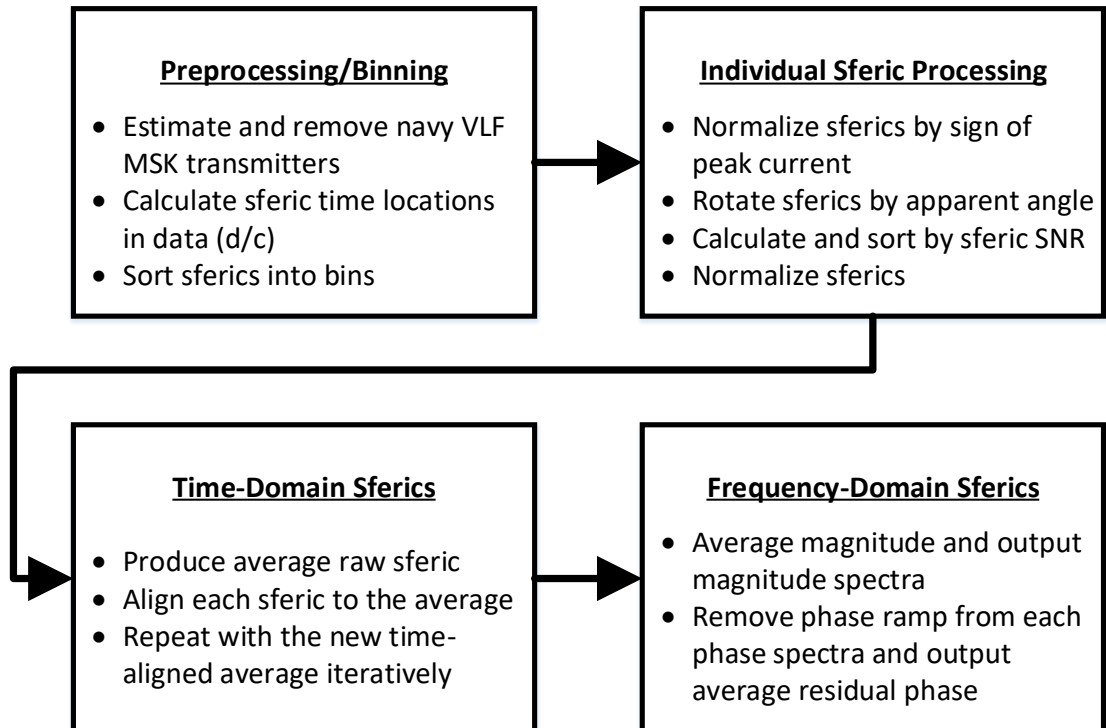


Figure 3.13: Block diagram of broadband sferic processing steps. Boxes group similar operations and each bullet represents an individual step.

along the ground is calculated and added to the reported time of the lightning stroke. We have empirically determined that the bulk of the sferic energy is captured in the first 700  $\mu\text{s}$  after the speed of light arrival time ( $d/c$ ).

As an example, we will use a set of lightning strokes depicted with blue dots in Figure 3.11. This thunderstorm consists of 1547 reported strokes occurring between 4:00 and 4:30 UT on 21-Aug-2015, all within 105 km of each other. The used GLD360-inferred peak currents were as high as 967 kA. We have excluded 579 strokes that were below 10 kA, as these are more likely to have been IC strokes.

The receiver has two orthogonally oriented antennas that measure the N/S and E/W components of the incident sferic's magnetic field. We rotate the two-channel data by multiplying the channels by the rotation matrix and solving for the minimum theta as

$$\begin{bmatrix} B_0 \\ B_1 \end{bmatrix} = \begin{bmatrix} \cos(\theta) & -\sin(\theta) \\ \sin(\theta) & \cos(\theta) \end{bmatrix} \begin{bmatrix} B_{N/S} \\ B_{E/W} \end{bmatrix} \quad (3.2)$$

$$\min_{\theta} \|\sin(\theta)B_{N/S} + \cos(\theta)B_{E/W}\| \quad (3.3)$$

where the  $\min \theta$  is the angle which maximizes the total energy on  $B_0$ , while minimizing it on the  $B_1$ . The N/S and E/W components are shown in Figures 3.14a and 3.14c. We digitally rotate the two channels to maximize the total energy on one channel over the period of 100  $\mu\text{s}$  before  $d/c$  and 1100  $\mu\text{s}$  after  $d/c$  producing a high-SNR, and a low-SNR channel plotted in Figures 3.14b and 3.14d. With no induced scattering along the source-to-receiver path, this is the same as rotating so that the high-SNR ( $B_0$ ) channel measured the perpendicular magnetic field or  $B_\phi$ , while the low-SNR ( $B_1$ ) channel measures the radial magnetic field or  $B_r$ . This is because the attenuation of  $B_r$  is significantly higher than  $B_\phi$ . It is worth noting that the direction of rotation is not necessarily the same direction as the source from the antenna. The discrepancy is likely due to site dependent scattering and induction that modifies the apparent angle-of-arrival due to buried power lines or mountains (see *Said* [2009, Pg. 93] and *Zoghzoghy* [2015, Pg. 45]). It is also significant that because VLF sferics are not perfectly linearly polarized, the low-SNR channel still has a detectable magnetic

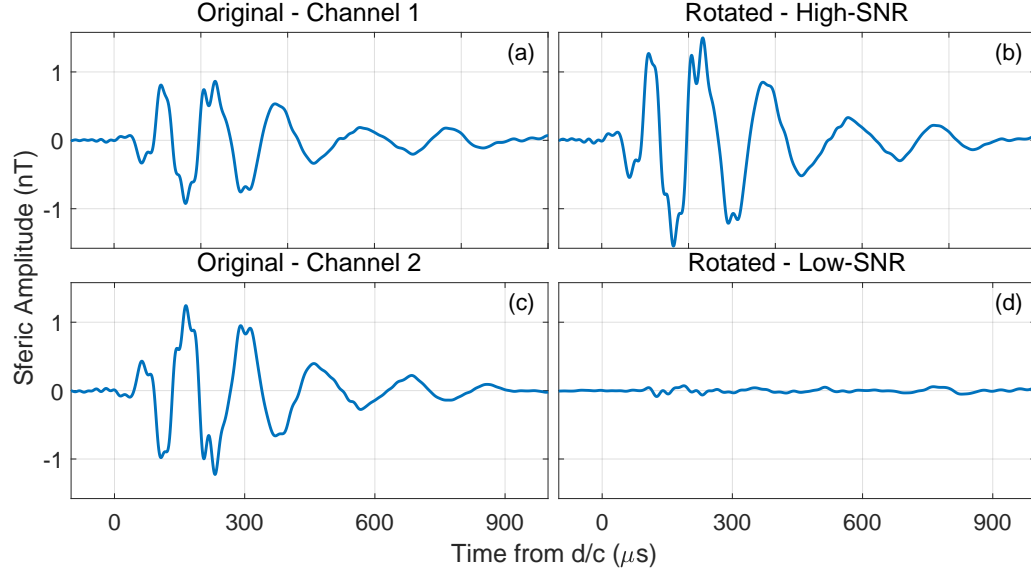


Figure 3.14: An example of digital rotation of a sferic. (a,c) Channel 1 and 2 before rotation. (b,d) Channel 1 and 2 after rotation known as ‘High-SNR’ and ‘Low-SNR’ or  $B_\phi$  and  $B_r$  respectively.

field which can be recovered with this technique, not yet considered in former sferic studies. Recent results from *Gross et al.* [2018] use phase and amplitude of both  $B_\phi$  and  $B_r$  of narrowband VLF signals to develop a polarization ellipse method to monitor the  $D$  Region and diagnose ionospheric perturbations, with advantages over previous narrowband studies. Similarly, amplitude and phase of both  $B_\phi$  and  $B_r$  of broadband sferics recovered in this study may reveal or clarify information on the  $D$  Region and related phenomena.

For lightning strokes occurring in a small time and location range, propagation conditions are very similar. We therefore use clustered sferics and use averaging to mitigate the effect of lightning source parameter variability since these would otherwise make successive strokes from the same storm look very different (see for example Figure 3.21).

We thus arrive at a representative sferic which is made up of all the sferics within that bin. Unfortunately, this result may be distorted by low-SNR sferics and by the timing jitter of received sferics as previously discussed. Therefore, we automatically deselect these low-SNR outliers. The SNR calculation is demonstrated in Figure 3.15. First, we smooth the sferic, shown in blue, by applying a moving average with a window size of  $40 \mu\text{s}$ , the result of which is shown in orange. The peak value of this moving average is taken to be

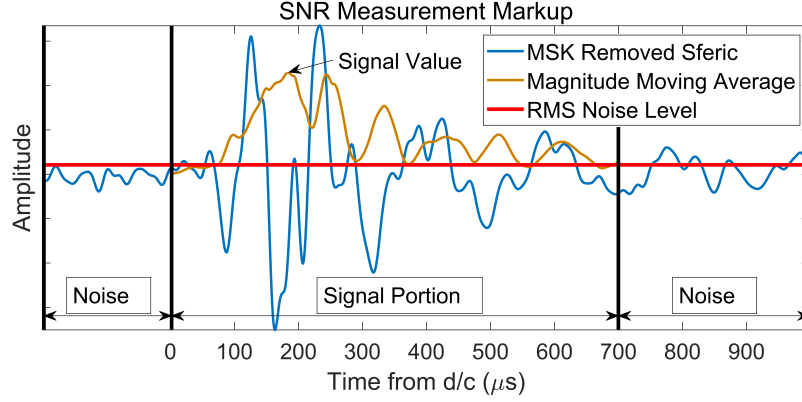


Figure 3.15: An illustration of SNR calculation. The sferic appears in blue in the ‘Signal Portion’. The red line represents the RMS of ambient noise on the channel. The yellow line is the moving average filtered portion of the signal.

the signal value, as indicated by the arrow. To calculate the noise level, we find the RMS value of two concatenated signal portions with the first starting 200  $\mu\text{s}$  before  $d/c$  until  $d/c$  and the second starting 700  $\mu\text{s}$  after  $d/c$  until 1000  $\mu\text{s}$  after  $d/c$ , shown by the red trace. Sferics with an SNR of less than 5 (or 7 dB) are removed for all the examples in this paper. For the thunderstorm system being considered in this example 122 of 968 were below the SNR cutoff threshold yielding a total of 846 sferics.

Having removed the low-SNR sferics, we equally weight the remaining sferics. We normalize all sferics by the maximum of their absolute value. This ensures that the averaging technique is not dominated by a small number of particularly intense sferics and effectively normalizes all sferics to have the same intensity. We are now ready to take an arithmetic average of the remaining normalized sferics, the result of which is the sferic shown Figure 3.12b. This representative sferic is improved from the initial sferic, but the subsequent processing steps will improve the SNR even further.

Next, we mitigate timing jitter in order to align all the sferics in each bin. We do this recursively. First, a raw average is taken of all the sferics within a bin with no adjustment to the sferic jitter. Then, each sferic within that bin is aligned to the raw average by finding the maximum cross correlation between the two. This cross-correlation is performed for both the raw sferic and a flipped (i.e. multiplied by -1) version of the raw sferic, accounting for the possibility of a polarity error in the GLD360 estimate. The highest cross-correlation

location is calculated using the upsampled sferic so that the smallest adjustment possible is  $1 \mu\text{s}$  and the sferic is delayed or advanced by the amount required to move this delay to zero. A new arithmetic average is taken with the aligned (and possibly flipped) sferics. We continue this process iteratively until convergence occurs (typically  $\sim 3\text{--}5$  steps). After convergence, the final time-domain output is the average of the aligned sferics. The final time-aligned sferics and time-domain output are shown in Figure 3.12c.

### 3.3.3 Representative Frequency-Domain Sferic

Past studies have used the spectral interference pattern for ionospheric sensing [Cummer *et al.*, 1998; Cheng *et al.*, 2006; Han and Cummer, 2010a,b], which is primarily a propagation effect, making their techniques independent of lightning source parameters. An important advantage of frequency-domain analysis is that the amplitude spectrum is insensitive to timing jitter.

After normalizing and time-aligning sferics in the time-domain, we now consider how to extract a reliable amplitude and phase spectra for the average sferic. Deriving the amplitude spectrum of the representative waveform is straightforward. We take the discrete Fourier transform (DFT) of each sferic within a bin and then take the mean of magnitude of the FFT coefficients of each sferic.

However, in order to recover stable phase spectrum an additional step is necessary. The FFT's  $t = 0$  reference is the beginning of the input signal, or  $d/c$ . Since the VLF/LF group velocity is slower than the speed of light reference chosen in this work, the sferic arrives after  $d/c$ , so there is a time-delay built into the signal. In the frequency-domain, this is equivalent to multiplying the Fourier transform by a complex exponential linearly proportional to the time delay  $e^{j \cdot 2\pi \cdot f \cdot t_{\text{delay}}}$ . The complex exponential adds a ‘ramp’ to the phase-frequency curve, with the slope proportional to the time delay. We refer to this feature as phase ramping which is equivalent to a small residual delay. Any small timing jitter still present in the time-domain sferics will manifest itself as additional phase ramping. Because of the sensitivity of phase spectrum to very small timing errors, we calculate and output a residual phase by removing all phase ramping. The phase ramp removed by this technique corresponds to a removal of the linear group delay that depends on distance and

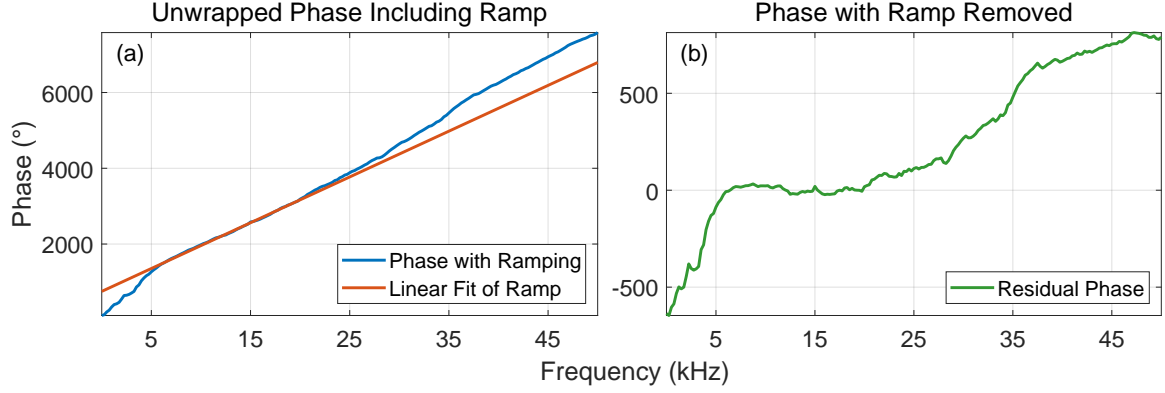


Figure 3.16: Removal of phase ramping. (a) The blue signal is a single sferic unwrapped phase with a 180-degree reference and the red line is the linear fit between 9 and 30 kHz interpolated for the rest of the signal. (b) The residual phase or the measured phase subtracted by the linear fit. This linear phase adjustment is similar to the technique used by *Dowden et al.* [2002] to estimate time of arrival in a lightning geolocation application, differing from the purpose here to calculate the  $B_\phi$  residual phase.

an additional time adjustment of at most 10s of  $\mu$ s.

Since phase wraps around and repeats every 360 degrees, each signal is then unwrapped with a 180-degree reference resulting in the raw phase. This results in a waveform similar to the blue  $B_\phi$  phase sferic in Figure 3.16a. A best-fit linear trend is calculated between 5 and 20 kHz of the  $B_\phi$  component, the portion of the signal we empirically determined to be a high-SNR and stable portion of the signal. This linear fit is removed from the unwrapped phase of the  $B_\phi$  and  $B_r$  signals leaving only the residual phases, as shown for the  $B_\phi$  signal in of Figure 3.16b. The final residual phase spectrum is the average of the residual phase of each sferic within a bin. Importantly, this result is now insensitive to even small timing jitter. One can view this as fine-scale timing adjustment, with course adjustments having been done in the time-domain stage of the analysis.

### 3.4 Sferic Processing Validation

Using the processed results, we are now able to investigate some prior assumptions about lightning stroke types, namely the spectral variations of processed representative sferics which may be induced by initial vs. subsequent strokes or positive vs. negative lightning.

To proceed, we classify GLD360-reported lightning as either a first or a subsequent



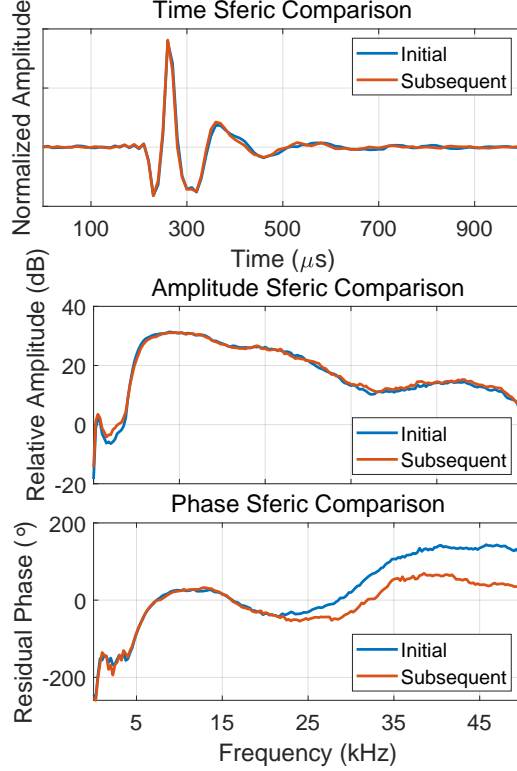


Figure 3.17: Comparison of initial strokes vs. subsequent strokes. All panels are processed representative sferics showing a direct comparison for time, amplitude and phase sferics in the top, middle, and bottom figures respectively. Information for the lightning regions used in the study is listed in Table 3.3.

stroke. A subsequent stroke was defined as having been geolocated within 100 meters and within 100 ms after another stroke. The sferic processing algorithm was repeated on only subsequent strokes, or only first strokes. The results are shown in Figure 3.17 and no significant difference between their characteristics for time-domain and frequency-domain amplitude spectrum is observed when processed with the processing technique. There is a noticeable and persistent difference in phase information above  $\sim 20$  kHz which is taken into account for comparison later. The repeatable spectra underlies the fact that the analysis technique isolates ionospheric variability and minimizes the effect of lightning source variability (geometry and current waveform).

To consider positive vs. negative lightning generated sferics we compare the results of the processing algorithm from using all positive strokes vs. all negative strokes as determined by GLD360. The results are shown in Figure 3.18. We observe a persistent difference between

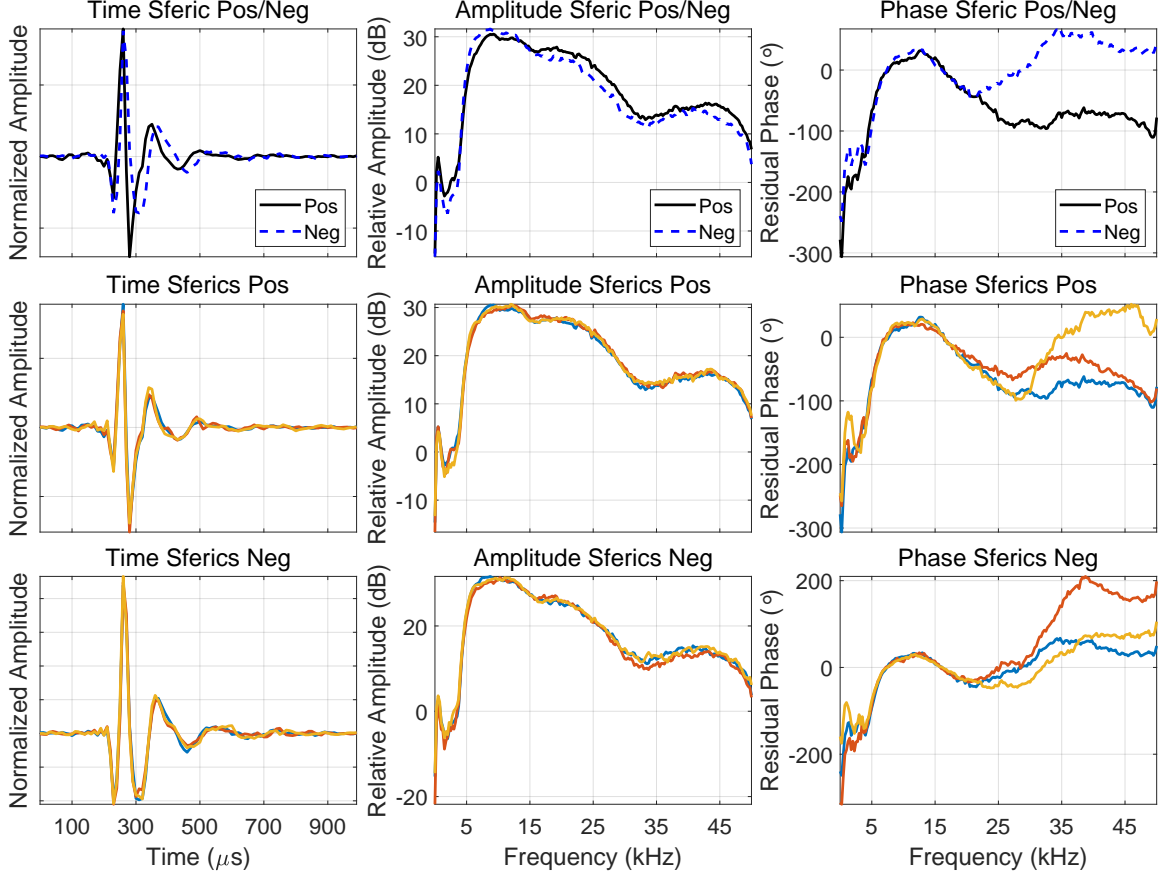


Figure 3.18: Comparison of positive vs. negative processed sferics for a specific example. The top row directly compares a positive and negative sferic for the same time and source-to-receiver geometry for all three sferic components. The middle and bottom row show different processed sferics from the same geometry for positive and negative polarities respectively. Information for the lightning regions used in the study is listed in Table 3.3.

the processed positive and negative sferic waveforms which can be observed in both the time and frequency-domain. We address these waveform differences by using different lightning stroke current parameters for positive and negative polarity sferics when we compare to LWPC in Section 4.1.

In order to quantify the effectiveness of the sferic processing technique, we measure sferic variability for two examples in order to arrive at measurement error bars. We focus on day-time cases where the  $D$  region ionosphere is known to be steady and reasonably predictable in the absence of a solar flare event [Thomson, 1993]. We select a 15-day period from 01-Sep-2015 to 15-Sep-2015 of which 9 days had a significant amount of lightning in the same

location near the Bahamas, as shown/detailed in Figure 3.11/Table 3.3. We then calculate the representative sferic for the same 15-minute period, from 18:45 to 19:00 UT, in each day. For the 9 lightning days, their binned/processed time-domain and amplitude/phase spectra of both magnetic field components are plotted in grey in Figure 3.19. The mean of the waveforms is plotted in black with some sample error bars around the mean in red, reflecting the variability of the result.

The described processing technique is generally applicable to sferics arriving from an arbitrary location and is only limited by the detectability of arriving sferics. To demonstrate this, we provide another example of error bar calculations from sferics from source lightning at region located farther away from PARI, located near the northern border of Colombia/Venezuela (Figure 3.20) for the same date region and 20:45:00–21:00:00 UT of which all 15 were lightning days. The time-domain and amplitude/phase spectra for both magnetic field components are shown again.

The recovered sferic waveforms for both magnetic field components follow the same temporal and spectral trends indicating the stability of the technique. In contrast, we plot 7 random sferics from one of the bins making up single representative sferic in Figure 3.19 (01-Sep-2015) that contains 547 sferics in Figure 3.21. The results for time-domain and amplitude/phase spectra demonstrate the highly varied nature of individual sferics for both magnetic field components, in contrast to the results of Figures 3.19–3.20.

Examination of GOES X-ray data shows no solar flare on these 15 days, so the sferics should in principle be very repeatable over this period due to the relative steadiness of the daytime  $D$  region ionosphere. The error bar calculation demonstrates the residual variation for the example geometry after our processing technique. The averaged time-domain sferics still seem to ‘jitter’ compared to each other since they are all time shifted according to the built-in timing bias of the lightning location network. Therefore, for visual clarity the output time-domain binned results are time-aligned to each other before producing the error bars in both examples. These time-domain results are very similar in both cases, with error bars increasing with relative sferic magnetic field strength for both components.

For both examples, the amplitude  $B_\phi$  error bars are smaller than  $B_r$  which reflects the relatively low SNR of the  $B_r$  channel. However, the  $B_r$  sferics still follow a clear trend. For

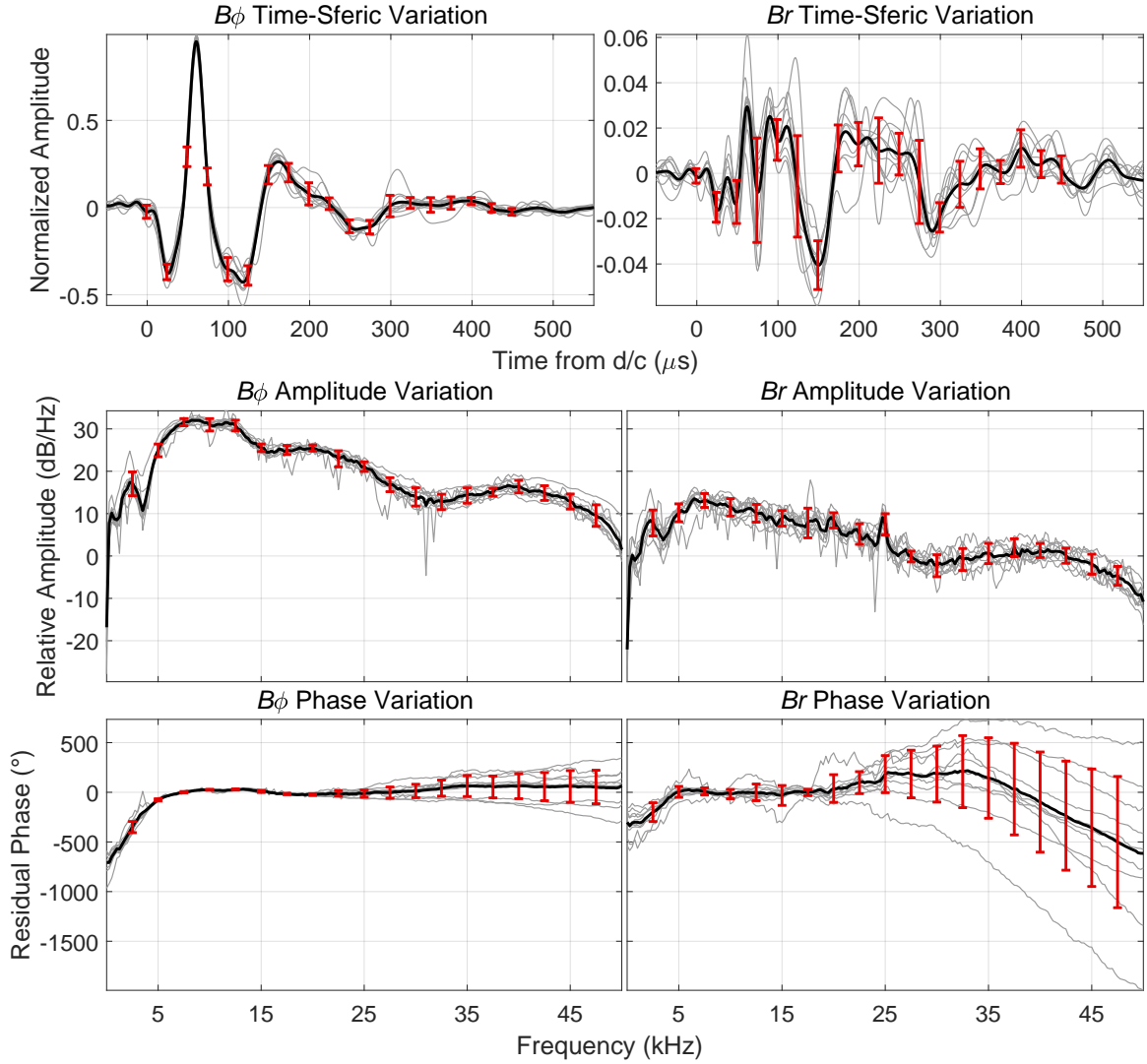


Figure 3.19: Illustration of calculated error bars for  $B_\phi$  and  $B_r$  from 01-Sep-2015 to 15-Sep-2015 and 18:45–19:00 UT. The source-to-receiver distance is 1150 km with further information for this example is given in Table 3.3 with the ‘Near Error Bars’ label. Each available representative waveform is plotted in grey, the mean is plotted in black, and the linear standard deviation is represented each direction from the mean in red plotted at 2.5 kHz intervals. The strokes used in these examples are plotted in green in Figure 3.11.

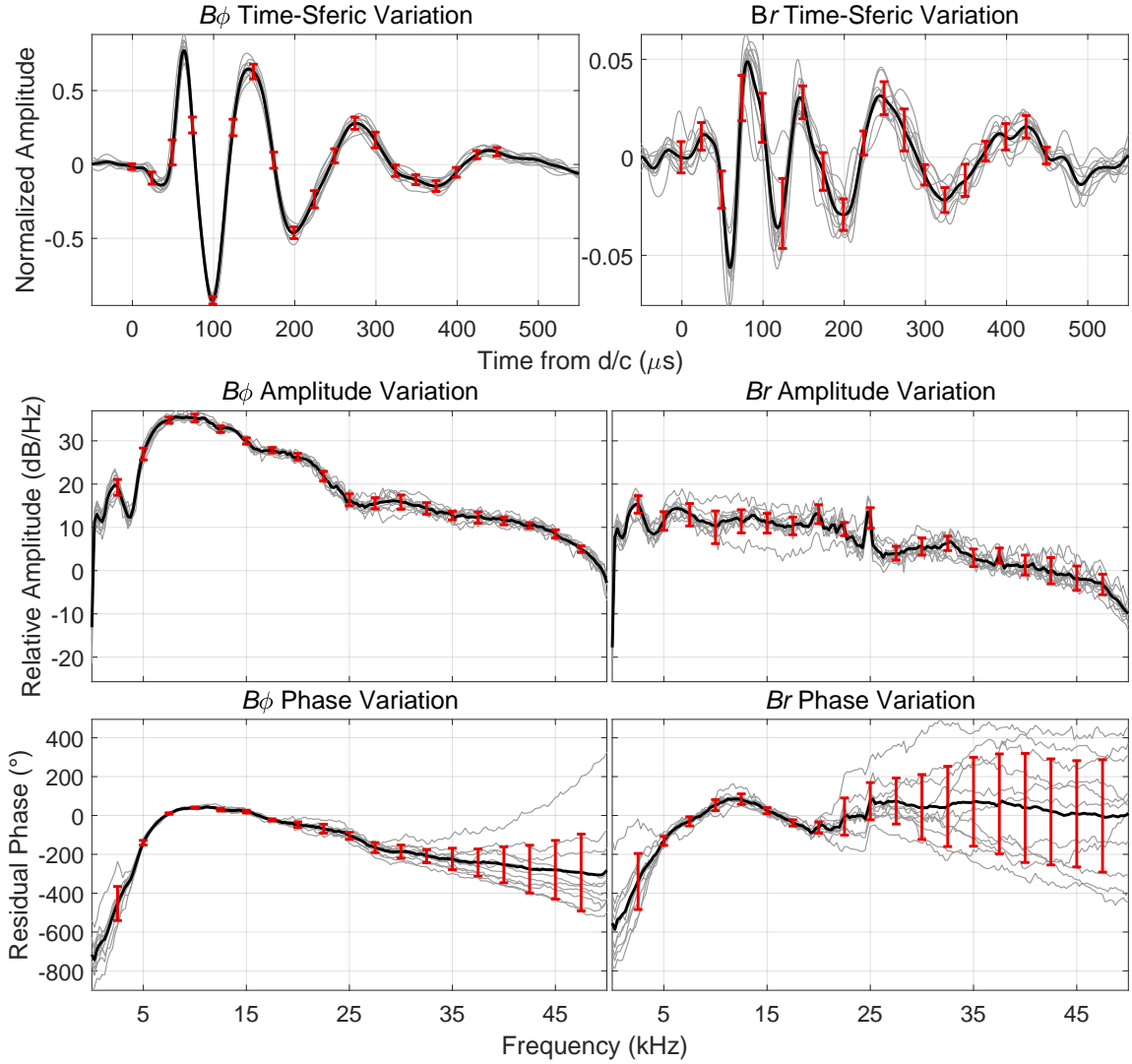


Figure 3.20: Illustration of calculated error bars for  $B_\phi$  and  $B_r$  from 01-Sep-2015 to 15-Sep-2015 and 20:45:00–21:00:00 UT. The source-to-receiver distance is 2900 km with further information for this example is given in Table 3.3 with the ‘Far Error Bars’ label. Each available representative waveform is plotted in grey, the mean is plotted in black, and the linear standard deviation is represented each direction from the mean in red plotted at 2.5 kHz intervals. The strokes used in these examples are plotted in yellow in Figure 3.11.

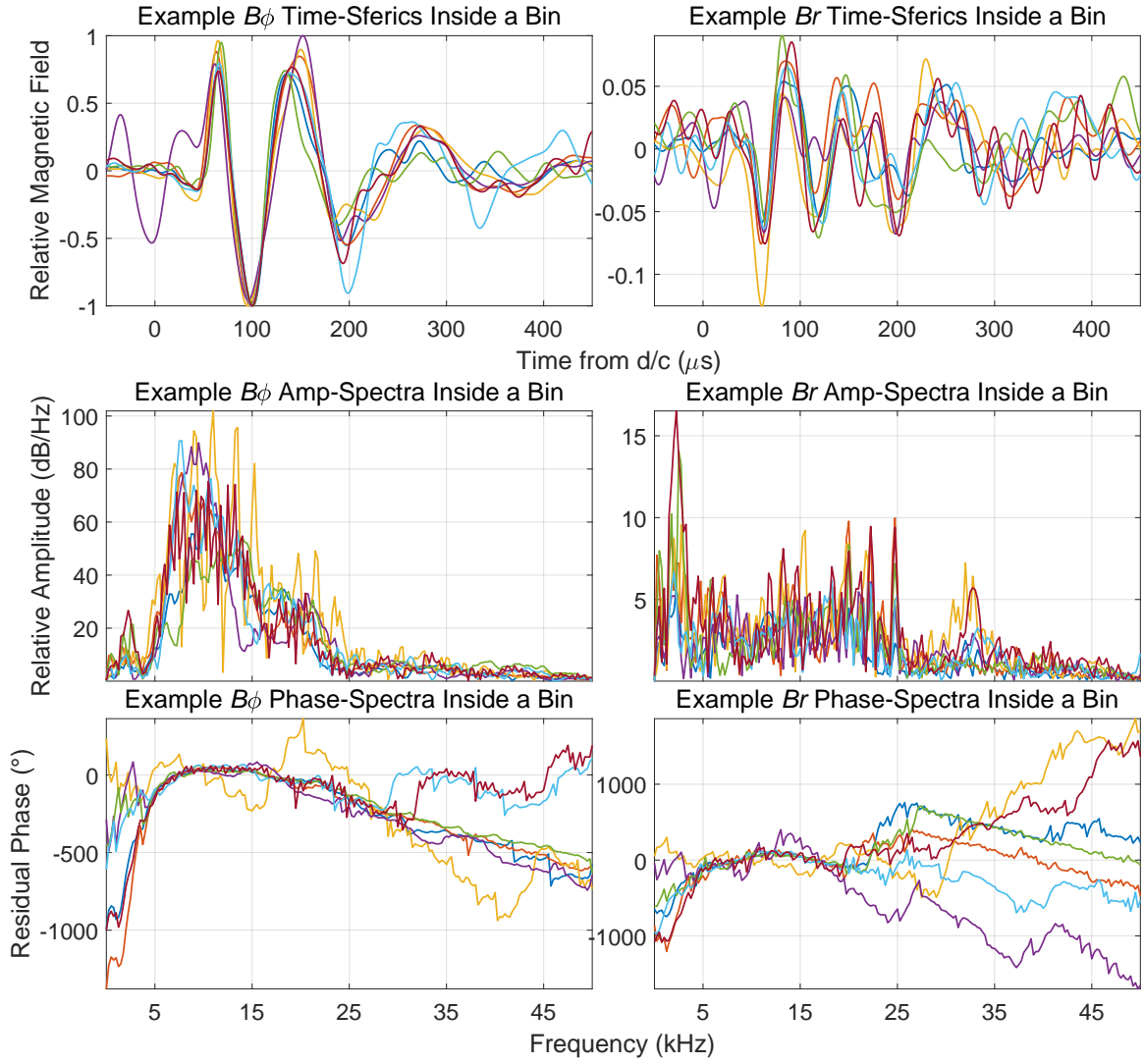


Figure 3.21: Example of individual sferics inside of a bin.

the shorter path, the error bars remain relatively steady across the sferic spectra. The  $B_\phi$  error bars from 5–48 kHz are between  $\sim 0.5$ –1 dB, whereas the  $B_r$  error bars are  $\sim 2$ –4 dB. The error bars for  $B_\phi$  phase are relatively uniform until nearly 30–35 kHz when the results begin to diverge slightly. The  $B_\phi$  spectral error bars are most stable from 5–30 kHz at  $\sim 5$  degrees. The error bars are very large in the  $B_r$  phase component compared to  $B_\phi$  because the phase offset adjustment is taken from the  $B_\phi$  component. The offset and linear trend that differs between each result in  $B_r$  phase is a physically meaningful result that may be obscured by a simple rendering of the error bars. Despite the large size of the error bars, the results follow similar trends.

For the longer path, spectral amplitude error bars are smaller for frequencies below 20 kHz in  $B_\phi$  compared to  $B_r$  but converge to very similar values above 25 kHz. The  $B_\phi$  error bars are  $\sim 0.5$  dB from 10–20 kHz, while they rise to  $\sim 1.5$  dB for 30–49 kHz.  $B_r$  amplitude bars are  $\sim 1.5$  dB for nearly the entire processed spectrum (10–49 kHz). The phase spectral magnetic field components have similar trends to the near path results.

For both examples, nearly the entire frequency band is usable as the error bars even at higher frequencies are fairly small compared to the general variability of sferics this is shown in Figures 3.22 and 3.23 and may be caused by unknowable factors such as the varying geometry of individual stroke channels or meteorological differences of varying thundercloud structures. A small amount of the variability we report may be due to a gradual seasonal shift in the  $D$  region ionospheric conditions but as we ignore this effect, our variability measurement represents an upper bound.

The results reported in *Carvalho et al.* [2017] argue the need to have well characterized source parameters for each lightning return stroke to be able to perform ionospheric inference. But this conclusion need only apply for the use of a single or a very small number of sferics. We know nothing precisely about the return stroke current or geometries of the channels used in this work. However, it is clear careful use of many lightning strokes can be used to calculate repeatable representative sferic waveforms, despite the natural variability of lightning source current and geometry. Full broadband information is now available with high fidelity and widely distributed sources in space/time. This is true for time-domain and amplitude/phase spectra sferics for both magnetic field components.

In principle, error bars like those shown in Figure 3.19 and 3.20 can be calculated for any path if there is enough lightning over a period of time to evaluate the measurement variability. Once the error bar is calculated, a sferic spectral feature that exceeds these bounds is likely due to changes in the ionospheric conditions. Hence, we now evaluate cases where the  $D$  region (and therefore the sferic spectra for a given path) are presumed to be different. Various ionospheric disturbances may affect sferic spectra differently, so the pattern of spectra changes may indicate the type of event. Figures 3.22 and 3.23 shows several sferic spectra measurements on 21-Aug-2015 for both  $B_\phi$  and  $B_r$  respectively. The strokes used in these examples are shown in red in Figure 3.11. The left-hand panels in Figures 3.22 and 3.23 show amplitude and phase for quiet solar conditions near local noon. Once again, the daytime sferic amplitude and phase spectra are highly repeatable and stable, reflecting the stability of both the  $D$  region and our analysis technique.

In the right column, sferics are shown for 4 very different ionospheric conditions: in particular, we show the sferic spectra during the nighttime (when the  $D$  region ionization is much lower), during midday, during sunset (when modal interference at the day/night terminator is important), and during a series of solar flares that commenced at 19:12 UT. The uniqueness of these waveforms compared to each other, taken with the stability of processing results for both  $B_\phi$  and  $B_r$ , gives us the ability to discern different ionospheric conditions. With high-quality average sferic estimates in both time and amplitude/phase spectra, we can develop a generalized approach to ionospheric characterization with comparison to a numerical model described later independent of specific sferic features.



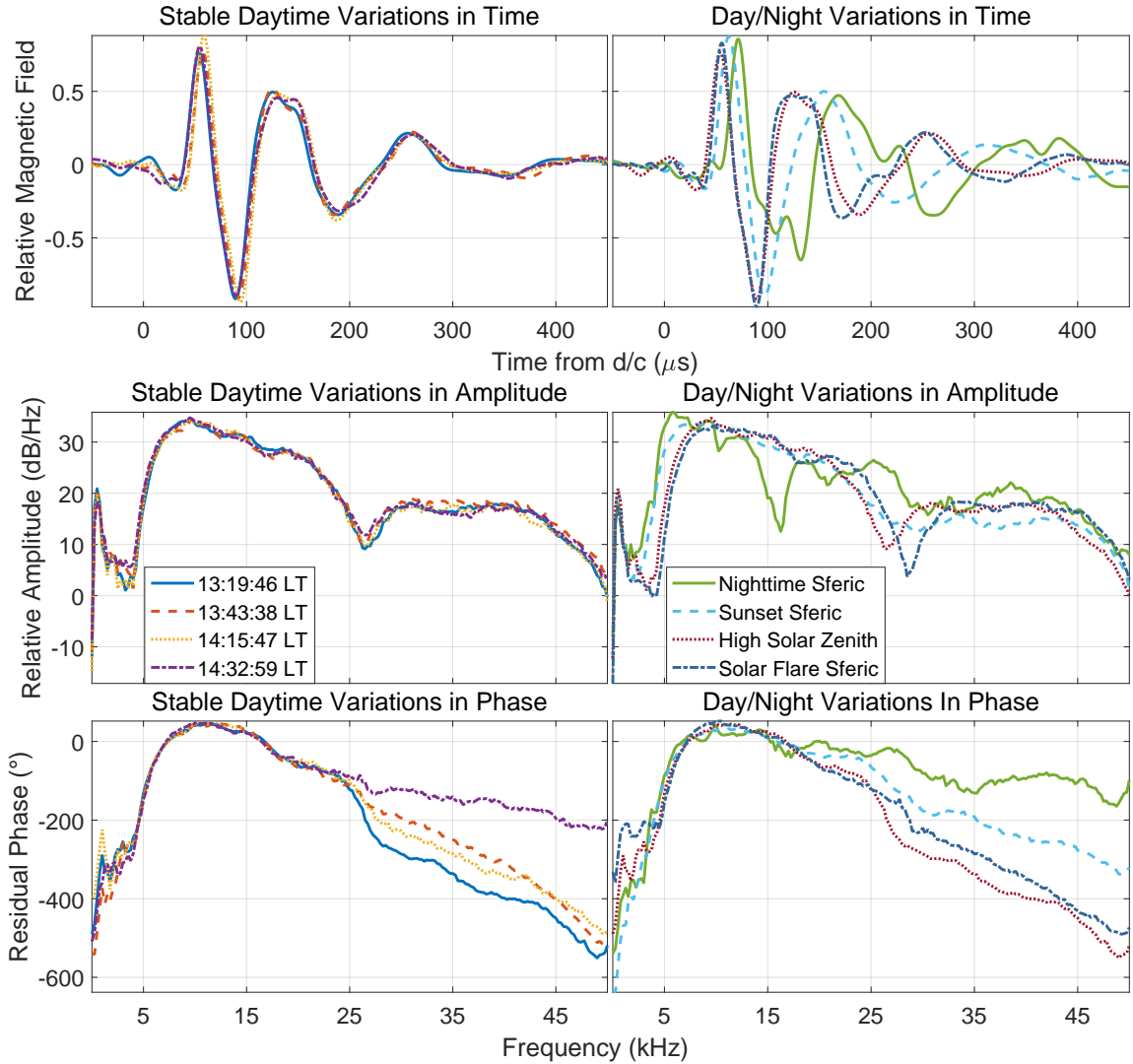


Figure 3.22: Example of processing stability for  $B_{\phi}$  and demonstration of detectability of variations in ionospheric structure on the test day of 21-Aug-2015. The center times of daytime sferics are given in the left legend. The center times of the Nighttime, Sunset, High Solar Zenith, and Solar Flare sferic are: 06:15:00, 00:22:30, 16:45:00, and 22:15:00 UT respectively.

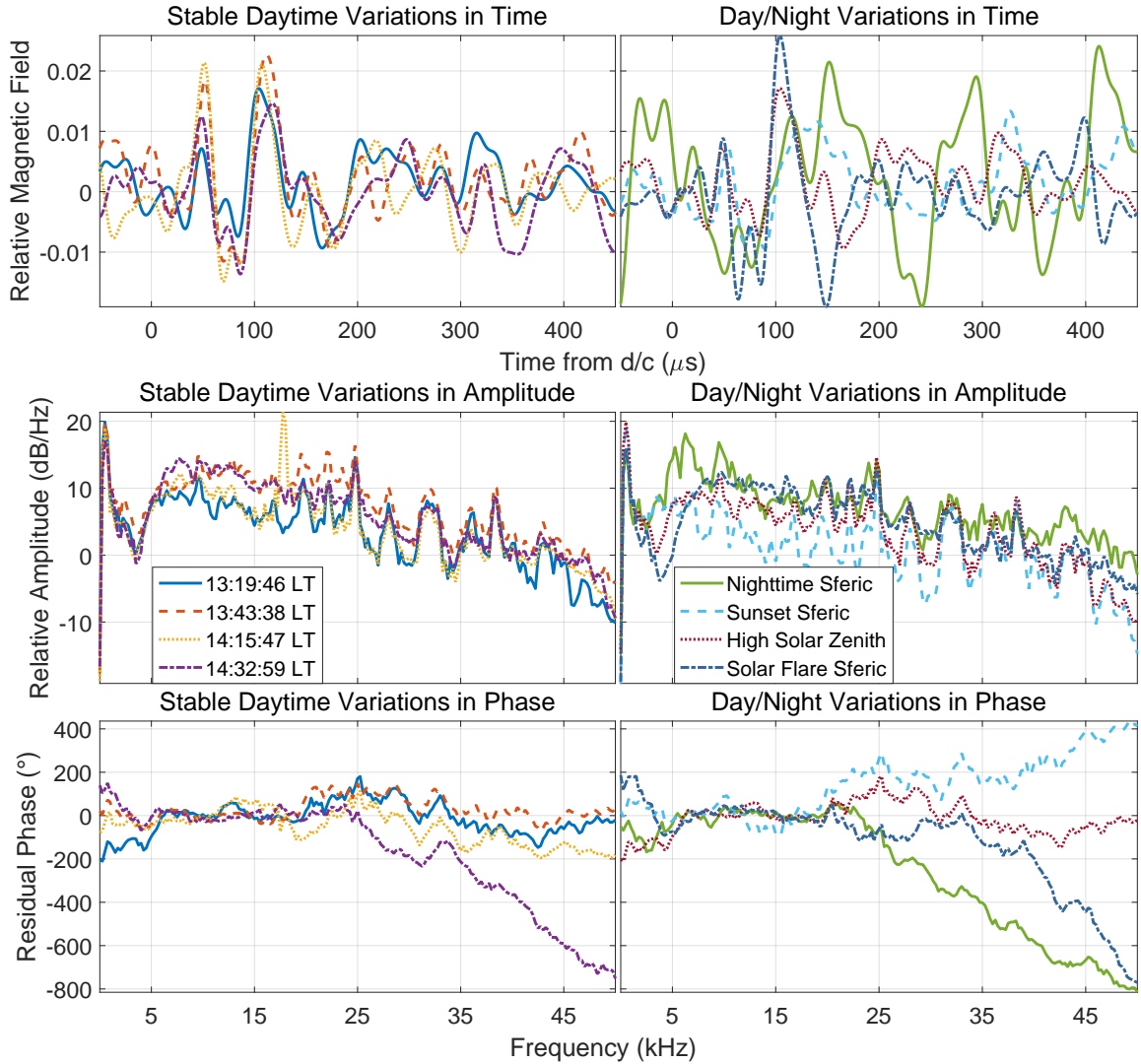


Figure 3.23: Example of processing stability for  $B_r$  and demonstration of detectability of variations in ionospheric structure on the test day of 21-Aug-2015. The center times of daytime sferics are given in the left legend. The center times of the Nighttime, Sunset, High Solar Zenith, and Solar Flare sferic are: 06:15:00, 00:22:30, 16:45:00, and 22:15:00 UT respectively.

## CHAPTER 4

### IONOSPHERIC ELECTRON DENSITY INFERENCES FROM SFERICS

With our sferic processing algorithm, we have access to a large database of representative stable broadband sources for remote sensing. To interpret the data, we aim to compare these observations to a theoretical model for the lightning source and propagation through the EIWG. First, we address the model for the lightning return stroke.

#### 4.1 Lightning Return Stroke Model

The return stroke of lightning is modeled in many ways, but these models can be broadly classified into four categories [Rakov and Uman, 2003, Section 12.2]: **1.** Gas Dynamic Models, **2.** Electromagnetic Models, **3.** Distributed-Circuit Models, and **4.** Engineering Models. As our purpose is to reproduce VLF sferic waveforms, as opposed to understanding the physics of the return stroke, this work uses an engineering model, an approach which does not directly describe the physics of the return stroke but defines a parameterized model as its main output specifying the current along the channel. The model is relatively simple yet achieves a good agreement with remotely measured sferics. An engineering model also requires prior specification lightning channel geometry, which for cloud-to-ground strokes is typically assumed to be a thin vertical column.

An engineering model of the return stroke typically specifies the base-current waveform, then describes how that waveform propagates up the lightning channel. The measured return stroke base-current waveforms are typically unipolar with a faster rise than fall time. We use the Bruce-Golde model of the return stroke which is a sum of two exponentials

$$I(z = 0, t) = I_0[e^{-t/\tau_f} - e^{-t/\tau_r}] \quad (4.1)$$

where  $I_0$  is the current constant,  $\tau_r$  is the rise time coefficient, and  $\tau_f$  is the fall time coefficient. As the pulse travels, the magnitude is attenuated due to various loss mechanisms

such as the emission of electromagnetic waves, light, and heating of the surrounding air (which launches thunder). The most common return stroke propagation models are the Modified Transmission Line-Linear (MTLL [Rakov and Dulzon, 1991]) and the Modified Transmission Line-Exponential (MTLE [Nucci *et al.*, 1988]). Both models can be described by

$$I(z, t) = u(t - z/v_f) \cdot P(z) \cdot I(0, t - z/v_f), \quad P(z) = \begin{cases} 1 - z/H, & \text{MTLL} \\ e^{-z/\lambda}, & \text{MTLE} \end{cases}$$

where  $u(\dots)$  is the unit step function,  $v_f$  is the current waveform front speed,  $H$  is the assumed return stroke height, and  $\lambda$  is the attenuation constant. We use MTLE for this work since MTLE is closer to the actual lightning returns stroke current attenuation, as approximated by recorded stroke luminosity.

An important goal of this work is to produce ionospheric images that are physically meaningful, and in this spirit our lightning model is constrained by the literature. The front speed  $v_f$  is typically between  $c/2$  and  $2c/3$  [Mallick *et al.*, 2014] (where  $c$  is the speed of light), therefore we use the average  $v_f = 7c/12$ . We fix the attenuation constant to  $\lambda = 1$  km to agree with past estimates [Nucci *et al.*, 1993].

With our model for the propagation of the lightning return stroke current fixed, we turn our attention to specifying the return stroke base current ( $I(z = 0, t)$ , Equation 4.1) by determining  $\tau_r$  and  $\tau_f$ . To begin, we consider the effects of these parameters on the spectral characteristics of an example sferic in Figure 4.1. The reference sferic is modeled by the Wait and Spies 2-parameter electron density model with  $h' = 82$  km and  $\beta = 0.5$  km<sup>-1</sup> occurring at (21°N, -78°E) propagating to Baxley.

The reference sferic is displayed in blue with base current parameters of  $\tau_r = 0.3$   $\mu$ s,  $\tau_f = 5$   $\mu$ s. The lightning channel is specified with  $\lambda$  and  $v_f$  as previously discussed,  $H = 4$  km, and lightning channel divisions of 1 km segments. The left column analyzes the effect of varying  $\tau_r$  and  $\tau_f$  for the sferic amplitude and the right shows the same variations and their effects on residual phase. The top row shows sferic variation with changing  $\tau_r$  and the middle shows variation with changing  $\tau_f$ . The bottom row shows the difference between waveforms for varying  $\tau_r$  while holding  $\tau_f$  constant and the reverse for amplitude and phase. Variations

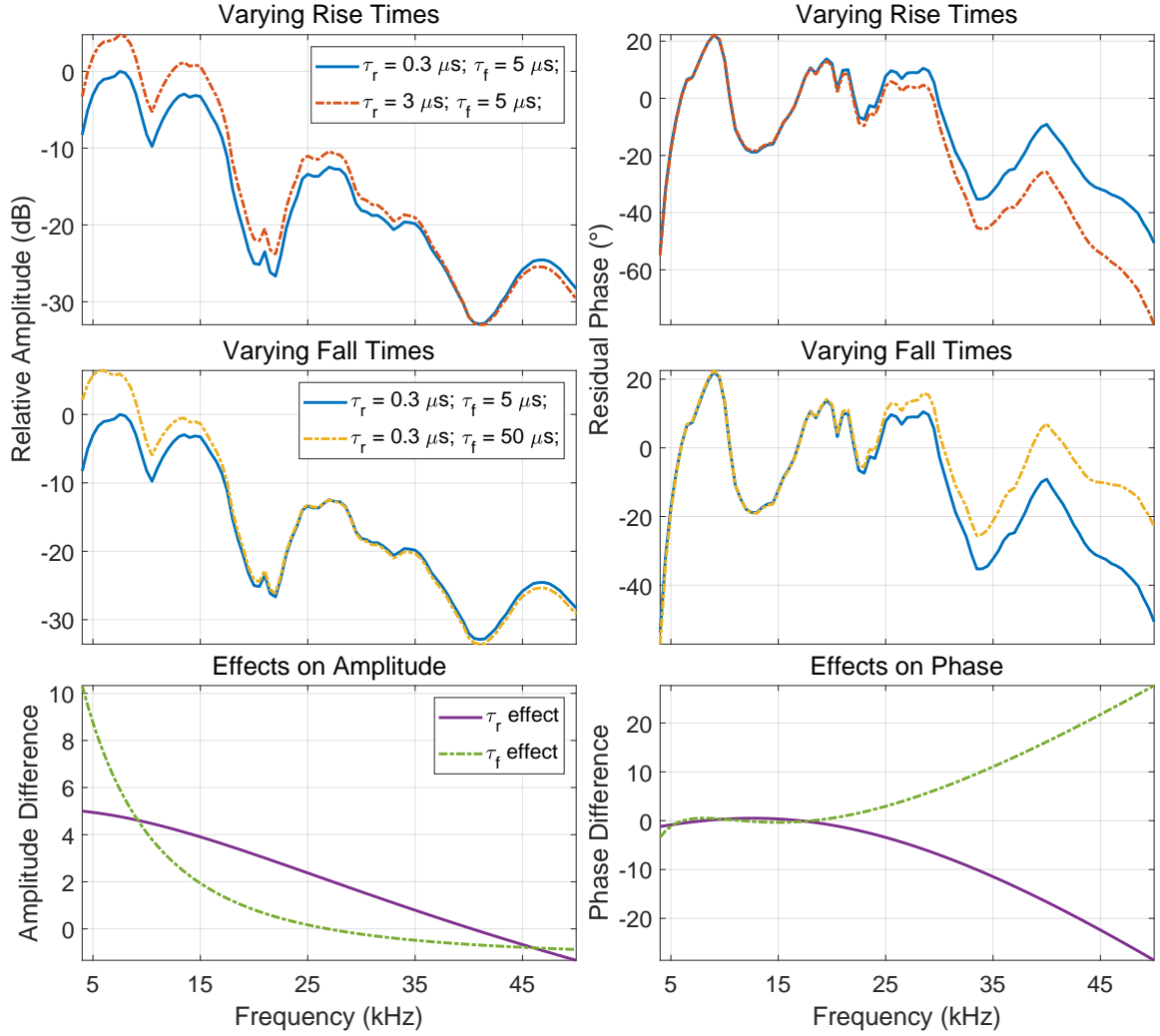


Figure 4.1: Analysis of the effects of rise and fall time coefficients ( $\tau_r$  and  $\tau_f$ ) on spheric amplitude spectrum. The left column shows the effects on the spheric spectra, while the right shows the effects on residual phase spectrum. The top row shows the effects of varying  $\tau_r$  and the middle row shows the effects of varying  $\tau_f$ . The bottom row shows the spectra differences for varying the base current rise and fall time coefficients.

Table 4.1: Current parameters used in this work for positive and negative lightning strokes.  $c$  is the speed of light.

Polarity	$\tau_r$	$\tau_f$	$v_f$	$\lambda$	$H$
Positive	$0.3 \mu s$	$5 \mu s$	$7c/12$	1 km	4 km
Negative	$0.3 \mu s$	$50 \mu s$	$7c/12$	1 km	1 km

in simulated sferics for both amplitude and phase are manifested as slowly varying curves, in contrast to the more rapid changes the sferic spectra caused by multi-mode propagation. This will be important when we consider the inverse modeling technique used to infer the electron density along each sferic cluster-to-receiver path.

Due to the difference between positive and negative lightning strokes (described in Section 1.2.1), different current parameters are used for each respective polarity. The fall time parameter  $\tau_f$  is highly variable with the fall time of negative strokes consistently much longer than positive [Rakov and Uman, 2003, Sections 4.6 and 5.1]. We set  $\tau_f = 5 \mu s$  for positive strokes and  $50 \mu s$  for negative strokes. The rise time of the base-current varies less than the fall-time so we fix  $\tau_r = 0.3 \mu s$  which corresponds to a 10% to 90% of peak current rise time of 0.45 or  $0.6 \mu s$  (for the two fall times used in this work specified by  $\tau_r$ ) agreeing with rocket-triggered measurements [Schoene et al., 2009]. Finally, the lightning channel of positive strokes is typically much longer than negative strokes due to the charge structure of a typical thundercloud (Figure 1.3). Furthermore, due to the branching nature of negative lightning flashes, the current may dissipate much faster than a positive stroke. Therefore, we specify  $H = 4$  km for positive strokes and 1 km for negative strokes. The final lightning model parameters are given in Table 4.1 and the resulting current waveforms are shown in Figure 4.2.

## 4.2 Ionospheric Model

As described in Section 1.1.4, there are several established  $D$  region measurement techniques and each method has its own advantages. Unfortunately, each technique tends to predict persistent features that are contradicted by other techniques as discussed by Sechrist [1974]. This is in part due to the general lack of unique solutions given by inverse modeling

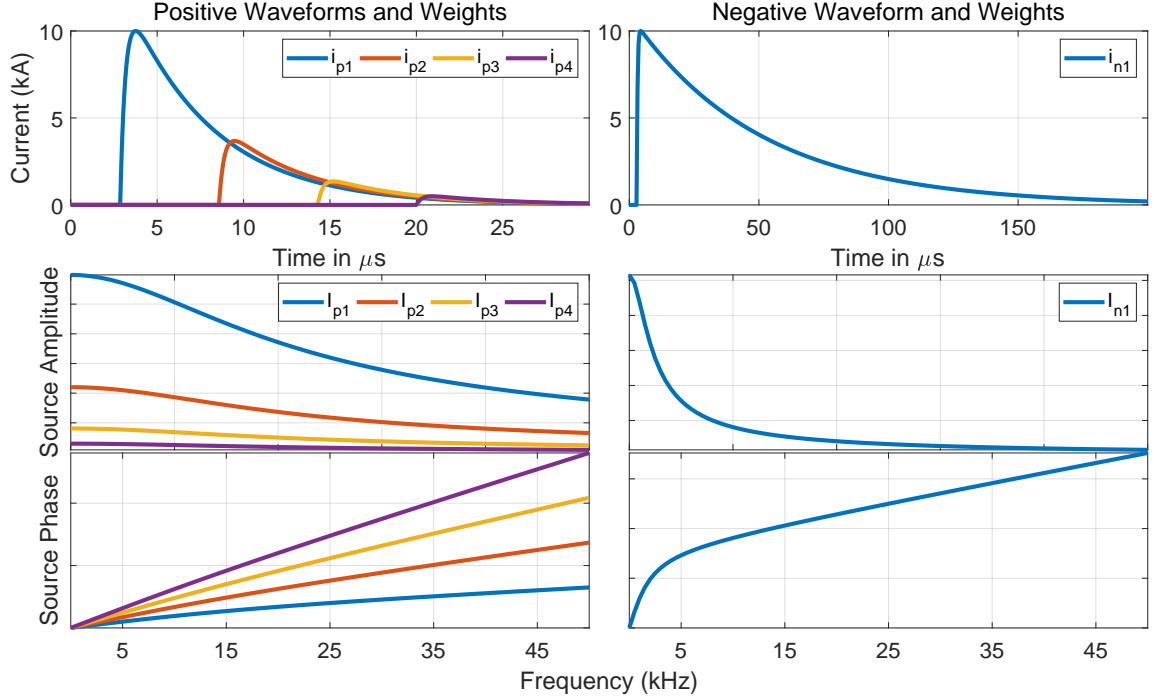


Figure 4.2: Current waveforms in time- and frequency-domains for the reconstruction of positive and negative simulated sferics.

techniques, causing a dependence and sensitivity on initial conditions or assumptions.

Remote sensing of the lower ionosphere using VLF/LF frequencies is a fundamentally different technique. While other highly accurate techniques, such as rocket or ISR measurements, measure arbitrarily complicated electron densities vs. altitude, they are essentially point-trajectory measurements (i.e. two altitude electron density profiles for the upward and downward trajectories). In contrast, VLF/LF remote sensing techniques contain information about the  $D$  region along the whole transmitter-to-receiver path. This is both a strength and a weakness. The weakness is that more detailed information is lost to averaging along the entire path and for that reason is often modeled with smoother and simpler ionospheres. The strength, though, is that specifying these waveguide parameters accurately predicts VLF/LF propagation, especially for narrowband sources. This fact along with a thorough review of much data, led *Wait and Spies* [1964] to propose a simple 2-parameter electron density description with altitude. The model has since become known as the ‘Wait

and Spies' model which is described as

$$N_{e1}(h) = 1.43 \times 10^7 \exp(-0.15h') \cdot \exp[(\beta - 0.15)(h - h')] \quad \text{cm}^{-3} \quad (4.2)$$

where  $h'$  describes the 'height' of the ionosphere and  $\beta$  describes the 'sharpness'. Importantly, most validation of the Wait and Spies model has been performed at a single frequency per transmitter-to-receiver path. Due to the spatial averaging that occurs with every medium or long-range VLF/LF path, this model is better thought of as waveguide parameters as opposed to the actual electron density. The use of this simple parametrized model has become extensive in subionospheric VLF propagation predictions, even if it represents waveguide conditions more than it represents the physical state of the  $D$  region. However, recent work comparing broadband VLF sferics with the Wait and Spies model has suggested that it is inadequate to explain VLF data during the daytime [*Han et al.*, 2011].

#### 4.2.1 Sensitivity to Electron Density

The Wait and Spies model is typically used with narrowband frequency signals for  $D$  region studies. However, our remote sensing signal is broadband, where a 2-parameter model may not be valid. Therefore, we will investigate possible ionospheric models that are capable of better describing daytime propagation. We will begin by examining previous work by *Cummer* [1997, Section 3.2.2] and *Cummer et al.* [1998] who determined, conservatively, that the electron density range important for VLF propagation extends from  $10^0$  to  $10^3 \text{ cm}^{-3}$ . To validate, we use the capability of LWPC to specify 'tabular' or arbitrary electron density profiles with height, using the default profiles of collision frequency and ions. Starting with some example Wait and Spies electron density profiles, we validate the lower bound of electron density sensitivity by 'clipping', or setting electron density to zero, until it resumes the Wait and Spies profile value. The full sferic simulation process is performed for these profiles until the simulated spectra are noticeably perturbed. A similar process is performed for the upper bound of electron density sensitivity, except at the 'clipping' level, where the electron density is held constant for the rest of  $D$  region altitude. The upper



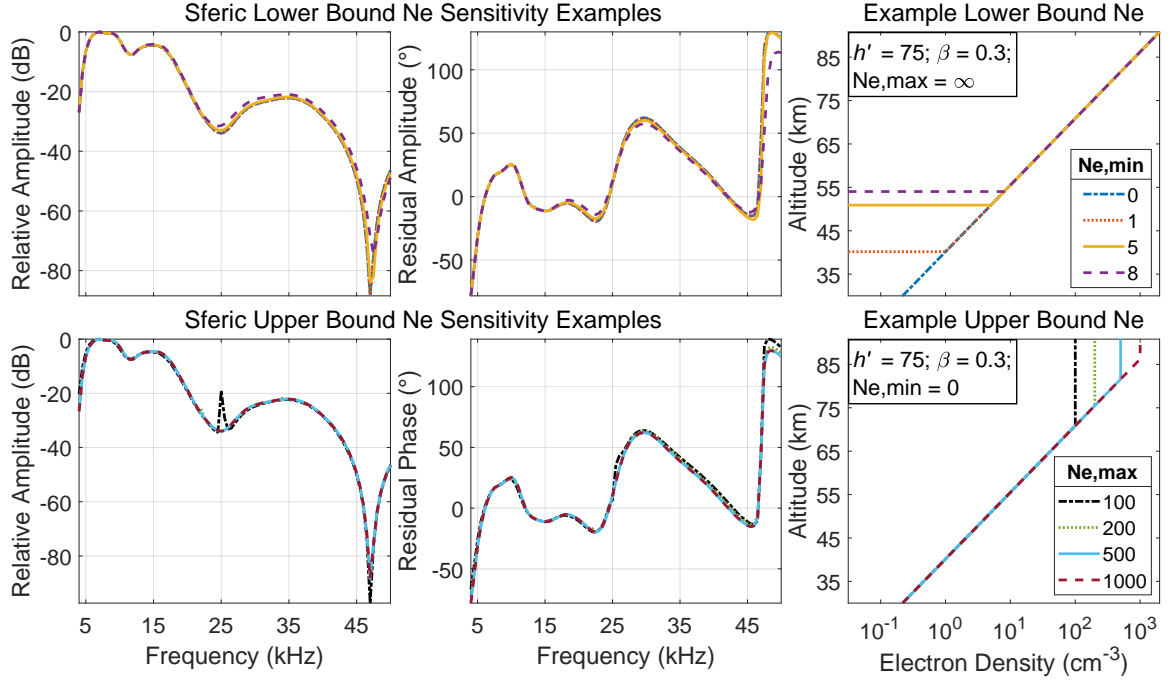


Figure 4.3: Example of the sensitivity of sferic propagation to electron density for  $h' = 75$  km and  $\beta = 0.3 \text{ km}^{-1}$ , a typical daytime profile for the Wait and Spies model. The simulated sferic spectra is reconstructed from the negative sferic current parameters given in Table 4.1, simulated at  $(0^\circ\text{N}, 0^\circ\text{W})$  propagating northward over the ocean to 1000 km. The top row corresponds to the lower bound sensitivity of electron density, and the bottom row corresponds to the upper bound.

boundary can be thought of in analogy to a perfectly matched layer (PML) often used in numerical techniques to prevent against numerical errors. Some examples are shown in Figures 4.3 and 4.4.

The daytime profile (Figure 4.3) is sensitive to a significantly smaller range of electron density than the nighttime (Figure 4.4) profile. One possible contributing factor is that the lower daytime profile is in a region with a much higher collision frequency which changes impinging wave action significantly. Furthermore, for nighttime propagation, significantly more modes can propagate to great distances due to the lower attenuation and each mode may be sensitive to different electron density values. We find that it may be possible to consider a smaller range of electron densities in matching ionospheric profiles to VLF/LF remote sensing results in these cases. However, a much more thorough analysis will be necessary to substantiate this considering the electron density variations while varying other EIWG parameters such as: propagation angle (with respect to the magnetic field), ground

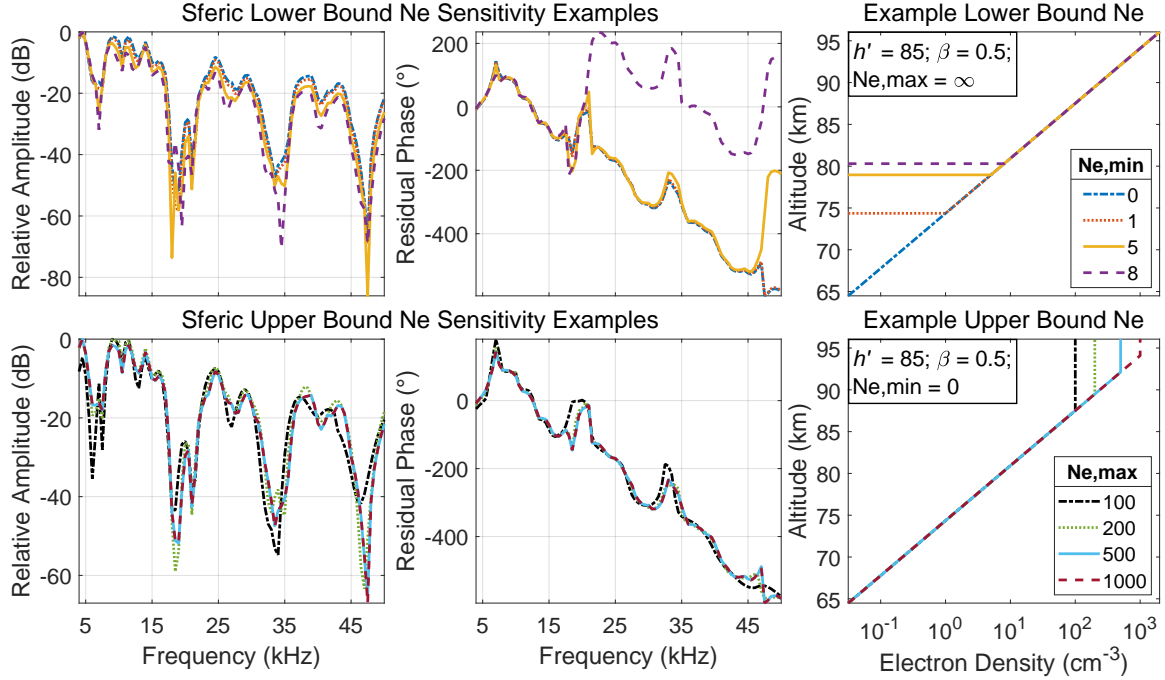


Figure 4.4: Example of the sensitivity of sferic propagation to electron density for  $h' = 85$  km and  $\beta = 0.5$  km<sup>-1</sup>, a typical nighttime profile for the Wait and Spies model. The simulated sferic spectra is reconstructed from the negative sferic current parameters given in Table 4.1, simulated at (0°N,0°E) propagating northward over the ocean to 1000 km. The top row corresponds to the lower bound sensitivity of electron density, and the bottom row corresponds to the upper bound.

conductivity/permittivity, etc. Therefore, we continue to use the conservative estimate of *Cummer et al.* [1998].

#### 4.2.2 The Split Model for Electron Density in the $D$ Region

To gather inspiration for a better electron density model capable of predicting broadband VLF signals, we consider the rocket measured data in the critical electron density range. Over many years, workers used high quality rocket measurements to make accurate  $D$  region electron density measurements [*Friedrich and Torkar*, 2001]. Using this information and a basic ion chemistry model, *Friedrich and Torkar* [2001] developed a semi-empirical model to address the lower ionosphere ( $D$  and  $E$  regions) where the measurements used to establish the IRI are sparse and not well understood. Some modeled results from FIRI are shown in Figure 4.5 for varying solar conditions over different time and space scales.

An inspection of the results over many different solar conditions shows a persistent

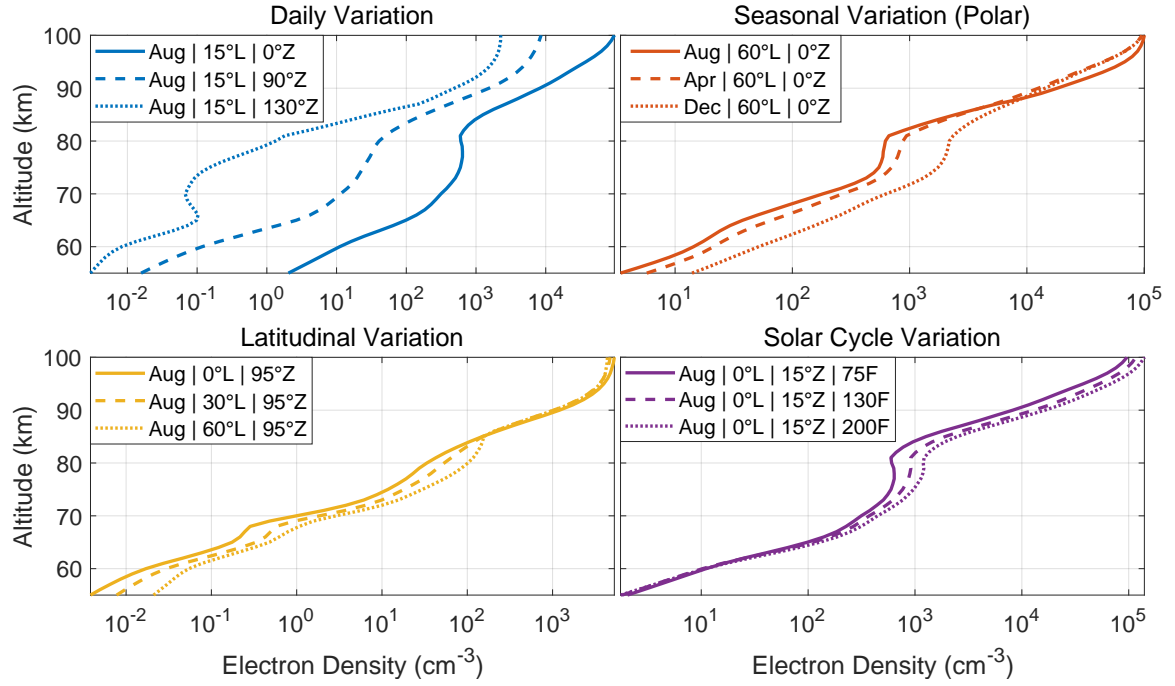


Figure 4.5: FIRM model of *D* region ionospheric variation. Each subplot demonstrates a variation of one parameter that affects the modeled electron density profile. The legend indicates these parameters as follows: L=latitude, Z=solar zenith angle, and F=F10.7

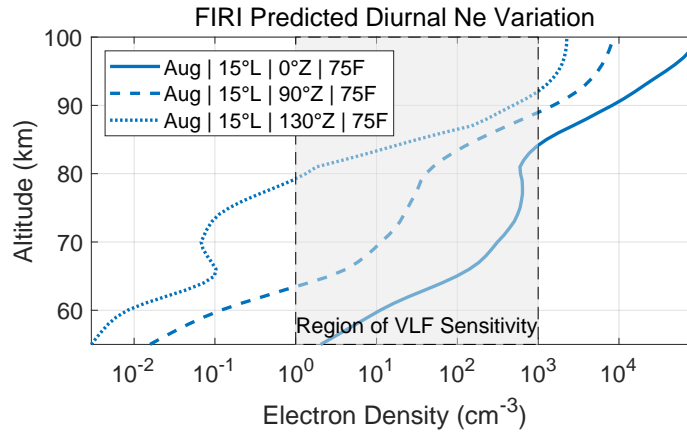


Figure 4.6: Examples of the FIRM predicted diurnal evolution of the electron density vs. altitude. The legend indicates these parameters as follows: L=latitude, Z=solar zenith angle, and F=F10.7

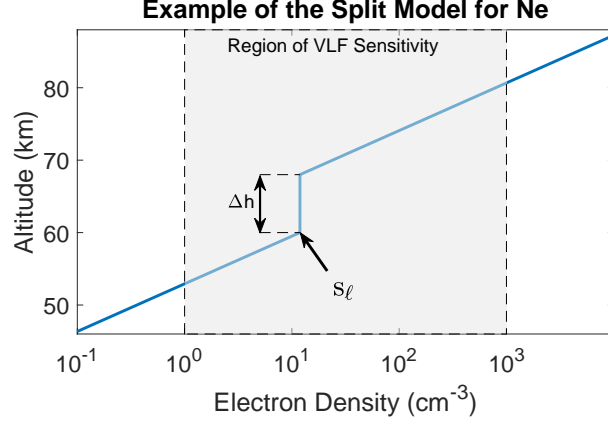


Figure 4.7: An example split model electron density parametrization for  $h' = 70$  km,  $\beta = 0.5$  km<sup>-1</sup>,  $\Delta h = 8$  km, and  $s_\ell = 60$  km.

‘split’ of the electron density into two exponentially increasing regions. This split may be important for predicting VLF propagation if this feature occurs within the sensitive range of electron density, which is common during the daytime as seen in Figures 4.5 and 4.6. Therefore, we will investigate if the simulated sferics produced by including this feature in the electron density model better agree with measured sferics. To do so, we extend the 2-parameter model developed by Wait and Spies to a 4-parameter model that we call the ‘split’ model. The split model can be described as an extension of the Wait and Spies formulation

$$N_e(h) = \begin{cases} N_{e1}(h), & \text{if } h \leq s_\ell \\ N_{e1}(s_\ell), & \text{if } s_\ell < h < s_\ell + \Delta h \\ \frac{N_{e1}(h) \cdot N_{e1}(s_\ell)}{N_{e1}(s_\ell + \Delta h)}, & \text{if } s_\ell + \Delta h \leq h \end{cases} \quad (4.3)$$

where we introduce  $s_\ell$  to denote the altitude of the split,  $\Delta h$  to indicate the magnitude of the gap in the increasing electron density where it is held at a constant value, and  $N_{e1}$  is the Wait and Spies model given in Equation 4.2. An example split model is given in Figure 4.7 for  $h' = 70$  km,  $\beta = 0.5$  km<sup>-1</sup>,  $\Delta h = 8$  km, and  $s_\ell = 60$  km.

#### 4.2.3 Evaluation of the Split Model

The split model seems to capture some important features of the  $D$  region as described by FIRI and others. However, to boost our confidence that we can represent the important

	Low	High
$h'$ (km)	60	100
$\beta$ (km <sup>-1</sup> )	0.15	1.0
$s_\ell$ (km)	$N_{e,f}(s_\ell) = A$	$N_{e,f}(s_\ell) = B$
$\Delta h$ (km)	0	20

Table 4.2: Search space for initial guesses in best fit split model search.  $N_{e,f}$  indicates the electron density for the  $m$ th FIRM profile being matched to.  $A$  is the first value where the electron density curve is greater than  $10^0$  cm<sup>-3</sup> and  $B$  the last value less than  $10^3$  cm<sup>-3</sup>.

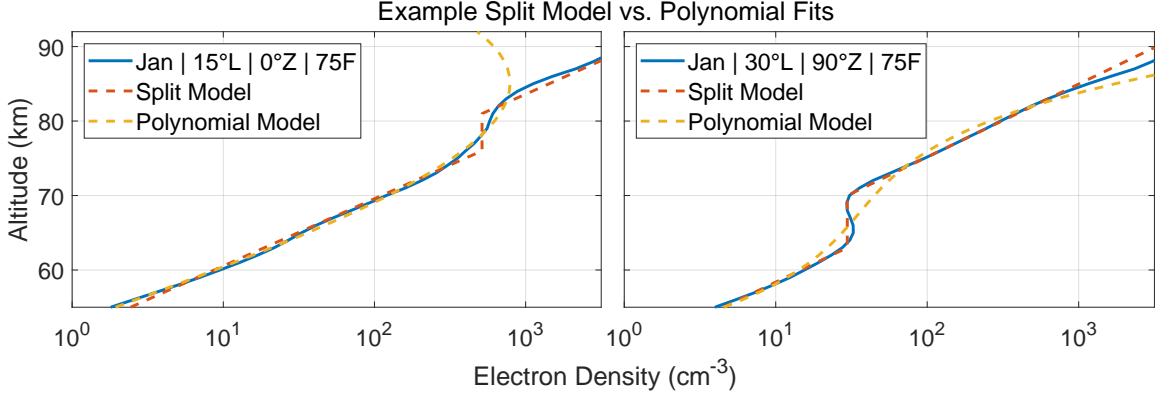


Figure 4.8: Two example fits of the split model vs. a third order polynomial fit. The legend indicates these parameters as follows: L=latitude, Z=solar zenith angle, and F=F10.7

non log-linear features of the lower ionosphere, we compare to a polynomial model, another natural extension of the Wait and Spies linear model.

We evaluate by taking FIRM to be ground truth and comparing the best fit split model and polynomial model from  $10^0$  to  $10^3$  cm<sup>-3</sup> as the  $\ell_2$  norm of the difference. The objective function for the split model is a non-convex problem, so to solve for the best fit, we solve with 100 different initial guesses over the parameter space in Table 4.2 for all 1440 daytime FIRM profiles, recording the lowest  $\ell_2$  norm as the best fit. The best fit for the polynomial model is a well-solved problem and the global minimum is readily determined. Some examples of the best fits are shown against some FIRM  $N_e$  profiles in Figure 4.8.

The statistics for the fits are summarized in Table 4.3. The median for daytime fit slightly favors the third order polynomial fit, but the standard deviation is markedly worse

Model	Median	Standard Deviation
Split	2.854	1.008
Third Order Polynomial	2.541	1.390

Table 4.3: Statistics of norms for all daytime profiles for the different fit methods.

Parameter	Minimum	Maximum	Delta Step
$h'$ (km)	64	90	1
$\beta$ (km <sup>-1</sup> )	0.3	0.9	0.025
$s_\ell$ (km)	55	95	5
$\Delta h$ (km)	0	20	4

Table 4.4: Search space for split model parameters to use for ionospheric matching.

indicating a less stable fit. This is borne out in the example curves in Figure 4.8. In the left panel, the polynomial fit has a lower residual, but the curve outside the fit space tends to suggest non-physical electron densities. In the right panel, the split model significantly outperforms the polynomial mode. In addition, the parameter space that spans the day-time solutions suggested by FIRI is significantly smaller, reducing the computational load required to cover the spheric propagation geometry in the Americas.

In order to determine which electron density profiles to use for ionospheric remote sensing, we discretize the 4 parameters describing the split model into a 4D grid with parameter spacing given in Table 4.4. The search space was chosen to exceed the possible range of ionospheric variability. Next, we perform the matching algorithm for the sensitive range of electron density and produce a 4D histogram for the best fit parametrized profile for every FIRI profile. Lastly, we step through each combination of  $s_\ell$  and  $\Delta h$  to empirically determine the profiles with 2 km  $h'$  and 0.05 km<sup>-1</sup>  $\beta$  spacing which would encompass most of the best fits. This procedure attempts to span the majority of ionospheric profiles as described by FIRI while only needing a tractable amount of simulations.

Inevitably, though, to compare our results to other past results, we need to reduce our split model back to a 2-parameter model. This will also be useful since the Wait and Spies model seems to predict broadband prediction at night quite well [Cummer *et al.*, 1998; Cummer, 2000; Hu and Cummer, 2006; Cheng *et al.*, 2006; Han and Cummer, 2010a,b; Han *et al.*, 2011], so we may not need the 4-parameter split model in all situations. Therefore, we conduct a literature search to determine which Wait and Spies profiles were inferred, expanding the list of profiles used in this work to include these profiles where applicable. The list of all 359 ionospheric profiles used in this work is in Appendix A, and the range of 2-parameter profiles determined in the broadband spheric-based  $D$  region sensing literature are listed in Table 4.5.

Table 4.5: Survey of sferic-based Wait and Spies  $N_e$  inferences

Reference	Cases Considered	$h'$ Range (km)	$\beta$ Range ( $\text{km}^{-1}$ )
<i>Cummer et al.</i> [1998]	Nighttime	85.0–86.1	0.49–0.52
<i>Cheng et al.</i> [2006]	Nighttime	82.0–85.6	0.40–0.55
<i>Han and Cummer</i> [2010a]	Nighttime	82.0–87.2	0.65*
<i>Han and Cummer</i> [2010b]	Daytime and Solar Flare	63–80	0.3*
<i>Han et al.</i> [2011]	Daytime	72.5–76	0.37–0.45
<i>Lay et al.</i> [2014]	Daytime	66.4–69**	0.65–0.85**
<i>Lay et al.</i> [2014]	Nighttime	79.0–82.9**	2.5–3.1**
<i>Lay et al.</i> [2014]	Nighttime Above T-Storm	82.5–84.2	0.90–1.50

\* Are assumed values by authors for inferred results.

\*\* Authors give results in standard deviations. The table results assume results span 1.5 standard deviations.

We have shown that the split model is a 4-parameter extension to the Wait and Spies model which is capable of matching measured ionospheric structure not well modeled by only 2 parameters. To verify that a split model can produce sferic features not predicted by a Wait and Spies model, we directly compare sferic simulations from electron density profiles similar to a split model in which the split location is in the center of the sensitive range of  $N_e$ . The analysis is shown in Figure 4.9.

Upon inspection, the split model clearly has different spectral content than any of the example Wait and Spies profiles. For amplitude, the spectral nulls are in a similar location, but the higher frequencies are relatively weaker compared to the Wait and Spies profiles considered here. Furthermore, the  $B_\phi$  phase spectrum differs significantly above 30 kHz with a simpler decay in phase than the Wait and Spies examples. The unique features predicted by the split model may important to infer VLF waveguide parameters from sferics.

### 4.3 Inverse Modeling Approach

With each component of the propagation model in place, we desire to compare the simulated sferics to processed sferics. First, we need to describe how to synthesize a simulated sferic using LWPC.

Real CG lightning strokes have a roughly unipolar current at the base which attenuates with time and altitude as it propagates toward the cloud. LWPC cannot directly model such a source, as LWPC uses dipole point source at a single frequency, and then calculates

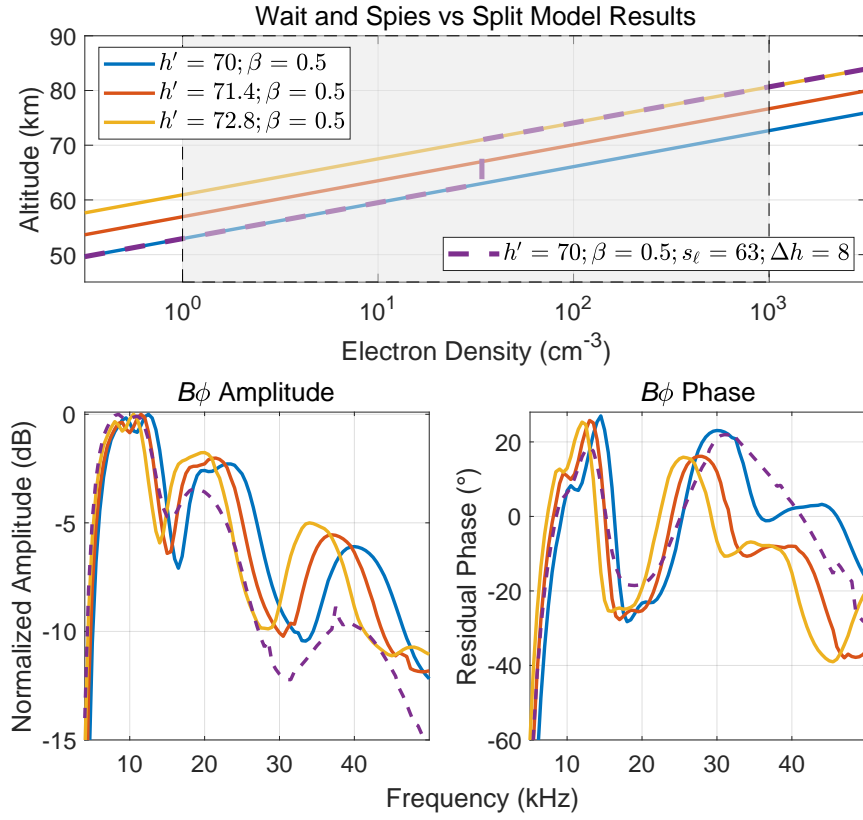


Figure 4.9: A comparison of simulated spheric spectra produced by the Wait and Spies vs. split model for electron density. The simulated path is from (20°N,-76°E) to Baxley (See Baxley information in Table 3.1).



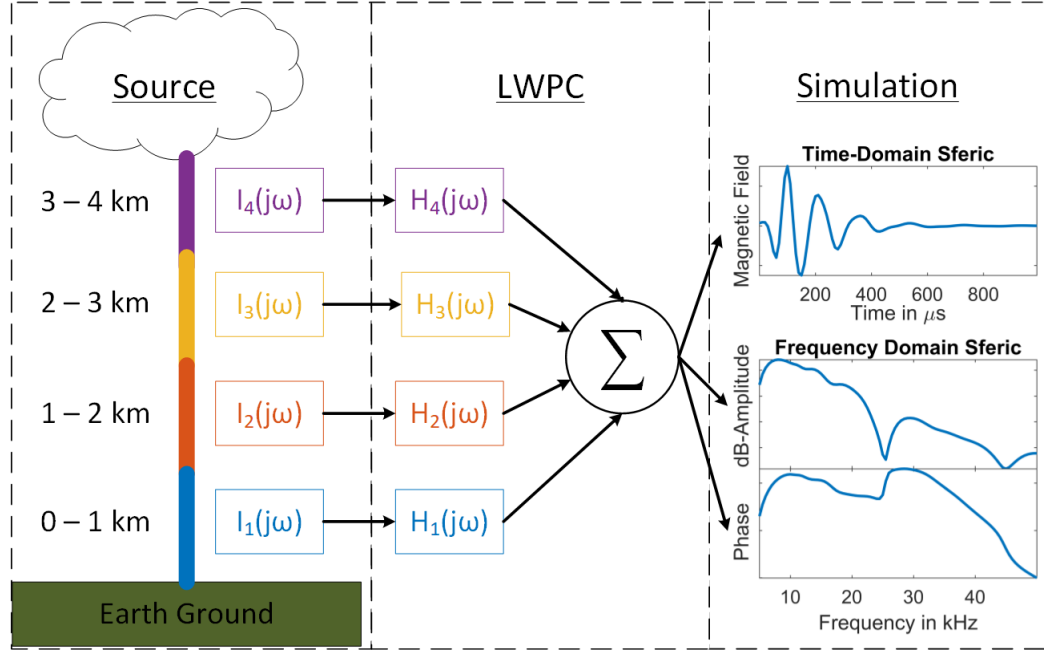


Figure 4.10: Cartoon demonstrating the process used to simulate sferics with LWPC.

the amplitude and phase with distance of the electric and magnetic fields.

EIWG propagation from a source to a receiver is linear. Therefore, we can model it as a transfer function and characterize the system directly in the frequency-domain. The altitude of the point dipole source has an impact on wave propagation. Therefore, for each frequency and altitude, we use LWPC to simulate both the amplitude and phase vs. distance. The complex number corresponding to the amplitude and phase result is the transfer coefficient for a single frequency and altitude at a set distance.

We can approximate the radiated fields from the lightning stroke by calculating the complex field strength for each segment. We assume the value at the center of each stroke segment to be the strength of a point dipole source to match LWPC. We make this calculation for each frequency and altitude, fully characterizing the input to our system. As an example, the entire process is shown in Figure 4.10 for a positive lightning stroke. The input frequency weights are calculated by the discrete Fourier transform. The output of the system will be in complex numbers which are easily converted to amplitude and phase values. Lastly, to match the sferic processing steps, we remove the phase ramp as shown in Figure 3.16.

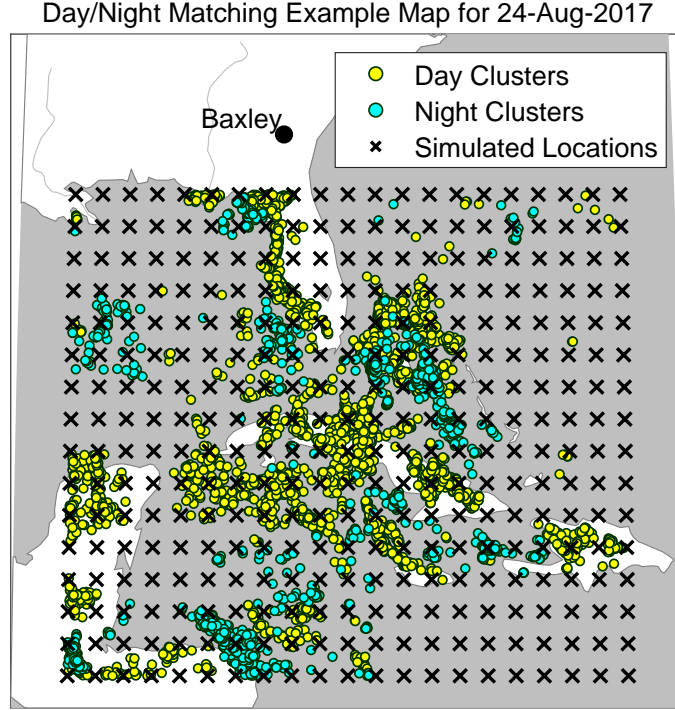


Figure 4.11: Map of the lightning data and simulation grid used for the matching examples of Figures 4.12–4.14. Each dot represents a clustered sferic group center location.

When comparing to a single processed sferic cluster, we first choose the appropriate lightning channel parameters to match the clustered sferic polarity. Next, we simulate sferics for all chosen 359 ionospheric profiles at the 4 simulated latitude/longitude locations surrounding the cluster location. We apply a 2D bi-linear interpolation on the 4 simulated locations for the log-amplitude and phase for each profile. This allows to infer the characteristics at the exact sferic cluster centroid location. It is then possible to determine the best-fit ionosphere by simply comparing the difference in log-amplitude and phase. The best fit is taken as the smallest  $\ell_2$  norm of the difference between the measured and the simulated sferics.

As an example, we choose an area defined by a geographic ‘square’ between  $15^\circ$  to  $30^\circ$  latitude and  $-90^\circ$  to  $-70^\circ$  longitude, with simulated sferics at each  $1^\circ$  step. For a test day of 20-Aug-2017, we consider processed sferics propagating to the receiver at Baxley. The measurement geography is shown on a map in Figure 4.11.

All the matches for the example geometry are shown in the scatter plot of Figure 4.12. The diurnal daytime vs. nighttime differences are the most obvious feature for all 4 split

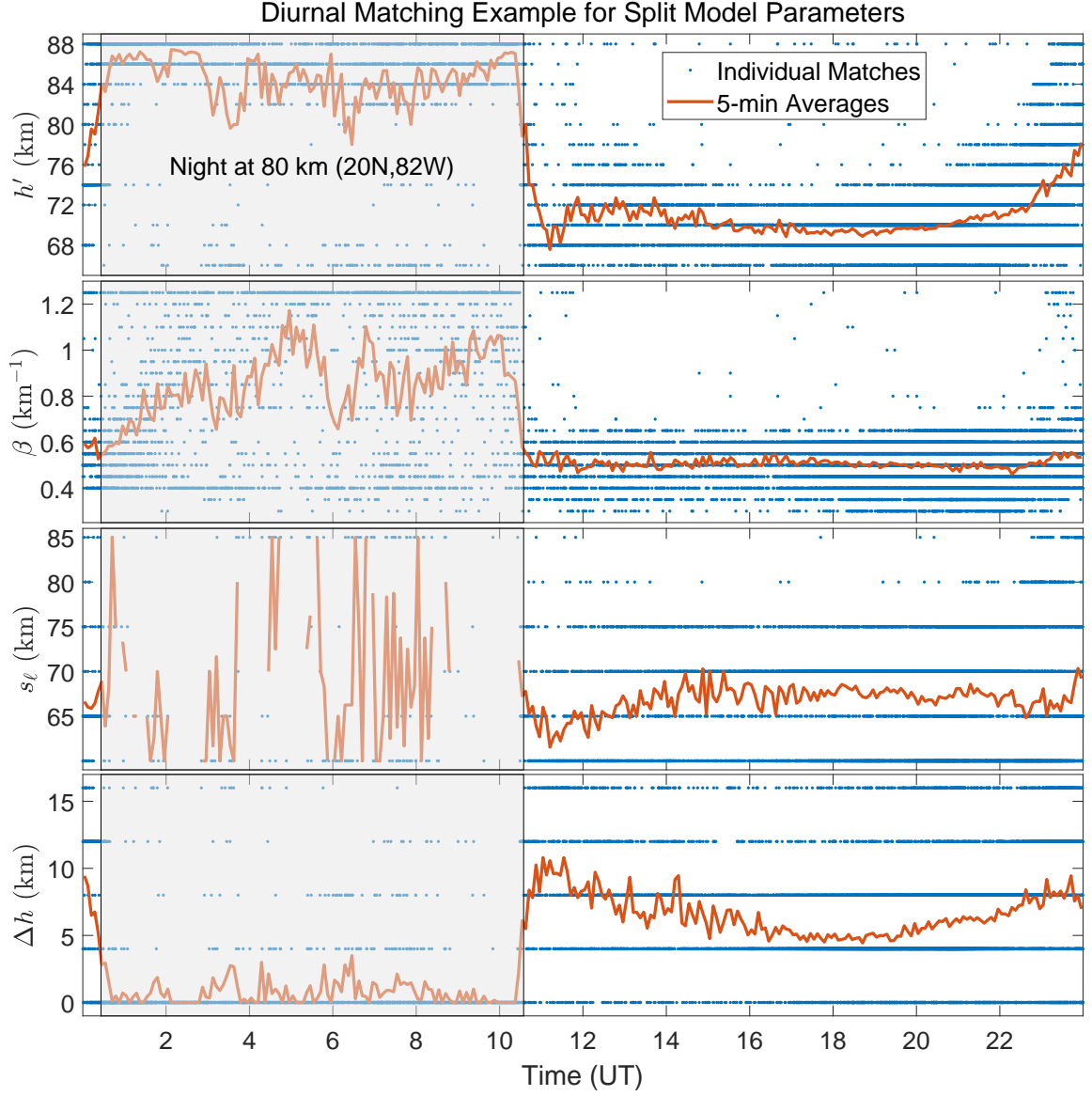


Figure 4.12: Scatter plot showing ionospheric matches vs. time of day for each of the split model profiles  $h'$ ,  $\beta$ ,  $s_\ell$ , and  $\Delta h$ . The matches are binned and averaged with 5 min windows for each parameter displayed as a red curve. The grey patch indicates nighttime at 80 km and (20°N, -82°E). The split model parameters are described in Section 4.2.

model parameters. In addition, most parameters seem to vary throughout the daytime and nighttime respectively. However,  $\beta$  remains relatively steady during the daytime and  $\Delta h$  during the nighttime.  $h'$  and  $\beta$  vary temporally more during nighttime than the daytime. The daytime  $h'$  variation corresponding to varying solar zenith angle is expected and in common with many  $D$  region studies (e.g. *Han and Cummer* [2010b]). A similar variation with solar zenith angle is observed in  $\Delta h$  and less obviously with  $s_\ell$ . For  $\Delta h = 0$ ,  $s_\ell$  is undefined, so the count of  $s_\ell$  diminishes during the nighttime. The nighttime average of  $\Delta h$  approaching 0 indicates that Wait and Spies model is better at predict nighttime sferic propagation. In contrast, a low  $\Delta h = 0$  count during the daytime indicates that the Split model better predicts daytime propagation. To further understand the pattern of matched electron density profile parameters, we isolate purely daytime and nighttime propagation matching for  $B_\phi$  amplitude in Figures 4.13 and 4.14.

For daytime propagation considered in Figure 4.13, there is a clear preference for split model results as seen by the count of  $\Delta h > 0$ . Because of this, direct comparisons of  $h'$  and  $\beta$  to previous work is not valid since the split predicts unique spectral features as seen in Figure 4.9. The distributions for  $h'$ ,  $\beta$ , and  $\Delta h$  are close to Gaussian, while  $s_\ell$  is not. Importantly, the results indicate that the split model is more capable of predicting propagated sferics while also remaining truer to modeled predictions of the  $D$  region.

In contrast, for nighttime propagating sferics (Figure 4.14), the Wait and Spies profiles were sufficient to accurately reproduce the sferic amplitude waveforms as evidenced by the high count of  $\Delta h = 0$ . The addition of split models did not significantly improve the best-fits.  $h'$  appears to be normally distributed again, but  $\beta$  is markedly more complicated. Because of the low counts of  $s_\ell$  we do not attempt to draw any conclusions about it.

#### 4.3.1 Matching Examples

To understand the structure and pattern of the ionospheric matches we consider some special cases. First, we identify regions with lightning that occurred persistently throughout a long period of time in order to consider changing ionospheric conditions as observed by our matching algorithm. We consider three cases: a quiet solar day, a solar eclipse, and a solar flare. The map and description of the regions of study are described in Figure 4.15 and

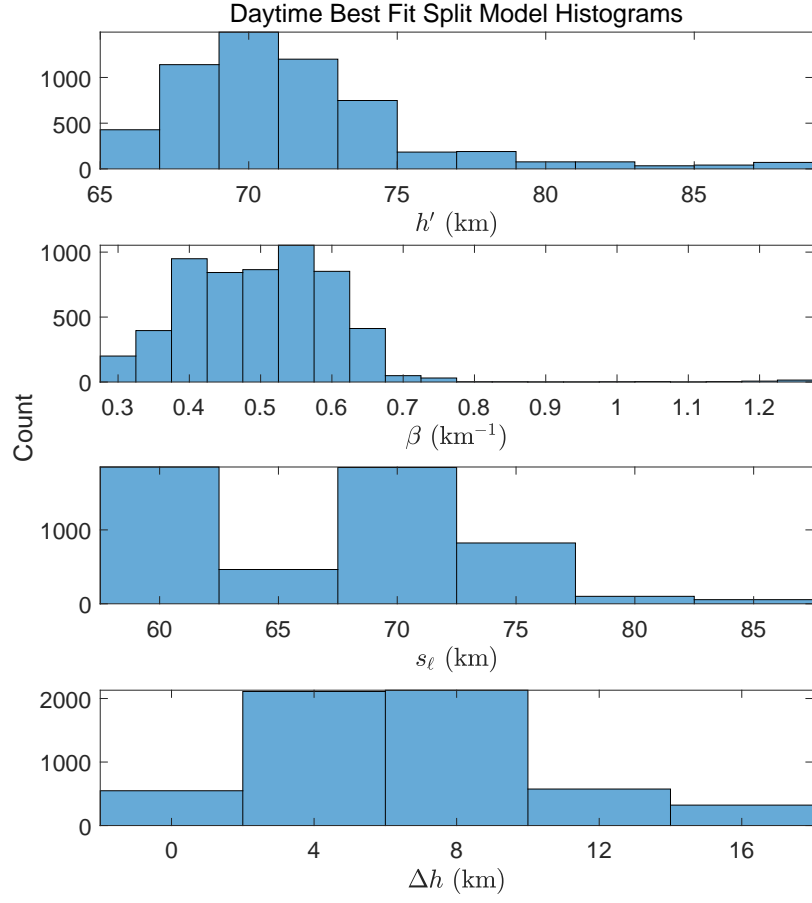


Figure 4.13: Histogram of matched split model parameters during the daytime for the example geometry shown in Figure 4.11. The used clusters occurred between 16:00 and 24:00 UT.

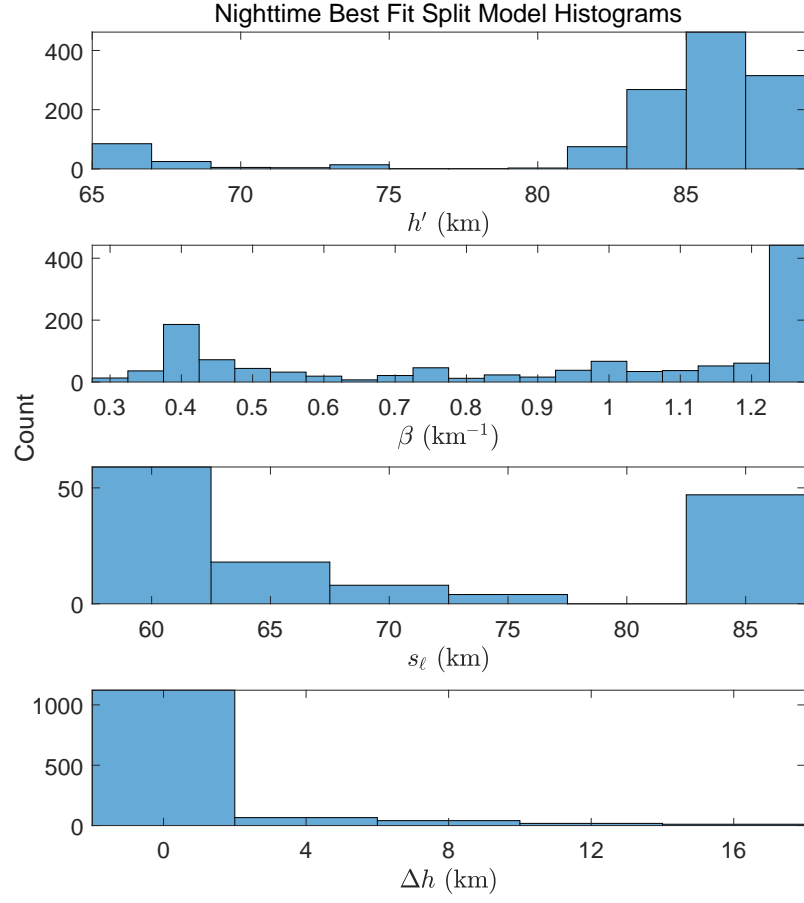


Figure 4.14: Histogram of matched split model parameters during the nighttime for the example geometry shown in Figure 4.11. The used clusters occurred between 2:00 and 8:00 UT.

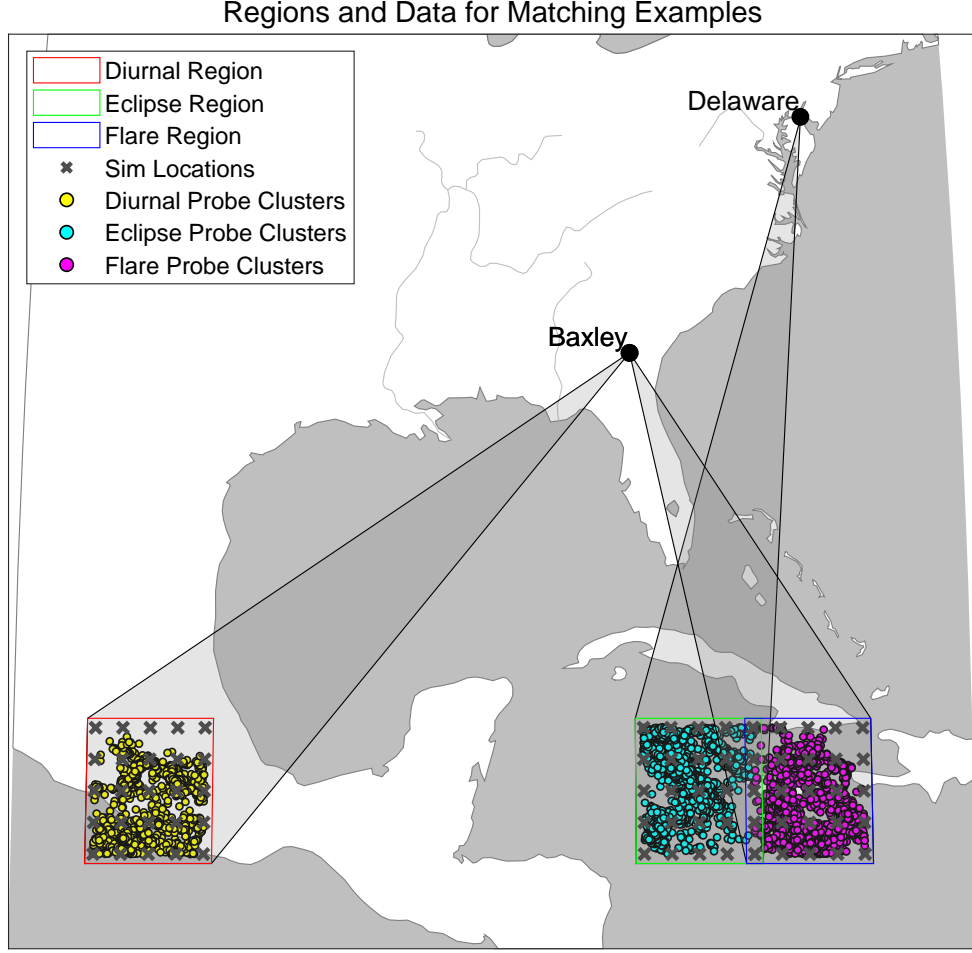


Figure 4.15: Map of the lightning location regions, simulated sferic locations, and clustered sferics used in the matching examples. The grey patches indicate the geographical regions which are sensed by the corresponding source region. More detailed information about the regions is given in Tables 4.6 and 4.7.

Tables 4.6 and 4.7.

The quiet day example is shown in Figure 4.16. The best fit simulation is obtained by the procedure described in this chapter considering the best combined fit of log-amplitude and phase from 5–25 kHz. In agreement with past work, the *D* region is more weakly ionized during the nighttime compared to the daytime. The nighttime sferics have more detailed spectral features due to the presence of more than one dominant mode, thereby making an interference pattern in frequency. In agreement with the statistical analysis, the nighttime matches are best predicted by a Wait and Spies model profile, whereas the daytime matches are best predicted by a split model profile. In all cases, the amplitude

Case Study	Day	Receiver	Number of Clusters
Diurnal Probe	24-Aug-2017	Baxley	2090
Solar Eclipse	21-Aug-2017	Delaware	2329
Solar Flare	20-Aug-2017	Baxley	1767

Table 4.6: Regions of study used for the ionospheric matching case studies.

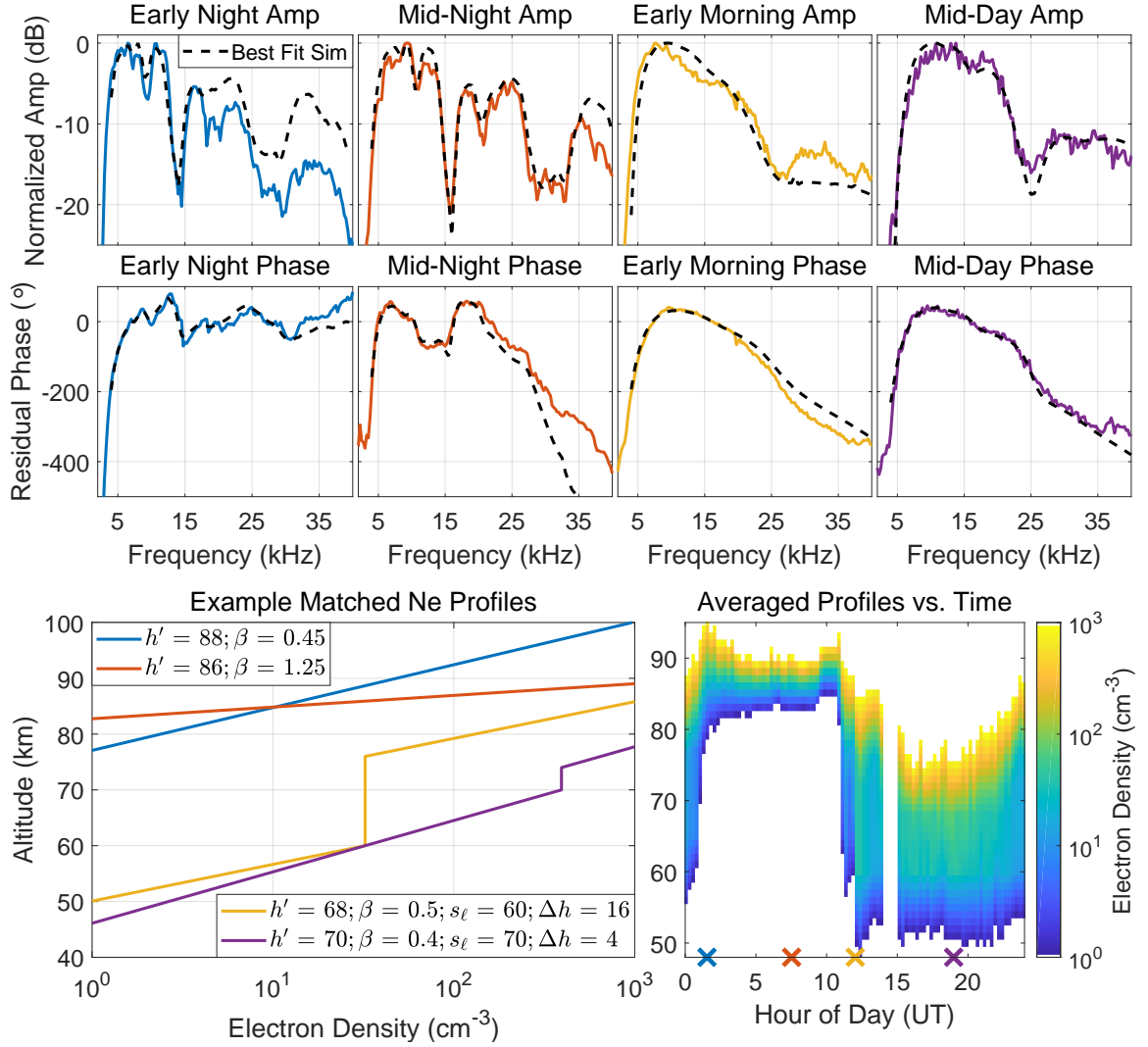


Figure 4.16: Matching examples for the diurnal variation of the ionosphere. Colored signals are processed sferics with more information given in Tables 4.6 and 4.7. The black curves are the best fit simulations with the model parameters given in the bottom-left panel along with the corresponding electron density curves. The bottom-right panel shows the electron density vs. altitude where each displayed profile is the mean of all present ionospheric inferences with at least 5 matches available. The white space indicates the electron density is above or below the range of  $10^0 - 10^3 \text{ cm}^{-3}$  or there were less than 5 matches available and then nothing is included.



Case Study	Probe Label	Number in Cluster	Mean Location(°)	Mean Time(UT)
Diurnal Probe	Early Night	5	18.94N, -98.24E	01:32 UT
Diurnal Probe	Mid-Night	15	16.94N, -101.18E	07:31 UT
Diurnal Probe	Early Morning	25	18.14N, -101.81E	12:02 UT
Diurnal Probe	Mid-Day	8	16.93N, -98.14E	18:59 UT
Solar Eclipse	Pre-Eclipse	30	19.73N, -81.23E	16:59 UT
Solar Eclipse	During Eclipse	15	19.99N, -81.52E	19:02 UT
Solar Eclipse	Eclipse Tail	11	18.06N, -80.26E	19:32 UT
Solar Eclipse	Post Eclipse	2	18.17N, -80.35E	21:00 UT
Solar Flare	Pre-Flare	26	18.94N, -76.51E	18:12 UT
Solar Flare	During Flare	22	16.00N, -75.80E	19:34 UT
Solar Flare	Flare Tail	24	16.15N, -76.26E	19:56 UT
Solar Flare	Post Flare	18	18.08N, -75.36E	21:56 UT

Table 4.7: Detailed information on sferic clusters used in the matching examples for each of the case studies. All clusters used in these examples are positive stroke polarity.

and phase of the processed sferics agree very well with the best fit simulation. For the early night and early morning amplitude, the fit is worse and may be related to the fact that the path consists of partial day and night propagation.

The diurnal effect is clearly observed in the mean inferred electron densities. At sunset and sunrise, a slow transition over a couple hours between nighttime ionospheres and daytime ionospheres can be clearly observed since the sunrise and sunset takes a few hours to fully cover the transmitter-to-receiver paths. During the times when the entire path is daytime or nighttime the results are consistent with expected values.

The eclipse case study is shown in Figure 4.17. Throughout the solar eclipse evolution, the ionizing radiation from the sun is at first gradually blocked and then the process is reversed. The solar eclipse totality crosses the path at  $\sim 18:52$  UT and because of the relatively quick recombination time in the lower ionosphere, we expect the maximum impact to occur at this time. The perturbation in the daytime ionosphere can be seen in the mean-inferred profiles which are shown in lower-right panel. Throughout the solar eclipse, the ionosphere becomes less ionized as expected, effectively moving upward, and then partially recovering close to the pre-eclipse state. The processed sferic waveform shows some interference pattern between 16-20 kHz not typically observed during the daytime and may be related to scattering directly off the totality as observed in *Cohen et al.* [2018a].

The solar flare case study is shown in Figure 4.18. The burst of X-rays that occur during

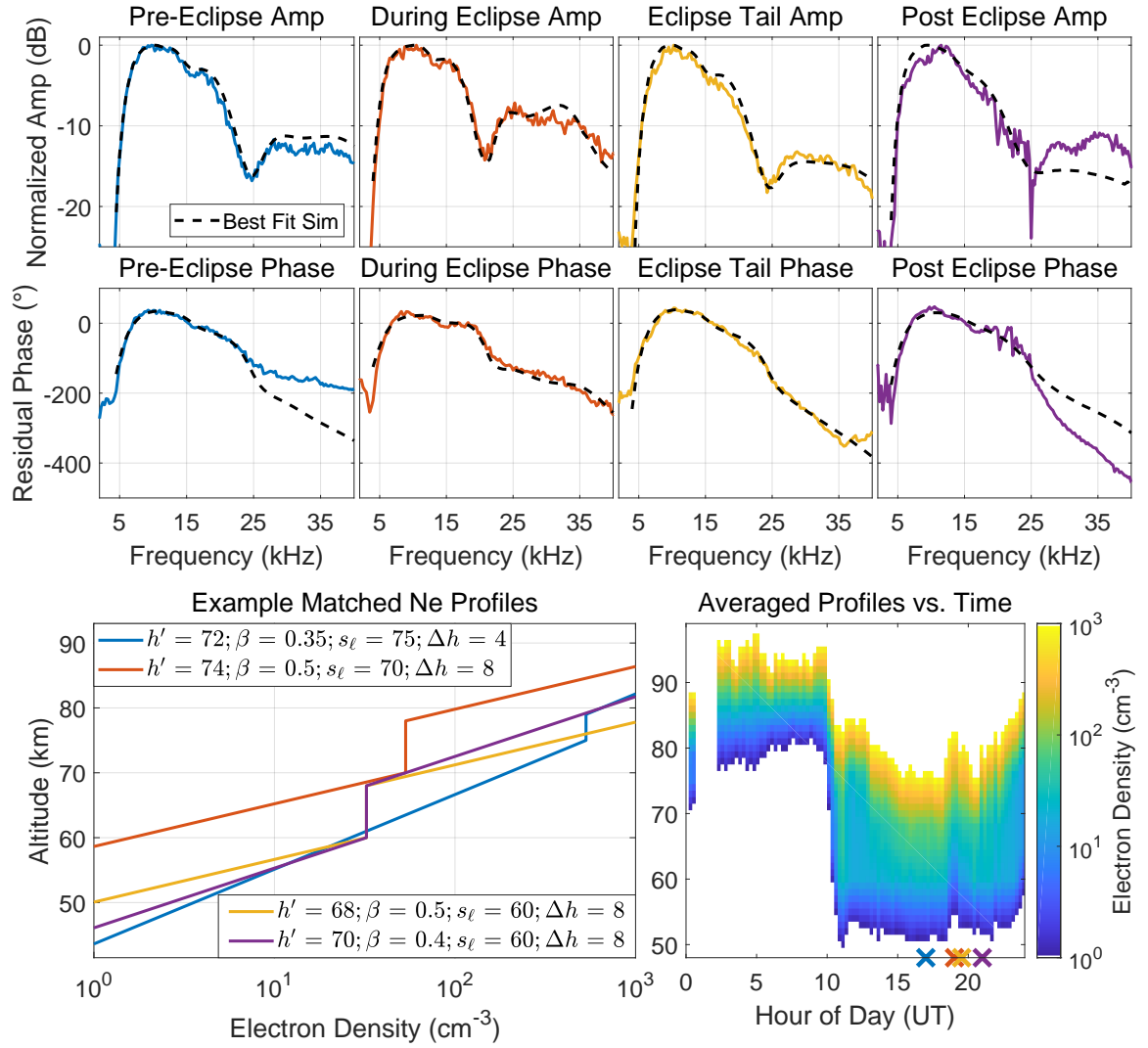


Figure 4.17: Matching examples for the inferred modification of the ionosphere during a solar eclipse. Colored signals are processed sferics with more information given in Tables 4.6 and 4.7. The black curves are the best fit simulations with the model parameters given in the bottom-left panel along with the corresponding electron density curves. The bottom-right panel shows the electron density vs. altitude where each displayed profile is the mean of all present ionospheric inferences with at least 5 matches available. The white space indicates the electron density is above or below the range of  $10^0 - 10^3$   $\text{cm}^{-3}$  or there were less than 5 matches available and then nothing is included.

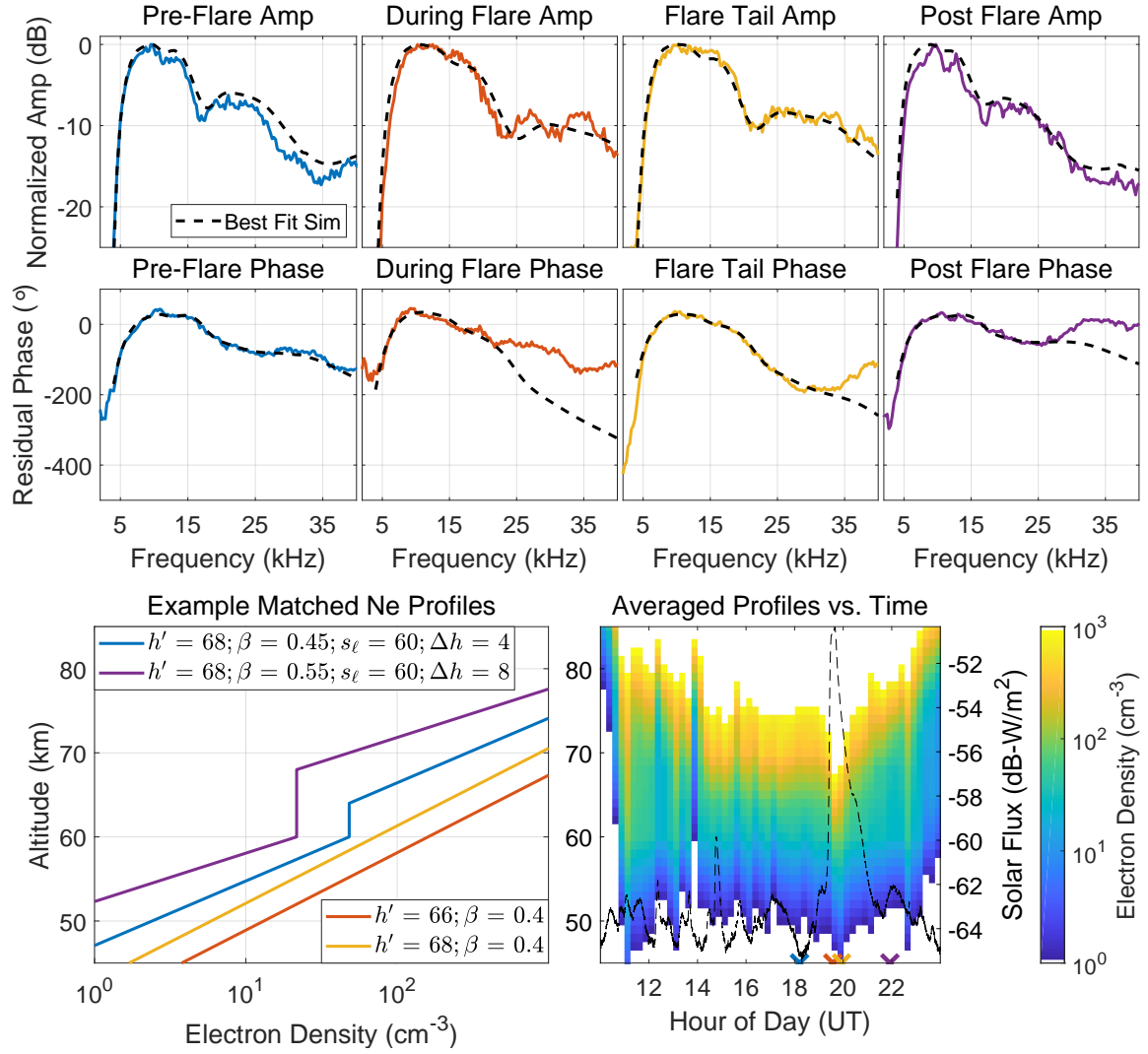


Figure 4.18: Matching examples for the inferred modification of the ionosphere during a solar flare. Colored signals are processed sferics with more information given in Tables 4.6 and 4.7. The black curves are the best fit simulations with the model parameters given in the bottom-left panel along with the corresponding electron density curves. The bottom-right panel shows the electron density vs. altitude where each displayed profile is the mean of all present ionospheric inferences with at least 5 matches available. The white space indicates the electron density is above or below the range of  $10^0 - 10^3 \text{ cm}^{-3}$  or there were less than 5 matches available and then nothing is included. The solar flux, as measured by GOES, is overlaid as a black dashed curve.

a solar flare can penetrate to the lower ionosphere and cause a significant perturbation to the electron density structure. As expected, and commonly observed, the increased electron density effectively lowers the  $D$  region. However, in contrast to the ambient daytime case where the split model consistently better predicts spheric propagation, the Wait and Spies model better predicts sferics propagating during a solar flare. As the solar flux diminishes, the ionosphere recovers to the ambient case, and the best fit ionosphere is represented by a split model again.

### 4.3.2 Discussion

#### *Implications of Profile Selections*

The solar flare matching example of Figure 4.18 highlights the utility of the matching technique and split model to better study the structure of the lower ionosphere. The scatter plot of matched profiles parameters vs. time is shown in Figure 4.19. We again observe a shifting of profile type during the brightest part of the solar flare as evidenced by  $\Delta h$  approaching 0. We also observe reduction in  $h'$ . The lowering  $h'$  implies a general increase in electron density, while a decreasing  $\Delta h$  implies an increase of electron density at certain altitudes. The combined effect indicates that the different altitudes of the  $D$  region are affected differently by solar flares. The effect on  $\beta$  is visible but less pronounced.

Although the ionospheric profiles we selected were informed by FIRM, this example highlights a potential weakness of the brute force inverse modeling technique used in this work and by others. Namely, the electron density profiles are pre-selected therefore intuition and past models guide profile selection but may not choose all relevant ionospheres. On the other hand, selection of too many profiles to cover ‘every’ potentially relevant case will quickly become intractable. Even for the moderate number of profiles used in this study, we estimate it would take a standard 4 core machine  $\sim 440$  years to complete. To complete the simulations required for such a general matching algorithm, we are indebted to the Partnership for an Advanced Computing Environment (PACE) operated at Georgia Tech [PACE, 2017].

Lightning-induced electron precipitation (LEP) is known to modify the  $D$  region of the

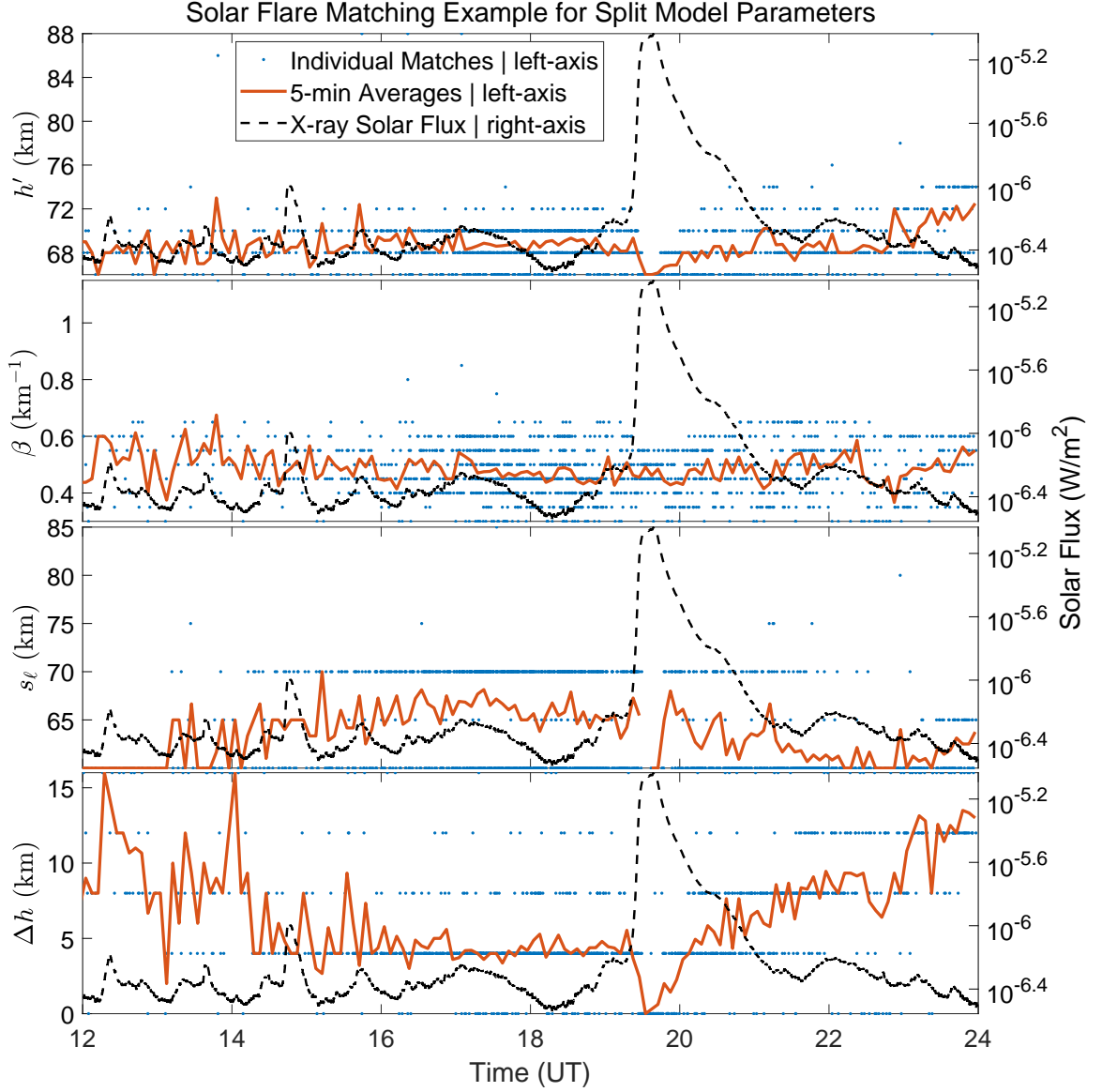


Figure 4.19: Scatter plot showing ionospheric matches vs. time of day for each of the split model profiles  $h'$ ,  $\beta$ ,  $s_e$ , and  $\Delta h$ . The matches are the same used for the solar flare example in Figure 4.18. Matches are binned and averaged with 5 min windows for each parameter and is displayed as a red curve. The solar flux observed by GOES is overlaid as a dashed black curve. The split model parameters are described in Section 4.2

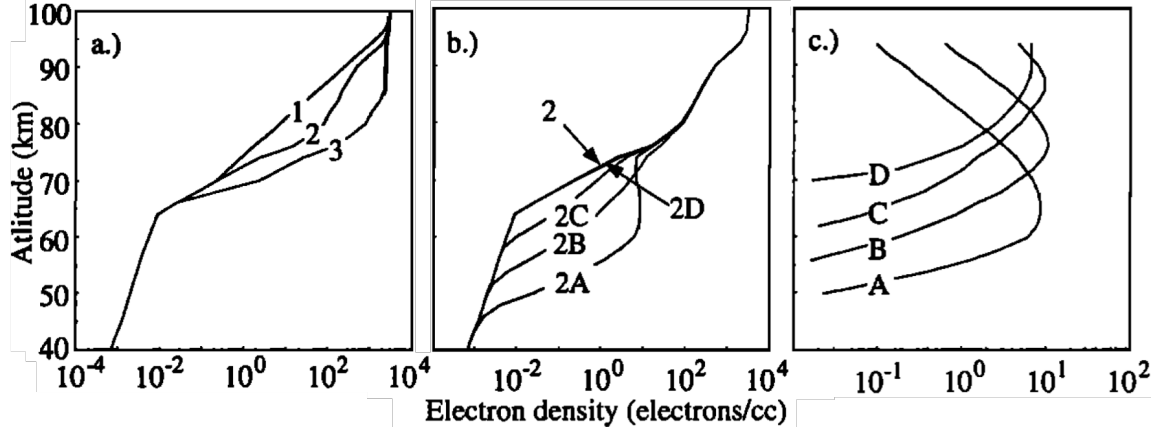


Figure 4.20: Figure describing the effect of lightning-induced electron precipitation (LEP) on the *D* region ionosphere adapted from *Lev-Tov et al.* [1995]. (a) Three assumed ambient ionospheres varying in density. (b) Possible perturbations to profile 2 caused by LEP at the center of the disturbance. (c) The excess ionization caused by different energy populations of precipitating electrons. Profiles 2A-2D are given as the sum of the excess ionization to profile 2. Further details given in *Lev-Tov et al.* [1995].

ionosphere. The exact nature of the perturbation depends on the intensity and particle energy distribution [*Lev-Tov et al.*, 1995]. However, the structure of the perturbed ionospheres qualitatively seems to take the form of a split model ionosphere. The profiles selected in this work did not extensively consider the possibility of measuring split ionospheres at night-time. Nonetheless, it may be possible to detect such an event if additional representative profiles were included.

Including more profiles may help to study a greater breadth of ionospheric phenomena such as LEP, extreme solar flares where the lower ionosphere is effectively lowered below the included profiles, or the polar regions where a myriad of energetic electrical storms are known to modify the lower ionosphere. However, for the ambient quiet day, solar eclipse, and solar flare shown here we can track changes in the lower ionosphere, and the results are similar in electron density ranges to past work. The summary of past events is shown in Table 4.8 with relevant results reproduced from Table 4.5 for convenience.

Table 4.8: Survey of relevant Wait and Spies  $N_e$  inferences

Reference	Method <sup>1</sup>	Case	$h'$ (km)	$\beta$ (km <sup>-1</sup> )
<i>Thomson et al.</i> [2005]	NB	Solar Flare	53–70	0.39–0.58
<i>Thomson et al.</i> [2007]	NB	Night	84.7–85.5	0.59–0.67
<i>Cummer et al.</i> [1998]	BB	Night	85.0–86.1	0.49–0.52
<i>Cheng et al.</i> [2006]	BB	Night	82.0–85.6	0.40–0.55
<i>Han and Cummer</i> [2010a]	BB	Night	82.0–87.2	0.65 <sup>2</sup>
<i>Han and Cummer</i> [2010b]	BB	Solar Flare	63.4–70 <sup>3</sup>	0.3 <sup>2</sup>
<i>Lay et al.</i> [2014]	BB	Night	79.0–82.9 <sup>4</sup>	2.5–3.1 <sup>4</sup>
<i>Lay et al.</i> [2014]	BB	Night Over T-Storm	82.5–84.2	0.90–1.50

<sup>1</sup> BB for broadband studies, NB for narrowband studies

<sup>2</sup> Are assumed values by authors for inferred results

<sup>3</sup> Estimated lowest ambient value from this work

<sup>4</sup> Authors give results in standard deviations, table results assume results span 1.5 standard deviations

### *Selected Comparisons to Past Models*

Since spheric propagation is often better predicted by the split model introduced in this work, it is difficult to directly compare the certain matches to past works (e.g. ambient daytime). However, since during a solar flare, the Wait and Spies model tends to better predicts spheric propagation, we can directly compare to past results. In addition, since the nighttime propagation is best explained by the Wait and Spies model, we will consider these two comparisons. Such a direct comparison across different methods, frequencies, occurrence times, path geometries, etc. should be taken with a grain of salt. Nonetheless it can be helpful to check for an agreement since these are all VLF-based methods.

In order to compare the results in this work more directly and improve fit confidence we average all the ionospheric inferences together during the peak of the solar flare considered earlier on Aug-20-2017 (19:30–19:47 UT) with results are given in Table 4.9. For all cases  $h'$  agrees closely. While  $\beta$  agrees much more closely to *Thomson et al.* [2005], it is difficult to consider the  $\beta$  of *Han and Cummer* [2010b], since it is an assumed value.

Past workers have found that the ionosphere tends to vary within a single night and between different nights. Therefore, we consider all available matches for the 2 months from Jul-01-2017 to Aug-31-2017. We use matches from 3:00–9:00 UT in order to ensure that the entire source-to-receiver path is in the nighttime. Next, limit lightning clusters to a grid

Table 4.9: Inferred  $h'$  and  $\beta$  parameters for a class M1 solar flare as determined by GOES. Values in literature estimated from figures contained within.

Reference	Method	$h'$ (km)	$\beta$ (km <sup>-1</sup> )
This work	Broadband	66.24	0.477
<i>Thomson et al.</i> [2005]	Narrowband	67	0.45
<i>Han and Cummer</i> [2010b]	Broadband	66	0.3*

\*  $\beta$  is assumed here in order to determine  $h'$

from 15° to 30° latitude and -90° to -70° longitude and use any available matches to every receiver except for Juneau. For each hour we take the statistics of the fits and the results are shown in Figure 4.21.

The standard deviation is plotted above and below the means of both  $h'$  and  $\beta$  with the area between shaded in grey. The general long-term trends show  $h'$  decreasing over time and  $\beta$  increasing over time. The standard deviation in both parameters are similar throughout the date range giving similar confidence throughout. The values should be interpreted as a broad spatial averages of the lower ionosphere in the Caribbean and the southeast US since the paths cover the entire region. The mean for the entire date range for  $h'/\beta$  is 86.1/0.79 and the standard deviation is 1.7/0.25. For the nighttime case considered here, the results are most consistent with the results of *Han and Cummer* [2010a], although the  $\beta$  is fixed in that work and therefore it is not possible to directly compare. The variation of results is greater here than most of the past work as well, but this may be a reflection of the larger geographical area being sensed in comparison to most studies. Furthermore, the  $\beta$  found in this work does not directly agree with any of the past VLF-based methods but does agree with the FIRI prediction.

The results discussed here are mostly consistent with past results despite the differences between the techniques. In contrast to past broadband sferic-based work, ionospheric inferences are based on spectral signal values, not specific inferred features, and are thus more generally applicable to general lightning source-to-receiver paths.



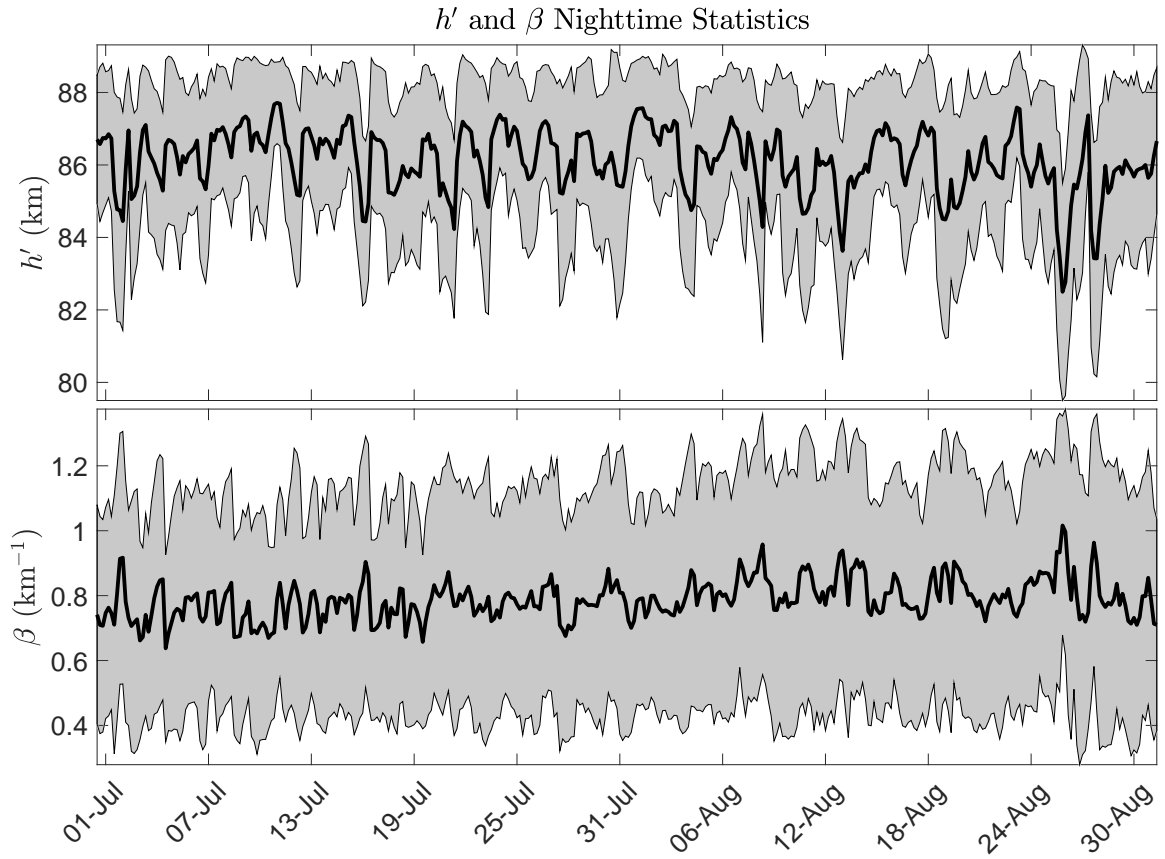


Figure 4.21: Matching statistics for  $h'$  and  $\beta$  for the two months of data considered in this study using the nighttime Wait and Spies profile matches (profiles 43-132). The heavy black curve is the mean for the respective ionospheric parameter. The light black curves above and below the mean represent a standard deviation from the mean. The general data availability is given in Figure 3.5.

## CHAPTER 5

### TOMOGRAPHIC $D$ REGION IMAGING

Tomography is a technique which uses line-integral measurements to understand an underlying object of which it is difficult or impossible to make direct observations. The most widespread use of tomography today is the computed tomography (CT) scan for medical imaging. CT and related technologies have revolutionized the medical industry leading to multiple Nobel prizes.  $D$  region tomography shares some common ideas with CT because through our VLF lighting-to-receiver paths, we also obtain a set of line-integral measurements which are inferred through the inverse modeling technique of Chapter 4.

#### 5.1 Basic Principles

The essential components of the traditional CT approach are present in the path-averaged inferred profiles of the  $D$  region, but some important differences exist. First, in contrast with the well-solved CT approach, the data is not uniformly spaced as it is dependent on the geographical and temporal pseudo-random distribution of natural lightning as well as the operational receiver network. Secondly, the lightning-to-receiver paths are all entirely enclosed inside of the ‘image’. For these reasons, we approach the problem with more generalized signal processing techniques rather than common CT techniques which require a known and controllable measurement scheme.

$D$  region tomography is a linear inverse problem which will use the full set of path-averaged measurements to produce a 4D image of the  $D$  region ionosphere (latitude, longitude, altitude, and time). Even when using every available measurement, an ‘exact’ solution may not be possible in general, due to two major factors. The first is that the sampling system is assumed to be sparse. Unfortunately, we lack ‘ground-truth’ for comparison so there will be no way to guarantee or quantify convergence. As such, we must make a sparse assumption. Second, errors in the path-averaged inferences exist. Some sources of these errors may be due to discretization of the assumed profiles, incomplete set of assumed profiles,

the non-unique nature of an inverse problem, or measurement errors and outliers. Again, the lack of a ‘ground-truth’ makes it difficult to assess the magnitude of these errors. It may be possible to assess the magnitude of measurement errors on imaging performance when considering synthetic data as performed later, but this is beyond the scope of this thesis. Despite these uncertainties, there are well established signal processing methods we adapt to perform  $D$  region tomography.

## 5.2 $D$ Region Tomography with Pixel Representation

As a first approach, we take the  $D$  region to consist of square pixels in latitude/longitude space, and at a set of altitudes. Then each path is curvilinear along the latitude/longitude grid. Because the Earth is an oblate spheroid, we require an accurate geodesic solution for high accuracy of path calculations. The effect of Earth’s curvature on great circle paths can be seen in Figure 5.1, where distortion of paths from the straight lines are worse for higher latitudes. Furthermore, the pixel dimensions are not equal in length, and they are not quite square in terms of geographical lengths. In the highest row,  $85^\circ$  latitude, the squares have length 49 km and height 558 km. In the lower row, corresponding to  $0^\circ$  latitude, the squares have length 557 km and height 553 km. As such, we must account the varying size and shape of each pixel.

The example map uses the equirectangular projection, a map projection that contains grid lines of constant latitude/longitude, which is the most direct comparison to traditional square pixel images. The information about the image from each path is distributed along the image pixels in which it crosses, and importance of each respective pixel is proportional its crossing line segment. In order to accurately calculate path segments and minimize distortion, we use the world geodetic system, wgs84 datum, to determine intra-pixel segment lengths.

Figure 5.2 shows an example of a potential measurement setup for  $D$  region tomography with a small number of paths and receivers with  $5^\circ$  latitude/longitude spacing. The measurement scheme can be written as a matrix-vector product as

$$\mathbf{y} = \mathbf{Ax} \tag{5.1}$$

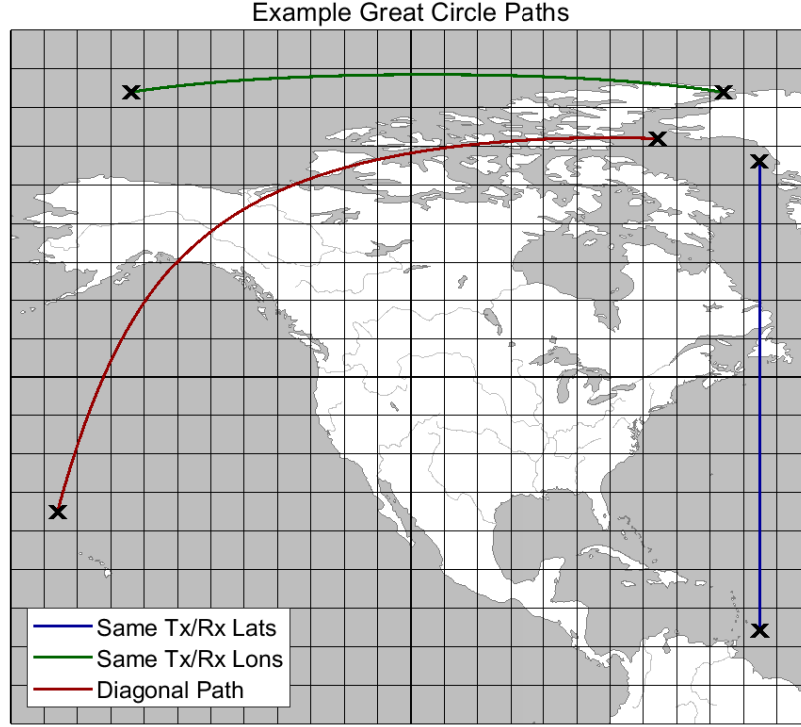


Figure 5.1: Example of curvilinear great circle paths overlaid onto the equirectangular projection.

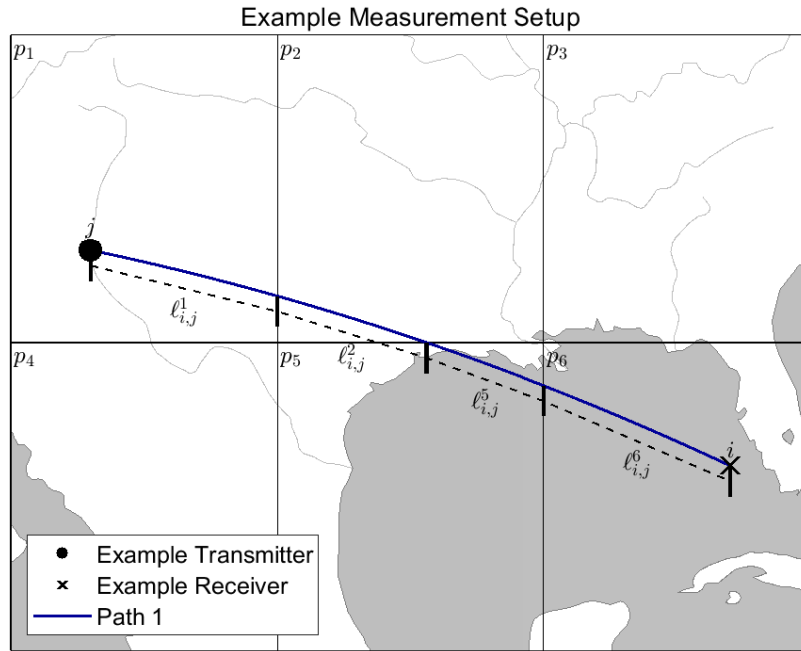


Figure 5.2: Example measurement geometry for the pixel-based  $D$  region tomography method. Paths are overlaid on an example map to show the scale of curvature of the great circle paths.

where  $\mathbf{A}$  represents the line-integral operator against some underlying image  $\mathbf{x}$ , and  $\mathbf{y}$  are the line-integral inferences (or path averaged measurement times the respective path length).  $\mathbf{A}$  is an  $M$  by  $N$  matrix with  $M = I \cdot J$ , where  $I$  is the number of receivers and  $J$  is the number of lightning clusters.  $N$  is the number of pixels in the target image (the image is vectorized to complete the matrix multiplication). Each entry represents the respective pixel's contribution to a line-integral measurement. We can write the example from Figure 5.2 as

$$\begin{bmatrix} y_m \end{bmatrix} = \begin{bmatrix} \ell_{i,j}^1 & \ell_{i,j}^2 & 0 & 0 & \ell_{i,j}^5 & \ell_{i,j}^6 \end{bmatrix} \begin{bmatrix} p_1 \\ p_2 \\ p_3 \\ p_4 \\ p_5 \\ p_6 \end{bmatrix} \quad (5.2)$$

where  $y_m$  are the line-integral measurements and  $\ell_{i,j}^n$  are the line segments present in the respective pixels  $p_n$  for the  $i^{\text{th}}$  receiver and the  $j^{\text{th}}$  cluster. In order to investigate the performance of the pixel basis image reconstruction technique, we consider an assumed ionosphere and the performance of synthetic data. First, we investigate the nature of errors by considering variation in matching performance as described in Chapter 4 for a test case on 24-Aug-2017 from  $24^\circ$  to  $28^\circ$  latitude and  $-94^\circ$  to  $-90^\circ$  longitude. We consider the variation in optimally matched ionospheres for nighttime and daytime cases from 7–9 and 17–18 UT respectively.

We consider the variation of inferred electron density vs. altitude for these time ranges. In order to get a statistically significant number of matches, we consider a relatively long-time window of 2 and 1 hours for the nighttime and daytime cases respectively. We expect the ionosphere to change over the time window and the spatial scales considered. Therefore, our assumption of variation as error in the matching algorithm should be considered the worst-case scenario. The nighttime and daytime cases are shown in a map in Figure 5.3 and the analysis is summarized in Figure 5.4. The nighttime case is shown in the left-hand column and daytime case is shown in the right-hand column. The top row shows the matches over the respective time windows with different colors to increase contrast between

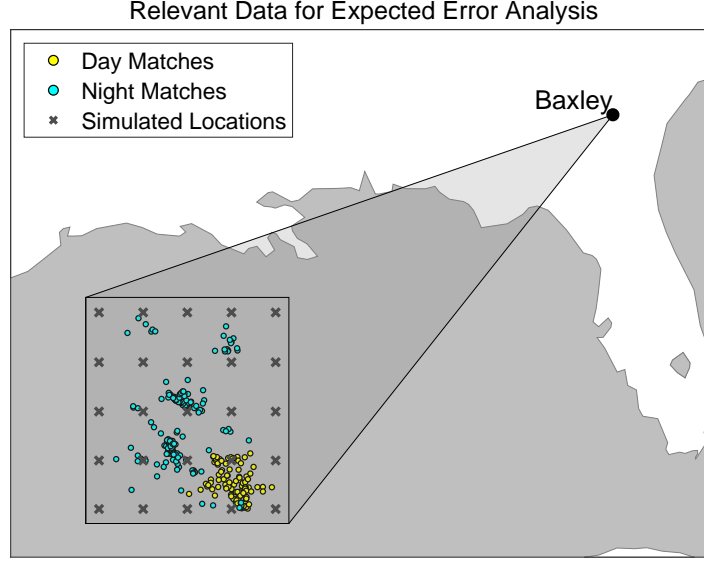


Figure 5.3: Map of the daytime and nighttime cluster locations, receivers, and sensed ionospheric patches used in the matching error analysis.

the curves.

The middle row shows the statistics of the matches showing the median, 16<sup>th</sup>, and 84<sup>th</sup> percentile. We choose this range to capture the statistics that correspond to one standard deviation of a normal distribution. The difference between the 84<sup>th</sup> and 16<sup>th</sup> percentile is shown in the bottom panels. As discussed in Section 4.2.1, nighttime propagation is more sensitive to a wider range of electron density, but the most important range seems to be between 10 and 100 electrons  $\text{cm}^{-3}$ . In this critical range, the nighttime variation is less than  $1.07 \text{ cm}^{-3}$ . In the daytime case, the variation is less than  $4 \text{ cm}^{-3}$  with a minimum of  $\sim 1.6 \text{ cm}^{-3}$  in the middle of the critical electron density range. In conclusion, we establish three error profiles: small, with a variation of 2.1; moderate, with a variation of 3.2; and extreme, with a variation of 8.

In order to examine the effect of matching or measurement error on the imaging algorithms, we will consider synthetically generated ionospheres with the error profiles. We generate random maps of an ionospheric ‘feature’. Next, we synthesize the path integral measurements of Chapter 4 by calculating along the assumed ionosphere. This ionospheric feature could be thought of as a parametrized value like  $h'$ , the electron density at a specific altitude, or some other path-averaged inferred quantity. For this case, we choose a value of

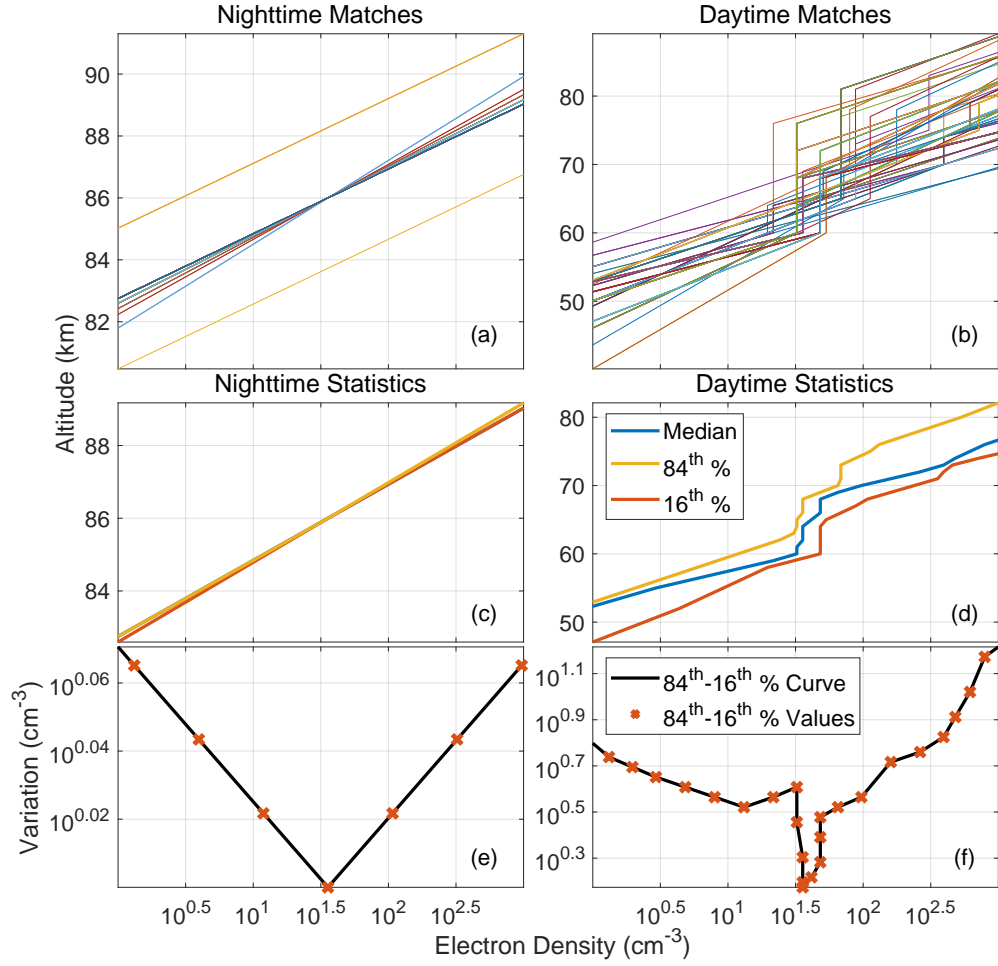


Figure 5.4: Nighttime and daytime variation of ionospheric inferences from a small spatial location to Baxley. The map showing the processed sferic cluster locations is shown in Figure 5.3. (a) The nighttime ionospheric inferences from 7–9 UT. The  $y$ -axis is adjusted to show details in the inferred ionosphere but excludes two outliers which are considered in the subsequent analysis. (b) The daytime ionospheric inferences from 17–18 UT. (c, d) Median, 84<sup>th</sup>, and 16<sup>th</sup> percentile levels of the daytime/nighttime matching ionospheric profiles. (e,f) The difference between daytime/nighttime 84<sup>th</sup> and 16<sup>th</sup> percentile matches.

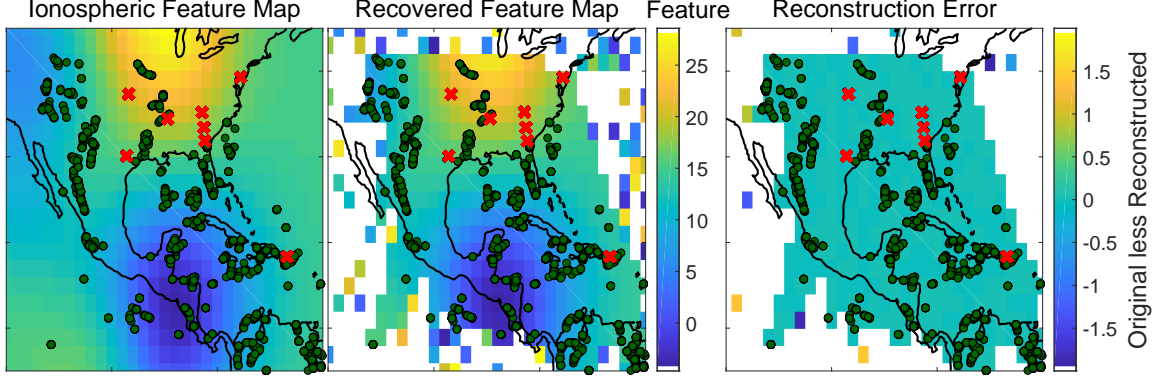


Figure 5.5: Example of the performance of the pixel basis  $D$  region tomography algorithm with noiseless inferences. The left panel is the assumed ionosphere with a  $2^\circ$  by  $2^\circ$  latitude/longitude pixel size. The middle panel is the reconstruction with clipped values exceeding the range of the original. The right panel shows the difference between the original and reconstructed synthetic ionospheric feature map.

15 to correspond to the logarithmic center of the critical electron density range. On top of the center value, we superimpose the summation of 50 random 2D Gaussian functions in the form of

$$f(\phi, \theta) = A \exp \left( - \left( \frac{(\theta - \theta_0)^2}{2\sigma_\theta^2} + \frac{(\phi - \phi_0)^2}{2\sigma_\phi^2} \right) \right) \quad (5.3)$$

where  $\theta$  is latitude,  $\phi$  is longitude,  $A$  is amplitude, and  $\sigma$  are the standard deviations. For each Gaussian, we choose a random center value  $(\phi_0, \theta_0)$  from a uniform random distribution over the image target. Similarly, we choose  $A$  uniformly from the range  $[-5, 5]$ , and both  $\sigma$  from  $[6, 12]$ . This generates a smoothly varying ionospheric feature with large spatial variations consistent with or exceeding the ionospheric variations that we expect based on past work. For each case, we consider the same constellation of processed sferics shown in all the following figures which occur between 20:00–20:05 UT on 20-Aug-2017 and in the image target range of  $5$  to  $45^\circ$  and  $-120$  to  $-60^\circ$  latitude/longitude with  $2^\circ$  spacing. For the following cases, we calculate the path pixel segments as in the example of Equation 5.2/Figure 5.2. We solve for the underlying image with the singular value decomposition method.

First, we consider the performance of the noiseless case in Figure 5.5. The algorithm is able to accurately reconstruct the image in the region defined by all pixels crossed by



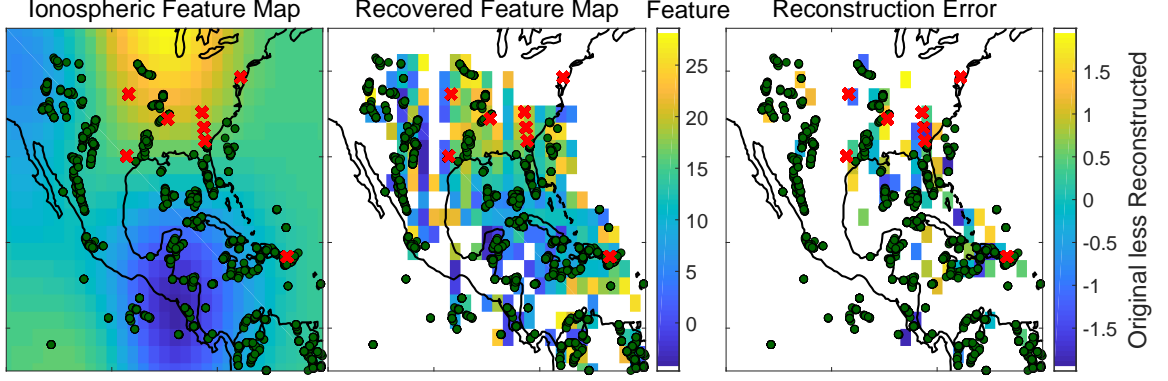


Figure 5.6: Example of the performance of the pixel basis  $D$  region tomography algorithm with moderately noisy inferences. The left panel is the assumed ionosphere with a  $2^\circ$  by  $2^\circ$  latitude/longitude pixel size. The middle panel is the reconstruction with clipped values exceeding the range of the original. The right panel shows the difference between the original and reconstructed synthetic ionospheric feature map.

one or more transmitter-to-receiver path. Outside of this range there is no constraining information therefore an infinite number of solutions exists and small singular values will cause it to blow up.

In the real world, we always need to have a procedure to deal with noisy measurements. We begin by considering the effect of moderate noise on the reconstruction in Figure 5.6. The reconstruction performance is markedly worse in this case with only a small geographical location having reasonable error. In order to help condition the effect of error on the solution, we investigate the effect of Tikhonov regularization on reconstruction.

First, we consider the effect of Tikhonov regularization in the absence of noise in Figure 5.7. Adding Tikhonov regularization poses the minimization problem

$$\min_{\mathbf{B}} \|\mathbf{y} - \mathbf{A}\mathbf{x}\|_2^2 + \|\delta\mathbf{x}\|_2^2 \quad (5.4)$$

where  $\delta$  is the regularization parameter which controls the tradeoff between the best least squares solution and lower solution energy. We show an example with a relatively large value for  $\delta = 3$ . The solution is degraded over the noiseless case since the reconstruction downplays the contribution of small singular values. The image performance is still only reasonable inside of the measurement region. However, imaging performance is only acceptable in a

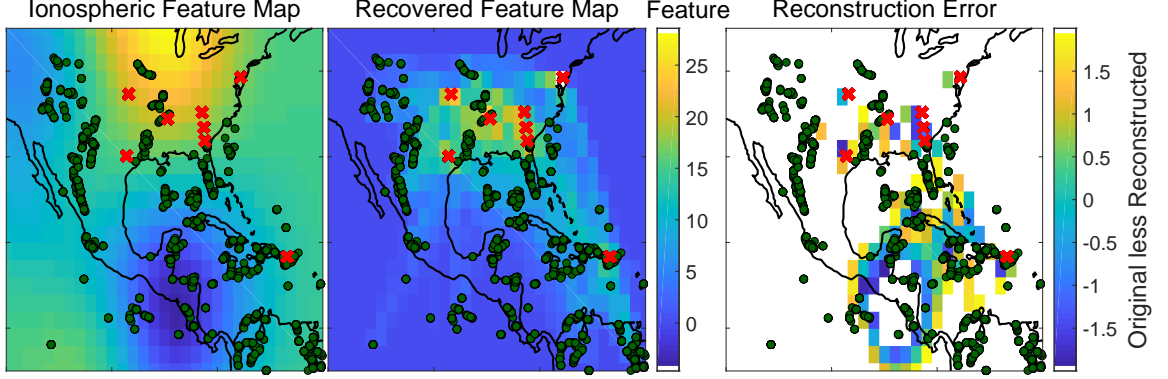


Figure 5.7: Example of the performance of the pixel basis  $D$  region tomography algorithm with noiseless inferences and Tikhonov regularization. The left panel is the assumed ionosphere with a  $2^\circ$  by  $2^\circ$  latitude/longitude pixel size. The middle panel is the reconstruction with clipped values exceeding the range of the original. The right panel shows the difference between the original and reconstructed synthetic ionospheric feature map.

smaller region which is covered by more transmitter-to-receiver paths. For the measurement geometries in this work, Tikhonov regularization tends to downplay the effect of more sparsely measured pixels.

Finally, we consider the moderate error case with Tikhonov regularization and  $\delta = 0.3$  in Figure 5.8. The regularized solution tends to lower the value of reconstructed pixels towards the outer bounds of the measured region. Since the notion of ‘energy’ in the context of Tikhonov regularization has to do with the  $\ell_2$  norm, it tends to force lesser measured pixels to low values and clip pixels outside of the measured region to zero. Therefore, in terms of measured ionospheric features, the tradeoff of Tikhonov regularization is between a noisy inferred image and a smaller imaged region that we can rely on.

Modeling the target image with a pixel basis is challenging because of the measurement geometry used in this work. Namely, regularization causes solutions where pixels with more transmitter-to-receiver path crossings will be preferred in the reconstruction. With no ground truth, it may be difficult to know what is trustworthy. In addition, it is desirable to have higher resolution than  $2^\circ$  pixel widths. Furthermore, using noise profiles expected during the daytime from the matching variation analysis, degrades the solutions considerably. Therefore, we consider other ways to constrain the solution, namely we seek to take advantage of the known structure of the  $D$  region electron density.

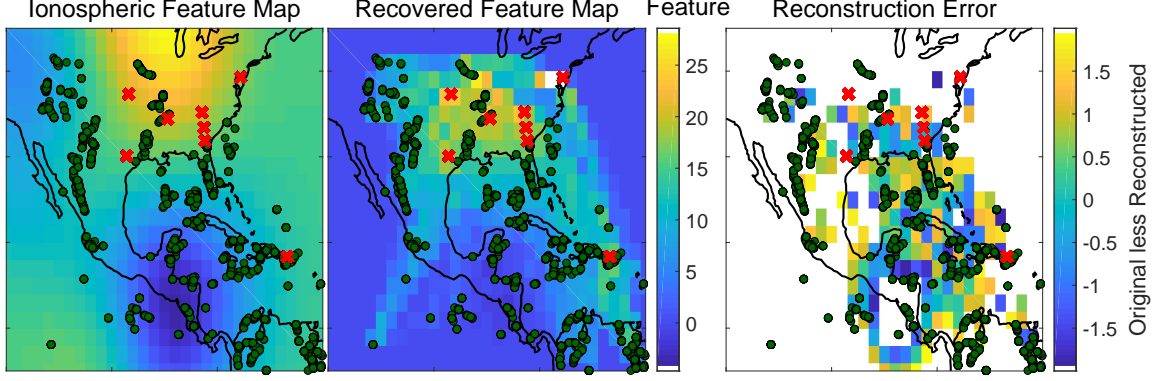


Figure 5.8: Example of the performance of the pixel basis  $D$  region tomography algorithm with moderately noisy inferences and Tikhonov regularization. The left panel is the assumed ionosphere with a  $2^\circ$  by  $2^\circ$  latitude/longitude pixel size. The middle panel is the reconstruction with clipped values exceeding the range of the original. The right panel shows the difference between the original and reconstructed synthetic ionospheric feature map.

### 5.3 $D$ Region Tomography Using a DCT Basis Representation

When performing traditional CT, no assumptions need to be made about the underlying object. This is desirable because arbitrary images should be possible in case foreign objects are present when imaging inside the human body (e.g. a tumor, shrapnel, etc.). It is also perfectly valid, because the measurement system is controlled, so we can guarantee the convergence of an image. In contrast, with little control over our measurement setup for the  $D$  region, it may not be possible to guarantee convergence of a pixel-based approach.

Therefore, we take advantage of the fact that we expect the  $D$  region to be smoothly varying over large geographical regions. In this spirit, we employ the 2D discrete cosine transform, or DCT [CCITT, 1993]. The DCT is a basis representation of a signal related to the discrete Fourier transform, differing in that it only uses real valued weights. The DCT is used, for instance, in image compression of the jpeg compression scheme. The form of the DCT used in this work is written as

$$A_{mn} = \sum_{p=0}^{M-1} \sum_{q=0}^{N-1} \alpha_p \gamma_q B_{pq} \cos\left(\frac{\pi(2m+1)p}{2M}\right) \cos\left(\frac{\pi(2n+1)q}{2N}\right), \quad \begin{array}{l} 0 \leq m \leq M-1 \\ 0 \leq n \leq N-1 \end{array}$$

where,

$$\alpha_p = \begin{cases} \frac{1}{\sqrt{M}}, & p = 0 \\ \sqrt{\frac{2}{M}}, & 1 \leq p \leq M-1 \end{cases}$$

$$\gamma_q = \begin{cases} \frac{1}{\sqrt{N}}, & q = 0 \\ \sqrt{\frac{2}{N}}, & 1 \leq q \leq N-1 \end{cases}$$

and  $B_{pq}$  are the DCT coefficients.

The line integral of a single ionospheric measurement can be written as

$$\nu = Le = \int_c I(\theta, \phi) ds \quad (5.5)$$

where  $I$  is some ionospheric value function defined for  $\theta$  as latitude,  $\phi$  as longitude.  $e$  is a path-averaged inferred value along a path of length  $L$ . We then represent  $I$  as a basis expansion of DCT coefficients and take each measurement as a line-integral along the DCT expansion replacing  $\theta$  for  $m$  and  $\phi$  for  $n$  written as

$$\nu = \int_c \sum_{p=0}^{M-1} \sum_{q=0}^{N-1} \alpha_p \gamma_q B_{pq} \cos\left(\frac{\pi(2\theta(r)+1)p}{2M}\right) \cos\left(\frac{\pi(2\phi(r)+1)q}{2N}\right) ds \quad (5.6)$$

To perform the integration, we use the trapezoid numerical technique. The numerical error will be small if the path segments are small enough. For  $R$  segments the approximate integration can be expressed as

$$\begin{aligned} \simeq \sum_{r=1}^R \sum_{p=0}^{M-1} \sum_{q=0}^{N-1} \left[ \alpha_p \gamma_q B_{pq} \cos\left(\frac{\pi(2\theta(r)+1)p}{2M}\right) \cos\left(\frac{\pi(2\phi(r)+1)q}{2N}\right) \right. \\ \left. + \cos\left(\frac{\pi(2\theta(r)+1)p}{2M}\right) \cos\left(\frac{\pi(2\phi(r)+1)q}{2N}\right) \right] \left( \frac{\Delta\ell(r)}{2} \right) \end{aligned} \quad (5.7)$$

We can rewrite and rearrange terms to make

$$\sum_{p=0}^{M-1} \sum_{q=0}^{N-1} B_{pq} \sum_{r=1}^R K_r \Delta\ell(r) \left( \frac{\alpha_p \gamma_q}{2} \right) \cos\left(\frac{\pi(2\theta(r)+1)p}{2M}\right) \cos\left(\frac{\pi(2\phi(r)+1)q}{2N}\right) \quad (5.8)$$

which can be written as vectorized product between  $p * q$  DCT coefficients ( $B_{pq}$ ) and the

rest of the line integral term and where

$$K_r = \begin{cases} 1, & r = 1, R \\ 2, & 2 \leq r \leq R - 1 \end{cases}$$

By adding more line integral observations, we arrive at a measurement system as follows

$$\boldsymbol{\nu} = \mathbf{A}\mathbf{B} \tag{5.9}$$

where  $\mathbf{B}$  is the vectorized matrix of DCT coefficients and  $\boldsymbol{\nu}$  is the vector of all line measurements in the lightning-to-receiver system. By using a sufficiently large set of accurate and unique DCT coefficients, an arbitrary image can be produced. Unfortunately, these conditions cannot be guaranteed. Fortunately, a smoothly varying ionosphere can be represented by a much smaller set of the low frequency components of the DCT. To examine the performance of the DCT basis reconstruction, we repeat the analysis performed for the pixel basis technique as described in Section 5.2. We use the same synthetic ionospheric feature map generation as in the pixel basis case and assume that the 100 lowest frequency DCT components will span the image. The path-average calculation proceeds similarl to the pixel basis case except the line-integral is performed against each 2D cosine function with path segments small enough to reduce distortion. We use the same lighting/receiver data as the previous section.

We begin with the noiseless case in Figure 5.9. The algorithm can accurately reconstruct the entire image even outside of the bounds of the measurements. This is possible due to the noiseless synthetic measurements taken with the fact that the reconstruction can accurately determine the DCT coefficients. Since the gaussian synthetic image generation creates a smoothly varying ionosphere, it is well represented by a small number of low frequency DCT components. Therefore, the image is correct even outside of the measurement region since the DCT basis is a unique representation of the image.

Next, we consider the effect of noisy measurements on image reconstruction performance in Figure 5.10. The added noise degrades the imaging performance as expected, however, the DCT approach seems to be more resilient to noise than the pixel approach. Inside

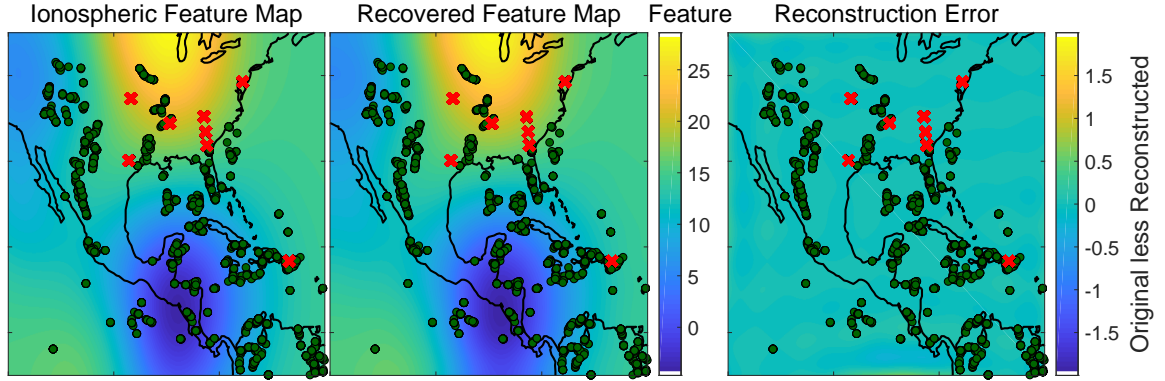


Figure 5.9: Example of the performance of the DCT basis  $D$  region tomography algorithm with noiseless inferences. The left panel is the assumed ionosphere displayed with  $0.1^\circ$  by  $0.1^\circ$  latitude/longitude pixel size. The middle panel is the reconstruction with clipped values exceeding the range of the original. The right panel shows the difference between the original and reconstructed synthetic ionospheric feature map.

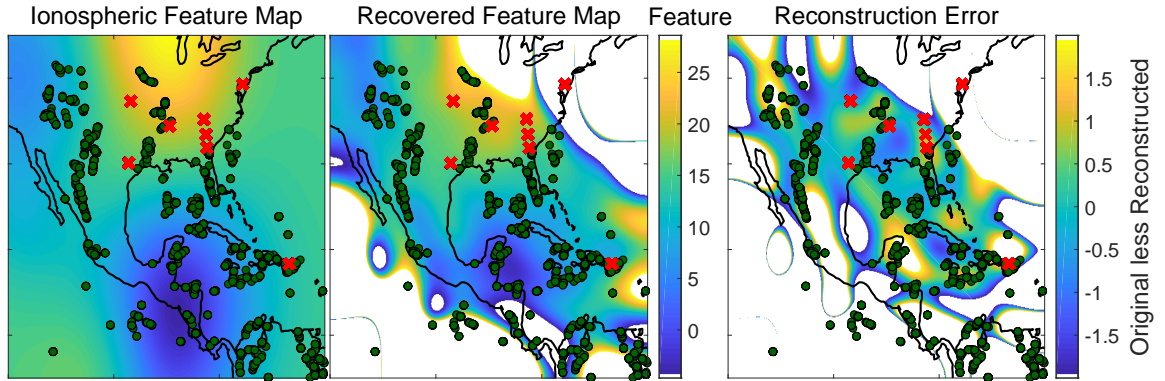


Figure 5.10: Example of the performance of the DCT basis  $D$  region tomography algorithm with moderately noisy inferences. The left panel is the assumed ionosphere displayed with  $0.1^\circ$  by  $0.1^\circ$  latitude/longitude pixel size. The middle panel is the reconstruction with clipped values exceeding the range of the original. The right panel shows the difference between the original and reconstructed synthetic ionospheric feature map.

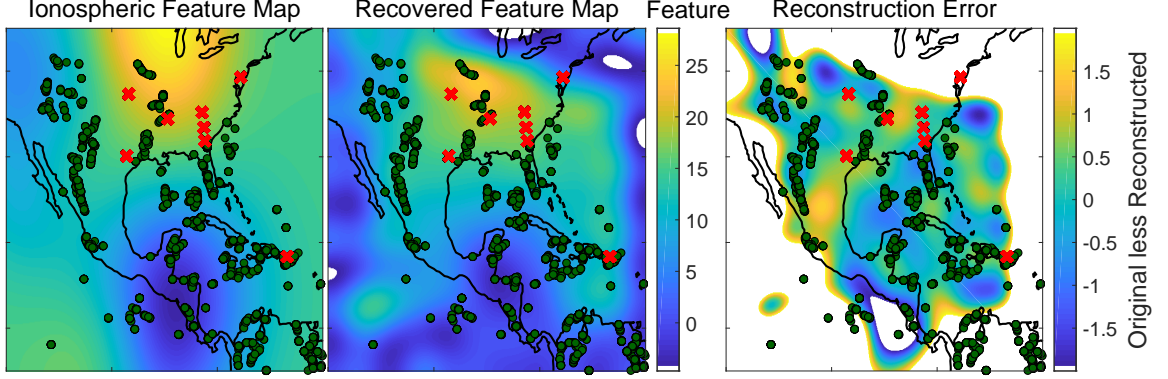


Figure 5.11: Example of the performance of the DCT basis  $D$  region tomography algorithm with noiseless inferences and Tikhonov regularization. The left panel is the assumed ionosphere displayed with  $0.1^\circ$  by  $0.1^\circ$  latitude/longitude pixel size. The middle panel is the reconstruction with clipped values exceeding the range of the original. The right panel shows the difference between the original and reconstructed synthetic ionospheric feature map.

of the measurement boundary, a constrained solution does acceptably well for a relatively large geographical area where the reconstruction error consists of higher spatial frequency content.

Next, we consider the effect of Tikhonov regularization on the DCT reconstruction in the absence of noise in Figure 5.11. We show an example with a relatively large value for  $\delta = 10^5$ . Tikhonov regularization seems to have a similar effect on the DCT basis reconstruction to the pixel basis. In particular, the area with a valid solution shrinks with increasing  $\delta$  to the region that is better covered with transmitter-to-receiver paths.

Finally, we consider the moderate error case with Tikhonov regularization for  $\delta = 1000$  in Figure 5.12. Tikhonov regularization with the moderately noisy case significantly increases performance. The acceptable reconstructed image area is similar in size to case without noise, again demonstrating the noise resiliency of the DCT basis for  $D$  region tomography.

We introduced the DCT basis in order to take advantage of the generally sparse measurement geometry of the  $D$  region tomography problem. The new approach outperforms the pixel-based approach with lower error and higher spatial resolution. Tikhonov regularization effectively controls the tradeoff between high energy singular value contributions and the accuracy of the best fit solution which can be perturbed by noise. However, there



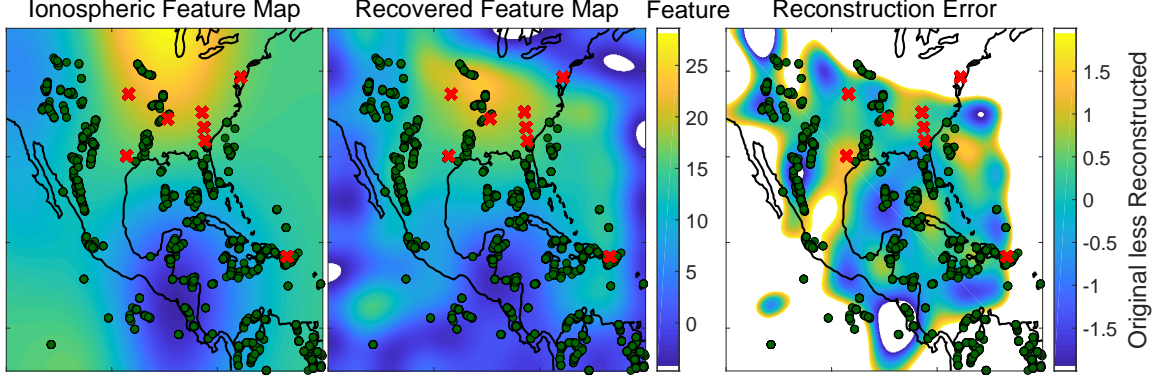


Figure 5.12: Example of the performance of the DCT basis  $D$  region tomography algorithm with moderately noisy inferences and Tikhonov regularization. The left panel is the assumed ionosphere displayed with  $0.1^\circ$  by  $0.1^\circ$  latitude/longitude pixel size. The middle panel is the reconstruction with clipped values exceeding the range of the original. The right panel shows the difference between the original and reconstructed synthetic ionospheric feature map.

are many methods of regularization with different tradeoffs.

One promising method is the basis pursuit denoising (BPDN) algorithm [Chen *et al.*, 1996]. BPDN controls the tradeoff between the best least squares solution and a sparse solution (i.e. the total value of the DCT coefficients). Smooth solutions tend to have most of the energy in the low frequency components which may allow for an adequate solution even with only a small set of DCT reconstructed components. BPDN solves the optimization problem given by

$$\min_{\mathbf{B}} \frac{1}{2} \|\boldsymbol{\nu} - \mathbf{AB}\|_2^2 + \lambda \|\mathbf{B}\|_1 \quad (5.10)$$

where  $\lambda$  is the regularization parameter which controls the tradeoff between forcing a sparse solution and best agreement to the measurements. With  $\lambda$  set too low, we risk overfitting the solution to the data but too high and the solution will be ‘too sparse’. We use Matlab scripts written by Michael P. Friedlander and Michael Saunders (<https://friedlander.io/software/asp/>), which use the Basis Pursuit Dual method to solve the optimization problem. Since  $\ell_1$  problems are guaranteed convex, the dual solution agrees with the primal (i.e. no duality gap). To tune for the optimal  $\lambda$ , we use a holdout set of path-averaged measurements and calculate the SSE. We take an example day of 20-Aug-2017 and use all available receiver data except Juneau. Throughout the day, we take time windows of 60 and 300 seconds and



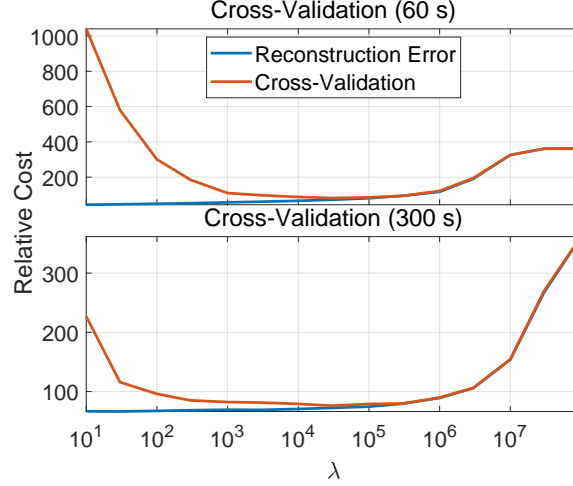


Figure 5.13: Reconstruction and validation curves to tune for the optimal regularization parameter lambda described in Equation 5.10.

vary  $\lambda$  while measuring the reconstruction error and validation error. The mean errors are taken for the entire day for all 60 and 300 second windows separately. The results are shown in Figure 5.13.

As  $\lambda$  approaches zero, the reconstruction error continues to decrease but this tends to cause over-fitting (as seen by increasing cross-validation cost) and does not generalize well. Therefore, the validation set is better for choosing the lambda value to use. For the example day considered, the optimal  $\lambda = 3 \cdot 10^4$  with similar performance for  $\lambda$  values with a relatively wide range of values. This is especially true for the 300 second time window lowering our confidence in our choice of  $\lambda$ .

For this reason, it is advantageous to consider imaging performance with synthetic data to fine-tune  $\lambda$  since the least-squares error of path-averaged measurements can be determined simultaneously with imaging error. With this procedure, we will choose a  $\lambda$  value that produces low imaging and path-averaged inference errors simultaneously. Furthermore, it may be possible to directly compare the synthetic case to the real case and allow us to make a reasonable expectation of imaging performance with real data where there is no ground-truth. To cover many possible ionospheres, we use a Monte-Carlo method to generate 25 random measurement error realizations (for the moderate error profile) and 25 randomly synthesized ionospheres with the same procedure and parameters as before. The reconstructed image target assumes the lowest 100 DCT components. We summarize the

Table 5.1: BPDN synthetic imaging analysis cases

Case	Date	Time Range (UT)	# of Clusters
Day 60 s	20-Aug-2017	20:00-20:01	534
Day 300 s	20-Aug-2017	20:00-20:05	2604
Night 60 s	20-Aug-2017	2:00-2:01	379
Night 300 s	20-Aug-2017	2:00-2:05	1798

All cases consider 25 procedurally generated ionospheres with 25 realizations of the moderate noise profile.

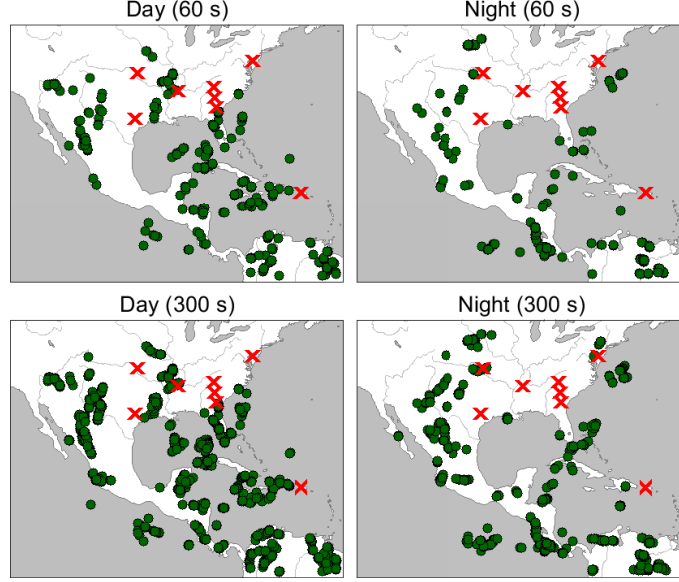


Figure 5.14: Map of the cases used for the synthetic vs. real error analysis. The maps correspond to the cases of Table 5.1 and Figure 5.13.

test cases in Table 5.1 and the measurement maps in Figure 5.14.

For each random ionosphere, we infer an image from the synthetic path integral measurements and measure the  $\ell_2$  error and a validation error with a holdout set. We also directly measure the reconstruction error by comparing the synthetic ‘ground truth’ to the inferred image over the region defined by  $20^\circ$  to  $32^\circ$  latitude and  $-98^\circ$  to  $-82^\circ$  longitude. We choose this region to define the image reconstruction error as it is the region we empirically determined to perform well under all error profiles. The results are summarized in Figure 5.15.

The top row shows the  $\ell_2$  errors for the real imaging cases and the middle row shows the errors for the synthetic cases. The bottom row compares the normalized synthetic  $\ell_2$  validation error compared to the normalized reconstruction error. Both real imaging cases

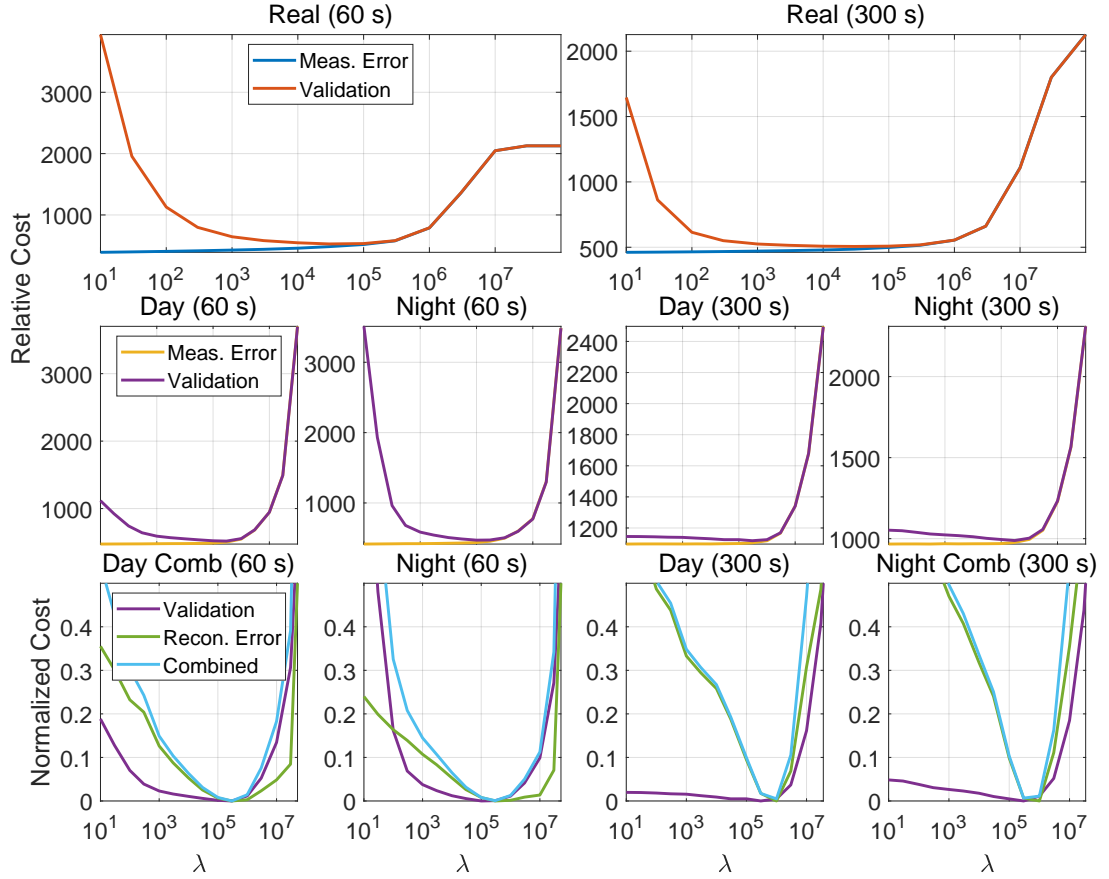


Figure 5.15: Error analysis of synthetic vs. real imaging. The top row shows the  $\ell_2$  errors averaged throughout the entire day with the corresponding time window. The middle panel shows  $\ell_2$  errors for the synthetic case using the sferic clusters of Table 5.1 and Figure 5.14. The bottom row compares the validation  $\ell_2$ , the reconstruction error in the synthetic images, and the combined normalized results.

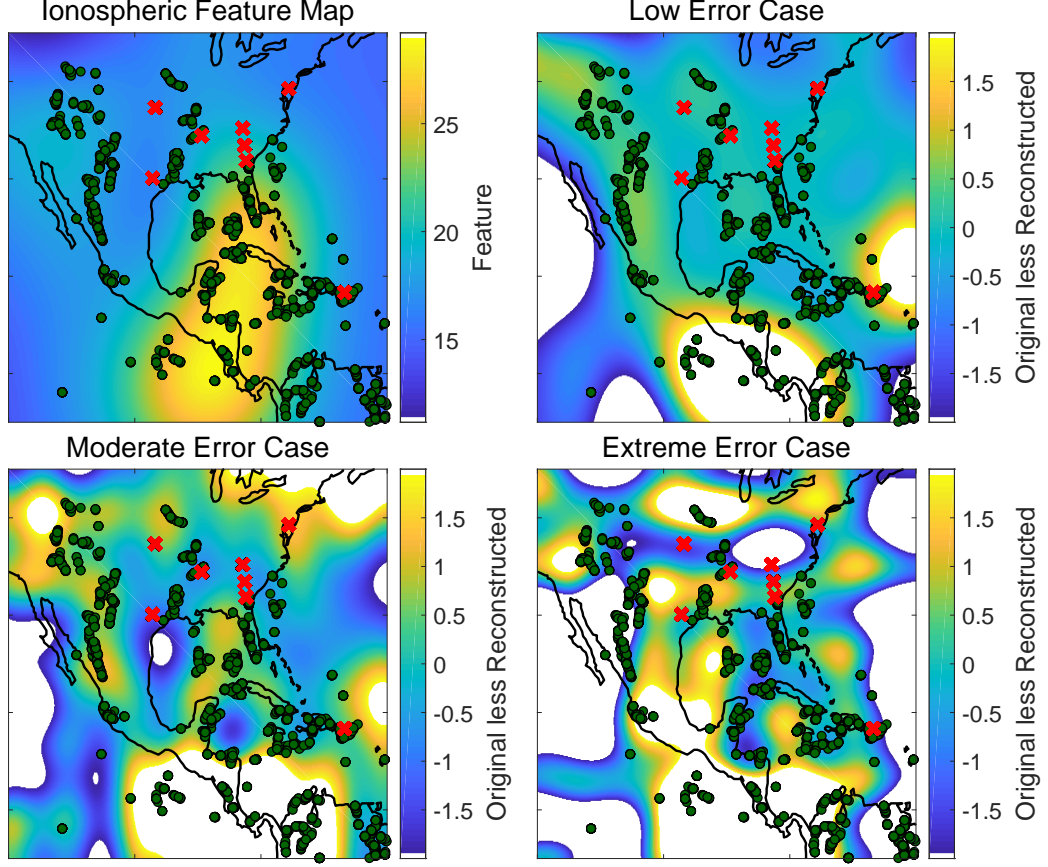


Figure 5.16: Performance of the DCT-based  $D$  region imaging approach with BPDN for the three error profiles considered in this work.

show overfitting and oversmoothing for extreme cases of  $\lambda$ . However, both have a wide range of values near the minimum. For the synthetic day and night cases and both time windows, we get similar results, with overfitting more pronounced for the 60 s time window. However, in all synthetic cases the best  $\lambda$  is similar to the tuned lambda from the real case which allows us to directly compare. Therefore, we use synthetic ground truth to fine-tune lambda. For all cases, the reconstruction error has a deeper minimum and all agree with  $\lambda = 3 \cdot 10^5$ .

Therefore, for all imaging examples we will use the fine-tuned  $\lambda$  value. Finally, we show an imaging example for all three error profiles with the fine-tuned lambda in Figure 5.16. All the examples use the DCT basis with BPDN, and each assumes the 100 lowest DCT frequency components. The initial random ionosphere is shown in the top-left panel with the difference between the original and reconstructed ionospheres shown in the next three

panels. The imaging performance degrades as we increase the magnitude of errors, but even for the extreme case, good performance is achieved over the Gulf of Mexico. Therefore, we consider this region for the imaging results discussed in the next section.

The  $D$  region tomography technique using the DCT basis and BPDN outperforms the pixel basis technique. The solutions tend to be more resilient to noise and since the sparse solutions are given in DCT coefficients the spatial resolution can be arbitrarily specified. Because of these advantages, we choose this method to perform  $D$  region tomography for the remainder of this work.

#### 5.4 $D$ Region Image Results

To extend the  $D$  region tomography to 4 dimensions, we perform the imaging at each relevant altitude and time step. With this method, each time solution is in principle independent from the next. The solution at each altitude could also be viewed as independent, with a couple of caveats. First, the inversion technique for the electron density profile is not freely varying, so there is effectively an altitude constraint. Secondly, by forcing smooth solutions via the DCT basis, there is a spatial constraint on the solutions. These constraints will help yield a reasonable solution. To further help with a well-conditioned problem at each altitude, we only consider profiles with electron density within an order of magnitude of the sensitive range, namely from  $0.1-10000 \text{ cm}^{-3}$ .

To begin our investigation of the imaging results, we consider cases where the ionosphere is known to vary due to diurnal effects. The imaging examples in this section use the BPDN method with  $\lambda = 3 \cdot 10^5$  assuming a solution with only the 100 lowest frequency DCT components. First, we consider some examples of the inferred electron density from day and night with time windows of 300 seconds on 22-Aug-2017 starting at 20 and 2 UT respectively. These results are shown in Figure 5.17.

The left column shows the day case and the right column shows the night case. The maps show the locations of imaged example electron density traces which are displayed in the middle row. The map also shows the region that we have empirically determined capable of producing an image, even in the extreme noise case (as seen in the example of

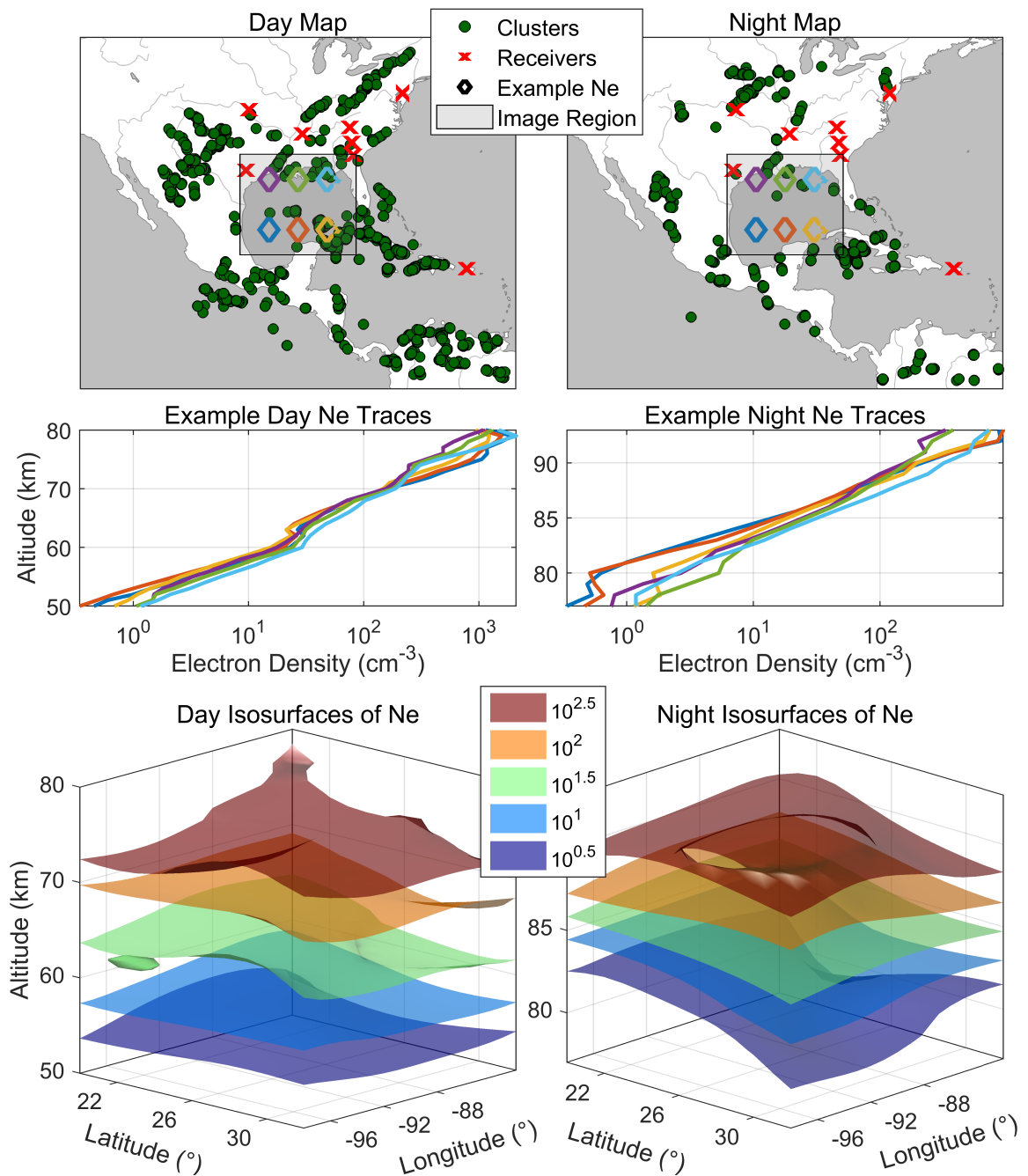


Figure 5.17: Day and night image examples. Both examples are from 22-Aug-2017. The left column shows results from the daytime case from 20:00 to 20:05 UT. The right column shows nighttime results from 2:00 to 2:05 UT. The top rows are example maps with relevant data including the source-to-receiver network used to produce the image, color-coded example trace locations, and the geographical region used to produce the 3D image during each time slice. The middle row shows example traces for each case corresponding to the map. The bottom row shows relevant isosurfaces for electron densities important to VLF propagation.

Figure 5.16). As expected, the daytime traces are much lower than the nighttime profiles and not as sharp. In contrast, the nighttime profiles are higher in altitude, sharper, and appear more log-linear. The nighttime example traces show slightly more variation in the image region than the daytime examples. The bottom row shows selected isosurfaces in the sensitive electron density range. Both sets of isosurfaces vary over the region, but neither have any sharp or dominant features.

To contrast the relative steadiness over the image region for all day or night, we consider a case with known variation: the day-night terminator. For our purposes, the terminator occurs when the sun sets at 80 km, a height at which the electron density is important for VLF propagation at all times. As the ionizing solar flux dissipates, especially as the terminator passes over a region, the lower ionosphere quickly recombines effectively moving the  $D$  region higher. The figure format is the same as in Figure 5.18. The sunset case appears more turbulent which is especially visible in the isosurface plot. In contrast, the sunrise case appears smoother, but sharper, indicating that the ionizing action is faster than recombination and that it may be a non-reciprocal process.

Lastly, we consider a solar flare imaging example. We use the same solar flare considered in the matching analysis of Section 4.3.2 with results shown in Figure 5.19. Before the solar flare occurs, the image results are similar to the results of Figure 5.17. However, during the solar flare, the image is much more turbulent as observed in the isosurfaces. Some of the example profiles are slightly depressed although some are increased. While we don't have a ground truth to compare to, we expect the image to be lowered on average which is not clearly observed in the data. Some of the possible reasons for this effect will be discussed in the following section.

## 5.5 Discussion

The  $D$  region images largely agree with our expectations of real ionospheric conditions. However, there are many factors and parameters that affect the exact reconstructed image shape. Therefore, it will be useful to consider the various parameters used in this work to produce the images, along with a qualitative discussion of their impact on performance. As

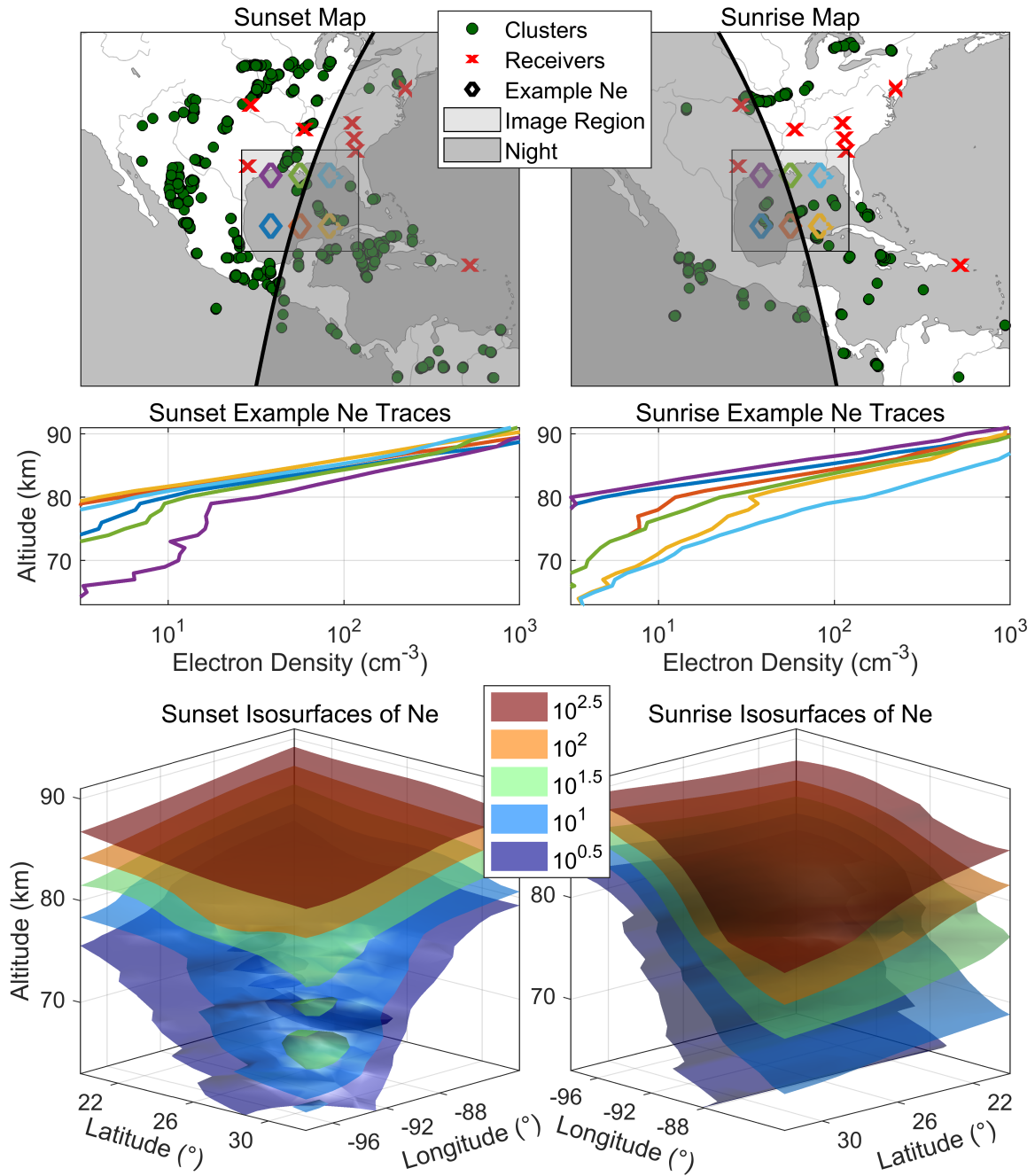


Figure 5.18: Sunset and Sunrise image examples. Both examples are from 22-Aug-2017. The left column shows results from the sunset case from 1:05 to 1:10 UT. The right column shows sunrise results from 10:55 to 11:00 UT. The top rows are example maps with relevant data, including the source-to-receiver paths used to produce the image, color-coded example trace locations and the geographical region used to produce the 3D image for each time slice. It also shows the terminator as a bold black line and the portion of the map in the dark. The middle row shows example traces for each case corresponding to the map. The bottom row shows relevant isosurfaces for electron densities important to VLF propagation.



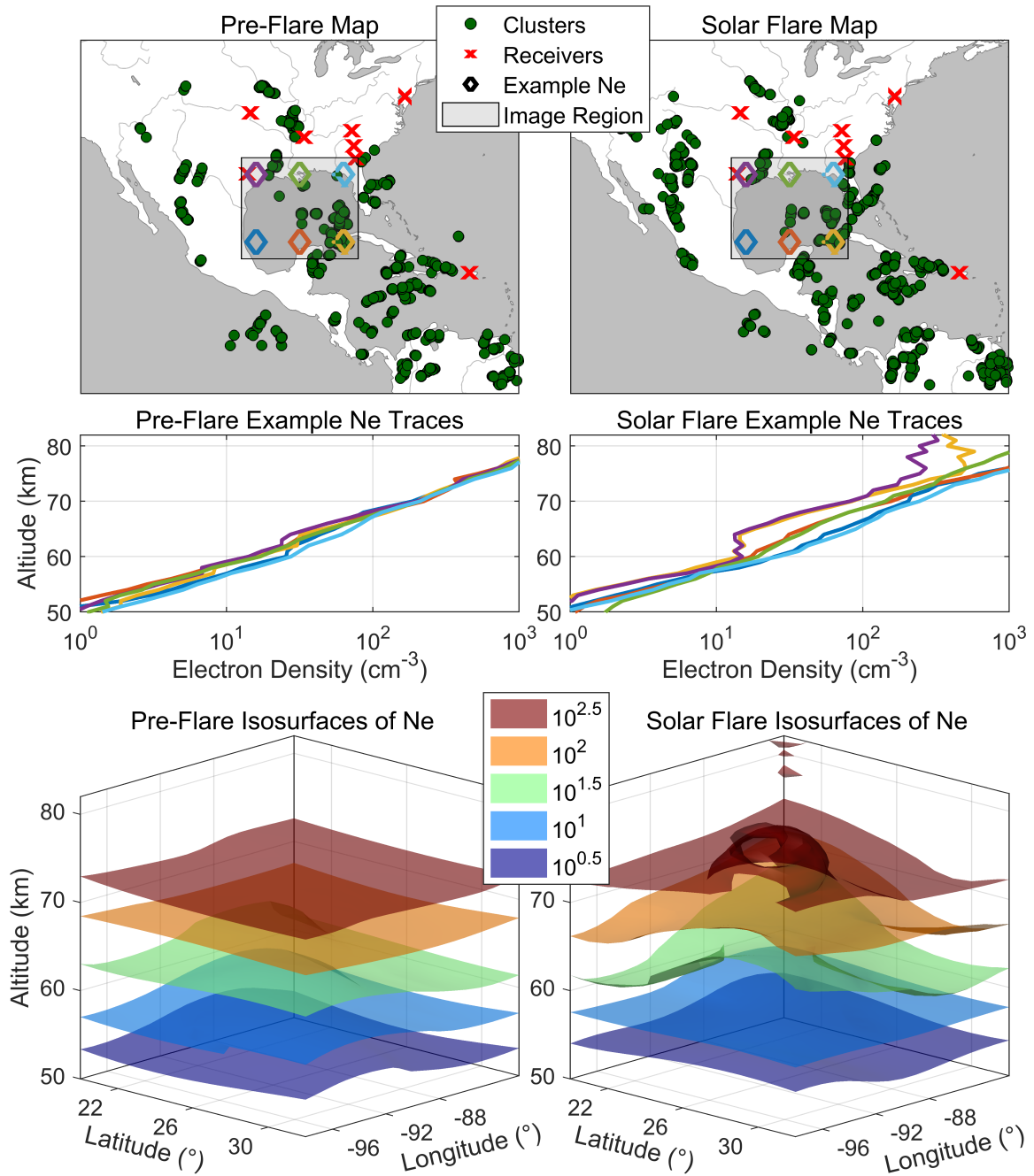


Figure 5.19: Example effect of solar flares on the  $D$  region tomography algorithms. Both examples are taken from 20-Aug-2017. The left column shows results before the solar flare occurred from 18:27:30 to 18:32:30 UT. The right column shows image produced during the solar flare from 19:30 to 19:35 UT. The top rows are example maps with relevant data, including the source-to-receiver network used to produce the image, color-coded example trace locations and the geographical region used to produce the 3D image during each time slice. The middle row shows example traces for each case corresponding to the map. The bottom row shows relevant isosurfaces for electron densities important to VLF propagation.

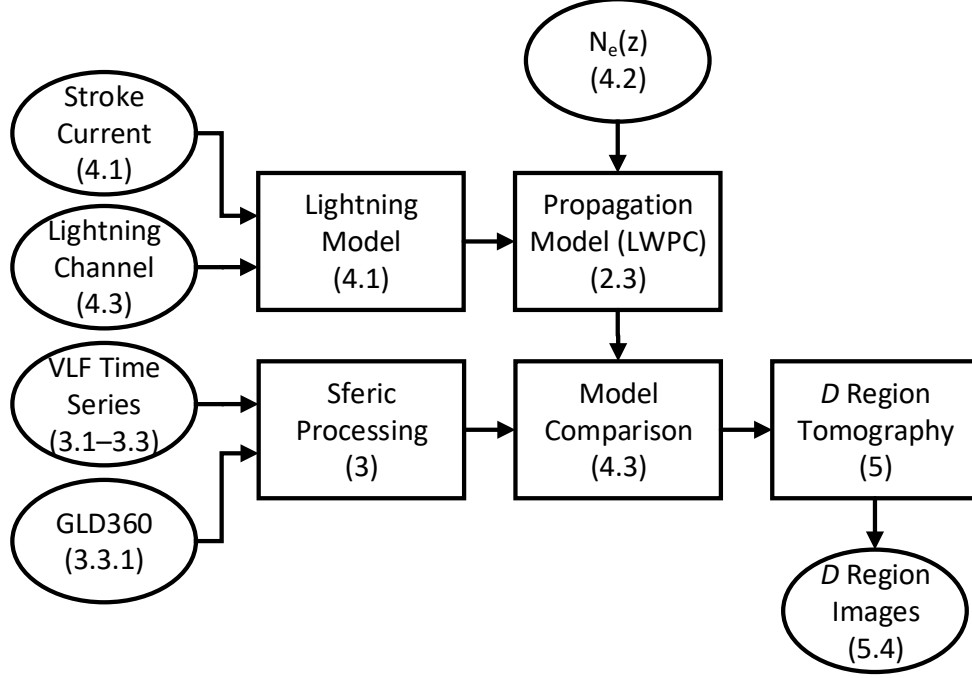


Figure 5.20: Overall block diagram of this work. Boxes indicate steps of the overall algorithm and ellipses represent the inputs/outputs. Chapter/section references to relevant sections are given in parentheses.

there are many steps and complex portions that contribute to the final  $D$  region image, we will keep each step in context where possible. To assist this discussion, we repeat the system block diagram in Figure 5.20.

We begin with the sferic processing algorithm, which is primarily limited by the error in the inputs. Of particular importance is the location and timing error of lightning data and the quality of received VLF data. The algorithm is intended to reduce the variability of lightning and produce stable and representative sferics. Thus, the primary tradeoff is between number of sferics in the clusters vs. the number of clusters. More sferics per cluster, implying less clusters, will have a higher effective SNR and less variability. However, if there are too many sferics per cluster, the total number of clusters decreases, and this will affect imaging performance in a different manner. The ideal cluster size needs further investigation.

The lightning model depends on assumed parameters such as the return stroke and lightning channel. We determined these parameters by a comparison to past literature, but

the total effect on imaging has not been quantified. We fixed one model for each stroke polarity, but did not consider initial vs. subsequent strokes. In addition, it is known that the lightning stroke will vary as a function of location and season, so a fixed model may be too simplistic. Furthermore, it may be possible to use an entirely different class of lightning stroke model. One of the most important aspects to our lightning stroke model and parameters is computational tractability, which may require some sacrifice in model accuracy.

The propagation model for VLF is largely the out of the box version of LWPC with some custom modifications. The synthesized model for a received spheric will depend on the lightning model and the propagation model (especially the electron density vs. altitude profile). We chose the 359 electron density profiles in this work based on an investigation of FIRM, the best known representation of the electron density of the lower ionosphere. Unfortunately, FIRM was empirically fortified by rocket measurements largely launched in the polar and other small geographical regions, introducing possible biases. In addition, ionospheric perturbations such as solar flares or gravity waves are not considered at all. Biased, incomplete, or coarse selections of electron density profiles will negatively impact imaging results.

With modeled and representative spherics in hand, we still have several methods to compare them together to infer the best fit electron density profile. The matching results of Chapter 4 depend on the spectral band used, with the most stable results at lower frequencies. In addition, the phase matching results had similar trends to amplitude but were more variable. All of these variabilities may be due to the lightning model or processing steps or an unknown combination of both.

The  $D$  region tomography algorithm may have the most free parameters. Choosing the DCT basis as the imaging target helped address the sparsity of the problem, however it is only one of many possible image representations. Other parameters that directly affect the imaging performance are the time window, assumed number of DCT coefficients, and the regularization parameter  $\lambda$ . The interpretation of all imaging results, and even path-average inferences, have been limited by the lack of a ground truth. This makes it difficult to assess the potential impact of this work in terms of electron density inferences or technologies. We

look forward to having these data in-hand to refine these methods.

The general results of this chapter, including the regions of the ionosphere which can be imaged with high fidelity, will depend on the receiver network. They will also depend on the geographical distribution of lightning which will vary by day, season, etc. Lastly, we make a very important assumption that the ionospheric inferences are the path-averaged quantity. This assumption has little validation, but it is crucial to the basic problem setup.

When considering ionospheric perturbations, such as during the solar flare image example of Figure 5.19, many of these factors may be at play in the chaotic results. However, one strong suspect is the limited ionospheric profiles we selected in this work to consider solar flares. Furthermore, the relevant settings were tuned for ambient cases and may need to be re-tuned to be valid for ionospheric perturbations.

## CHAPTER 6

### CONCLUSIONS AND SUGGESTIONS FOR FUTURE WORK

#### 6.1 Summary

Although there is a rich history of radio science in the study of the lower ionosphere, many basic questions remain unanswered. This is partly due to the difficulty of making direct measurements of the lower ionosphere, and partly due to the limitations of remote sensing techniques. In this work, we introduce the algorithms and tools to use the natural constellation of lightning with a network of VLF receivers, to produce images of electron density in space and time, expanding the current capability.

In Chapter 1, we give a literature survey of the ionosphere and lightning with an introduction to tomography. We begin with an overview of the Earth-ionosphere system, discussing the dynamics and electrical characteristics of the various regions of the ionosphere. Next, we discuss several common techniques that have been used in the literature to study the ionosphere and some of the common drivers and perturbations. We finish the ionosphere section with a focus on the past  $D$  region work. We discuss the lightning flash and some of the common technologies that have been developed to protect against and study it. Lastly, we introduce tomography, its historical development, and some modern uses.

In Chapter 2, we discuss several facets of the study of propagating VLF waves in the Earth-ionosphere waveguide system. First, we discuss two common methods of studying electromagnetic waves in a waveguide, ray-hop analysis from optics, and the Finite-Difference Time-Domain method. Next, we transition to a discussion of mode theory and the Long Wave Propagation Capability (LWPC) code. We look at the underlying principles to wave action in a plasma, which is critical in understanding impinging electromagnetic wave action on the  $D$  region. Next, we introduce the method that LWPC uses to solve for VLF wave propagation. We finish the chapter with a brief discussion of the assumptions of LWPC.

In Chapter 3, we describe the network of VLF receivers and describe the algorithm to normalize the sources to reduce spurious details caused by the uniqueness of each lightning flash. First, we describe variations of natural lightning, paying special attention to the lightning channel and the current waveform of the return stroke. Then, we describe our VLF/LF receiver and network, and give some examples of the data and phenomenology of terrestrial VLF/LF. Next, we describe the details of the sferic processing algorithm from raw time-domain data to the clustered and final representative sferic. We finish the chapter with validation that the sferic sources are stable and reduce the variability of lightning. We give an example application by investigating the effects of lightning polarity and stroke order on received sferic waveforms.

In Chapter 4, we detail our method to remotely sense the  $D$  region of the ionosphere using the representative sferics. We begin by describing our model for the return stroke of lightning, the dominant source of VLF/LF sferics. Next, we validate previous work on the sensitivity of VLF waves to the electron density in the  $D$  region to help interpret the results of the chapter. We continue by introducing a new parametrized model for the  $D$  region, the ‘split’ model, which is truer to the real electron density structure than the Wait and Spies model. Next, we evaluate the split model against another choice for an expanded  $D$  region model, a polynomial model. Lastly, we look at the  $D$  region inferences for several cases of a known varying ionosphere and discuss the implications of the results. Importantly, as in the literature, we interpret the ionospheric inferences as path-averaged results.

In Chapter 5, we introduce the  $D$  region tomography algorithm for producing 4D images of the electron density in the lower ionosphere. We start with a discussion of tomography as a mathematical technique. We draw a comparison between the measurement setup of computed tomography (CT) and the  $D$  region tomography problem. We then consider the performance of matching with synthetic data, to estimate the magnitude of errors of produced images. Next, we consider the straightforward approach of tomography with a pixel basis and analyze the results. Then, we constrain the problem with known features of the lower ionosphere of which the most important is our expectation that it will vary smoothly. To constrain this problem, we write each path average as an integration against the discrete cosine transform (DCT). We force a solution with the lowest frequency components

to employ the smoothness constraint and help condition the problem, since we assume our measurements are sparse.

## 6.2 Suggestions for Future Work

This work details the methods we developed to use a network of VLF receivers to image large regions of the lower ionosphere. It is only limited only by number and geographical distribution of natural lightning and the geometry of VLF receivers. As the advancement of this thesis is mostly in methods and data processing, we hope to inspire the further investigation of the lower ionosphere using these or similar methods. To this end, we briefly discuss some suggestions for future endeavors.

### 6.2.1 Refinement of the $D$ Region Tomography Algorithms

One of the most significant challenges in this work is the lack of a ground-truth of the  $D$  region. This is primarily because current techniques lack the capability of remotely sensing large areas of the lower ionosphere and is in turn one of the motivators of this work. However, it may be possible to perform a campaign to validate the results and fine-tune the imaging algorithms. The  $D$  region is the primary cause of HF absorption as it refracts through the ionosphere. Combined with the relatively low cost of a HF beacon, it may be possible to combine the  $D$  region tomography algorithm with a network of HF transmitters and receivers to predict HF absorption with simultaneous validation of direct measurements.

### 6.2.2 $B_r$ for $D$ Region Studies

We demonstrated the stability of the radial component of the magnetic field, or  $B_r$  in Section 3.4. However, in this work we do not use  $B_r$  for imaging. There are significant challenges in using  $B_r$ , since it is radiated from the lightning return stroke more weakly than  $B_\phi$  and attenuated faster. However, there may be more spectral information than  $B_\phi$  and the signal shape appears to change faster with distance. This implies that if used correctly and carefully, it may be more sensitive to the  $D$  region.

### 6.2.3 Expanded Inverse Modeling for Nighttime and Local Perturbations

As described in Section 4.3.2, a limitation of this work is the selection of  $D$  region electron density profiles. We were motivated to expand the Wait and Spies 2-parameter model based on the more complicated and persistent features commonly observed by many techniques in  $D$  region electron density profiles. This new profile may allow us to remotely sense a broader class of perturbations to the  $D$  region, but we must expand our database of profiles.

### 6.2.4 A Modified Technique for Better Propagation Prediction

Long range lightning detection algorithms depend on the current state of the  $D$  region. State of the art networks use a data-driven propagation model [*Said and Murphy*, 2016]. However, this method will be fundamentally limited by the unknown present  $D$  region state. For mission critical propagation applications, a real-time implementation of  $D$  region imaging could allow for better prediction of VLF propagation and in turn the improvement of technologies which depend on it such as lightning geolocation, HF absorption prediction, or ground-based navigation.

### 6.2.5 An Iterative Technique for the Study of Lightning

The first step of  $D$  region tomography is the normalization of lightning VLF broadband sources. However, an iterative approach could allow for remote and statistical studies into the variation of lightning on large scales. Such a study could be performed as follows: First, perform the  $D$  region tomography algorithm as described in this work. Second, use the image to predict the expected source spectral characteristics of an individual lightning stroke. Third, expand the lightning return stroke model to describe the variation of observed lightning stroke characteristics from the propagation-corrected and normalized lightning stroke.

### 6.2.6 VLF Transmitters and Other Data Sources

The results and algorithms of this thesis are constrained to band-limited VLF/LF lightning sferics ( $\sim 1\text{--}47$  kHz). However, this excludes common and reliable VLF sources for  $D$



region studies, most notably VLF narrowband transmitters. In addition, lightning generates powerful radiation in the LF and even the medium frequency (MF, 300–3000 kHz) spectral band. Recent work has highlighted the effectiveness of these higher frequency bands for  $D$  region studies [*Higginson-Rollins and Cohen, 2017*]. The ideal  $D$  region study would then include these LF/MF beacons as well as the LF/MF spectral band of lightning.

# Appendices

# **APPENDIX A** **IONOSPHERIC PROFILES**

Table A.1: The split model parameters of the  $D$  region electron density profiles used in this work.

Profile	$h'$ (km)	$\beta$ (km <sup>-1</sup> )	$s_\ell$ (km)	$\Delta h$ (km)
1	66	0.3	—	—
2	66	0.35	—	—
3	66	0.4	—	—
4	66	0.45	—	—
5	66	0.5	—	—
6	66	0.55	—	—
7	68	0.3	—	—
8	68	0.35	—	—
9	68	0.4	—	—
10	68	0.45	—	—
11	68	0.5	—	—
12	68	0.55	—	—
13	70	0.3	—	—
14	70	0.35	—	—
15	70	0.4	—	—
16	70	0.45	—	—
17	70	0.5	—	—
18	70	0.55	—	—
19	72	0.3	—	—
20	72	0.35	—	—

*Continued on next page*

Table A.1 – *Continued from previous page*

Profile	$h'$ (km)	$\beta$ (km <sup>-1</sup> )	$s_\ell$ (km)	$\Delta h$ (km)
21	72	0.4	—	—
22	72	0.45	—	—
23	72	0.5	—	—
24	72	0.55	—	—
25	74	0.3	—	—
26	74	0.35	—	—
27	74	0.4	—	—
28	74	0.45	—	—
29	74	0.5	—	—
30	74	0.55	—	—
31	76	0.3	—	—
32	76	0.35	—	—
33	76	0.4	—	—
34	76	0.45	—	—
35	76	0.5	—	—
36	76	0.55	—	—
37	78	0.3	—	—
38	78	0.35	—	—
39	78	0.4	—	—
40	78	0.45	—	—
41	78	0.5	—	—
42	78	0.55	—	—
43	80	0.4	—	—
44	80	0.45	—	—
45	80	0.5	—	—
46	80	0.55	—	—
47	80	0.6	—	—

*Continued on next page*

Table A.1 – *Continued from previous page*

Profile	$h'$ (km)	$\beta$ (km <sup>-1</sup> )	$s_\ell$ (km)	$\Delta h$ (km)
48	80	0.65	—	—
49	80	0.7	—	—
50	80	0.75	—	—
51	80	0.8	—	—
52	80	0.85	—	—
53	80	0.9	—	—
54	80	0.95	—	—
55	80	1.0	—	—
56	80	1.05	—	—
57	80	1.1	—	—
58	80	1.15	—	—
59	80	1.2	—	—
60	80	1.25	—	—
61	82	0.4	—	—
62	82	0.45	—	—
63	82	0.5	—	—
64	82	0.55	—	—
65	82	0.6	—	—
66	82	0.65	—	—
67	82	0.7	—	—
68	82	0.75	—	—
69	82	0.8	—	—
70	82	0.85	—	—
71	82	0.9	—	—
72	82	0.95	—	—
73	82	1.0	—	—
74	82	1.05	—	—

*Continued on next page*

Table A.1 – *Continued from previous page*

Profile	$h'$ (km)	$\beta$ (km <sup>-1</sup> )	$s_\ell$ (km)	$\Delta h$ (km)
75	82	1.1	—	—
76	82	1.15	—	—
77	82	1.2	—	—
78	82	1.25	—	—
79	84	0.4	—	—
80	84	0.45	—	—
81	84	0.5	—	—
82	84	0.55	—	—
83	84	0.6	—	—
84	84	0.65	—	—
85	84	0.7	—	—
86	84	0.75	—	—
87	84	0.8	—	—
88	84	0.85	—	—
89	84	0.9	—	—
90	84	0.95	—	—
91	84	1.0	—	—
92	84	1.05	—	—
93	84	1.1	—	—
94	84	1.15	—	—
95	84	1.2	—	—
96	84	1.25	—	—
97	86	0.4	—	—
98	86	0.45	—	—
99	86	0.5	—	—
100	86	0.55	—	—
101	86	0.6	—	—

*Continued on next page*

Table A.1 – *Continued from previous page*

Profile	$h'$ (km)	$\beta$ (km <sup>-1</sup> )	$s_\ell$ (km)	$\Delta h$ (km)
102	86	0.65	—	—
103	86	0.7	—	—
104	86	0.75	—	—
105	86	0.8	—	—
106	86	0.85	—	—
107	86	0.9	—	—
108	86	0.95	—	—
109	86	1.0	—	—
110	86	1.05	—	—
111	86	1.1	—	—
112	86	1.15	—	—
113	86	1.2	—	—
114	86	1.25	—	—
115	88	0.4	—	—
116	88	0.45	—	—
117	88	0.5	—	—
118	88	0.55	—	—
119	88	0.6	—	—
120	88	0.65	—	—
121	88	0.7	—	—
122	88	0.75	—	—
123	88	0.8	—	—
124	88	0.85	—	—
125	88	0.9	—	—
126	88	0.95	—	—
127	88	1.0	—	—
128	88	1.05	—	—

*Continued on next page*

Table A.1 – *Continued from previous page*

Profile	$h'$ (km)	$\beta$ (km <sup>-1</sup> )	$s_\ell$ (km)	$\Delta h$ (km)
129	88	1.1	—	—
130	88	1.15	—	—
131	88	1.2	—	—
132	88	1.25	—	—
133	66	0.4	60	4
134	66	0.45	60	4
135	66	0.5	60	4
136	66	0.55	60	4
137	68	0.4	60	4
138	68	0.45	60	4
139	68	0.5	60	4
140	68	0.55	60	4
141	70	0.4	60	4
142	70	0.45	60	4
143	70	0.5	60	4
144	70	0.55	60	4
145	72	0.4	60	4
146	72	0.45	60	4
147	72	0.5	60	4
148	72	0.55	60	4
149	66	0.35	60	8
150	66	0.4	60	8
151	66	0.45	60	8
152	66	0.5	60	8
153	66	0.55	60	8
154	66	0.6	60	8
155	66	0.65	60	8

*Continued on next page*



Table A.1 – *Continued from previous page*

Profile	$h'$ (km)	$\beta$ (km <sup>-1</sup> )	$s_\ell$ (km)	$\Delta h$ (km)
156	68	0.35	60	8
157	68	0.4	60	8
158	68	0.45	60	8
159	68	0.5	60	8
160	68	0.55	60	8
161	68	0.6	60	8
162	68	0.65	60	8
163	70	0.35	60	8
164	70	0.4	60	8
165	70	0.45	60	8
166	70	0.5	60	8
167	70	0.55	60	8
168	70	0.6	60	8
169	70	0.65	60	8
170	72	0.35	60	8
171	72	0.4	60	8
172	72	0.45	60	8
173	72	0.5	60	8
174	72	0.55	60	8
175	72	0.6	60	8
176	72	0.65	60	8
177	68	0.4	60	12
178	68	0.45	60	12
179	68	0.5	60	12
180	68	0.55	60	12
181	68	0.6	60	12
182	70	0.4	60	12

*Continued on next page*

Table A.1 – *Continued from previous page*

Profile	$h'$ (km)	$\beta$ (km <sup>-1</sup> )	$s_\ell$ (km)	$\Delta h$ (km)
183	70	0.45	60	12
184	70	0.5	60	12
185	70	0.55	60	12
186	70	0.6	60	12
187	72	0.4	60	12
188	72	0.45	60	12
189	72	0.5	60	12
190	72	0.55	60	12
191	72	0.6	60	12
192	66	0.5	60	16
193	66	0.55	60	16
194	66	0.6	60	16
195	68	0.5	60	16
196	68	0.55	60	16
197	68	0.6	60	16
198	70	0.35	65	4
199	70	0.4	65	4
200	70	0.45	65	4
201	70	0.5	65	4
202	72	0.35	65	4
203	72	0.4	65	4
204	72	0.45	65	4
205	72	0.5	65	4
206	74	0.35	65	4
207	74	0.4	65	4
208	74	0.45	65	4
209	74	0.5	65	4

*Continued on next page*

Table A.1 – *Continued from previous page*

Profile	$h'$ (km)	$\beta$ (km <sup>-1</sup> )	$s_\ell$ (km)	$\Delta h$ (km)
210	76	0.35	65	4
211	76	0.4	65	4
212	76	0.45	65	4
213	76	0.5	65	4
214	70	0.35	65	8
215	70	0.4	65	8
216	70	0.45	65	8
217	70	0.5	65	8
218	70	0.55	65	8
219	72	0.35	65	8
220	72	0.4	65	8
221	72	0.45	65	8
222	72	0.5	65	8
223	72	0.55	65	8
224	74	0.35	65	8
225	74	0.4	65	8
226	74	0.45	65	8
227	74	0.5	65	8
228	74	0.55	65	8
229	70	0.4	65	12
230	70	0.45	65	12
231	70	0.5	65	12
232	70	0.55	65	12
233	72	0.4	65	12
234	72	0.45	65	12
235	72	0.5	65	12
236	72	0.55	65	12

*Continued on next page*

Table A.1 – *Continued from previous page*

Profile	$h'$ (km)	$\beta$ (km <sup>-1</sup> )	$s_\ell$ (km)	$\Delta h$ (km)
237	74	0.4	65	12
238	74	0.45	65	12
239	74	0.5	65	12
240	74	0.55	65	12
241	70	0.45	65	16
242	70	0.5	65	16
243	68	0.35	70	4
244	68	0.4	70	4
245	68	0.45	70	4
246	68	0.5	70	4
247	68	0.55	70	4
248	68	0.6	70	4
249	70	0.35	70	4
250	70	0.4	70	4
251	70	0.45	70	4
252	70	0.5	70	4
253	70	0.55	70	4
254	70	0.6	70	4
255	72	0.35	70	4
256	72	0.4	70	4
257	72	0.45	70	4
258	72	0.5	70	4
259	72	0.55	70	4
260	72	0.6	70	4
261	74	0.35	70	4
262	74	0.4	70	4
263	74	0.45	70	4

*Continued on next page*

Table A.1 – *Continued from previous page*

Profile	$h'$ (km)	$\beta$ (km <sup>-1</sup> )	$s_\ell$ (km)	$\Delta h$ (km)
264	74	0.5	70	4
265	74	0.55	70	4
266	74	0.6	70	4
267	72	0.4	70	8
268	72	0.45	70	8
269	72	0.5	70	8
270	72	0.55	70	8
271	72	0.6	70	8
272	72	0.65	70	8
273	74	0.4	70	8
274	74	0.45	70	8
275	74	0.5	70	8
276	74	0.55	70	8
277	74	0.6	70	8
278	74	0.65	70	8
279	76	0.4	70	8
280	76	0.45	70	8
281	76	0.5	70	8
282	76	0.55	70	8
283	76	0.6	70	8
284	76	0.65	70	8
285	70	0.55	70	8
286	70	0.5	70	12
287	74	0.65	70	12
288	70	0.35	75	4
289	70	0.4	75	4
290	70	0.45	75	4

*Continued on next page*

Table A.1 – *Continued from previous page*

Profile	$h'$ (km)	$\beta$ (km <sup>-1</sup> )	$s_\ell$ (km)	$\Delta h$ (km)
291	70	0.5	75	4
292	72	0.35	75	4
293	72	0.4	75	4
294	72	0.45	75	4
295	72	0.5	75	4
296	74	0.35	75	4
297	74	0.4	75	4
298	74	0.45	75	4
299	74	0.5	75	4
300	76	0.4	75	4
301	76	0.45	75	4
302	76	0.5	75	4
303	76	0.55	75	4
304	76	0.6	75	4
305	76	0.65	75	4
306	76	0.7	75	4
307	76	0.75	75	4
308	76	0.8	75	4
309	78	0.4	75	4
310	78	0.45	75	4
311	78	0.5	75	4
312	78	0.55	75	4
313	78	0.6	75	4
314	78	0.65	75	4
315	78	0.7	75	4
316	78	0.75	75	4
317	78	0.8	75	4

*Continued on next page*

Table A.1 – *Continued from previous page*

Profile	$h'$ (km)	$\beta$ (km <sup>-1</sup> )	$s_\ell$ (km)	$\Delta h$ (km)
318	80	0.4	75	4
319	80	0.45	75	4
320	80	0.5	75	4
321	80	0.55	75	4
322	80	0.6	75	4
323	80	0.65	75	4
324	80	0.7	75	4
325	80	0.75	75	4
326	80	0.8	75	4
327	70	0.4	75	8
328	70	0.45	75	8
329	70	0.5	75	8
330	70	0.55	75	8
331	72	0.4	75	8
332	72	0.45	75	8
333	72	0.5	75	8
334	72	0.55	75	8
335	74	0.4	75	8
336	74	0.45	75	8
337	74	0.5	75	8
338	74	0.55	75	8
339	76	0.4	75	8
340	76	0.45	75	8
341	76	0.5	75	8
342	76	0.55	75	8
343	78	0.4	75	8
344	78	0.45	75	8

*Continued on next page*

Table A.1 – *Continued from previous page*

Profile	$h'$ (km)	$\beta$ (km <sup>-1</sup> )	$s_\ell$ (km)	$\Delta h$ (km)
345	78	0.5	75	8
346	78	0.55	75	8
347	78	0.45	80	4
348	78	0.5	80	4
349	78	0.55	80	4
350	78	0.6	80	4
351	78	0.65	80	4
352	80	0.45	80	4
353	80	0.5	80	4
354	80	0.55	80	4
355	80	0.6	80	4
356	80	0.65	80	4
357	78	0.6	80	8
358	82	0.7	85	4
359	82	0.75	85	4



## BIBLIOGRAPHY

- Abarca, S. F., K. L. Corbosiero, and T. J. Galarneau (2010), An evaluation of the Worldwide Lightning Location Network (WWLLN) using the National Lightning Detection Network (NLDN) as ground truth, *Journal of Geophysical Research*, *115*(D18), D18,206, doi:10.1029/2009JD013411.
- Adachi, T., H. Fukunishi, Y. Takahashi, and M. Sato (2004), Roles of the EMP and QE field in the generation of columniform sprites, *Geophysical Research Letters*, *31*(4), L04,107, doi:10.1029/2003GL019081.
- Alfonsi, L., A. J. Kavanagh, E. Amata, P. Cilliers, E. Correia, M. Freeman, K. Kauristie, R. Liu, J.-P. Luntama, C. N. Mitchell, and G. A. Zherebtsov (2008), Probing the high latitude ionosphere from ground-based observations: The state of current knowledge and capabilities during IPY (2007-2009), *Journal of Atmospheric and Solar-Terrestrial Physics*, *70*(18), 2293–2308.
- Appleton, E. (1927), The existence of more than one ionised layer in the upper atmosphere, *Nature*, *120*(3018), 330–330, doi:10.1038/120330a0.
- Appleton, E. (1929), The equivalent heights of the atmospheric ionised regions in England and America, *Nature*, *123*(3099), 445–445, doi:10.1038/123445a0.
- Appleton, E. (1931), A method of measuring upper atmospheric ionisation, *Nature*, *127*(3197), 197–197, doi:10.1038/127197a0.
- Appleton, E. (1932), Wireless studies of the ionosphere, *Institution of Electrical Engineers - Proceedings of the Wireless Section of the Institution*, *7*(21), 257–265, doi:10.1049/pws.1932.0027.
- Appleton, E. (1933), Fine-structure of the ionosphere, *Nature*, *131*(3320), 872–873, doi:10.1038/131872a0.
- Appleton, E. V. (1928), Some notes on wireless methods of investigating the electrical structure of the upper atmosphere. I, *Proceedings of the Physical Society*, *41*(1), 43–59, doi:10.1088/0959-5309/41/1/305.
- Appleton, E. V., and M. A. F. Barnett (1925a), On some direct evidence for downward atmospheric reflection of electric rays, *Proceedings of the Royal Society A: Mathematical, Physical and Engineering Sciences*, *109*(752), 621–641, doi:10.1098/rspa.1925.0149.
- Appleton, E. V., and M. A. F. Barnett (1925b), Local reflection of wireless waves from the upper atmosphere, *Nature*, *115*(2888), 333–334, doi:10.1038/115333a0.
- Appleton, E. V., and G. Builder (1932), Wireless echoes of short delay, *Proceedings of the Physical Society*, *44*(1), 76–87, doi:10.1088/0959-5309/44/1/310.
- Appleton, E. V., and J. A. Ratcliffe (1927a), On the nature of wireless signal variations. I, *Proceedings of the Royal Society A: Mathematical, Physical and Engineering Sciences*, *115*(771), 291–305, doi:10.1098/rspa.1927.0093.

- Appleton, E. V., and J. A. Ratcliffe (1927b), On the nature of wireless signal variations. II, *Proceedings of the Royal Society A: Mathematical, Physical and Engineering Sciences*, 115(771), 305–317, doi:10.1098/rspa.1927.0094.
- Appleton, E. V., and J. A. Ratcliffe (1930), Some simultaneous observations on down-coming wireless waves, *Proceedings of the Royal Society A: Mathematical, Physical and Engineering Sciences*, 128(807), 133–158, doi:10.1098/rspa.1930.0101.
- Armistead, G. W., J. V. Evans, and W. A. Reid (1972), Measurements of D - and E -region electron densities by the incoherent scatter technique at Millstone Hill, *Radio Science*, 7(1), 153–162, doi:10.1029/RS007i001p00153.
- Armstrong, W. C. (1983), Recent advance from studies of the Trimpf effect, *Antarctic Journal*, 18, 281–290.
- Arnoldy, R. L. (1974), Auroral particle precipitation and Birkeland currents, *Reviews of Geophysics*, 12(2), 217, doi:10.1029/RG012i002p00217.
- Backus, G., and F. Gilbert (1970), Uniqueness in the inversion of inaccurate gross Earth data, *Philosophical Transactions of the Royal Society A: Mathematical, Physical and Engineering Sciences*, 266(1173), 123–192, doi:10.1098/rsta.1970.0005.
- Bailey, V. A., and D. F. Martyn (1934), Interaction of radio waves, *Nature*, 133(3354), 218–218, doi:10.1038/133218a0.
- Barkhausen, H. (1930), Whistling tones from the Earth, *Proceedings of the IRE*, 18(7), 1155–1159, doi:10.1109/JRPROC.1930.222122.
- Barr, R. (1970a), The ELF and VLF amplitude spectrum of atmospherics with particular reference to the attenuation band near 3 kHz, *Journal of Atmospheric and Terrestrial Physics*, 32(6), 977–990, doi:10.1016/0021-9169(70)90111-X.
- Barr, R. (1970b), The attenuation of ELF and VLF radio waves propagating below inhomogeneous isotropic ionospheres, *Journal of Atmospheric and Terrestrial Physics*, 32(11), 1781–1791, doi:10.1016/0021-9169(70)90136-4.
- Barr, R. (1971a), The propagation of ELF and VLF radio waves beneath an inhomogeneous anisotropic ionosphere, *Journal of Atmospheric and Terrestrial Physics*, 33(3), 343–353, doi:10.1016/0021-9169(71)90139-5.
- Barr, R. (1971b), The effect of the Earth’s magnetic field on the propagation of ELF and VLF radio waves, *Journal of Atmospheric and Terrestrial Physics*, 33(10), 1577–1583, doi:10.1016/0021-9169(71)90075-4.
- Barr, R., P. Stubbe, M. T. Rietveld, and H. Kopka (1986), ELF and VLF signals radiated by the “polar electrojet antenna”: Experimental results, *Journal of Geophysical Research*, 91(A4), 4451, doi:10.1029/JA091iA04p04451.
- Barr, R., D. Jones, and C. Rodger (2000), ELF and VLF radio waves, *Journal of Atmospheric and Solar-Terrestrial Physics*, 62(17-18), 1689–1718, doi:10.1016/S1364-6826(00)00121-8.

- Belrose, J., and L. Thomas (1968), Ionization changes in the middle latitude D-region associated with geomagnetic storms, *Journal of Atmospheric and Terrestrial Physics*, *30*(7), 1397–1413, doi:10.1016/S0021-9169(68)91260-9.
- Belrose, J. S. (1970), Radio wave probing of the ionosphere by the partial reflection of radio waves (from heights below 100 km), *Journal of Atmospheric and Terrestrial Physics*, *32*(4), 567–596, doi:10.1016/0021-9169(70)90209-6.
- Belrose, J. S., and M. J. Burke (1964), Study of the lower ionosphere using partial reflection: 1. Experimental technique and method of analysis, *Journal of Geophysical Research*, *69*(13), 2799–2818, doi:10.1029/JZ069i013p02799.
- Belrose, J. S., M. J. Burke, T. N. R. Coyne, and J. E. Reed (1972), D -region measurements with the differential-absorption, differential-phase partial-reflection experiments, *Journal of Geophysical Research*, *77*(25), 4829–4838, doi:10.1029/JA077i025p04829.
- Bennett, F., J. Hall, and P. Dickinson (1972), D-region electron densities and collision frequencies from Faraday rotation and differential absorption measurements, *Journal of Atmospheric and Terrestrial Physics*, *34*(8), 1321–1335, doi:10.1016/0021-9169(72)90188-2.
- Best, J. E., J. A. Ratcliffe, and M. V. Wilkes (1936), Experimental investigations of very long waves reflected from the ionosphere, *Proceedings of the Royal Society A: Mathematical, Physical and Engineering Sciences*, *156*(889), 614–633, doi:10.1098/rspa.1936.0171.
- Beynon, W., and E. Williams (1976), Rocket measurements of D-region electron density profiles, *Journal of Atmospheric and Terrestrial Physics*, *38*(12), 1319–1325, doi:10.1016/0021-9169(76)90140-9.
- Bilitza, D., D. Altadill, V. Truhlik, V. Shubin, I. Galkin, B. Reinisch, and X. Huang (2017), International Reference Ionosphere 2016: From ionospheric climate to real-time weather predictions, *Space Weather*, *15*(2), 418–429, doi:10.1002/2016SW001593.
- Bracewell, R. (1952), Theory of formation of an ionospheric layer below E layer based on eclipse and solar flare effects at 16 kc/sec, *Journal of Atmospheric and Terrestrial Physics*, *2*(4), 226–235, doi:10.1016/0021-9169(52)90033-0.
- Bracewell, R., K. Budden, J. Ratcliffe, T. Straker, and K. Weekes (1951), The ionospheric propagation of low- and very-low-frequency radio waves over distances less than 1000 km, *Proceedings of the IEE - Part III: Radio and Communication Engineering*, *98*(53), 221–236, doi:10.1049/pi-3.1951.0043.
- Bracewell, R. N. (1956), Strip integration in radioastronomy, *Australian Journal of Physics*, *9*, 198–217.
- Breit, G., and M. A. Tuve (1926), A Test of the existence of the conducting layer, *Physical Review*, *28*(3), 554–575, doi:10.1103/PhysRev.28.554.
- Brook, M., N. Kitagawa, and E. J. Workman (1962), Quantitative study of strokes and continuing currents in lightning discharges to ground, *Journal of Geophysical Research*, *67*(2), 649–659, doi:10.1029/JZ067i002p00649.
- Brown, J. N., and J. M. Watts (1950), Ionosphere observations at 50 kc, *Journal of Geophysical Research*, *55*(2), 179–181, doi:10.1029/JZ055i002p00179.

- Budden, K. G. (1955a), The numerical solution of differential equations governing reflexion of long radio waves from the ionosphere, *Proceedings of the Royal Society of London. Series A. Mathematical and Physical Sciences*, 227(1171), 516–537, doi:10.1098/rspa.1955.0027.
- Budden, K. G. (1955b), The numerical solution of the differential equations governing the reflexion of long radio waves from the ionosphere. II, *Philosophical Transactions of the Royal Society A: Mathematical, Physical and Engineering Sciences*, 248(939), 45–72, doi:10.1098/rsta.1955.0009.
- Budden, K. G. (1961), *The Waveguide-Mode Theory of Propagation*, 1st ed., 325 pp., Prentice Hall, Englewood Cliffs.
- Budden, K. G. (1962), The influence of the Earth’s magnetic field on radio propagation by wave-guide modes, *Proceedings of the Royal Society A: Mathematical, Physical and Engineering Sciences*, 265(1323), 538–553, doi:10.1098/rspa.1962.0041.
- Burton, E., and E. Boardman (1933), Audio-frequency atmospherics, *Proceedings of the IRE*, 21(10), 1476–1494, doi:10.1109/JRPROC.1933.227485.
- Carvalho, F. L., M. A. Uman, D. M. Jordan, J. D. Hill, S. A. Cummer, D. A. Kotovsky, and R. C. Moore (2017), Triggered lightning sky waves, return stroke modeling, and ionosphere effective height, *J. Geophys. Res. Atmos.*, 122(6), 3507–3527.
- Cave, C. J. P., and E. A. Watson Watt (1922), The study of radiotelegraphic atmospherics in relation to meteorology, *Quarterly Journal of the Royal Meteorological Society*, 49(205), 35–39, doi:10.1002/qj.49704920508.
- CCITT (1993), Information technology-digital compression and coding of continuous-tone still images-requirements and guidelines, *Tech. rep.*, International Telecommunication Union.
- Cecil, D. J., D. E. Buechler, and R. J. Blakeslee (2014), Gridded lightning climatology from TRMM-LIS and OTD: Dataset description, *Atmospheric Research*, 135-136, 404–414, doi:10.1016/J.ATMOSRES.2012.06.028.
- Chapman, F. W., and R. C. V. Macario (1956), Propagation of audio-frequency radio waves to great distances, *Nature*, 177(4516), 930–933, doi:10.1038/177930a0.
- Chapman, F. W., D. L. Jones, J. D. W. Todd, and R. A. Challinor (1966), Observations on the propagation constant of the Earth-ionosphere waveguide in the frequency band 8 c/s to 16 kc/s, *Radio Science*, 1(11), 1273–1282, doi:10.1002/rds19661111273.
- Chapman, J., and E. Pierce (1957), Relations between the character of atmospherics and their place of origin, *Proceedings of the IRE*, 45(6), 804–806, doi:10.1109/JRPROC.1957.278478.
- Chau, J. L., and R. F. Woodman (2005), D and E region incoherent scatter radar density measurements over Jicamarca, *Journal of Geophysical Research*, 110(A12), A12,314, doi:10.1029/2005JA011438.
- Chen, S. S., D. L. Donoho, and M. A. Saunders (1996), Atomic decomposition by basis pursuit, *Tech. rep.*

- Cheng, Z., S. A. Cummer, D. N. Baker, and S. G. Kanekal (2006), Nighttime D region electron density profile and variabilities inferred from broadband measurements using VLF radio emissions from lightning, *Journal of Geophysical Research*, *111*(A05302), doi:10.1029/2005JA011308.
- Chrissan, D. A., and A. C. Fraser-Smith (1996), Seasonal variations of globally measured ELF/VLF radio noise, *Radio Sci.*, *31*(5), 1141–1152.
- Christian, H. J., R. J. Blakeslee, D. J. Boccippio, W. L. Boeck, D. E. Buechler, K. T. Driscoll, S. J. Goodman, J. M. Hall, W. J. Koshak, D. M. Mach, and M. F. Stewart (2003), Global frequency and distribution of lightning as observed from space by the Optical Transient Detector, *J. Geophys. Res.*, *108*(D1), ACL 4–1—ACL 4–15.
- Chubb, T. A., H. Friedman, R. W. Kreplin, and J. E. Kupperian (1957), Lyman alpha and X-ray emissions during a small solar flare, *Journal of Geophysical Research*, *62*(3), 389–398, doi:10.1029/JZ062i003p00389.
- Clilverd, M. A., C. J. Rodger, N. R. Thomson, J. Lichtenberger, P. Steinbach, P. Cannon, and M. J. Angling (2001), Total solar eclipse effects on VLF signals: Observations and modeling, *Radio Sci.*, *36*(4), 773–788.
- Clilverd, M. A., D. Nunn, S. J. Lev-Tov, U. S. Inan, R. L. Dowden, C. J. Rodger, and A. J. Smith (2002), Determining the size of lightning-induced electron precipitation patches, *Journal of Geophysical Research: Space Physics*, *107*(A8), SIA 10–1–SIA 10–11, doi:10.1029/2001JA000301.
- Cohen, I. M. (1963), Asymptotic theory of spherical electrostatic probes in a slightly ionized, collision-dominated gas, *Physics of Fluids*, *6*(10), 1492, doi:10.1063/1.1710972.
- Cohen, M. B. (2009), ELF/VLF phase array generation via frequency-matched steering of a continuous HF ionospheric heating beam, Ph.D. thesis, Stanford University.
- Cohen, M. B., and M. Gołkowski (2013), 100 days of ELF/VLF generation via HF heating with HAARP, *Journal of Geophysical Research: Space Physics*, *118*(10), 6597–6607, doi:10.1002/jgra.50558.
- Cohen, M. B., U. S. Inan, M. Gołkowski, and M. J. McCarrick (2010), ELF/VLF wave generation via ionospheric HF heating: Experimental comparison of amplitude modulation, beam painting, and geometric modulation, *Journal of Geophysical Research: Space Physics*, *115*(A2), doi:10.1029/2009JA014410.
- Cohen, M. B., N. C. Gross, M. A. Higginson-Rollins, R. A. Marshall, M. Gołkowski, W. Liles, D. Rodriguez, and J. Rockway (2018a), The lower ionospheric VLF/LF response to the 2017 great American solar eclipse observed across the continent, *Geophysical Research Letters*, *45*(8), 3348–3355, doi:10.1002/2018GL077351.
- Cohen, M. B., R. K. Said, E. W. Paschal, J. C. McCormick, N. C. Gross, L. Thompson, M. Higginson-Rollins, U. S. Inan, and J. Chang (2018b), Broadband longwave radio remote sensing instrumentation, *Review of Scientific Instruments*, *89*(9), 094,501, doi:10.1063/1.5041419.

- Cooray, V., and K. P. S. C. Jayaratne (1994), Characteristics of lightning flashes observed in Sri Lanka in the tropics, *Journal of Geophysical Research*, *99*(D10), 21,051, doi:10.1029/94JD01519.
- Cooray, V., and H. Pérez (1994), Some features of lightning flashes observed in Sweden, *Journal of Geophysical Research*, *99*(D5), 10,683, doi:10.1029/93JD02366.
- Cormack, A. M. (1963), Representation of a function by its line integrals, with some radiological applications, *Journal of Applied Physics*, *34*(9), 2722–2727, doi:10.1063/1.1729798.
- Cotts, B. R. T., and U. S. Inan (2007), VLF observation of long ionospheric recovery events, *Geophysical Research Letters*, *34*(14), L14,809, doi:10.1029/2007GL030094.
- Coyne, T. N. R. (1973), Analysis of the pulsed wave interaction experiment, *Journal of Geophysical Research*, *78*(1), 206–217, doi:10.1029/JA078i001p00206.
- Crombie, D. D. (1964), Periodic fading of VLF signals received over long paths during sunrise and sunset, *RADIO SCIENCE Journal of Research NBSjUSNC-URSI*, *680*(I).
- Croom, D. (1964), The frequency spectra and attenuation of atmospherics in the range 1–15 kc/s, *Journal of Atmospheric and Terrestrial Physics*, *26*(11), 1015–1046, doi:10.1016/0021-9169(64)90089-3.
- Cummer, S. (2000), Modeling electromagnetic propagation in the Earth-ionosphere waveguide, *IEEE Transactions on Antennas and Propagation*, *48*(9), 1420–1429, doi:10.1109/8.898776.
- Cummer, S. A. (1997), Lightning and ionospheric remote sensing using vlf/elf radio atmospherics, Ph.D. thesis, Stanford University.
- Cummer, S. A., and U. S. Inan (1997), Measurement of charge transfer in sprite-producing lightning using ELF radio atmospherics, *Geophysical Research Letters*, *24*(14), 1731–1734, doi:10.1029/97GL51791.
- Cummer, S. A., U. S. Inan, and T. F. Bell (1998), Ionospheric D region remote sensing using VLF radio atmospherics, *Radio Science*, *33*(6), 1781–1792.
- Cummins, K. L., M. J. Murphy, E. A. Bardo, W. L. Hiscox, R. B. Pyle, and A. E. Pifer (1998), A combined TOA/MDF technology upgrade of the U.S. National Lightning Detection Network, *Journal of Geophysical Research: Atmospheres*, *103*(D8), 9035–9044, doi:10.1029/98JD00153.
- Dahlgren, H., T. Sundberg, A. B. Collier, E. Koen, and S. Meyer (2011), Solar flares detected by the new narrowband VLF receiver at SANAE IV, *South African Journal of Science*.
- Deeks, D. G. (1966), D-region electron distributions in middle latitudes deduced from the reflexion of long radio waves, *Proceedings of the Royal Society A: Mathematical, Physical and Engineering Sciences*, *291*(1426), 413–437, doi:10.1098/rspa.1966.0103.
- Dowden, R., C. Adams, J. Brundell, and P. Dowden (1994), Rapid onset, rapid decay (RORD), phase and amplitude perturbations of VLF subionospheric transmissions, *Journal of Atmospheric and Terrestrial Physics*, *56*(11), 1513–1527, doi:10.1016/0021-9169(94)90118-X.

- Dowden, R. L., and C. D. D. Adams (1989), Phase and amplitude perturbations on the NWC signal at Dunedin from lightning-induced electron precipitation, *Journal of Geophysical Research*, *94* (A1), 497, doi:10.1029/JA094iA01p00497.
- Dowden, R. L., and C. D. D. Adams (1990), Location of lightning-induced electron precipitation from measurement of VLF phase and amplitude perturbations on spaced antennas and on two frequencies, *Journal of Geophysical Research*, *95* (A4), 4135, doi:10.1029/JA095iA04p04135.
- Dowden, R. L., J. B. Brundell, and W. A. Lyons (1996), Are VLF rapid onset, rapid decay perturbations produced by scattering off sprite plasma?, *Journal of Geophysical Research: Atmospheres*, *101* (D14), 19,175–19,183, doi:10.1029/96JD01346.
- Dowden, R. L., J. B. Brundell, and C. J. Rodger (2002), VLF lightning location by time of group arrival (TOGA) at multiple sites, *Journal of Atmospheric and Solar-Terrestrial Physics*, *64* (7), 817–830, doi:http://doi.org/10.1016/S1364-6826(02)00085-8.
- Dwyer, J. R. (2003), A fundamental limit on electric fields in air, *Geophysical Research Letters*, *30* (20), doi:10.1029/2003GL017781.
- Dwyer, J. R., and M. A. Uman (2014), The physics of lightning, *Physics Reports*, *534* (4), 147–241, doi:10.1016/J.PHYSREP.2013.09.004.
- Eccles, W. H. (1912), On the diurnal variations of the electric waves occurring in nature, and on the propagation of electric waves round the bend of the Earth, *Proceedings of the Royal Society A: Mathematical, Physical and Engineering Sciences*, *87* (593), 79–99, doi:10.1098/rspa.1912.0061.
- Eckersley, T. L. (1921), The effect of the Heaviside layer on the apparent direction of electromagnetic waves, *Radio Review*, *2*, 60.
- Eftaxias, K., P. Kaperis, J. Polygiannakis, N. Bogris, J. Kopanas, G. Antonopoulos, A. Peratzakis, and V. Hadjicontis (2001), Signature of pending earthquake from electromagnetic anomalies, *Geophysical Research Letters*, *28* (17), 3321–3324, doi:10.1029/2001GL013124.
- Egeland, A., G. Bjøntegård, and T. Aggson (1970), Evaluation of electron density from VLF Doppler measurements in a rocket, *Journal of Atmospheric and Terrestrial Physics*, *32* (7), 1191–1204, doi:10.1016/0021-9169(70)90051-6.
- Evans, J. (1965), Ionospheric backscatter observations at Millstone Hill, *Planetary and Space Science*, *13* (11), 1031–1074, doi:10.1016/0032-0633(65)90138-8.
- Farley, D. T., J. P. McClure, D. L. Sterling, and J. L. Green (1967), Temperature and composition of the equatorial ionosphere, *Journal of Geophysical Research*, *72* (23), 5837–5851, doi:10.1029/JZ072i023p05837.
- Farley, D. T., B. B. Balsey, R. F. Woodman, and J. P. McClure (1970), Equatorial spread F : Implications of VHF radar observations, *Journal of Geophysical Research*, *75* (34), 7199–7216, doi:10.1029/JA075i034p07199.
- Farley, D. T., H. M. Ierke, and B. G. Fejer (1981), Radar interferometry: A new technique for studying plasma turbulence in the ionosphere, *Journal of Geophysical Research*, *86* (A3), 1467, doi:10.1029/JA086iA03p01467.

- Fejer, J. (1955), The interaction of pulsed radio waves in the ionosphere, *Journal of Atmospheric and Terrestrial Physics*, *7*, 322–332, doi:10.1016/0021-9169(55)90137-9.
- Fejer, J. (1970), Radio wave probing of the lower ionosphere by cross-modulation techniques, *Journal of Atmospheric and Terrestrial Physics*, *32*(4), 597–607, doi:10.1016/0021-9169(70)90210-2.
- Ferguson, J. A. (1993), A review of the ionospheric model for the long wave prediction capability, *Tech. rep.*, Ocean and Atmospheric Sciences Division of the Naval Command.
- Ferguson, J. A. (1995), Ionospheric model validation at VLF and LF, *Radio Science*, *30*(3), 775–782, doi:10.1029/94RS03190.
- Ferguson, J. A. (1998), Computer programs for assessment of long-wavelength radio communications, *Tech. Rep. 3030*, Space and Naval Warfare Systems Center, San Diego.
- Ferguson, J. A., and F. P. Snyder (1980), Approximate VLF/LF waveguide mode conversion Model. computer applications: FASTMC and BUMP, *Tech. rep.*, Naval Ocean Systems Center, San Diego, CA.
- Ferraro, A., H. Lee, J. Rowe, and A. Mitra (1974), An experimental and theoretical study of the D-region—I. Mid-latitude D-region electron density profiles from the radio wave interaction experiment, *Journal of Atmospheric and Terrestrial Physics*, *36*(5), 741–754, doi:10.1016/0021-9169(74)90022-1.
- Ferraro, A., H. Lee, R. Allshouse, K. Carroll, A. Tomko, F. Kelly, and R. Joiner (1982), VLF/ELF radiation from the ionospheric dynamo current system modulated by powerful HF signals, *Journal of Atmospheric and Terrestrial Physics*, *44*(12), 1113–1122, doi:10.1016/0021-9169(82)90022-8.
- Ferraro, A. J., and H. S. Lee (1968), Capability of a high-power wave interaction facility, *Journal of Geophysical Research*, *73*(13), 4427–4429, doi:10.1029/JA073i013p04427.
- Flood, W. A. (1968), Revised theory for partial reflection D -region measurements, *Journal of Geophysical Research*, *73*(17), 5585–5598, doi:10.1029/JA073i017p05585.
- Franz, R. C., R. J. Nemzek, and J. R. Winckler (1990), Television image of a large upward electrical discharge above a thunderstorm system., *Science (New York, N.Y.)*, *249*(4964), 48–51, doi:10.1126/science.249.4964.48.
- Friedman, H. (1974), Solar ionizing radiation, *Journal of Atmospheric and Terrestrial Physics*, *36*(12), 2245–2253, doi:10.1016/0021-9169(74)90150-0.
- Friedrich, M., and K. M. Torkar (2001), FIRI: A semiempirical model of the lower ionosphere, *Journal of Geophysical Research*, *106*(A10), 21,409–21,418, doi:10.1029/2001JA900070.
- Friedrich, M., K. M. Torkar, G. A. Lehmacher, C. L. Croskey, J. D. Mitchell, E. Kudeki, and M. Milla (2006), Rocket and incoherent scatter radar common-volume electron measurements of the equatorial lower ionosphere, *Geophysical Research Letters*, *33*(8), L08,807, doi:10.1029/2005GL024622.



- Friedrich, M., C. Pock, and K. Torkar (2017), Long-term trends in the D- and E-region based on rocket-borne measurements, *Journal of Atmospheric and Solar-Terrestrial Physics*, *163*, 78–84, doi:10.1016/J.JASTP.2017.04.009.
- Füllekrug, M., A. Mezentsev, R. Watson, S. Gaffet, I. Astin, N. Smith, and A. Evans (2015a), Map of low-frequency electromagnetic noise in the sky, *Geophysical Research Letters*, *42*(11), 4648–4653, doi:10.1002/2015GL064142.
- Füllekrug, M., N. Smith, A. Mezentsev, R. Watson, I. Astin, S. Gaffet, A. Evans, and M. Rycroft (2015b), Multipath propagation of low-frequency radio waves inferred from high-resolution array analysis, *Radio Science*, *50*(11), 1141–1149, doi:10.1002/2015RS005781.
- Füllekrug, M., Z. Liu, K. Koh, A. Mezentsev, S. Pedebay, S. Soula, S.-E. Enno, J. Sugier, and M. J. Rycroft (2016), Mapping lightning in the sky with a mini array, *Geophysical Research Letters*, *43*(19), 10,448–10,454, doi:10.1002/2016GL070737.
- Gabow, H. (2007), *Proceedings of the Eighteenth Annual ACM-SIAM Symposium on Discrete Algorithms*, Society for Industrial and Applied Mathematics, Philadelphia, PA, USA.
- Gardner, F., and J. Pawsey (1953), Study of the ionospheric D-region using partial reflections, *Journal of Atmospheric and Terrestrial Physics*, *3*(6), 321–344, doi:10.1016/0021-9169(53)90084-1.
- Getmantsev, G. G., N. A. Zuikov, D. S. Kotik, L. F. Mironenko, N. A. Mitiakov, V. O. Rapoport, I. A. Sazonov, V. I. Trakhtengerts, and V. I. Eidman (1974), Combination frequencies in the interaction between high-power short-wave radiation and ionospheric plasma, (*ZHETF Pis'ma v Redaktsiiu*, vol. 20, Aug. 20, 1974, p. 229-232.) *JETP Letters*, vol. 20, Aug. 20, 1974, p. 101, 102. Translation., 20, 229–232.
- Goodman, S. J., R. J. Blakeslee, W. J. Koshak, D. Mach, J. Bailey, D. Buechler, L. Carey, C. Schultz, M. Bateman, E. McCaul, and G. Stano (2013), The GOES-R Geostationary Lightning Mapper (GLM), *Atmospheric Research*, *125-126*, 34–49, doi:10.1016/J.ATMOSRES.2013.01.006.
- Gordon, W. (1958), Incoherent scattering of radio waves by free electrons with applications to space exploration by radar, *Proceedings of the IRE*, *46*(11), 1824–1829, doi:10.1109/JRPROC.1958.286852.
- Gordon, W., and L. LaLonde (1961), The design and capabilities of an ionospheric radar probe, *IRE Transactions on Antennas and Propagation*, *9*(1), 17–22, doi:10.1109/TAP.1961.1144946.
- Green, A. (1974), Early history of the ionosphere, *Journal of Atmospheric and Terrestrial Physics*, *36*(12), 2159–2165, doi:10.1016/0021-9169(74)90146-9.
- Gross, N. C., M. B. Cohen, R. K. Said, and M. Gołkowski (2018), Polarization of narrowband VLF transmitter signals as an ionospheric diagnostic, *Journal of Geophysical Research: Space Physics*, *123*(1), 901–917, doi:10.1002/2017JA024907.

- Grubor, D. P., D. M. Šulić, and V. Žigman (2008), Classification of X-ray solar flares regarding their effects on the lower ionosphere electron density profile, *Annales Geophysicae*, *26*, 1731–1740.
- Hall, J., and J. Fooks (1965), The electron distribution in the quiet D-region derived from rocket measurements of low-frequency propagation, *Planetary and Space Science*, *13*(11), 1013–1030, doi:10.1016/0032-0633(65)90137-6.
- Hall, J., and J. Fooks (1967), D-region electron distributions from further rocket measurements of L.F. propagation, *Planetary and Space Science*, *15*(11), 1717–1722, doi:10.1016/0032-0633(67)90009-8.
- Han, F., and S. A. Cummer (2010a), Midlatitude nighttime D region ionosphere variability on hourly and monthly time scales, *Journal of Geophysical Research*, *115*(A09323), doi:10.1029/2010JA015437.
- Han, F., and S. A. Cummer (2010b), Midlatitude daytime D region ionosphere variations measured from radio atmospherics, *Journal of Geophysical Research*, *115*(A103314), doi:10.1029/2010JA015715.
- Han, F., S. A. Cummer, J. Li, and G. Lu (2011), Daytime ionospheric D region sharpness derived from VLF radio atmospherics, *Journal of Geophysical Research*, *116*(A05314), doi:10.1029/2010JA016299.
- Hargreaves, J. (1969), Auroral absorption of HF radio waves in the ionosphere: A review of results from the first decade of riometry, *Proceedings of the IEEE*, *57*(8), 1348–1373, doi:10.1109/PROC.1969.7275.
- Hartree, D. R. (1929), The propagation of electromagnetic waves in a stratified medium, *Mathematical Proceedings of the Cambridge Philosophical Society*, *25*(01), 97, doi:10.1017/S0305004100018600.
- Hartree, D. R. (1931), The propagation of electromagnetic waves in a refracting medium in a magnetic field, *Mathematical Proceedings of the Cambridge Philosophical Society*, *27*(01), 143, doi:10.1017/S0305004100009440.
- Hayakawa, M., Y. Kasahara, T. Nakamura, Y. Hobara, A. Rozhnoi, M. Solovieva, and O. Molchanov (2010), On the correlation between ionospheric perturbations as detected by subionospheric VLF/LF signals and earthquakes as characterized by seismic intensity, *Journal of Atmospheric and Solar-Terrestrial Physics*, *72*(13), 982–987, doi:10.1016/J.JASTP.2010.05.009.
- Headrick, J., and M. Skolnik (1974), Over-the-Horizon radar in the HF band, *Proceedings of the IEEE*, *62*(6), 664–673, doi:10.1109/PROC.1974.9506.
- Helliwell, R. A., A. J. Mallinckrodt, and F. W. Kruse (1951), Fine structure of the lower ionosphere, *Journal of Geophysical Research*, *56*(1), 53–62, doi:10.1029/JZ056i001p00053.
- Helliwell, R. A., J. P. Katsufakis, and M. L. Trimpi (1973), Whistler-induced amplitude perturbation in VLF propagation, *Journal of Geophysical Research*, *78*(22), 4679–4688.

- Higginson-Rollins, M. A., and M. B. Cohen (2017), Exploiting LF/MF signals of opportunity for lower ionospheric remote sensing, *Geophysical Research Letters*, *44*(16), 8665–8671, doi:10.1002/2017GL074236.
- Hocking, W. K. (1979), Angular and temporal characteristics of partial reflections from the D-region of the ionosphere, *Journal of Geophysical Research*, *84*(A3), 845, doi:10.1029/JA084iA03p00845.
- Hocking, W. K., and R. A. Vincent (1982), Comparative observations of D region HF partial reflections at 2 and 6 MHz, *Journal of Geophysical Research*, *87*(A9), 7615, doi:10.1029/JA087iA09p07615.
- Hollingworth, J. (1926), The propagation of radio waves, *Journal of the Institution of Electrical Engineers*, *64*(353), 579–589, doi:10.1049/jiee-1.1926.0048.
- Hounsfield, G. N. (1973), Computer transverse axial scanning (tomography). Part I. Description of system., *British Journal of Radiology*, *46*(1016).
- Hu, W., and S. Cummer (2006), An FDTD model for low and high altitude lightning-generated EM fields, *IEEE Transactions on Antennas and Propagation*, *54*(5), 1513–1522, doi:10.1109/TAP.2006.874336.
- Hulburt, E. (1974), Early theory of the ionosphere, *Journal of Atmospheric and Terrestrial Physics*, *36*(12), 2137–2140, doi:10.1016/0021-9169(74)90144-5.
- Hutchins, M. L., R. H. Holzworth, and J. B. Brundell (2014), Diurnal variation of the global electric circuit from clustered thunderstorms, *J. Geophys. Res. Space Physics*, *119*(1), 620–629.
- Inan, U. S. (1990), VLF heating of the lower ionosphere, *Geophysical Research Letters*, *17*(6), 729–732, doi:10.1029/GL017i006p00729.
- Inan, U. S., W. C. Burgess, T. G. Wolf, D. C. Shater, and R. E. Orville (1988a), Lightning-associated precipitation of MeV electrons from the inner radiation belt, *Geophysical Research Letters*, *15*(2), 172–175, doi:10.1029/GL015i002p00172.
- Inan, U. S., T. G. Wolf, and D. L. Carpenter (1988b), Geographic distribution of lightning-induced electron precipitation observed as VLF/LF perturbation events, *Journal of Geophysical Research*, *93*(A9), 9841, doi:10.1029/JA093iA09p09841.
- Inan, U. S., D. C. Shafer, W. Y. Yip, and R. E. Orville (1988c), Subionospheric VLF signatures of nighttime D region perturbations in the vicinity of lightning discharges, *Journal of Geophysical Research*, *93*(A10), 11,455, doi:10.1029/JA093iA10p11455.
- Inan, U. S., T. F. Bell, and J. V. Rodriguez (1991), Heating and ionization of the lower ionosphere by lightning, *Geophysical Research Letters*, *18*(4), 705–708, doi:10.1029/91GL00364.
- Inan, U. S., T. F. Bell, V. P. Pasko, D. D. Sentman, E. M. Wescott, and W. A. Lyons (1995), VLF signatures of ionospheric disturbances associated with sprites, *Geophysical Research Letters*, *22*(24), 3461–3464, doi:10.1029/95GL03507.

- Inan, U. S., V. P. Pasko, and T. F. Bell (1996), Sustained heating of the ionosphere above thunderstorms as evidenced in “early/fast” VLF events, *Geophysical Research Letters*, *23*(10), 1067–1070, doi:10.1029/96GL01360.
- Inan, U. S., S. A. Cummer, and R. A. Marshall (2010), A survey of ELF and VLF research on lightning-ionosphere interactions and causative discharges, *J. Geophys. Res.*, *115*(A6), 147–241.
- Jakowski, N., S. Schlüter, and E. Sardon (1999), Total electron content of the ionosphere during the geomagnetic storm on 10 January 1997, *Journal of Atmospheric and Solar-Terrestrial Physics*, *61*(3-4), 299–307, doi:10.1016/S1364-6826(98)00130-8.
- Jean, A. G., W. L. Taylor, and J. R. Wait (1960), VLF phase characteristics deduced from atmospheric wave forms, *Journal of Geophysical Research*, *65*(3), 907–912, doi:10.1029/JZ065i003p00907.
- Jones, T., and I. Wand (1970), An investigation of the reflection properties of various ionospheric models for radio waves in the frequency range 16–3000 kHz, *Journal of Atmospheric and Terrestrial Physics*, *32*(10), 1705–1719, doi:10.1016/0021-9169(70)90176-5.
- Kamide, Y., and J. F. Vickrey (1983), Relative contribution of ionospheric conductivity and electric field to the auroral electrojets, *Journal of Geophysical Research*, *88*(A10), 7989, doi:10.1029/JA088iA10p07989.
- Kitchen, F., B. Pressey, and K. Tremellen (1953), *Proceedings of the institution of electrical engineers, part 3: Radio and communication engineering.*, vol. 100, 100–108 pp., The Institution of Engineering and Technology.
- Knoebel, H. W., and D. O. Skaperdas (1966), Rocket Measurements of Faraday Rotation and Differential Absorption, *Review of Scientific Instruments*, *37*(10), 1395–1400, doi:10.1063/1.1719990.
- Kockarts, G. (2002), Aeronomy, a 20th Century emergent science: the role of solar Lyman series, *Annales Geophysicae*, *20*, 585–598.
- Kolarski, A., and D. Grubor (2014), Sensing the Earth’s low ionosphere during solar flares using VLF signals and goes solar X-ray data, *Advances in Space Research*, *53*, 1595–1602, doi:10.1016/j.asr.2014.02.022.
- Krehbiel, P. R., J. A. Riouset, V. P. Pasko, R. J. Thomas, W. Rison, M. A. Stanley, and H. E. Edens (2008), Upward electrical discharges from thunderstorms, *Nature Geoscience*, *1*(4), 233–237, doi:10.1038/ngeo162.
- Kumar, S., S. K. Dixit, and A. K. Gwal (1994), Propagation of tweek atmospherics in the Earth-ionosphere wave guide, *Il Nuovo Cimento C*, *17*(3), 275–280, doi:10.1007/BF02509168.
- Kumar, S., A. Deo, and V. Ramachandran (2009), Nighttime D-region equivalent electron density determined from tweek sferics observed in the South Pacific region, *Earth, Planets and Space*, *61*(7), 905–911, doi:10.1186/BF03353201.
- Laby, T. H., F. G. Nicholls, A. F. B. Nickson, and J. J. McNeill (1938), Reflection of atmospherics by the ionosphere, *Nature*, *142*(3590), 353–354, doi:10.1038/142353a0.

- Larkina, V., V. Migulin, O. Molchanov, I. Kharkov, A. Inchin, and V. Schvetcova (1989), Some statistical results on very low frequency radiowave emissions in the upper ionosphere over earthquake zones, *Physics of the Earth and Planetary Interiors*, 57(1-2), 100–109, doi:10.1016/0031-9201(89)90219-7.
- Lastovicka, J. (2006), Forcing of the ionosphere by waves from below, *Journal of Atmospheric and Solar-Terrestrial Physics*, 68(3-5), 479–497, doi:10.1016/J.JASTP.2005.01.018.
- Lay, E. H., and X.-M. Shao (2011a), High temporal and spatial-resolution detection of D-layer fluctuations by using time-domain lightning waveforms, *J. Geophys. Res.*, 116(A1), A01,317.
- Lay, E. H., and X.-M. Shao (2011b), Multi-station probing of thunderstorm-generated D-layer fluctuations by using time-domain lightning waveforms, *Geophys. Res. Lett.*, 38(23), L23,806.
- Lay, E. H., X.-M. Shao, and A. R. Jacobson (2014), D region electron profiles observed with substantial spatial and temporal change near thunderstorms, *J. Geophys. Res. Space Physics*, 119(6), 4916–4928.
- Lay, E. H., X.-M. Shao, A. K. Kendrick, and C. S. Carrano (2015), Ionospheric acoustic and gravity waves associated with midlatitude thunderstorms, *Journal of Geophysical Research: Space Physics*, 120(7), 6010–6020, doi:10.1002/2015JA021334.
- Le Vine, D. M. (1980), Sources of the strongest RF radiation from lightning, *Journal of Geophysical Research: Oceans*, 85(C7), 4091–4095, doi:10.1029/JC085iC07p04091.
- Lev-Tov, S. J., U. S. Inan, and T. F. Bell (1995), Altitude profiles of localized D region density disturbances produced in lightning-induced electron precipitation events, *Journal of Geophysical Research: Space Physics*, 100(A11), 21,375–21,383, doi:10.1029/95JA01615.
- Liu, H.-L., W. Wang, A. D. Richmond, and R. G. Roble (2010), Ionospheric variability due to planetary waves and tides for solar minimum conditions, *Journal of Geophysical Research: Space Physics*, 115(A6), doi:10.1029/2009JA015188.
- Liu, N., J. R. Dwyer, and H. K. Rassoul (2012), Effects of pressure and humidity on positive corona inception from thundercloud hydrometeors, *Journal of Atmospheric and Solar-Terrestrial Physics*, 80, 179–186, doi:10.1016/J.JASTP.2012.01.012.
- Lyu, F., S. A. Cummer, R. Solanki, J. Weinert, L. McTague, A. Katko, J. Barrett, L. Zigoneanu, Y. Xie, and W. Wang (2014), A low-frequency near-field interferometric-TOA 3-D Lightning Mapping Array, *Geophysical Research Letters*, 41(22), 7777–7784, doi:10.1002/2014GL061963.
- Lyu, F., S. A. Cummer, and L. McTague (2015), Insights into high peak current in-cloud lightning events during thunderstorms, *Geophysical Research Letters*, 42(16), 6836–6843, doi:10.1002/2015GL065047.
- Lyu, F., S. A. Cummer, G. Lu, X. Zhou, and J. Weinert (2016), Imaging lightning intracloud initial stepped leaders by low-frequency interferometric lightning mapping array, *Geophysical Research Letters*, 43(10), 5516–5523, doi:10.1002/2016GL069267.

- Macgorman, D. R., and W. D. Rust (1998), *The Electrical Nature of Storms*, Oxford University Press.
- Mallick, S., V. Rakov, D. Tsalikis, A. Nag, C. Biagi, D. Hill, D. Jordan, M. Uman, and J. Cramer (2014), On remote measurements of lightning return stroke peak currents, *Atmospheric Research*, 135-136, 306–313, doi:10.1016/J.ATMOSRES.2012.08.008.
- Mannucci, A. J., B. D. Wilson, D. N. Yuan, C. H. Ho, U. J. Lindqwister, and T. F. Runge (1998), A global mapping technique for GPS-derived ionospheric total electron content measurements, *Radio Science*, 33(3), 565–582, doi:10.1029/97RS02707.
- Marconi, G. (1902), A Note on the effect of daylight upon the propagation of electromagnetic impulses over long distances, *Proceedings of the Royal Society of London*, 70(459-466), 344–347, doi:10.1098/rspl.1902.0035.
- Marconi, G. (1922), Radio telegraphy, *Journal of the American Institute of Electrical Engineers*, 41(8), 561–570, doi:10.1109/JoAIEE.1922.6591020.
- Marshall, R. A. (2012), An improved model of the lightning electromagnetic field interaction with the D-region ionosphere, *Journal of Geophysical Research: Space Physics*, 117(A3), doi:10.1029/2011JA017408.
- Marshall, R. A., and U. S. Inan (2010), Two-dimensional frequency domain modeling of lightning EMP-induced perturbations to VLF transmitter signals, *Journal of Geophysical Research: Space Physics*, 115(A6), doi:10.1029/2009JA014761.
- Martyn, D. F. (1948), Atmospheric tides in the ionosphere. IV. Studies of the solar tide, and the location of the regions producing the diurnal magnetic variations, *Proceedings of the Royal Society A: Mathematical, Physical and Engineering Sciences*, 194(1039), 445–463, doi:10.1098/rspa.1948.0091.
- Massey, H. (1974), Theories of the ionosphere—1930–1955, *Journal of Atmospheric and Terrestrial Physics*, 36(12), 2141–2158, doi:10.1016/0021-9169(74)90145-7.
- Mathews, J. (1984), The incoherent scatter radar as a tool for studying the ionospheric D-region, *Journal of Atmospheric and Terrestrial Physics*, 46(11), 975–986, doi:10.1016/0021-9169(84)90004-7.
- Mathews, J. (1998), Sporadic E: current views and recent progress, *Journal of Atmospheric and Solar-Terrestrial Physics*, 60(4), 413–435, doi:10.1016/S1364-6826(97)00043-6.
- Maurya, A. K., B. Veenadhari, R. Singh, S. Kumar, M. B. Cohen, R. Selvakumaran, S. Gokani, P. Pant, A. K. Singh, and U. S. Inan (2012), Nighttime D region electron density measurements from ELF-VLF tweek radio atmospherics recorded at low latitudes, *Journal of Geophysical Research: Space Physics*, 117(A11), A11,308, doi:10.1029/2012JA017876.
- Maurya, A. K., D. V. Phanikumar, R. Singh, S. Kumar, B. Veenadhari, Y.-S. Kwak, A. Kumar, A. K. Singh, and K. Niranjana Kumar (2014), Low-mid latitude D region ionospheric perturbations associated with 22 July 2009 total solar eclipse: Wave-like signatures inferred from VLF observations, *Journal of Geophysical Research: Space Physics*, 119(10), 8512–8523, doi:10.1002/2013JA019521.

- Mayaud, P. (1977), The equatorial counter-electrojet—a review of its geomagnetic aspects, *Journal of Atmospheric and Terrestrial Physics*, *39*(9-10), 1055–1070, doi:10.1016/0021-9169(77)90014-9.
- McClure, J. P., W. B. Hanson, and J. H. Hoffman (1977), Plasma bubbles and irregularities in the equatorial ionosphere, *Journal of Geophysical Research*, *82*(19), 2650–2656, doi:10.1029/JA082i019p02650.
- McCormick, J. C., M. B. Cohen, N. C. Gross, and R. K. Said (2018), Spatial and temporal ionospheric monitoring using broadband spheric measurements, *Journal of Geophysical Research: Space Physics*, *123*(4), 3111–3130, doi:10.1002/2017JA024291.
- McDiarmid, I. B., and J. R. Burrows (1965), Electron fluxes at 1000 kilometers associated with the tail of the magnetosphere, *Journal of Geophysical Research*, *70*(13), 3031–3044, doi:10.1029/JZ070i013p03031.
- McPherron, R. L. (1970), Growth phase of magnetospheric substorms, *Journal of Geophysical Research*, *75*(28), 5592–5599, doi:10.1029/JA075i028p05592.
- McRae, W. M., and N. R. Thomson (2000), VLF phase and amplitude: daytime ionospheric parameters, *Journal of Atmospheric and Solar-Terrestrial Physics*, *62*, 609–618.
- McRae, W. M., and N. R. Thomson (2004), Solar flare induced ionospheric D-region enhancements from VLF phase and amplitude observations, *Journal of Atmospheric and Solar-Terrestrial Physics*, *66*, 77–87, doi:10.1016/j.jastp.2003.09.009.
- Mechtly, E. A. (1974), Accuracy of rocket measurements of lower ionosphere electron concentrations, *Radio Science*, *9*(3), 373–378, doi:10.1029/RS009i003p00373.
- Mechtly, E. A., S. A. Bowhill, L. G. Smith, and H. W. Knoebel (1967), Lower ionosphere electron concentration and collision frequency from rocket measurements of Faraday rotation, differential absorption, and probe current, *Journal of Geophysical Research*, *72*(21), 5239–5245, doi:10.1029/JZ072i021p05239.
- Megill, L. R., G. W. Adams, J. C. Haslett, and E. C. Whipple (1971), Measurement of the effective electron loss rates in the D region during polar cap absorption events, *Journal of Geophysical Research*, *76*(19), 4587–4595, doi:10.1029/JA076i019p04587.
- Mika, A., C. Haldoupis, T. Neubert, H. T. Su, R. R. Hsu, R. J. Steiner, and R. A. Marshall (2006), Early VLF perturbations observed in association with elves, *Tech. rep.*
- Miller, K. L., and L. G. Smith (1978), Incoherent scatter radar observations of irregular structure in mid-latitude sporadic E layers, *Journal of Geophysical Research*, *83*(A8), 3761, doi:10.1029/JA083iA08p03761.
- Mitra, A. P. (1964), *Ionospheric Effects of Solar Flares*, Springer, New York.
- Moore, R. C., U. S. Inan, T. F. Bell, and E. J. Kennedy (2007), ELF waves generated by modulated HF heating of the auroral electrojet and observed at a ground distance of -4400 km, *Journal of Geophysical Research: Space Physics*, *112*(A5), A05,309, doi:10.1029/2006JA012063.

- Morfitt, D. G., and C. H. Shellman (1976), 'MODESRCH', an improved computer program for obtaining ELF/VLF/LF mode constants in an Earth-ionosphere waveguide.
- Morgan, R. R. (1968a), World-wide VLF effective-conductivity map, *Tech. rep.*, Office of Naval Research, Washington, D.C.
- Morgan, R. R. (1968b), Preparation of a worldwide VLF effective conductivity map, *Tech. rep.*, Office of Naval Research, Washington, D.C.
- Müller, E. A. W. (1935), Die Schwächung extraterrestrischer Röntgenstrahlen in der Atmosphäre Mit 5 Abbildungen., *Zeitschrift für Astrophysik*, 10, 52–55.
- Narcisi, R. S., and A. D. Bailey (1965), Mass spectrometric measurements of positive ions at altitudes from 64 to 112 kilometers, *Journal of Geophysical Research*, 70(15), 3687–3700, doi:10.1029/JZ070i015p03687.
- NFPA (2017), NFPA 780 - Standard for the installation of lightning protection systems, *Tech. rep.*, NFPA.
- Nicolet, M., and A. C. Aikin (1960), The formation of the D region of the ionosphere, *Journal of Geophysical Research*, 65(5), 1469–1483, doi:10.1029/JZ065i005p01469.
- Nina, A., and V. M. Čadež (2014), Electron production by solar Ly- $\alpha$  line radiation in the ionospheric D-region, *Advances in Space Research*, 54(7), 1276–1284, doi:10.1016/J.ASR.2013.12.042.
- Nucci, C., F. Rachidi, M. Ianoz, and C. Mazzetti (1993), Lightning-induced voltages on overhead lines, *IEEE Transactions on Electromagnetic Compatibility*, 35(1), 75–86, doi:10.1109/15.249398.
- Nucci, C. A., C. Mazzetti, F. Rachidi, and M. Ianoz (1988), On lightning return stroke models for LEMP calculations.
- of the Computation Laboratory at Cambridge, Mass, S. (1945), *Tables of the modified Hankel functions of order one-third and of their derivatives*, Harvard University Press, Cambridge, Mass.
- Ohya, H., M. Nishino, Y. Murayama, K. Igarashi, and A. Saito (2006), Using tweek atmospherics to measure the response of the low-middle latitude D-region ionosphere to a magnetic storm, *Journal of Atmospheric and Solar-Terrestrial Physics*, 68(6), 697–709, doi:10.1016/J.JASTP.2005.10.014.
- Orville, R. E., G. R. Huffines, W. R. Burrows, R. L. Holle, K. L. Cummins, R. E. Orville, G. R. Huffines, W. R. Burrows, R. L. Holle, and K. L. Cummins (2002), The North American Lightning Detection Network (NALDN)—First results: 1998–2000, *Monthly Weather Review*, 130(8), 2098–2109, doi:10.1175/1520-0493(2002)130<2098:TNALDN>2.0.CO;2.
- PACE (2017), *Partnership for an Advanced Computing Environment (PACE)*.
- Pappert, R. A. (1970), Effects of elevation and ground conductivity on horizontal dipole excitation of the Earth-ionosphere waveguide, *Radio Science*, 5(3), 579–590, doi:10.1029/RS005i003p00579.



- Pappert, R. A., and J. E. Bickel (1970), Vertical and horizontal VLF fields excited by dipoles of arbitrary orientation and elevation, *Radio Science*, 5(12), 1445–1452, doi:10.1029/RS005i012p01445.
- Pappert, R. A., and J. A. Ferguson (1986), VLF/LF mode conversion model calculations for air to air transmissions in the Earth-ionosphere waveguide, *Radio Science*, 21(4), 551–558, doi:10.1029/RS021i004p00551.
- Pappert, R. A., and D. G. Morfitt (1975), Theoretical and experimental sunrise mode conversion results at VLF, *Radio Science*, 10(5), 537–546, doi:10.1029/RS010i005p00537.
- Pappert, R. A., and F. P. Snyder (1972), Some results of a mode-conversion program for VLF, *Radio Science*, 7(10), 913–923, doi:10.1029/RS007i010p00913.
- Pappert, R. A., E. E. Gossard, and I. J. Rothmuller (1967), A numerical investigation of classical approximations used in VLF Propagation, *Radio Science*, 2(4), 387–400, doi:10.1002/rds196724387.
- Pappert, R. A., R. R. Smith, and L. R. Shockey (1971), Numerical results for VLF mode conversion in the Earth-ionosphere waveguide.
- Parrot, M., and M. Mogilevsky (1989), VLF emissions associated with earthquakes and observed in the ionosphere and the magnetosphere, *Physics of the Earth and Planetary Interiors*, 57(1-2), 86–99, doi:10.1016/0031-9201(89)90218-5.
- Pasko, V. P., U. S. Inan, T. F. Bell, and Y. N. Taranenko (1997), Sprites produced by quasi-electrostatic heating and ionization in the lower ionosphere, *Journal of Geophysical Research: Space Physics*, 102(A3), 4529–4561, doi:10.1029/96JA03528.
- Pasko, V. P., U. S. Inan, and T. F. Bell (1998), Ionospheric effects due to electrostatic thundercloud fields, *Journal of Atmospheric and Solar-Terrestrial Physics*, 60(7-9), 863–870, doi:10.1016/S1364-6826(98)00022-4.
- Pessi, A. T., S. Businger, K. L. Cummins, N. W. S. Demetriades, M. Murphy, B. Pifer, A. T. Pessi, S. Businger, K. L. Cummins, N. W. S. Demetriades, M. Murphy, and B. Pifer (2009), Development of a long-range lightning detection network for the Pacific: Construction, calibration, and performance\*, *Journal of Atmospheric and Oceanic Technology*, 26(2), 145–166, doi:10.1175/2008JTECHA1132.1.
- Proctor, D. E., R. Uytendogaardt, and B. M. Meredith (1988), VHF radio pictures of lightning flashes to ground, *Journal of Geophysical Research*, 93(D10), 12,683, doi:10.1029/JD093iD10p12683.
- Radon, J. H. (1917), Über die bestimmung von funktionen durch ihre integralwerte längs gewisser mannigfaltigkeiten., in *Berichte über die Verhandlungen der Königlich-Sächsischen Akademie der Wissenschaften zu Leipzig, Mathematisch-Physische Klasse*, vol. 69, pp. 262–277.
- Raizada, S., M. P. Sulzer, C. A. Tepley, S. A. Gonzalez, and M. J. Nicolls (2008), Inferring D region parameters using improved incoherent scatter radar techniques at Arecibo, *Journal of Geophysical Research: Space Physics*, 113(A12), A12,302, doi:10.1029/2007JA012882.

- Rakov, A. V., and A. M. Uman (2003), *Lightning Physics and Effects*, Cambridge University Press.
- Rakov, V. A., and A. A. Dulzon (1991), A modified transmission line model for lightning return stroke field calculations, in *Proc. 9th Int. Symp. on Electromagnetic Compatibility*, pp. 229–235, Zurich.
- Rakov, V. A., and M. A. Uman (1990), Long continuing current in negative lightning ground flashes, *Journal of Geophysical Research*, *95*(D5), 5455, doi:10.1029/JD095iD05p05455.
- Ratcliffe, J. (1974), The formation of the ionosphere. ideas of the early years (1925–1955), *Journal of Atmospheric and Terrestrial Physics*, *36*(12), 2167–2181, doi:10.1016/0021-9169(74)90147-0.
- Reeve, C., and M. Rycroft (1972), The eclipsed lower ionosphere as investigated by natural very low frequency radio signals, *Journal of Atmospheric and Terrestrial Physics*, *34*(4), 667–672, doi:10.1016/0021-9169(72)90154-7.
- Reid, G. C. (1970), Production and loss of electrons in the quiet daytime D region of the ionosphere, *Journal of Geophysical Research*, *75*(13), 2551–2562, doi:10.1029/JA075i013p02551.
- Reid, G. C. (1977), The production of water-cluster positive ions in the quiet daytime D region, *Planetary and Space Science*, *25*(3), 275–290, doi:10.1016/0032-0633(77)90138-6.
- Reinisch, B., and X. Huang (2001), Deducing topside profiles and total electron content from bottomside ionograms, *Advances in Space Research*, *27*(1), 23–30, doi:10.1016/S0273-1177(00)00136-8.
- Rishbeth, H. (1974), Ionospheric dynamics 1945–1970, *Journal of Atmospheric and Terrestrial Physics*, *36*(12), 2309–2319, doi:10.1016/0021-9169(74)90153-6.
- Rison, W., R. J. Thomas, P. R. Krehbiel, T. Hamlin, and J. Harlin (1999), A GPS-based three-dimensional lightning mapping system: Initial observations in central New Mexico, *Geophysical Research Letters*, *26*(23), 3573–3576, doi:10.1029/1999GL010856.
- Robinson, R. M., and R. R. Vondrak (1984), Measurements of E region ionization and conductivity produced by solar illumination at high latitudes, *Journal of Geophysical Research*, *89*(A6), 3951, doi:10.1029/JA089iA06p03951.
- Row, R. V. (1967), Acoustic-gravity waves in the upper atmosphere due to a nuclear detonation and an earthquake, *Journal of Geophysical Research*, *72*(5), 1599–1610, doi:10.1029/JZ072i005p01599.
- Rudlosky, S. D., and D. T. Shea (2013), Evaluating WWLLN performance relative to TRMM/LIS, *Geophysical Research Letters*, *40*(10), 2344–2348, doi:10.1002/grl.50428.
- Saba, M. M. F., K. L. Cummins, T. A. Warner, E. P. Krider, L. Z. S. Campos, M. G. Balarotti, O. Pinto, and S. A. Fleenor (2008), Positive leader characteristics from high-speed video observations, *Geophysical Research Letters*, *35*(7), doi:10.1029/2007GL033000.
- Said, R. K. (2009), Accurate and efficient long-range lightning geo-location using a VLF radio atmospheric waveform bank, Ph.D. thesis, Stanford University.

- Said, R. K., and M. J. Murphy (2016), GLD360 Upgrade: Performance analysis and applications, in *2016 ILDC/ILMC*.
- Said, R. K., U. S. Inan, and K. L. Cummins (2010), Long-range lightning geolocation using a VLF radio atmospheric waveform bank, *Journal of Geophysical Research*, *115*(D23), doi:10.1029/2010JD013863.
- Said, R. K., M. B. Cohen, and U. S. Inan (2013), Highly intense lightning over the oceans: Estimated peak currents from global GLD360 observations, *J. Geophys. Res. Atmos.*, *118*(13), 6905–6915.
- Saunders, C. P. R. (1993), A review of thunderstorm electrification processes, *Journal of Applied Meteorology*, *32*(4), 642–655, doi:10.1175/1520-0450(1993)032<0642:AROTEP>2.0.CO;2.
- Schafer, J. P., and W. M. Goodall (1933), Characteristics of the ionosphere, *Nature*, *131*(3318), 804–804, doi:10.1038/131804a0.
- Scherrer, D., M. Cohen, T. Hoeksema, U. Inan, R. Mitchell, and P. Scherrer (2008), Distributing space weather monitoring instruments and educational materials worldwide for IHY 2007: The AWESOME and SID project, *Advances in Space Research*, *42*(11), 1777–1785, doi:10.1016/J.ASR.2007.12.013.
- Schoene, J., M. A. Uman, V. A. Rakov, K. J. Rambo, J. Jerauld, C. T. Mata, A. G. Mata, D. M. Jordan, and G. H. Schnetzer (2009), Characterization of return-stroke currents in rocket-triggered lightning, *Journal of Geophysical Research*, *114*(D3), D03,106, doi:10.1029/2008JD009873.
- Sechrist, C. F., E. A. Mechtly, J. S. Shirke, and J. S. Theon (1969), Coordinated rocket measurements on the D-region winter anomaly-I. Experimental results, *Journal of Atmospheric and Terrestrial Physics*, *31*(1), 145–153, doi:https://doi.org/10.1016/0021-9169(69)90088-9.
- Sechrist, C. F. J. (1974), Comparisons of techniques for measurements of D-region electron densities, *Radio Science*, *9*(2), 137–149.
- Seddon, J. C. (1953), Propagation measurements in the ionosphere with the aid of rockets, *Journal of Geophysical Research*, *58*(3), 323–335, doi:10.1029/JZ058i003p00323.
- Seddon, J. C. (1958), Differential absorption in The D and lower- E regions, *Journal of Geophysical Research*, *63*(1), 209–216, doi:10.1029/JZ063i001p00209.
- Sen, H. K., and A. A. Wyller (1960), On the generalization of the Appleton-Hartree magnetoionic formulas, *Journal of Geophysical Research*, *65*(12), 3931–3950, doi:10.1029/JZ065i012p03931.
- Shao, X.-M., and A. R. Jacobson (2009), Model simulation of very low-frequency and low-frequency lightning signal propagation over intermediate ranges, *IEEE Transactions on Electromagnetic Compatibility*, *51*(3), 519–525, doi:10.1109/TEMPC.2009.2022171.
- Shao, X.-M., E. H. Lay, and A. R. Jacobson (2013), Reduction of electron density in the night-time lower ionosphere in response to a thunderstorm, *Nature Geosci*, *6*(1), 29–33.

- Sheddy, C. H. (1968), A general analytic solution for reflection from a sharply bounded anisotropic ionosphere, *Radio Science*, *3*(8), 792–795, doi:10.1002/rds196838792.
- Shellman, C. H. (1970), Electron-density distributions in the lower ionosphere with associated error limits derived from VLF and LF sounder data, *Radio Science*, *5*(8-9), 1127–1135, doi:10.1029/RS005i008p01127.
- Shindo, T., and M. A. Uman (1989), Continuing current in negative cloud-to-ground lightning, *Journal of Geophysical Research*, *94*(D4), 5189, doi:10.1029/JD094iD04p05189.
- Singer, W., R. Latteck, M. Friedrich, M. Wakabayashi, and M. Rapp (2011), Seasonal and solar activity variability of D-region electron density at 69°N, *Journal of Atmospheric and Solar-Terrestrial Physics*, *73*(9), 925–935, doi:10.1016/J.JASTP.2010.09.012.
- Singh, A. K., A. K. Singh, R. Singh, and R. P. Singh (2013), Solar flare induced D-region ionospheric perturbations evaluated from VLF measurements, *Astrophysics and Space Science*, *350*, 1–9, doi:10.1007/s10509-013-1699-4.
- Smith, A. M., C. N. Mitchell, R. J. Watson, R. W. Meggs, P. M. Kintner, K. Kauristie, and F. Honary (2008), GPS scintillation in the high arctic associated with an auroral arc, *Space Weather*, *6*(3), doi:10.1029/2007SW000349.
- Smith, L. G., and E. A. Mechtly (1972), Rocket observations of sporadic- E layers, *Radio Science*, *7*(3), 367–376, doi:10.1029/RS007i003p00367.
- Stolzenburg, M., T. C. Marshall, W. D. Rust, E. Bruning, D. R. MacGorman, and T. Hamlin (2007), Electric field values observed near lightning flash initiations, *Geophysical Research Letters*, *34*(4), L04,804, doi:10.1029/2006GL028777.
- Storey, L. R. O. (1953), An investigation of whistling atmospherics, *Philosophical Transactions of the Royal Society A: Mathematical, Physical and Engineering Sciences*, *246*(908), 113–141, doi:10.1098/rsta.1953.0011.
- Strobel, D., C. Opal, and R. Meier (1980), Photoionization rates in the night-time E- and F-region ionosphere-, *Planetary and Space Science*, *28*(11), 1027–1033, doi:10.1016/0032-0633(80)90050-1.
- Šulić, D., V. Srećković, and A. Mihajlov (2016), A study of VLF signals variations associated with the changes of ionization level in the D-region in consequence of solar conditions, *Advances in Space Research*, *57*(4), 1029–1043, doi:10.1016/J.ASR.2015.12.025.
- Šulić, D. M., and V. A. Srećković (2014), A comparative study of measured amplitude and phase perturbations of VLF and LF radio signals induced by solar flares, *Serbian Astronomical Journal*, *188*, 45–54, doi:10.2298/SAJ1488045S.
- Sulzer, M. P., J. D. Mathews, and A. A. Tomko (1982), A UHF cross-modulation D region heating experiment with aeronomic implications, *Radio Science*, *17*(2), 435–443, doi:10.1029/RS017i002p00435.
- Taylor, W. L. (1967), VLF transmission loss calculated from spectral analyses of atmospherics, *Radio Science*, *2*(2), 139–145, doi:10.1002/rds196722139.

- Taylor, W. L., and K. Sao (1970), ELF attenuation rates and phase velocities observed from slow-tail components of atmospherics, *Radio Science*, *5*(12), 1453–1460, doi:10.1029/RS005i012p01453.
- Tellegen, B. D. H. (1933), Interaction between radio-waves?, *Nature*, *131*(3319), 840–840, doi:10.1038/131840a0.
- Thomas, J. O. (1963), Canadian Satellite: The Topside Sounder, *Tech. Rep. 3551*, Thomas1963.
- Thomas, J. O., A. R. Long, and D. Westover (1963), The calculation of electron density profiles from topside sounder records, *Journal of Geophysical Research*, *68*(10), 3237–3242, doi:10.1029/JZ068i010p03237.
- Thomas, L., and M. Bowman (1985), Model studies of the D-region negative-ion composition during day-time and night-time, *Journal of Atmospheric and Terrestrial Physics*, *47*(6), 547–556, doi:10.1016/0021-9169(85)90037-6.
- Thomas, L., P. Gondhalekar, and M. Bowman (1973), The negative-ion composition of the daytime D-region, *Journal of Atmospheric and Terrestrial Physics*, *35*(3), 397–404, doi:10.1016/0021-9169(73)90031-7.
- Thome, G. D., and L. S. Wagner (1971), Electron density enhancements in the E and F regions of the ionosphere during solar flares, *Journal of Geophysical Research*, *76*(28), 6883–6895, doi:10.1029/JA076i028p06883.
- Thomson, N. R. (1993), Experimental daytime VLF ionospheric parameters, *Journal of Atmospheric and Terrestrial Physics*, *55*(2), 173–184.
- Thomson, N. R. (2010), Daytime tropical D region parameters from short path VLF phase and amplitude, *Journal of Geophysical Research*, *115*(A09313), doi:10.1029/2010JA015355.
- Thomson, N. R., and M. A. Clilverd (2001), Solar flare induced ionospheric D-region enhancements from VLF amplitude observations, *Journal of Atmospheric and Solar-Terrestrial Physics*, *63*, 1729–1737.
- Thomson, N. R., and W. M. McRae (2009), Nighttime ionospheric D region: Equatorial and nonequatorial, *Journal of Geophysical Research*, *114*(A08305), doi:10.1029/2008JA014001.
- Thomson, N. R., C. R. Rodger, and M. A. Clilverd (2005), Large solar flares and their ionospheric D region enhancements, *Journal of Geophysical Research*, *110*(A06306), doi:10.1029/2005JA011008.
- Thomson, N. R., M. A. Clilverd, and W. M. McRae (2007), Nighttime ionospheric D region parameters from VLF phase and amplitude, *Journal of Geophysical Research*, *112*(A07304), doi:10.1029/2007JA012271.
- Thomson, N. R., C. R. Rodger, and M. A. Clilverd (2011), Daytime D region parameters from long-path VLF phase and amplitude, *Journal of Geophysical Research*, *116*(A11305), doi:10.1029/2011JA016910.

- Thottappillil, R., J. D. Goldberg, V. A. Rakov, M. A. Uman, R. J. Fisher, and G. H. Schnetzer (1995), Properties of M components from currents measured at triggered lightning channel base, *Journal of Geophysical Research*, *100*(D12), 25,711, doi:10.1029/95JD02734.
- Thrane, E., A. Haug, B. Bjelland, M. Anastassiades, and E. Tsagakis (1968), Measurements of D-region electron densities during the international quiet sun years, *Journal of Atmospheric and Terrestrial Physics*, *30*(1), 135–150, doi:10.1016/0021-9169(68)90047-0.
- Titheridge, J. (1995), Winds in the ionosphere—A review, *Journal of Atmospheric and Terrestrial Physics*, *57*(14), 1681–1714, doi:10.1016/0021-9169(95)00091-F.
- Tsugawa, T., A. Saito, Y. Otsuka, M. Nishioka, T. Maruyama, H. Kato, T. Nagatsuma, and K. Murata (2011), Ionospheric disturbances detected by GPS total electron content observation after the 2011 off the Pacific coast of Tohoku earthquake, *Earth, Planets and Space*, *63*(7), 875–879, doi:10.5047/eps.2011.06.035.
- Turunen, E. (1996), Incoherent scatter radar contributions to high latitude D-region aeronomy, *Journal of Atmospheric and Terrestrial Physics*, *58*(6), 707–725, doi:10.1016/0021-9169(95)00069-0.
- Unz, H. (1966), On the derivation of Booker’s quartic from Appleton-Hartree equation, *Proceedings of the IEEE*, *54*(2), 304–304, doi:10.1109/PROC.1966.4658.
- Volland, H. (1995), *Handbook of Atmospheric Electrodynamics*, CRC Press.
- Voss, H. D., W. L. Imhof, M. Walt, J. Mobilia, E. E. Gaines, J. B. Reagan, U. S. Inan, R. A. Helliwell, D. L. Carpenter, J. P. Katsufakis, and H. C. Chang (1984), Lightning-induced electron precipitation, *Nature*, *312*(5996), 740–742, doi:10.1038/312740a0.
- Wait, J. (1957), The attenuation vs frequency characteristics of VLF radio waves, *Proceedings of the IRE*, *45*(6), 768–771, doi:10.1109/JRPROC.1957.278470.
- Wait, J. R. (1958), Propagation of very-low-frequency pulses to great distances, *Tech. Rep. 3*.
- Wait, J. R. (1970), *Electromagnetic waves in stratified media*, 1st ed., 620 pp., Pergamon Press.
- Wait, J. R., and K. P. Spies (1964), Characteristics of the Earth-ionosphere waveguide for VLF radio waves, *Technical Note 300*, National Bureau of Standards.
- Wannberg, G., I. Wolf, L.-G. Vanhainen, K. Koskenniemi, J. Röttger, M. Postila, J. Markkanen, R. Jacobsen, A. Stenberg, R. Larsen, S. Eliassen, S. Heck, and A. Huuskonen (1997), The EISCAT Svalbard radar: A case study in modern incoherent scatter radar system design, *Radio Science*, *32*(6), 2283–2307, doi:10.1029/97RS01803.
- Watson, G. N. (1918), The diffraction of electric waves by the Earth, *Proceedings of the Royal Society A: Mathematical, Physical and Engineering Sciences*, *95*(666), 83–99, doi:10.1098/rspa.1918.0050.
- Watson, G. N. (1919), The transmission of electric waves round the Earth, *Proceedings of the Royal Society A: Mathematical, Physical and Engineering Sciences*, *95*(673), 546–563, doi:10.1098/rspa.1919.0032.

- Watt, A. D. (1967), *VLF radio engineering*, 703 pp., Pergamon Press.
- Whitehead, J. (1961), The formation of the sporadic-E layer in the temperate zones, *Journal of Atmospheric and Terrestrial Physics*, *20*(1), 49–58, doi:10.1016/0021-9169(61)90097-6.
- Whitehead, J. (1989), Recent work on mid-latitude and equatorial sporadic-E, *Journal of Atmospheric and Terrestrial Physics*, *51*(5), 401–424, doi:10.1016/0021-9169(89)90122-0.
- Whitehead, J. D. (1970), Production and prediction of sporadic E, *Reviews of Geophysics*, *8*(1), 65, doi:10.1029/RG008i001p00065.
- Yao, Y., J. Tang, P. Chen, S. Zhang, and J. Chen (2014), An improved iterative algorithm for 3-D ionospheric tomography reconstruction, *IEEE Transactions on Geoscience and Remote Sensing*, *52*(8).
- Yau, A. W., E. G. Shelley, W. K. Peterson, and L. Lenchyshyn (1985), Energetic auroral and polar ion outflow at DE 1 altitudes: Magnitude, composition, magnetic activity dependence, and long-term variations, *Journal of Geophysical Research*, *90*(A9), 8417, doi:10.1029/JA090iA09p08417.
- Yavuz, D. (1990), Meteor burst communications, *IEEE Communications Magazine*, *28*(9), 40–48, doi:10.1109/35.57696.
- Yee, K. (1966), Numerical solution of initial boundary value problems involving maxwell’s equations in isotropic media, *IEEE Transactions on Antennas and Propagation*, *14*(3), 302–307, doi:10.1109/TAP.1966.1138693.
- Yeh, K. C., and C. H. Liu (1974), Acoustic-gravity waves in the upper atmosphere, *Reviews of Geophysics*, *12*(2), 193, doi:10.1029/RG012i002p00193.
- Yue, J., S. L. Vadas, C.-Y. She, T. Nakamura, S. C. Reising, H.-L. Liu, P. Stamus, D. A. Krueger, W. Lyons, and T. Li (2009), Concentric gravity waves in the mesosphere generated by deep convective plumes in the lower atmosphere near Fort Collins, Colorado, *Journal of Geophysical Research*, *114*(D6), D06,104, doi:10.1029/2008JD011244.
- Yue, J., L. Hoffmann, and M. Joan Alexander (2013), Simultaneous observations of convective gravity waves from a ground-based airglow imager and the AIRS satellite experiment, *Journal of Geophysical Research: Atmospheres*, *118*(8), 3178–3191, doi:10.1002/jgrd.50341.
- Zbinden, P., M. Hidalgo, P. Eberhahdt, and J. Geiss (1975), Mass spectrometer measurements of the positive ion composition in the D- and E-regions of the ionosphere, *Planetary and Space Science*, *23*(12), 1621–1642, doi:10.1016/0032-0633(75)90090-2.
- Zhang, J., K. P. Dere, R. A. Howard, M. R. Kundu, and S. M. White (2001), On the temporal relationship between coronal mass ejections and flares, *The Astrophysical Journal*, *559*(1), 452–462, doi:10.1086/322405.
- Zoghzoghy, F. G. (2015), Statistical analysis and modeling of lightning using radio remote sensing, phdthesis, Stanford University.